Università degli Studi della Tuscia di Viterbo

Dipartimento di Scienze Ecologiche e Biologiche

Corso di Dottorato di Ricerca in
Ecologia e Gestione Sostenibile delle Risorse Ambientali (XXXIII ciclo)

TITOLO TESI DI DOTTORATO DI RICERCA

Biotechnological applications of renewable polyphenols in the development of functional nanomaterials:
Biocatalysts, bioinks and biosensors

Settore scientifico-disciplinare
s.s.d. CHIM/06

Tesi di dottorato di:
Dott.ssa Capecchi Eliana
Firma

Coordinatore del corso
Prof. Claudio Carere
Firma

Tutor
Prof. Raffaele Saladino
Firma

A.A. 2019/20

Thesis advisor
Raffaele Saladino

Author
Eliana Capecchi

Biotechnological applications of renewable polyphenols in the development of functional nanomaterials:
Biocatalysts, bioinks and biosensors

Abstract

This study concerns the valorization of lignin in the context of three green industrial applications: a) nano-materials and biocatalysis; b) bio-inks; and c) biosensors.

In the first section of the thesis, the production of novel nanocapsules of lignin and lignin mixed polyphenols is reported, and their antioxidant activity, UV-shielding properties, and electrochemical responsiveness adequately discussed. Mixed nanodevices showed physical and chemical properties higher than the homopolymer counterpart and of the native polyphenol, highlighting the presence of synergistic effects between the different components. The presence of UV-visible bathochromic shift in the analysis of the novel devices confirmed the occurrence of J-aggregates between the aromatic moieties of the polymers, affording a parallel orientation of the molecular units along the longitudinal direction by a head-to-tail repetitive motif. In addition, nanocapsules of mixed polyphenols showed a layer aggregation state higher than references, the specific morphology of their surface being dependent on the structural arrangement of the different components.

In the second section of the thesis, lignin nanoparticles have been applied in the immobilization of tyrosinase by different technologies, including physical adsorption, encapsulation and layer-by-layer (LbL) deposition, with or without the assistance of the glutaraldehyde reticulation procedure. Functionalized lignin nanoparticles were stable after the immobilization of tyrosinase, and the enzyme retained the catalytic activity in the selective synthesis of a large panel of bioactive catechols. The efficacy of the catalyst was dependent from the specific immobilization procedure. In the preparation of a second set of biocatalysts, lignin nanoparticles were used in the immobilization of laccase from *Trametes versicolor* using the procedure previously reported for tyrosinase. The activity

parameters and kinetic properties of the novel catalysts are described in detail, and cyclic voltammetry and amperometric analyses highlighted the occurrence of pseudo direct electron transfer (pseudo-DET) and mediated electron transfer (MET) mechanisms in the performance of the immobilized enzyme. The novel catalysts converted alcohols to the corresponding aldehydes with high selectivity in the presence of low molecular weight redox mediators, retaining the activity for more runs. Finally, lignin nanoparticles were used as a platform for the immobilization of horseradish peroxidase, in order to prepare biocatalysts useful for the bio-desulfurization of liquid fuel from recalcitrant and pollutant sulfur derivatives. In this latter case, the immobilization of the enzyme was facilitated by the use of concanavalin A. The novel catalysts were applied in the oxidative degradation of dibenzothiophene, that is a well recognized model of the recalcitrant sulfur derivatives. The reactions were performed with hydrogen peroxide as a green oxidant in a water biphasic system at 45 °C and room pressure. The catalytic activity was retained for more transformations highlighting the beneficial effect of the support in the reusability of the catalyst.

In the second section of the thesis, enzyme functionalized lignin nanoparticles were applied in the preparation of polyvalent bioinks, in order to remove toxic ingredients from the actual ink formulations. In these bioinks, the pigment, vehicle, binder, and additive are included in a single confined spherical space, that is the lignin nanoparticle. Bioinks with different shades of color, encompassing black, gray, yellow-like, pink-like, and red/brown hues, have been prepared by appropriate selection of the reactants and of the pigmentation process. In addition, lignin nanoparticles were able to protect the pigments from alkaline and UV-degradation treatments.

In the third section of the thesis, lignin nanoparticles have been used in the layer-by-layer immobilization of cascade of enzymes, namely horseradish peroxidase (HRP) and glucose oxidase (GOX). The role of concanavalin A as a molecular spacer in ensuring the correct orientation and distance between the two enzymes was confirmed by Forster resonance energy transfer measurements. Polyelectrolyte layers with different physical and chemical properties finely tuned the activity and kinetic parameters of the enzymatic cascade, cationic lignin performing as the best polyelectrolyte in the retention of the sensoring activity. Electrochemical properties, temperature and pH stability, and reusability of the novel nanodevices have been studied, as well as their capacity to perform as colorimetric biosensors in the detection of glucose using ABTS as redox mediator and dopamine as chromogenic substrate. The limit of detection (LOD) of these

devices was better than, or comparable to, that previously reported for other sensors. Thus, renewable lignin platforms worked as smart and functional devices for the preparation of green biosensors in the detection of glucose.

Table of Contents

Title Page i
Abstract iii
Table of Contents vi
List of Figures and tables viii
List of Papers xiii
Acknowledgments xiv

1 INTRODUCTION: Chemistry of renewable polyphenols

1.1 Renewable polyphenols from lignocellulosic biomass 16
1.2 Lignin: structure and properties 17
1.2.1 Lignin biosynthesis and biological functions. 18
1.3 Lignin isolation method: technical lignin 21
1.4 Chemo-physical and rheological properties. 23
1.4.1 Chromophores group and lignin colour. 24
1.4.2 Thermal and rheological properties of technical lignin. 25
1.4.3 Antioxidant activities and UV shielding properties. 26
1.4.4 Electron transfer and boosting effect on redox enzymes . .. 27

2 MICRO-NANO SCALED LIGNIN

2.1 Polyphenols: π-π supramolecular interaction. 29
2.2 Synthesis of lignin nanostructures. . . . .…30
2.2.1 Nanoprecipitation and Ouzo-Effect 31
2.2.2 Biocompatibility and biodegradable lignin nanoparticles . . 33
2.3 Functionalized lignin nanoparticles
2.3.1 Protein interaction. 35
2.3.2 Layer by Layer technology. 37
2.3.3 Bionanocatalysts: procedures and benefits 38
2.4 Layer-by-Layer preparation of microcapsules and nanocapsules of mixed polyphenols with high antioxidant and UV-shielding properties
2.4.1 Aim of work. 42
2.4.2 Experimental. 43
2.4.3 Results and discussion. 48

3 BIOCATALYSTS

3.1 Functionalized tyrosinase-lignin nanoparticles as sustainable catalysts for the oxidation of phenols
3.1.1 Aim of work. 61
3.1.2 Experimental. 62
3.1.3 Results and discussion. 67
3.2 Layer by layer supported laccase on lignin nanoparticles catalyzes the selective oxidation of alcohols to aldehydes
3.2.1 Aim of work. 77
3.2.2 Experimental. 79
3.2.3 Results and discussion. 83
3.3 Oxidative bio-desulfurization by nanostructured peroxidase mediator system
3.3.1 Aim of work. 95
3.3.2 Experimental. 96
3.3.3 Results and discussion. 100

4 BIOINKS

4.1 Enzyme-lignin nanocapsules are sustainable catalysts and vehicles for the preparation of unique polyvalent bioinks
4.1.1 Aim of work. 108
4.1.2 Experimental. 109
4.1.3 Results and discussion. 114

5 BIOSENSORS

5.1 Lignin nanoparticles are renewable and functional platforms for the concanavalin a oriented immobilization of glucose oxidase-peroxidase in cascade biosensing
5.1.1 Aim of work. 131
5.1.2 Experimental. 132
5.1.3 Results and discussion. 137

CONCLUSIONS

REFERENCES

List of figures

Figure 1.1 Hierarchal structure of wood.

Figure 1.2 Actual lignin valorization strategies for the production of biofuels, products and composites.

Figure 1.3 Proposed model for lignin oligomer (in upper part) and protolignin from gymnospermous wood.

Figure 1.4 An overview of lignin distribution, biosynthesis, and structure.

Figure 1.5 Pathways for the biosynthesis of monolignols.

Figure 1.6 Kraft reactions and β-O-4 cleavage.

Table 1 Main properties of common technical lignins.

Figure 1.7 Colour of 45 lignin samples arranged in order of decreasing brightness

Figure 1.8 Chromophores and leucochromphores from lignin

Figure 1.9. Structural characteristics and rheological behaviors of two technical lignin. Organosolv lignin and a kraft lignin. Representative chemical structural units of Organosolv lignin (A) and chemical structural unit of Kraft lignin (B).

Figure 1.10 Semi-commercial products with lignin

Figure 1.11 Possible reaction pathways of lignin with DPPH• free radical.

Figure 1.12 Chromophores in lignin structure and their approximates wavelenghts in the top part, and lignin UV absorption spectrum in the bottom part.

Figure 1.13 Lignin structure and the reversible redox reaction between quinone and hydroquinone

Figure 2.1 Typically visualization of benzene interaction, in panel A the four possible motifs. In panel B, the most stable π-π interactions.

Figure 2.2 Schematic representation of the arrangement for H and J aggregation and their different energy levels. θ is defined as the tilt angle between the axis connecting the center of chromophores in the aggregate and a transition dipole moment of each chromophore

Scheme 2.1 Summary of methods and procedure used for synthesis of LNP classified as precipitation method and non-precipitation method.

Figure 2.3 Schematic illustration of the nanoprecipitation process for production of CLPs.

Figure 2.4 Phase diagram of the ternary solute/solvent/water system with the bimodal line that represent the miscibility limit, the spinodal line that represent the limit of thermodinamical stability and the ouzo region (supersaturation zone) in wich the nanoparticles formation may occur.

Figure 2.5 Saturated concentration of lignin in γ-valerolactone water soluble mixture with different Solvent and lignin contents

Figure 2.6 Synthesis of a suspension of concentrated lignin nanoparticles by impinging jet mixer in semi-continuous flow

Figure 2.7 Trypan Blue staining of larvae after treatment with LNPs. In panel A and phenotypic changes in adult in panel B.

Figure 2.8 Main chemical interactions between lignin nanoparticles and proteins.

Figure 2.9 The layer by layer technology based on the self assembly of anionic and cationic polyelectrolytes

Figure 2.10. Chemical structure of synthetic and natural polyelectrolytes.

Figure 2.11 The main chemical approaches to immobilize multienzymatic complex.

Table 2. Total amount of polyphenols deposited in microcapsules and nanocapsules.

Figure 2.12. Procedure for the preparation of microcapsules of mixed polyphenols LS and TA using MnCO3 particles as templates. Positive polyelectrolyte: PDDA or CH. Negative polyelectrolyte: LS and TA. The layer deposition was performed at pH 5.

Figure 2.13. SEM image of (PDDA/LS)3 1 (panels A and B) and (PDDA/LS)5 2 (panels C and D).

Figure 2.14. SEM image of (CH/LS)5 3 (panel A and panel C). Panel B shows microcapsules of CH alone.

Figure 2.16. SEM images of (PDDA/TA/PDDA/LS)5 6 at different magnification. Panel A: General particles view. Panel B: Detail of the predominant regular spherical shape motif. Panel C: Detail of the scratched surface motif.

Figure 2.17 SEM images of (CH/TA/CH/LS)5 7 at different magnification

Figure 2.18. SEM images of (PDDA/LS+TA)5 8 at different magnification. Panel A: large aggregates of partial fused spherical capsules. Panel B: magnification of the surface film-like motif

Figure 2.19. Preparation of mixed LS and TA nanocapsules. Panel A: Organosolv Lignin (OL) dissolved in THF was dialyzed against deionized water to yield NOL. Panel B: Preparation of NOL(CH/TA)5 9, NOL(CH/LS)5 10 and NOL(CH/TA/CH/LS)5 11. Cationic layers: CH. Anionic layers: TA and LS.

Figure 2.20. SEM images of NOL(CH/TA/CH/LS)5 **11** at different magnification. Quantitative 31P-NMR characterization of microcapsules and nanocapsules of mixed polyphenols.

Figure 2.21. Quantitative 31P-NMR spectra and signal assignment of commercial CH, LS, OL and TA, and of capsules.

Table 3. Functional group distribution (mmol/gram) for LS, OL, TA, (CH/TA/CH/LS)5 **7** and NOL(CH/TA/CH/LS)5 **11.**a

Figure 2.22. DPPH antioxidant scavenging activity of investigated microcapsules and nanocapsules presented as % of DPPH radicals inhibitions and IC50 values (μg/mL).

Figure 2.23. UV-Visible radiation absorbing capacity of investigated micro and nano-capsules.

Figure 2.24. CVs performed with GCE (dash-dotted line), NOL (black line), NOL(CH/TA)5 **9** (bluline), NOL(CH/LS)5 **10** (red line), and NOL(CH/TA/CH/LS)5 **11** (purple line).

Figure 2.25. CVs of NOL (A), NOL(CH/TA)5 **9** (C), NOL(CH/LS)5 **10** (B), and NOL(CH/TA/CH/LS)5 **11** (D)**.**

Figure 2.20. (A) Amperograms of NOL (black line), NOL(CH/TA)5 **9** (blu line), NOL(CH/LS)5 **10** (red line), and NOL(CH/TA/CH/LS)5 **11** (purple line).

Table 4. Functional OH distribution (mmol/gram) for parent OL and for OL-tyr after treatment with tyrosinase.

Table 5. M_w, M_n and M_w/M_n of OL tyr compared with the parent OL

Figure 3.1. Schematic representation for the preparation of catalysts **I-IV**.

Figure 3.2. SEM images of catalyst **I** and catalyst **II**. (**a**) General overview of catalyst **I**; (**b**) Selected magnification of catalyst **I;** (**c**) General overview of catalyst **II.**

Figure 3.3. Particle diameter distributions of OL nanocapsules and Catalyst **I-IV**

Figure 3.4. Confocal images of (**a**) Catalyst **I**; (**b**) Catalyst **II**

Figure 3.5 Zeta potential values of OL nanoparticles, OL PDDA nanoparticles and catalysts **I-IV**

Figure 3.6. SEM images of catalyst **III** in the first panel (**a**) and of catalyst **IV** in the second panel (**b**).

Table 6. Activity parameters of catalysts **I-IV.**

Figure 3.7. Cyclic voltammograms of OL nanocapsules (black line, A-D), Catalist **I** (red line, A), Catalyst **II** (red line, B), Catalyst **III** (red line, C) and Catalyst **IV** (red line, D) performed in 250 μM catechol solution (50 mM PBS buffer pH 6.5 + 100 mM KCl) at scan rate 5 mV s^{-1}.

Table 7. Kinetic parameters of Tyr and catalysts **I-IV**.

Figure 3.8. Oxidation of phenols **1**–**4** with catalysts **I–IV.**

Table 8. Oxidation of Phenols **1**−**4** with Native Tyrosinase and Catalysts **I-IV**.

Table 9. Recycling of catalyst **I-IV** in the oxidation of *para*-cresol **1.**

Figure 3.9. ^{31}P NMR analysis of phosphitylated lignin organosolv and cationic lignin (CATLIG) in presence of internal standard (N-hydroxy-5-norbornene-2,3-dicarboxylic acid imide).

Figure 3.10 Schematic representation for the preparation of catalysts **I**–**V**. Encapsulation (pathway A), physical adsorption (pathway B) and layer by layer (pathways C–E) immobilization procedures.

Figure. 3.11 SEM images of catalysts **I–V**.

Figure 3.12. ATR-FTIR spectra of catalysts **I–V**

Table 10 Activity parameters of catalysts **I–V**

Figure 3.13 Cyclic voltammetry analysis of catalysts **I–V** under pseudo-DET conditions.

Figure 3.14 Cyclic voltammetry analysis of catalysts **I–V** under MET conditions.

Figure 3.15 Amperograms of catalyst **I** (black), catalyst **II** (red), catalyst **III** (blue), catalyst **IV** (purple), and catalyst **V** (green) are reported in panel A. The fitting of the data by using Michaelis–Menten kinetic model are reported in panel B. The analyses were recorded by applying a fixed potential Eapp = −0.050 V vs. SCE under constant stirring (400 rpm). ABTS (25 μM) was injected every 40 s.

Table 11 Amperograms of catalysts **I–V** were recorded by applying a fixed potential of −0.050 V (vs. SCE) and injecting 25 μM ABTS every 40 s

Table 12 Kinetic parameters of catalysts **I**–**V**[a]

Figure 3.16 Application of catalysts **I–V** or native laccase in the oxidation of alcohols 1–5 to the corresponding aldehydes 6–10.

Figure 3.17 Conversion (%) of compound 2 after 6 runs.

Figure 3.18. SEM analysis of catalyst **IV** after the sixth run of oxidation of alcohol 3.

Table 14 Oxidation of compound 3 with catalyst **III** in the presence of different redox mediators
Figure 3.19. Preparation of biocatalysts **I-X**.

Figure 3.20. FT-IR analysis of Con A after deposition on organosolv lignin (OL)-LNPs (red line) and kraft lignin (KL)-LNPs (blue line). The FT-IR spectra of native OL-LNPs and KL-LNPs (yellow line and black line) are reported as references. The amide I (C=O) stretching band typical of the Con A structure is located at c.a. 1644 cm^{-1}.

Figure 3.21. Confocal image of **cat I** (Panel **A**) after fluorescein isothiocyanate (FITC) labeling and magnification of the emission site (Panel **B**).

Figure 3.22 Upper panel: Scanning Electron Microscopy (SEM) images of OL-LNPs and KL-LNPs. Lower panel: SEM images of **cat I-II** and **cat VII-X**, separately.

Figure 3.23. Upper panel: SEM images of **cat III-IV**. Lower panel: SEM images of **cat V-VI**.

Table 15. Activity parameters and kinetic data of **cat I–X**. [1.]

Table 16. Application of cat **I-X** in the oxidation of dibenzothiophene (DBT) as a model of oxidative desulfurization (ODS).

Figure 4.1. Structure model of lignin, and schematic preparation of functionalized lignin nanocapsules supporting tyrosinase and laccase.

Table 17. Kinetic parameters of functionalized lignin nanocapsules (**I-IV**).

Figure 4.2. SEM images of lignin nanocapsules. Panel A: organosolv lignin nanocapsules. Panel B: OL/CH/tyrosinase (II).

Figure 4.3. Size distribution and polydispersity index (PDI) of OL nanocapsules (blue line, PDI=0.349), compound (**I**) (red line, PDI=0.353), and compound (**II**) (orange line, PDI=0.382).

Figure 4.4 SEM images of OL/PDDA/laccase (III) (Panel A) and of OL/CH/laccase (IV) (Panel B).

Figure 4.5. Schematic representation of the synthesis and subsequent deposition of melanin in the reaction of OL/CH/tyrosinase (**II**).

Figure 4.5. TEM images of lignin nanocapsules. Panel A: Organosolv lignin nanocapsules. Panel B: Black lignin nanocapsules (**V**). Agglomerates of amorphous melanin are clearly evident on the surface of lignin.

Figure 4.6 SEM images of lignin nanocapsules. Panel A: Organosolv lignin nanocapsules. Panel B: Black lignin nanocapsules (**V**)

Figure 4.7. Comparison between the UV−vis-spectra of the KOH solution recovered during the preparation of compound (**V**) and the standard sample.

Figure 4.8 Melanin concentration after the work-up in KOH solution. Commercial melanin was used as reference.

Figure 4.9. Panel A: ATR-FTIR-spectra of melanin recovered from the KOH solution (blue line), and standard melanin (red line).

Figure 4.10. The first-derivative EPR analysis of sample (**V**). Red line: standard melanin. Green line: sample (**V**). Blue line: OL nanocapsules.

Table 18. Mean values of *g*-factor of samples (**V-VII**).

Figure 4.11. Schematic representation of the synthesis and subsequent deposition of pigments during the reaction of OL/CH/laccase (**IV**) with phenol derivatives.

Figure 4.12. Panel A: SEM image of the yellow-like lignin nanocapsules (**VIII**). Panel B: TEM image of the yellow-like lignin nanocapsules (**VIII**).

Figure 4.13. UV-visible titration of the reaction between OL/CH/laccase (**IV**) and epicatechin. Newly synthesized epicatechin polymer showed a characteristic absorption peak in the 325–800 nm range.

Figure 4.14. ATR-FTIR spectra of compounds (**VIII**) and (**IXa**). Panel A (red line): absorption bands of compound (**IV**).

Figure 4.15. TEM image of nanocapsules (**IXa**).

Figure 4.16 Unproductive OL/CH/laccase (**IV**) catalyzed polymerization of phenol derivatives

Figure 4.17. Panel A: Reflectance spectra of colored lignin nanocapsules (**V-VIII**), (**IXa-b**), (**Xa-b**) and (**XIa-b**).

Table 19. Variations of the chromatic coordinates L*, a*, b* and total color change (ΔE*) of compound (**V**) and (**VIII**).

Figure 5.1 Schematic representation of the immobilization of HRP and GOX on LNPs.

Figure 5.2. Loading of Con A on LNPs during different adsorption procedures.

Figure 5.3. ATR FT-IR analysis of LNPs/Con A and LNPs/polyelectrolyte/Con A samples.

Figure 5.4 Size distribution of LNPs (Red line, 219 nm), LNPs/CATLIG (Black line, 234 nm) and LNPs/CATLIG/ConA (Blue line, 244 nm)

Figure 5.5 ATR FT-IR analysis of LNPs/PDDA (azure line), LNPs/CH (blue line) and LNPs/CATLIG (orange line)

Figure 5.6. Scanning electron microscopy images of Bio I (panel A), Bio II (panel B), Bio III (panel C), and Bio IV (panel D). Panel E and panel F: magnification (x 800 K) of Bio I and Bio IV, respectively.

Table 21. Immobilization and activity yield of enzymatic cascade systems produced by the random immobilization of HRP and GOX on the surface of LNPs.

Table 22. Activity and kinetic parameters of **Bio I-IV**.

Table 23 Activity retained after different temperature condition and reusability test of **Bio I-III** and **IV**

Figure 5.7. pH stability of Bio I and Bio III-IV.

Figure 5.8: Cyclic voltammetry analysis of LNPs compare to GCE alone. LNPs and GCE (blue line and grey line, respectively).

Figure 5.9 Cyclic voltammetry analysis of Con A/HRP-GOX compared to Bio I and the random immobilization of HRP and GOX on LNPs without the use of Con A.

Figure 5.10. Laser confocal scanning microscopy of **Bio IV**.

Figure 5.11. ABTS and dopamine colorimetric assay of **Bio IV.**

Figure 5.11. ABTS and dopamine colorimetric assay of **Bio IV.**

Figure 5.12. Limit of detection (LOD) of HRP-GOX, ConA/HRP-GOX, and Bio I and Bio III devices.

Table 24. Limit of detection value (LOD) for **Bio I** and **Bio III-IV**.

Figure 5.13: Scanning electron microscopy image (SEM) of **Bio IV** after biosensing performance with chromogenic substrates.

List of papers

- Capecchi, E., Piccinino, D., Tomaino, E., Bizzarri, B.M. Polli, F., Antiochia, R., Mazzei, F., Saladino R. (**2020**). Lignin nanoparticles are renewable and functional platforms for the concanavalin a oriented immobilization of glucose oxidase–peroxidase in cascade bio-sensing. RSC Advances, 10, 29031.

- Di Matteo, L., Bulletti, L., Capecchi E., La Viola, A., Piccinino, D., Piscopo, V. (**2020**). Perspectives of Using Lignin as Additive to Improve the Permeability of In-Situ Soils for Barrier Materials in Landfills. *Sustainability*, 12, 5197.

- Capecchi, E., Piccinino, D., Bizzarri, B.M., Botta, L., Crucianelli, M., Saladino, R. (**2020**). Oxidative Bio-Desulfurization by Nanostructured Peroxidase Mediator System. Catalysts, 10, 3-13.

- Piccinino, D., Capecchi, E., Botta, L., Bollella, P., Antiochia, R., Crucianelli, M., Saladino, R. (**2019**). Layer by layer-supported laccase on lignin nanoparticles catalyzes the selective oxidation of alcohols to aldehydes. Catalysis Science and Technology, 9, 4125-4134.

- Capecchi, E. Piccinino, D., Bizzarri, B.M., Avitabile, D., Pelosi, C., Colantonio, C., Calabrò, G., Saladino, R. (**2019**). Enzyme-Lignin Nanocapsules Are Sustainable Catalysts and Vehicles for the Preparation of Unique Polyvalent Bioinks. Biomacromolecules, 20, 1975−1988.

- Piccinino, D., Capecchi, E., Botta, L., Bizzarri, B.M., Bollella, P., Antiochia, R., Saladino, R. (2018). Layer-by-Layer Preparation of Microcapsules and Nanocapsules of Mixed Polyphenols with High Antioxidant and UV-Shielding Properties. Biomacromolecules, 19, 3883−3893.

- Capecchi E., Piccinino D., Delfino I., Bollella P., Antiochia R., Saladino R., Functionalized Tyrosinase-Lignin Nanoparticles as Sustainable Catalysts for the Oxidation of Phenols. *Nanomaterials,* **2018**, *8*(6).

- Bizzarri, B. M., Botta, L., Capecchi, E., Celestino, I., Checconi, P., Palamara, A. T., Saladino, R. (2017). Regioselective IBX-Mediated Synthesis of Coumarin Derivatives with Antioxidant and Anti-influenza Activities. Journal of Natural Products, 80(12), 3247–3254.

Acknowledgments

Un ringraziamento importante va fatto ai componenti della mia famiglia, mio padre, mia madre e mia sorella senza i quali non avrei potuto iniziare il percorso di studi e che mi hanno aiutato in tutti i momenti difficili.

Per il sostegno e per la fiducia ringrazio il mio tutor, il professore Raffaele Saladino che ha manifestato sempre interesse in tutti i miei progetti dandomi un aiuto fondamentale nel maturare una visione ottimista della ricerca. Nondimeno ringrazio tutto il team di ricerca del laboratorio di Chimica organica, soprattutto Bruno, Lorenzo e Davide.

Ringrazio Davide non solo come collega, ma anche come compagno di vita che mi ha sostenuta con amore nel migliore modo possibile insegnandomi la preziosa arte della pazienza.

Un ringraziamento speciale va anche a tutti gli amici, lontani e vicini che hanno sempre creduto in me stessa.

Chapter 1
Introduction: Chemistry of renewable polyphenols

1.1 Renewable polyphenols from lignocellulosic biomass

Circular Economy and Green Chemistry are the pillars for the emergence of a new eco-sustainable strategy based on the valorization of renewable materials and agroindustrial wastes, possibly avoiding the use of petroleum-based resources .[1]

The objective of this strategy is a new economical system in which the traditional market laws are balanced by environmental considerations. [2] In this thesis, green bio-nanotechnological processes have been developed to valorize polyphenols from lignocellulosic wastes.[3] The chemical composition of lignocellulosic biomass, comprising crystalline and partly amorphous cellulose fibrils (35-50%) embedded in a disordered matrix of hemicellulose (15-35%) and lignin (5-30%), is reported in **Figure 1.1** for the representative case of Coniferous tree.

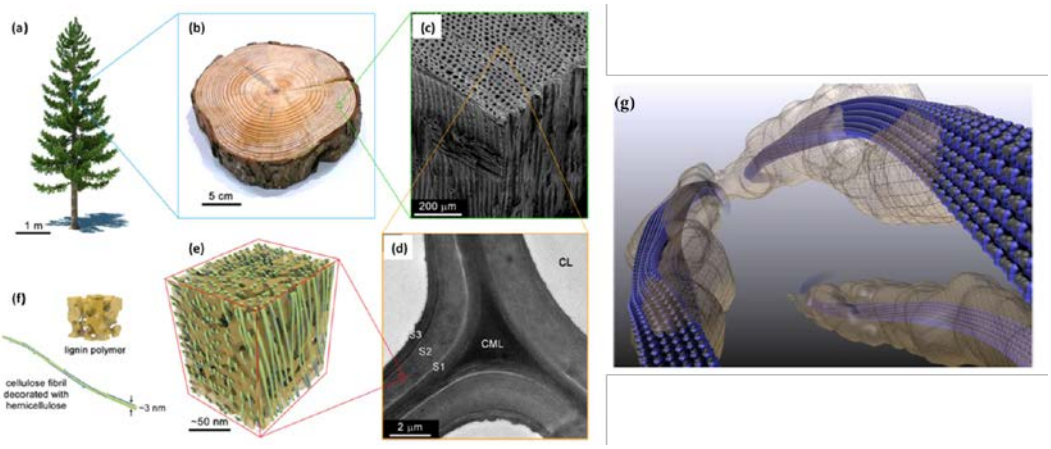

Figure 1.1 The hierarchal structure of wood. (a) Coniferous tree. (b) Photograph of trunk section from a pine tree. (c) Electron microscopy image of the tissue structure softwood. (d) Electron microscopy image showing the ultrastructure wood cell wall. CL, cell lumen; CML, compound middle lamella; S1, S2, and S3 denote layers of the secondary cell wall. (e) Schematic of the nanoscale architecture of lignocellulose. (f) Idealized depiction of an amorphous lignin polymer and a cellulose elementary fibril decorated with hemicellulose (microfibril). (g) Atomic models of cellulose elementary fibrils exhibiting the nanostructural geometry obtained by computational analysis of transmission electron tomographic reconstructions. Blue-color indicates cellulose, and gray color indicates lignin.

The production of lignocellulosic wastes is manly related to forestry and agro-industrial activities, catering, household garbage, and large-scale distribution. The use of these wastes as a primary/secondary material in industrial applications represents a big challenge, since they are responsible for pollution.[4] In fact, the inappropriate storage and the burning of lignocellulosic biomass results in the production of ammonia and methane that contribute to global greenhouse gas emission.[5,6]

In the last years, biorefinery platforms have been realized for the valorization of lignocellulosic materials. They encompass a cascade of operative units for the separation of the main components present in the raw material (extractives, cellulose, emicellulose and lignin), followed by the transformation of any fraction in high-added value products. In this context, polysaccharades are generally converted into bio-fuels by fermentative processes,[7] while extractives and lignin are used for the production of fine-chemicals, specialties and commodities.[8] Despite the efforts, further technological innovation is required for the complete valorization of lignin, due to the high amounts of wastes actually available for this polymer. [9,10] Potential applications can be envisaged in the preparation of advanced and functional materials, pharmaceutical products and devices, and sensoring.[11] In this thesis, the development of nano-materials and biocatalysis, bio-inks and biosensors, has been discussed in the context of the design and application of lignin nanoparticles.

1.2 Lignin: structure and properties

Lignin is the most abundant polyphenol in nature. It is produced as a waste from biorefinery and pulp and paper industries.[12] The attention for the valorization of lignin to high-added value products greately increased in the last 20 years[13] by developing novel technologies for its conversion to bio-fuels, specialties, commodities and advanced materials. A schematic representation of the targets actually proposed for lignin wastes is reported in **Figure 1.2**. Only a little part of these applications has come to the final market. This is in part due to the gap existing between the lignin producers and market off-takers, which slows down lignin market penetration, as well as to the necessity of developing a novel lignin targeted technology. Moreover, the new lignin applications need to be tested and adequately improved to meet market specifications and to become adequate to end-users. [14] The increment in the market of lignin is expected to increase in the context of Circular economy and Green chemistry perspectives.[15] The worldwide production of lignin is approximately 100 million tonnes/year, and the annual growth rate calculated to be 732.7 million of dollars in 2015, and evaluated in the future as 913.1 million of dollars in 2025.16 (CAGR) is expected to increase to 2.2% every year. The relative marked has been calculated to be 732.7 million of dollars in 2015, and evaluated in the future as 913.1 million of dollars in 2025.[16]

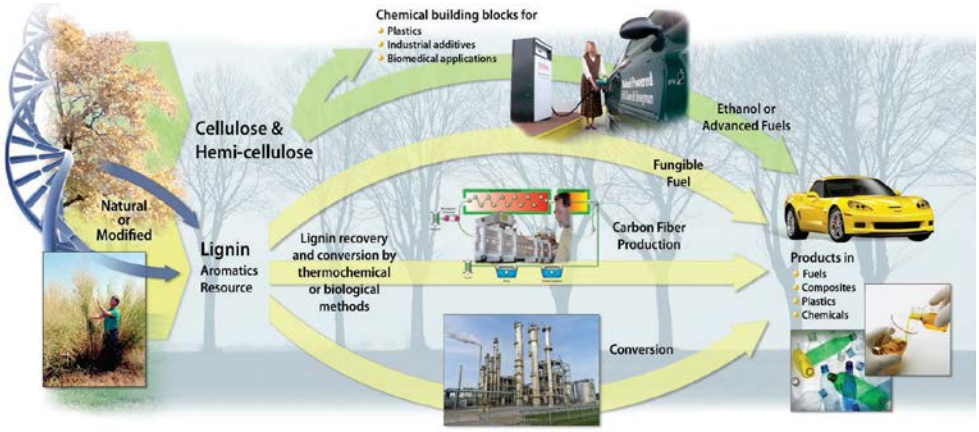

Figure 1.2 Actual lignin valorization strategies for the production of biofuels, products and composites.

1.2.1 Lignin biosynthesis and biological functions

Lignin is commonly distributed in primary and secondary cell walls in a wide range of plants.[17] It acts as a structural component adding strength and rigidity to the cell, and allowing the transport of water and solutes through the xylem system. In addition, it provides a physical barrier against pathogens and other environmental stresses.[18] Inside the cell lignin is usually indicated as protolignin. The 3D ultrastructure of protolignin is difficult to analyze without distruptive procedures. Computational analysis[19] suggests the presence of a certain degree of regularity in protolignin.[20] Fadon and Hatcher postulated for protolignin two different levels of conformational structure, represented by ordered helicoidal oligomers organized in a spiral-like network (**Figure 1.3**).[21, 22]

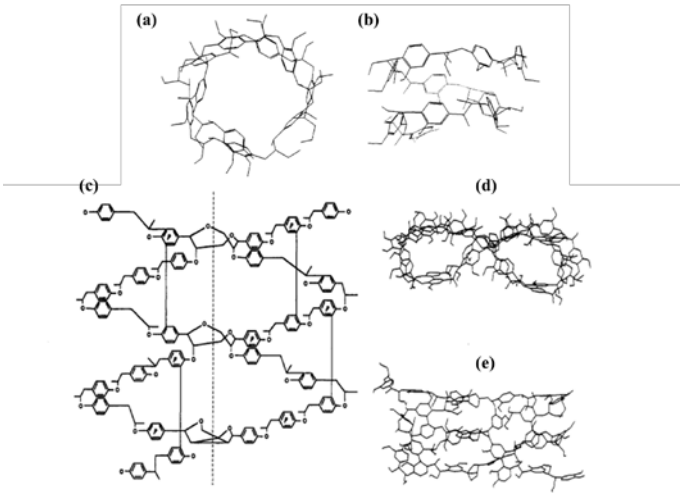

Figure 1.3 Proposed model for protolignin oligomer and lignin from gymnospermous wood. Helical conformation of protolignin oligomeric structure by computational model. (a) plan view, (b) side view. In panel (c-e) three-dimensional representation of the resulting structure of ordered lignin (c) The dashed line separates the two helical systems. (d) Three-dimensional representation of the structure in plan view (e) Three-dimensional representation of the structure viewed from the side.

The biosynthesis of lignin can be induced by various biotic and abiotic conditions, including wounding, pathogen infection, metabolic stress, and perturbations in the cell wall structure.[23]

Lignin is a polyphenol produced from the shichimic acid pathway by formation of phenyl alanine as a key intermediate (**Figure 1.4**). [24] After a deamination step, and a series of hydroxylation, *O*-methylation reactions, and reduction steps, the starting compound is transformed into three lignin monomers (monolignols), namely *p*-coumaryl (4-hydroxycinnamyl) alcohol, coniferyl (3-methoxy 4-hydroxycinnamyl) alcohol, and sinapyl (3,5-dimethoxy 4-hydroxycinnamyl) alcohol. Upon incorporation into the lignin structure these monomers are referred as p-hydroxyphenyl (H), guaiacyl (G), and syringyl (S) units.

Except for a few numbers of cases, lignin from Gymnosperms is abundant in G-units (with minor quantities of H-units), while in the angiosperm dicotyledonous consists mostly of both G- and S-units.[25] H-units are found in high amounts in softwood lignin and grass.

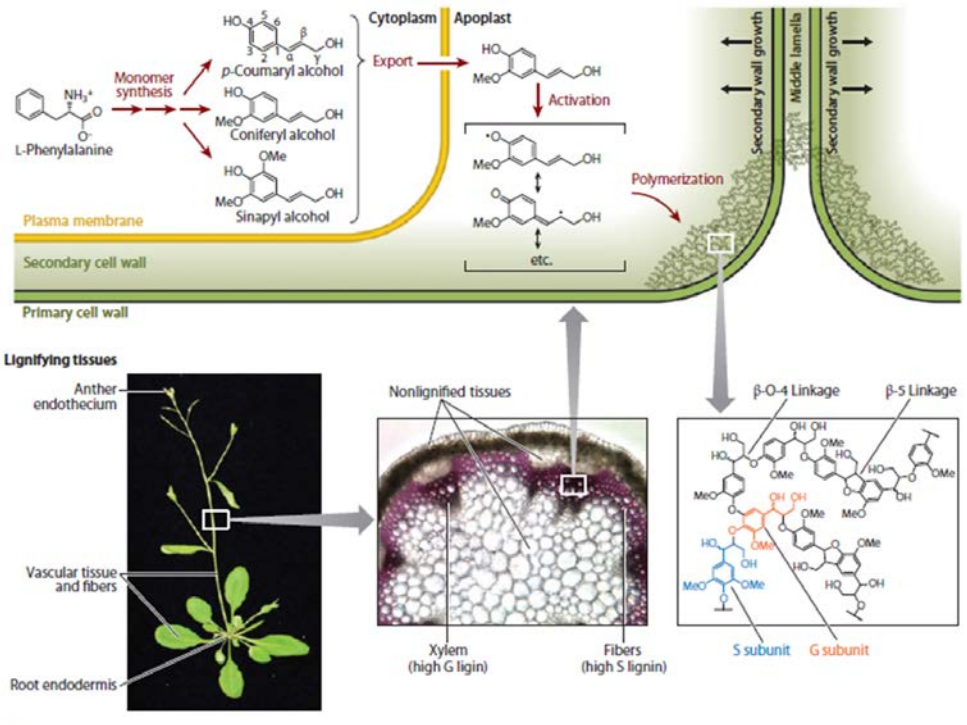

Figure 1.4 An overview of lignin distribution, biosynthesis, and structure. Gray arrows follow this progression from the whole organism to the tissue, cellular, and molecular levels.

Monolignols are exported at the extracellular space (apoplast) for incorporation into the polymer.[26] After reaching the apoplast, monolignols undergo single-electron

oxidation coupling mediated by wall-bound redox enzymes, laccases and peroxidases, that act in synergy to form reactive phenolic radical intermediates.[27] These radicals allow the formation of a large panel of dimeric sub-units, such as β-β, β-O-4, and β-5 dimers (**Figure 1.4**).

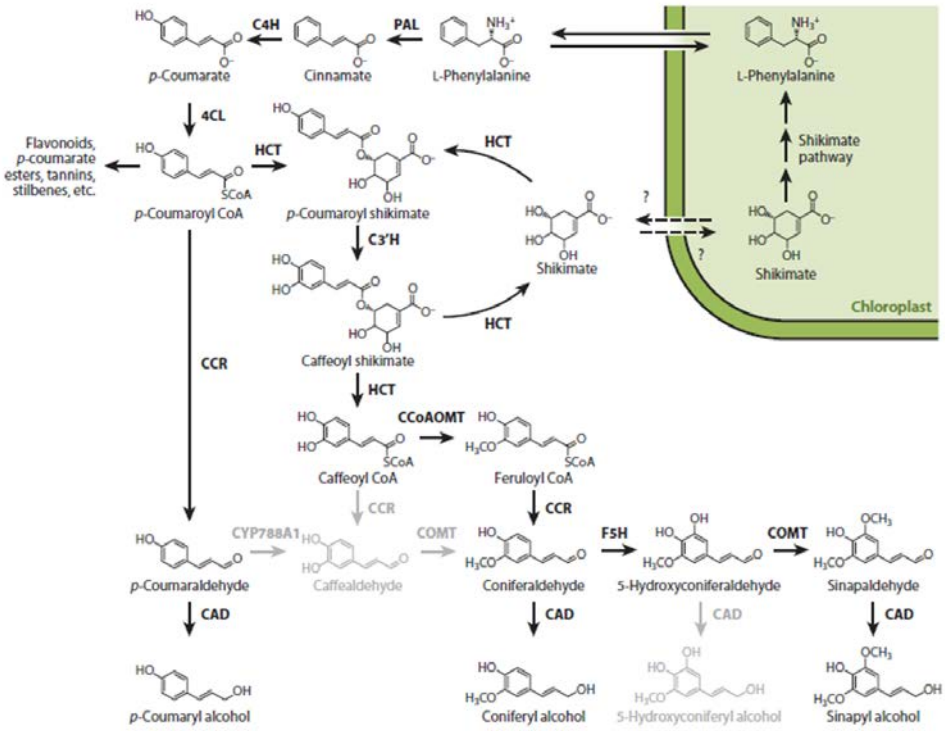

Figure 1.5. Pathways for the biosynthesis of monolignols. The enzymatic steps are catalyzed by PAL, (phenylalanine ammonia-lyase); C4H, (cinnamate4-hydroxylase); 4CL, (4-coumarate:CoA ligase); CCR, (cinnamoyl-CoA reductase);CAD, (cinnamylalcoholdehydrogenase) ;HCT, (hydroxycinnamoylCoA:shikimate/quinate hydroxycinnamoyl transferase); C3′H, (4-coumaroyl shikimate 3-hydroxylase); CCoAOMT, (caffeoyl-CoA 3-O-methyltransferase); COMT, (caffeic acid/5-hydroxyconiferaldehyde 3-O-methyltransferase); F5H, (ferulate/coniferaldehyde 5-hydroxylase).

The synthesis of monolignols from phenylalanine requires a series of enzymatic reactions: after the preliminary step of deamination, the hydroxylation step may occur at one, two, or three positions of the aromatic ring, successively the hydroxyl groups are methylated in one or two positions.[28] At the end of this biosynthetic pathway, two successive reductions of the monolignol side chain occur. (**Figure 1.5**). These enzymatic reactions are catalyzed by specific enzymes: ammonia-lyase (PAL), three different cytochrome P450-dependent monooxygenases (C4H, C3'H, and F5H), two methyltransferases (CCoAOMT and COMT), and two oxidoreductases (CCR and CAD). In addition to these enzymes 4CL and HCT are required to synthesize intermediates that serve as substrates for subsequent reactions (for the synthesis of flavonoids, tannins and stilbenes). 4CL is an ATP-dependent CoA ligase that catalyzes the synthesis of p-coumaroyl CoA.[29, 30]

1.3 Lignin isolation method: technical lignin

Large amounts of lignin wastes are obtained from biorefinery and pulp and paper industries. Lignin is present naturally in plants for approximately 300 billion tons,[31] and at least 100 million tons of technical or industrial lignins are collected per year. These industrial lignins are a useful material for the preparation of high value-added products.

The extraction processes for the separation of lignin from lignocellulosic biomass have a significant influence on the lignin structure, properties, and purity.[32] Expensive enzymatic extraction methods that allow the isolation and characterization of lignin with a structure as close as to protolignin have been developed for analytical purposes.[33] They are not useful for industrial aplications. At a larger scale, technical lignins with a highly modified structure are produced as a waste during the palp and paper process.[34] Industrial lignin wastes include: lignosulfonates from sulphite pulping,[35] kraft lignin from kraft pulping,[36] and soda lignin from the soda pulping process.[37] The latter processes are classified as alkaline treatments, otherwise, organosol lignin is obtained by organic solvent extraction under neutral conditions. [38]

i) Sulphite pulping

The sulphite pulping is based on the use of acids and sulphites (usually Ca/$MgSO_3$) at around 150°C.[39] In this case, sulphur is incorporated into the lignin as sulfonic acid functionalities. This confers to the product a relatively good water solubility.

ii) Kraft pulping

The kraft pulping requires the use of sodium hydroxide and hydrogen sulphide. This process results in hydroxylation and sulphytilation of lignin with concomitant degradation to relatively low molecular weight fragments.[36] One of the main degradative during the kraft pulping is the cleavege of the β-O-4 linkage[35] (see **Figure 1.6** for detailed information).

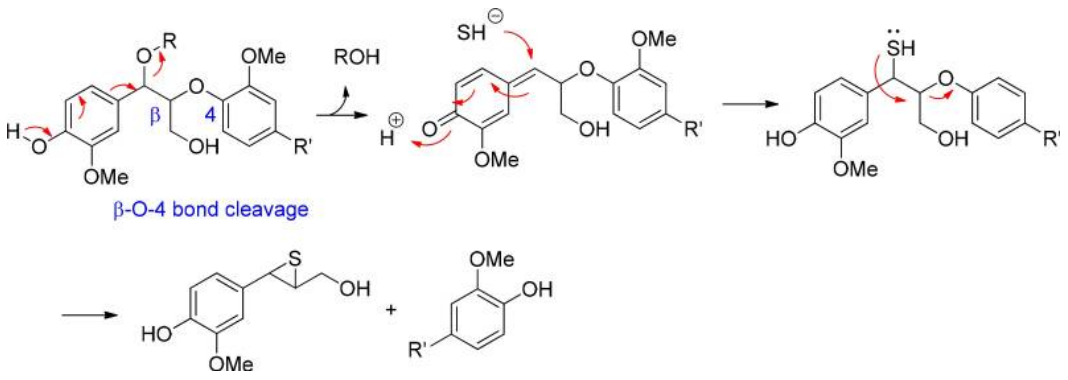

Figure 1.6 β-O-4 cleavage in kraft pulping.

i) Soda pulping process

The last alkaline process consists in the use of hydroxides and alkaline metals under relatively high pressure and temperature, favouring the cleavage of α– and β. ether linkages.[40] In this way, oligomeric lignin in the range of 1-5 KDa are produced.

ii) Organosolv process

Organosolv treatment is an extractive technique based on the use of organic solvents in combination with water. Acid catalysts can be added leading to relatively short lignin fragments (ca. 5 KDa). Organosolv is a promising alternative to standard pulping processes. In the organosolv treatment, lignin shows a lower content of residual carbohydrates and ash. Together with a cellulose pulp, high purity lignin and hemicellulose-derived products are coproduced and easily separated. Many types of organosolv processes have been developed based on different solvents and acids. Most commonly, organosolv processes use aqueous ethanol, typically adding sulphuric acid as a catalyst. However, Alcell lignin, which has been produced at the pilot scale, was generated without adding a catalyst.[41]

The isolation processes provide technical lignins with a different degree of polymerization and altered distribution of the functional groups.[42] For example, in the case of Kraft lignin or lignosulphonate, a significant amount of sulfur is introduced in the polymer. Low molecular weight lignin polymers and oligomers are usually obtained from the pulping processes. The most common types of technical lignin and their most representative properties are summarized in **Table 1**.

Lignin type	Sulfur-lignins		Sulfur-free lignins	
	Kraft	Lignosulfonate	Soda	Organosolv
Aspect				
Raw materials	Softwood Hardwood	Softwood Hardwood	Annual plants	Softwood Hardwood Annual plants
Solubility	Alkali Organic solvents	Water	Alkali	Wide range of organic solvents
Number-average molar mass (M_n – g mol^{-1})	1000–3000	15,000–50,000	800–3000	500–5000
Polydispersity	2.5–3.5	6–8	2.5–3.5	1.5–2.5
T_g (°C)	140–150	130	140	90–110

Table 1. Main properties of common technical lignins.

1.4 Chemo-physical and rheological properties

1.4.1 Chromophores group and lignin colour

The structure and color of technical lignins differ from their native counterpart. Native protolignin is expected to be a colorless or pale-yellow polymer.[43.44] After acid and alkali treatment, or organic solvent extraction, the color of lignin changes from light brown to dark brown (**Figure 1.7**). For example, kraft and sulphite pulping produce a reddish-brown lignin powder containing quinones and thiolic groups as chromophores.[45]

Figure 1.7 Colour of 45 lignin samples arranged in order of decreasing brightness

The complexity shade of color in technical lignins (Figure 1.7) is related to the fine modification of the chromophore groups. The chromophores in lignin include quinoids, catechols, aromatic ketones, stilbenes, conjugated carbonyls, and metal complexes.[46] All chromophores and leucochromophores (precursors of chromopheres) are summarized in **Figure 1.8**.

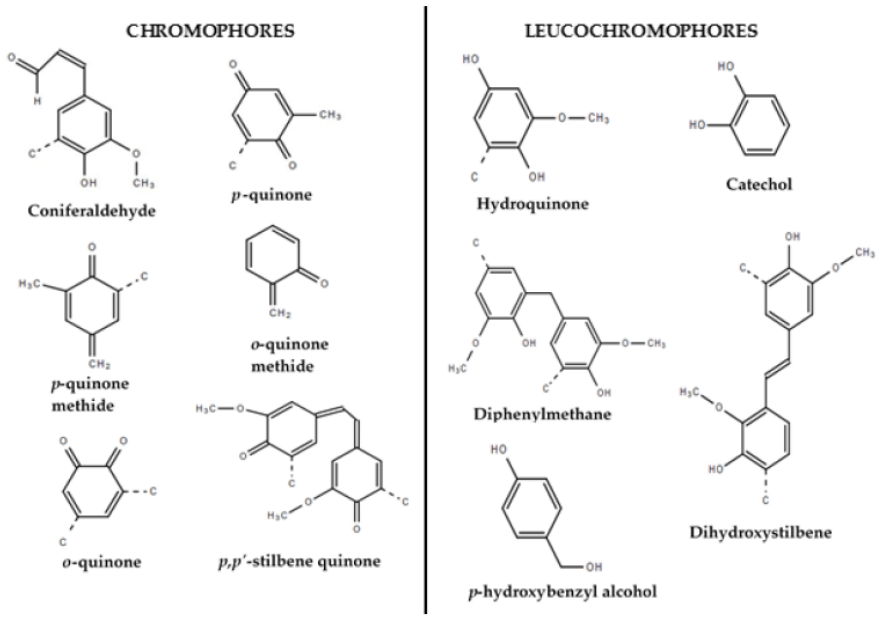

Figure 1.8 Chromophores and leucochromphores from lignin

The dark color of technical lignin is a limitation for the development of novel products.[47,48] For this reason, few examples are available for the application of technical lignins in cosmetic and cosmeceutical formulations.[46] Recently, procedures for the lightening of technical lignins have been reported,[49] they use both chemical and enzymatic treatments.[50] In addition, Wang and co-workers described a UV procedure combined to hydrogen peroxide oxidation for the lightening of lignin.[51]

1.4.2 Thermal and rheological properties of technical lignin

As previously stated, lignin contributes to the rheological behavior of cell walls, conferring rigidity and modulating the viscoelastic properties of wood. [52]

Technical lignins have been tested as rheology modifier in polymeric materials. In this context, kraft lignin showed a limited solubility and high thermal deformability than other lignin types. Instead, organosolv lignin showed higher rigidity and lower glass transition temperature (Tg) with respect to kraft lignin (170° for Organosolv lignin versus 190°C of kraft lignin) (**Figure 1.9**).[53] These effects are mainly due to the alteration of thermal viscosity and melting point of the composite. [54,55,56]

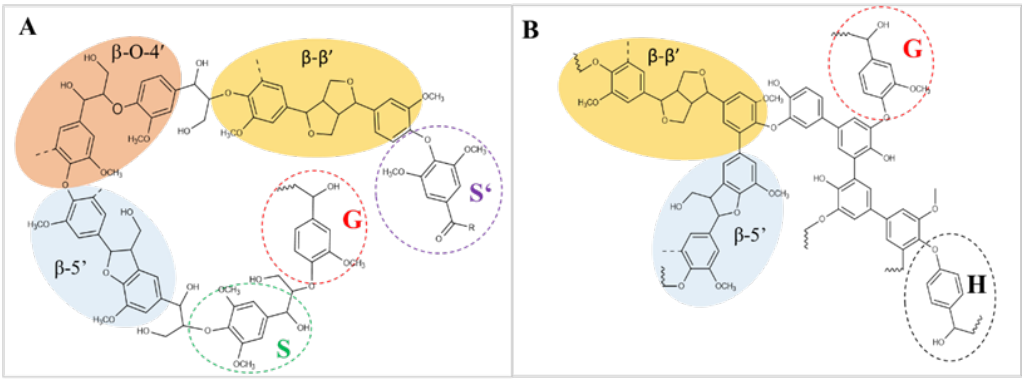

Figure 1.9. Structural characteristics and rheological behaviors of two technical lignin. Organosolv lignin and a kraft lignin. Representative chemical structural units of Organosolv lignin (A) and chemical structural unit of Kraft lignin (B).

The longest and most intensively application of technical lignins is reported in thermosetting materials and in a green alternative to toxic phenolic resins.[57] Organosolv lignin was used as a green alternative to phenol-formaldehyde resins, which are genotoxics.[58] Since 1980s, technical lignins have been used as stabilizers of thermoplastic materials,[59] being able to improve thermal properties, processability, oxidative and light stability. [60-62] For instance, a small amount of lignin added into polypropylene (PP) improves the mechanical and chemical stability of the composite under UV-light exposure.[63,64] Lignin is used as additive and filler in PE, ABS, PMMA, styrene-butadiene

rubbers,[65-67] and polylactic acid (PLA).[68] In particular, the Young module value of PLA was higher than the native polymer in the presence of lignin.[69] Amine salts of kraft lignin were used as dispersing agents in water-based pigments and binders in printing processes,[70] while organosolv lignin has been applied as a filler in ink formulations, improving the viscosity of the medium.[71] In a similar way, nitrate alkaline lignin esters, carboxylate softwood lignin, and acetylated lignin are binders in ink formulations.[72] The rheological properties of technical lignins is further improved by chemical functionalization procedures. The standard functionalization methods involve the use of crosslinking agents, such as isocyanate, polyamines, polyacrylate, and epoxy groups.[73] Recent examples of the application of technical lignin in advanced materials after functionalization procedures are reported in **Figure 1.10**.

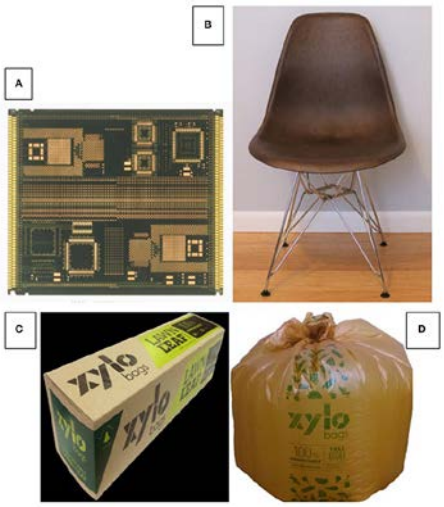

Figure 1.10 Semi-commercial products with lignin—(A) Prototype printed circuit board manufactured with glass fiber-reinforced (organosolv) lignin-containing (50%) epoxy resin (B) Prototype shell of injection-molded chair made from polypropylene/lignin derivative blend; and (C,D) commercial compostable waste bag made with melt-blown films of blends of hydroxypropyl (Kraft) lignin derivative and biodegradable polyester.[74]

1.4.3 Antioxidant activities and UV shielding properties

Lignin shows antioxidant property due to the huge amount of aromatic and phenolic moieties present in its structure.[75,76] The main factors that influence the antioxidant properties of lignin are the content of guaiacyl and syringyl units and the number of α-benzylic groups.[77] The antioxidant activity of lignin is usually evaluated by the 2, 2-diphenyl-1-picrylhydrazyl radical (DPPH•) assay.[78] A schematic pathways for the reaction of lignin with DPPH• is reported in **Figure 1.11**.

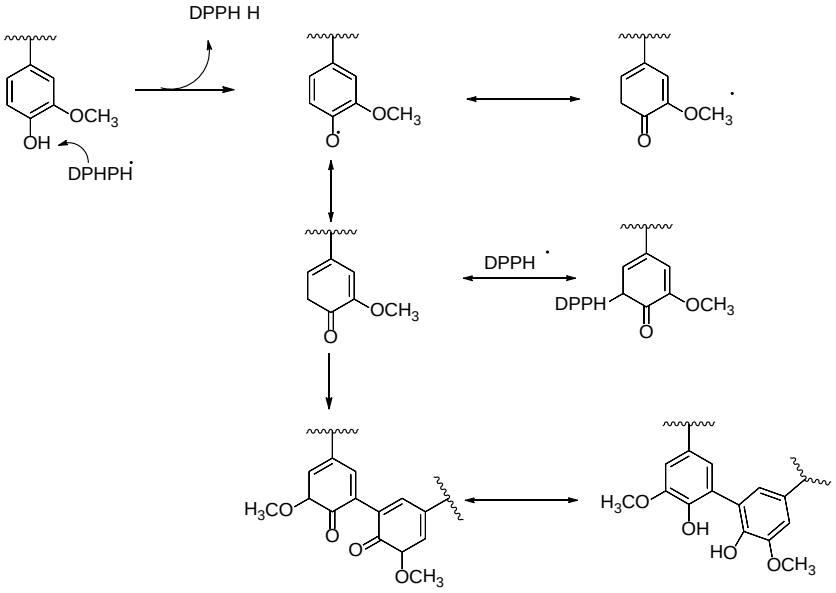

Figure 1.11 Possible reaction pathways of lignin with DPPH• free radical.

The applications of lignin as antioxidant have been reported in several studies,[79,80] making lignin a good alternative to toxic commercial compounds such as butylated hydroxytoluene (BHT) or butylated hydroxyanisole (BHA).[81]

Lignin has several UV chromophoric groups that absorb UV-A, UV-B and UVC radiation, such as carbonyl, cinnamaldehyde, hydroxyl groups and double bonds.[82] (see **Figure 1.12**).

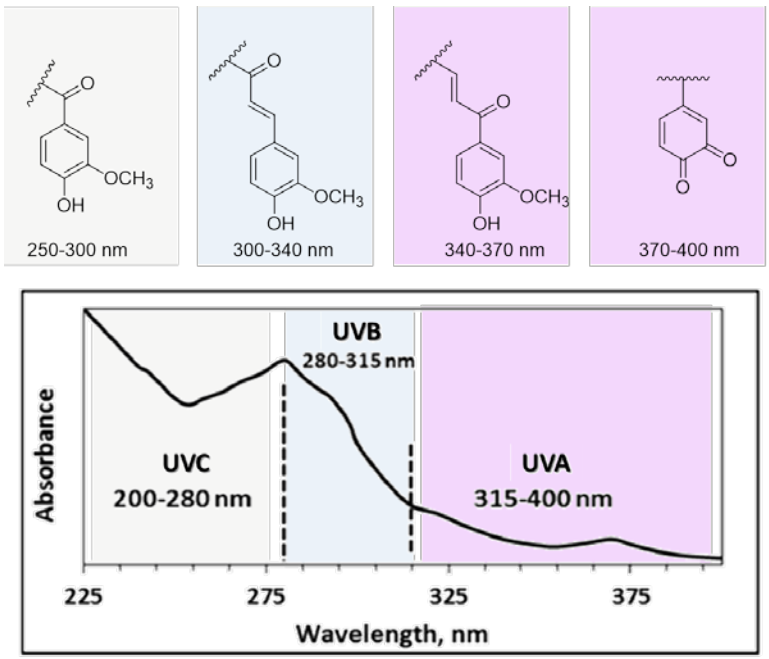

Figure 1.12 Chromophores in lignin structure and their approximates wavelenghts in the top part, and lignin UV absorption spectrum in the bottom part.

UV-radiation is responsible for biological damage due to formation of reactive oxygen species (ROSs) and superoxide anion radicals.[83] UV rays are also responsible for the degradation of organic compounds, discoloration of dyes and pigments, weathering and yellowing of plastics and films.[84-88] The presence of organosolv lignin in sunscreen formulations increased the sun protection factor (SPF) in a significant amount.[89] In addition, lignin can improve the photostability of UV sensitive natural substances, e.g. flavonoids.[90] Quercetin and other natural flavonoids are excellent antioxidants and have some benefits for human health, such as anti-cancer, anti-inflammatory, and anti-diabetic activities. The photostability of quercetin was significanly improved by lignin. [91]

1.4.4. Electron transfer and boosting effect on redox enzymes

The electron transfer properties and electrochemical responsiveness of lignin make it an attractive biopolymer for the development of biosensing and sustainable charge storage devices.[92,93] Lignin may work as an active component for reversible redox reactions through absorbing and releasing electrons and protons, due to the presence of reactive quinone/hydroquinone redox sites.[94,95,96] (see **Figure 1.13**)

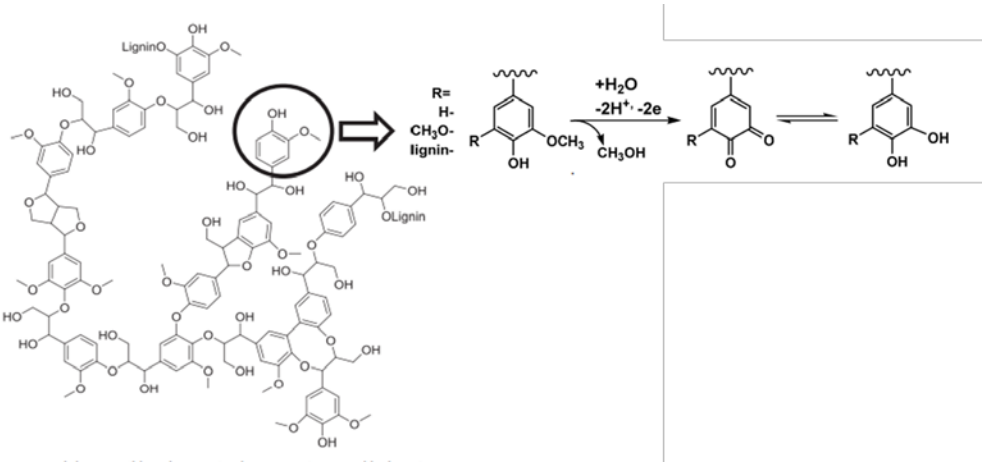

Figure 1.13 Lignin structure and the reversible redox reaction between quinone and hydroquinone

The application of lignin in electrochemistry includes the use of lignosulfonates and kraft lignin in the construction of renewable electrodes by incorporation into conductive electrode materials, such as glassy carbon, [97] conductive carbon, [98] and gold modified electrodes.[99] In all the cases, lignin exhibits high redox reversibility during the electro-oxidation cycle and the fastest electron transfer kinetics. Cyclic voltammetric investigations revealed that the surface modification of glassy carbon electrode with

lignin enhance the electroactivity of the overall system.[97,100] In particular, electrodes modified with lignin showed an efficient electroactivity towards the oxidation of histamine in phosphate buffer solution.[100] Glassy carbon electrodes functionalized with lignosulphonated showed a high sensibility in the detection of nicotinamide adenine dinucleotide (NADH) for biomedical applications. [101]

This promising technology was employed in the fabrication of eco-friendly lithium-ion batteries, [102] as well as for rechargeable batteries and supercapacitors.[103] A recent study evaluated the electrochemical responsivness of multi-walled carbon nanotubes (CNTs) functionalized with kraft lignin. The presence of lignin on the surface of CNTs exhibits higher electroactivity with respect to the pristine form, due to the formation of redox active quinone moieties. The reversible redox behavior of lignin after the adsorbtion on carbon nanotubes was utilized for charge storage purposes.[92]

The electron transfer properties of lignin increase the activity of copper-based enzymes.[104] Recently, it was demonstrated that lignin oligomers can act as a shuttle for the electron transfer processes to the active site of redox enzymes,[105] such as laccases, tyrosinase and Lytic Polysaccharide MonoOxygenases (LPMOs). [106]

Chapter 2
Micro-nano scaled lignin

2.1 Polyphenols: π-π supramolecular interaction

The π-π stacking interactions are effective in a broad range of biotechnological applications, such as protein immobilization, supramolecular interactions, and nanomaterial construction.[107]

The π-π stacking interactions are non-covalent interactions that occur between π orbitals of the aromatic rings. [108, 109] Four configurations of π-π stacking of the benzene rimg are possible as reported in **Figure 2.1** (panel A). [110] X-ray crystal analysis and computational studies[110,112] confirmed that the most stable conformations are the parallel (Y shaped geometry) and perpendicular conformations (T shaped geometry), representing a minimum of energy (**Figure 2.1** panel B).[113,114]

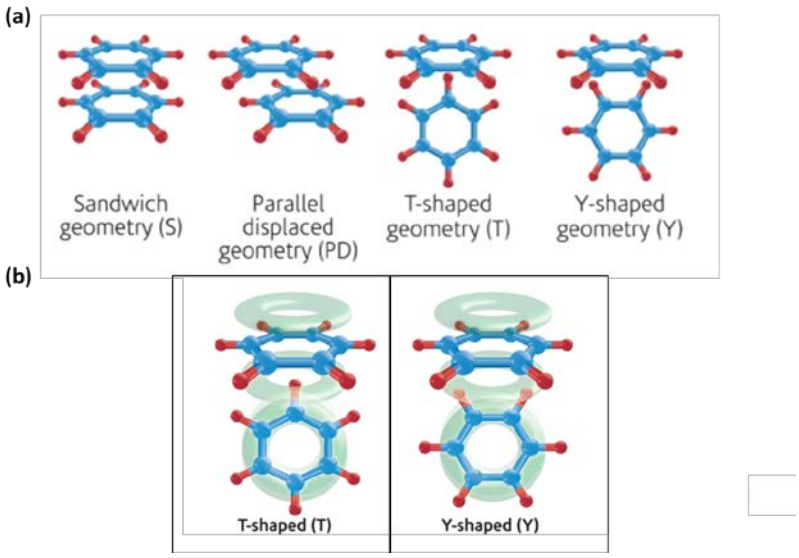

Figure 2.1 Typically visualization of benzene interaction, in panel A the four possible motifs. In panel B, the most stable π-π interactions.

The π-π supramolecular interactions influences the charge transfer processes and the spectral properties of polyphenols.[115] For example, in the case of lignin, the π–π interaction may result in two types of supramolecular aggregation states, namely H– and J–aggregations.[116] The energy level of H– and J–aggregations (in **Figure 2.2**) depends from the tilt angle θ between the molecular axis that connect the center of chromophores and the transition dipole moment of each chromophore. In particular, when the tilt angle is less than 54.7°, the aromatic groups of lignin form J–aggregates. When the tilt angle is higher than 54.7° the H- aggregates occurs.[117]

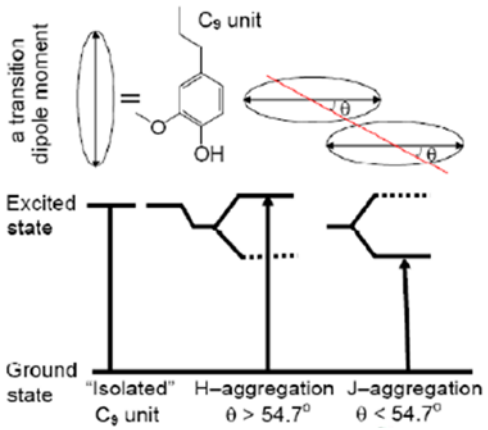

Figure 2.2 Schematic representation of the arrangement for H and J aggregation and their different energy levels. θ is defined as the tilt angle between the axis connecting the center of chromophores in the aggregate and a transition dipole moment of each chromophore.

When the aromatic groups are oriented in an ordered and stable structure, the abundance in J-aggregation modify the spectral properties of lignin.[118] According to this theory, called "coupling of molecular excitons", the enhancement of the J-aggregation would lead to a "redshift" of the UV and fluorescent spectrum (bathochromic shift).[119] The redshift favor the occurrence of electron and charge transfer processes, [120,121] providing novel redox and chemical patterns. In addition, π–π interactions regulate the self-assembly of lignin at the nanoscale level. The formation of these supramolecular interactions also provides the emergence of novel rheological and chemo–physical properties.[122,123,124]

2.2 Synthesis of lignin nanostructures

The application of renewable feedstocks in nanomaterials science received a great attention due to Green Chemistry and Circular economy concerns.[125-127] In this context, lignin polymers emerged as attractive alternatives to conventional organic materials.[128] Several procedures have been made in order to obtain nanostructured lignin, encompassing nanotubes, nanosheets, nanorods, nanoparticles, and empty nanocapsules. Nanoparticles and nanocapsules have proved to be very advantageous for many aspects, including their greater surface to volume ratio and electron transfer properties. In the last years, the methods for the preparation of lignin nanoparticles (LNPs) increased significantly overcoming drawbacks such as the low yield, the use of toxic solvents, and very long processing time. LNPs can be produced from different technical lignin under various synthetic methods as summarize in **Scheme 2.1**. These procedures can be classified into two main types; i) no precipitation methods and ii) precipitation

methods.[129] The no precipitation methods involve water/oil emulsion processes, [130] homogenization treatments,[131] and sonochemical preparations (with or without crosslinking agents).[132] These methods are ineffective for the scale-up due to the low yield of LNPs. Conversely, the precipitation methods provide high yield production of LNPs. The acid precipitation has been the earliest reported method for the preparation of size-controlled, biocompatible and stable LNPs.[133]

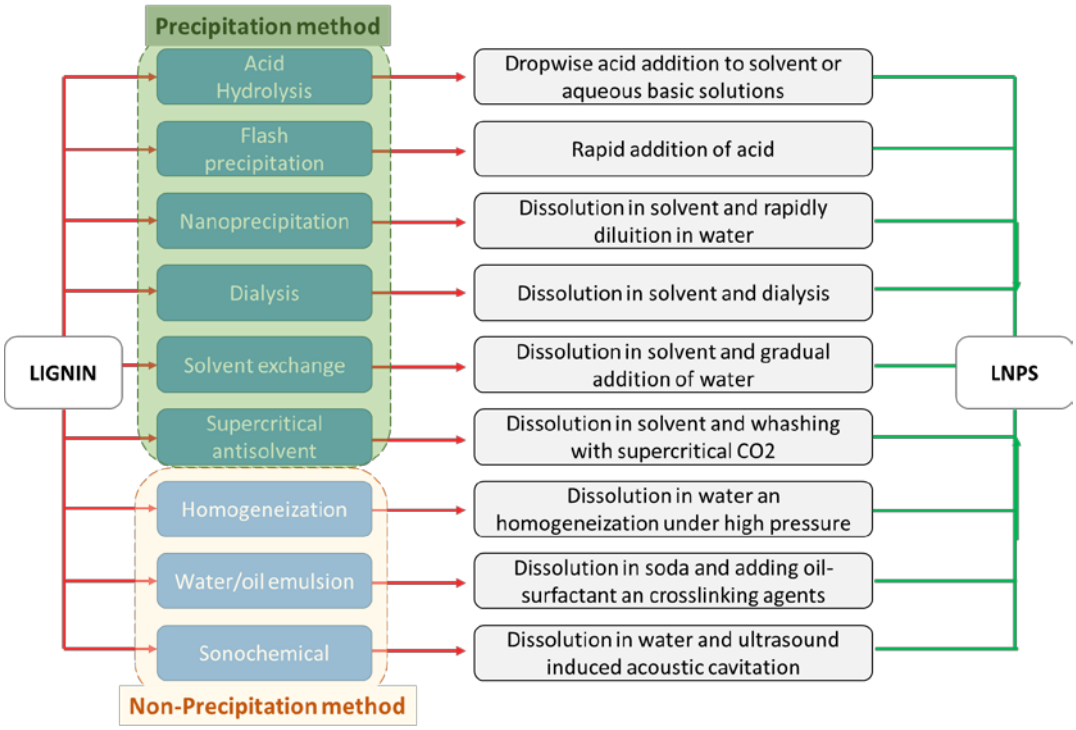

Scheme 2.1 Summary of methods and procedure used for synthesis of LNP classified as precipitation method and non-precipitation method.

Subsequently, Lievonen et al. introduced the dialysis procedure.[134] This process is based on a slow solvent exchange between a lignin solution in THF and a H_2O counterpart. Lignin, which is notoriously non-soluble in water, tends to minimize the contact with water, which slowly replaces THF. Some major drawbacks of dialysis procedure include its time-consuming feature and the need for treating large amounts of wastewater.

The nanoprecipitation procedure is another effective method for the preparation of LNPs. [135] In brief, lignin after solubilization in the organic solvent is poured fastly into water to yield lignin nanoparticles instantaneously. An example of nanoprecipitation of lignin nanoparticles in colloidal form (CLPs) is shown in **Figure 2.3**. CLPs were obtained with an average size of 80–100 nm, and remained stable for up to 30 days in different pHs conditions and temperatures.

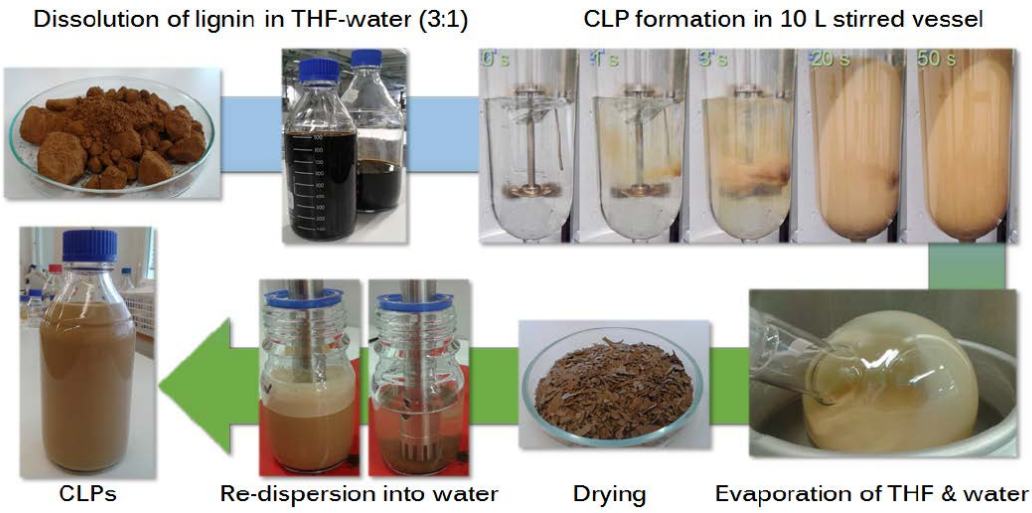

Figure 2.3 Schematic illustration of the nanoprecipitation process for production of CLPs

2.2.1 Nanoprecipitation and Ouzo-Effect

The nanoprecipitation mechanism is defined as a spontaneous microemulsification process, also denoted as ouzo effect.[135]

The "Ouzo effect" was named by Vitale and Katz from the generic example of the Greek beverage.[136] The major components of Ouzo (Pastis in France) are water (~55%), alcohol (~45%) and transanethol (~0.2%), a water-insoluble oil extracted from anise seeds. Upon dilution with water, anethol is no longer solubilized in the water/ethanol mixture. Ouzo becomes spontaneously milky due to the formation of long-lived metastable oil droplets.[137] A similar microemulsion process has been used for the synthesis of nanoparticles from poly(lactic acid) (PLA), poly(lactide-co-glycolide) (PLGA), poly(alkyl cyanoacrylate) (PACA), and poly(ε-caprolactone) (PCL).[138]

The theoretical background of the ouzo phenomena implies the study of the complex interactions that occur in a ternary system (solute, solvent, and water) (**Figure 2.4**). The efficiency and the overall stability of the nanostructuring process is mainly linked to the optimal concentration of the solute.[139,140] The optimal concentration of the solute must be very high; this concentration is called supersaturation, defined as ouzo region.

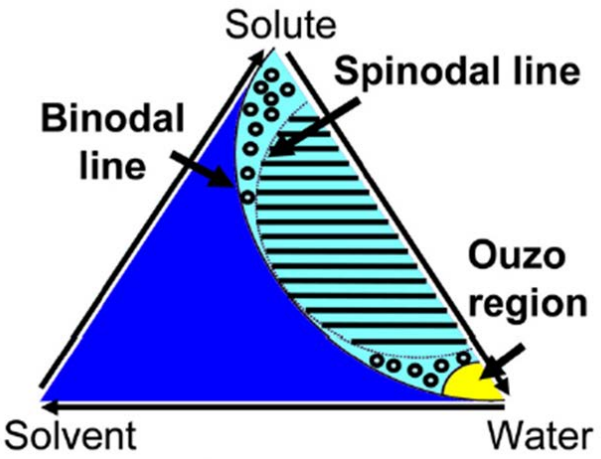

Figure 2.4 Phase diagram of the ternary solute/solvent/water system with the bimodal line that represent the miscibility limit, the spinodal line that represent the limit of thermodinamical stability and the ouzo region (supersaturation zone) in wich the nanoparticles formation may occur

At the supersaturation region, some nucleation centers are formed. The fluctuation around these nuclei led to the formation of a cluster of nanoparticles.[141] The efficiency of the nanoprecipitation process, the colloidal stability, and the number of cluster of nuclei, results to be strictly dependent from the supersaturation value, the interfacial tension, and the diffusion coefficients of the solute molecules.[138]

The supersaturation plays an important role in controlling the yield and size of nanoparticles. For example, the supersaturation region for the production of lignin nanoparticles was evaluated using the green solvent γ-valerolactone, (see **Figure 2.5**).[142] The supersaturation region comprised a range of concentration relatively higher with respect to other nanoprecipitation procedures, the amount of lignin in the final solution being in the range of 25 g/L to 125 g/L.

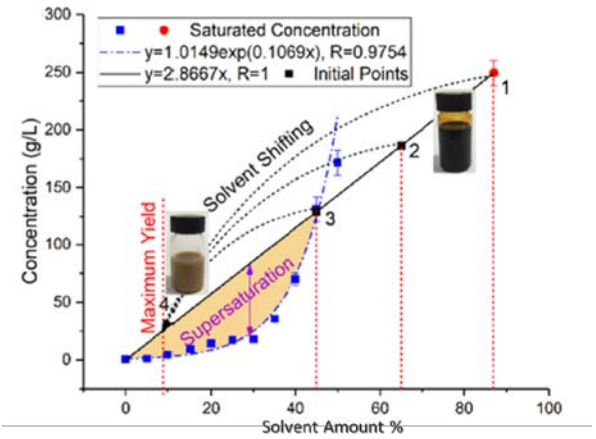

Figure 2.5 Saturated concentration of lignin in γ-valerolactone water soluble mixture with different Solvent and lignin contents.

In order to better perform the nanoprecipitation process there are four main type of technologies: [143,144] i) dropwise process, ii) pressure drive injection device; iii) impinging jet mixer; and iv) the Y junction. In the first case, the nanoprecipitation occurs by dropping the organic solution into the aqueous phase. Unfortunately, this technology induces a continuous change in the composition of the solute/solvent/ non-solvent mixture. On the other hand, the other processes, involve a rapid mixture of the two phases and a continuous flow apparatus for the recovery of nanoparticles.[138]

Recently, Conner et al.[145] set up a pilot scale process for the production of lignin nanoparticles with the technology of impinging jet mixer in semi-continuous flow (see **figure 2.6**). The technology consists of a vessel that holds the pure water at the beginning of the process and at the end contains the LNP suspension in acetone. In particular, water circulate through the system and it is recycled in a loop using a micropump. Contemporarly, a syringe pump continuously injects lignin into the flowing water stream.

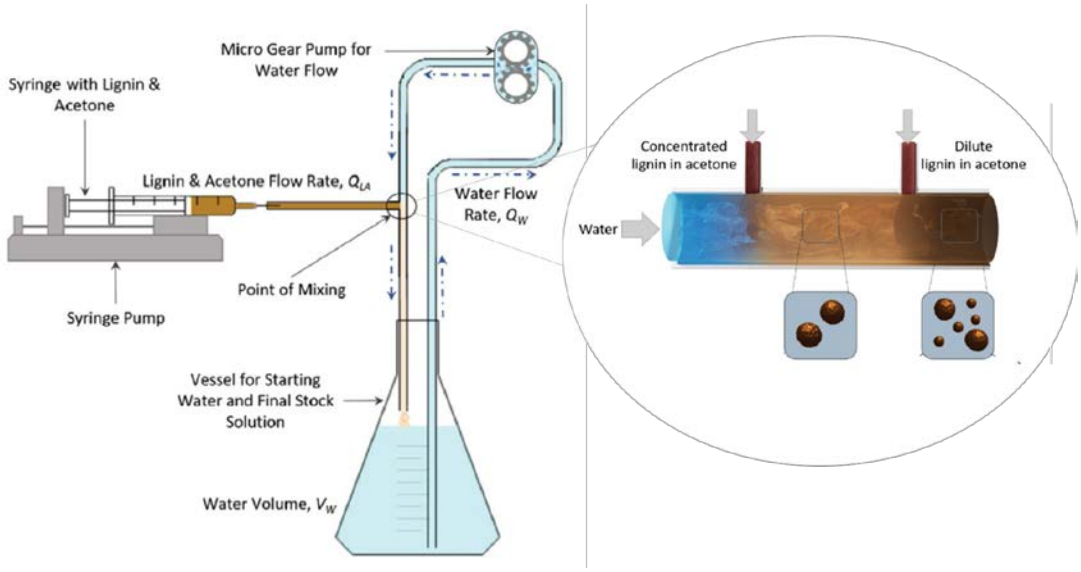

Figure 2.6 Synthesis of a suspension of concentrated lignin nanoparticles by impinging jet mixer in semi-continuous flow.

2.2.2 Biocompatibility and biodegradable lignin nanoparticles

Lignin can be considered safe, but the nano size level imposes some insights about the toxicity for the human cells and the environment. In humans, the nanostructures easily cross biological membranes and long exposure leads to their accumulation in cells, tissues and blood.[146] To overcome these issues, different authors have conducted biocompatibility studies. Recently, the cytotoxicity of lignin nanoparticles was performed on murine macrophage cell lines and the lignin nanoparticles showed high

biocompatibility for these immune cells.[147] Other authors incubate kraft lignin nanoparticles with three types of cell lines for 72 hours: human breast adenocarcinoma (MCF-7), human alveolar epithelial adenocarcinoma (A549) and human embryonic kidney (HEK-293). The cytotoxicity MTT assay showed that lignin nanoparticles are less toxic in the case of normal cell line HEK 293 than the other cases, the cytotoxicity increasing for human breast cancer cell lines.[148] The *in vivo* genotoxicity of different concentrations of kraft lignin nanoparticles was evaluated by the viability and phenotypic assay on the larvae and adults of *Drosophila melanogaster*. These tests demonstrated the lack of significant genotoxicity. For example, the trypan blue staining test of the larvae treated with lignin nanoparticles showed the absence of the typical yellow color that occur when trypan blue binds damaging cells (**Figure 2.7** panel A). In addition, a similar experiment was conducted for the *Drosophila Melanogaster* in adult form. The monitoring of the differences in the phenotypes after the treatment with lignin nanoparticles showed no relevant modifications in body, eyes, bristles and wing (**Figure 2.7** panel B).

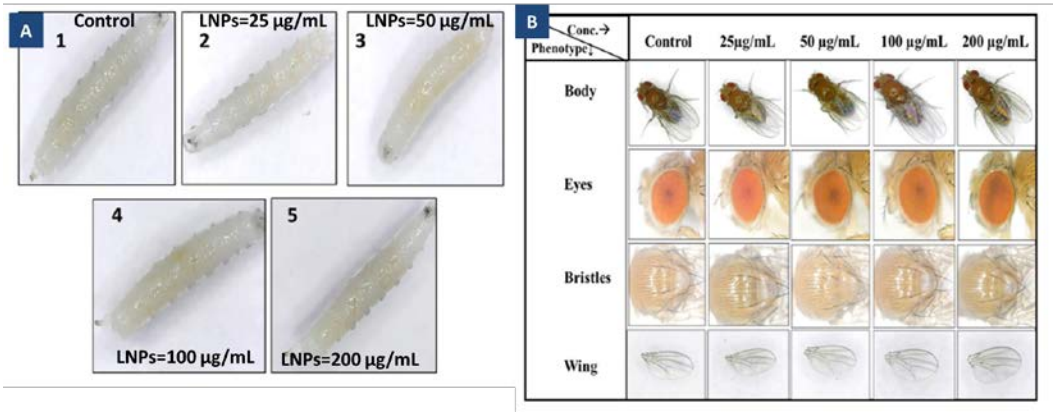

Figure 2.7 Trypan Blue staining of larvae after treatment with LNPs. In panel A and phenotypic changes in adult in panel B.

The biocompatibility of lignin at the nano-scale level opens a new scenario for the development of safe and environmentally friendly bionanotechnology in the field of biomedical and drug delivery devices.

Lignin nanoparticles are biodegradable in the soil[149] and could improve the biodegradability of bioplastics, as in the case of PLA.[150,151]

2.3 Functionalized lignin nanoparticles

The functionalization of lignin nanoparticles could improve the technological application of this polymer in the field of bionanotechnologies. In this thesis, lignin nanoparticles are used as a platform for the immobilization of different molecules (protein, enzymes, or other biopolymers). Mild and sustainable strategies were used in order to reach this objective. General informations about these procedures are reported in the following paragraphs.

2.3.1 Protein interactions

The protein-based nanomaterials offer a wide range of contributions in technological applications.[152] The functionalization of lignin nanoparticles by direct absorption of proteins provides an improvement in the development of functional materials, biobased technologies and sustainable biocatalysts. The understanding of the nature of the interactions between the lignin surface and the protein is based on two levels of complexity, that are the linear form of peptides and the 3D folding of protein. The first level comprises the interactions between lignin and linear peptides. In this case, Yamaguchi et al. in 2016 [153] showed the importance of various amino acid side-chains on the interaction with lignin. Peptides containing histidine, phenylalanine, proline, and serine residues showed the highest affinity to lignin surface. On the other hand, proteins are complex 3D-structured molecules with different folding structures (random coiled and globular folding). This 3D complexity affects the protein adsorption on lignin nanoparticles.[155] The main chemical interactions between lignin and proteins were identified and indicated in the **Figure 2.8** as coulombic forces and hydrogen bonds. [156]

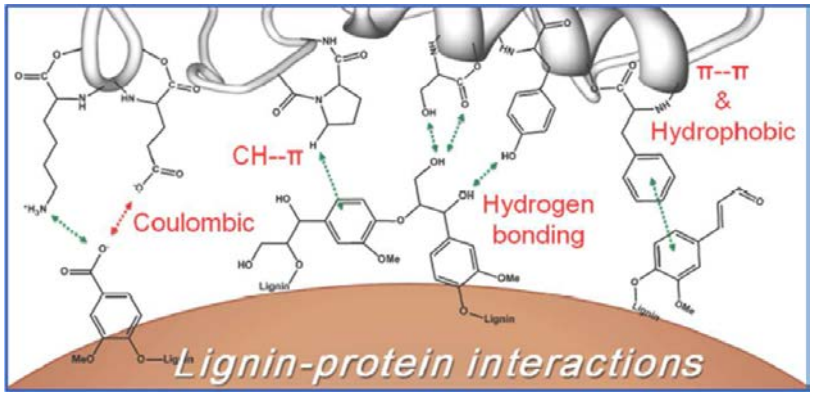

Figure 2.8 Main chemical interactions between lignin nanoparticles and proteins.

In addition, the hydrophobic force can improve the protein adsorption on lignin surface by π-π interactions between the aromatic moieties of lignin and the hydrophobic side chain of proteins.

2.3.2 Layer by layer technology

The Layer-by-layer technology (LbL) consists of the sequential deposition of poly-electrolytes with an opposite electrical charge.[157] The LbL is considered a self-assembly technique and an eco-friendly tool for the preparation of multi-component nanomaterials.[158,159] In the LbL technique the negative charge is overcompensated by one layer of cationic polyelectrolyte. Successively, stratification of double layers (positive and negative) stabilize the overall LbL system, the stability increasing with the increase of the electrostatic interactions (the steps are shown in **Figure 2.9**).[160]

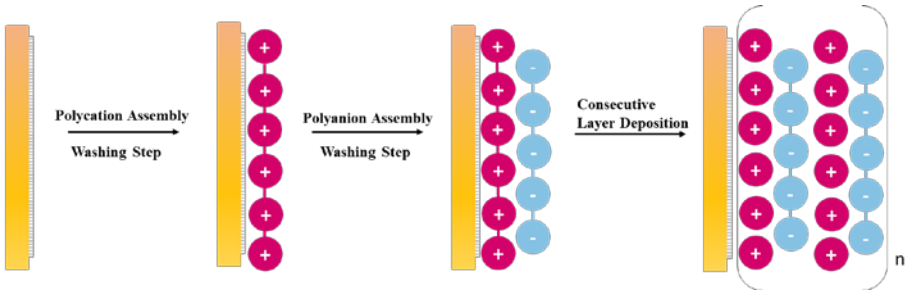

Figure 2.9 The layer by layer technology based on the self assembly of anionic and cationic polyelectrolytes

In the case of lignin nanoparticles, the LbL technique is beneficial for green functionalization methods. When lignin nanoparticles are dispersed in water, the phenolic hydroxyl groups and the carboxyl groups provide a negative surface charge. The negative charge of lignin nanoparticles is influenced by the lignin source.[161] Note that the zeta potential analysis shows two different values (-45 mV and -35 mV) for kraft lignin nanoparticles and for organosolv lignin nanoparticles, respectively. Some authors reported that the surface charge of the lignin nanoparticles could be reversed by the coating of an appropriate amount of synthetic cationic polyelectrolyte: poly(diallyl dimethylammonium chloride) PDDA.[134] The coating of lignin nanoparticles with cationic polymer can improve the stability of colloidal systems, conferring higher thermal stability and resistance to a wide range of pHs. Towards a more sustainable process, the layer-by-layer technology was tested with natural cationic polyelectrolytes instead of synthetic PDDA; the structure of these three polymers is shown in **Figure 2.10**.

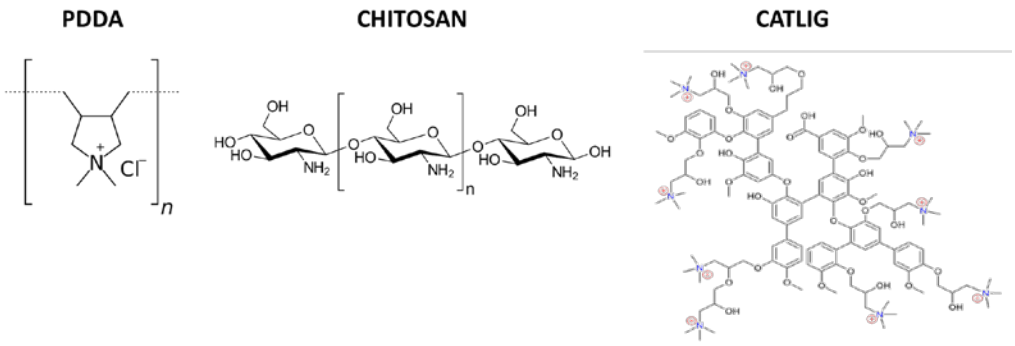

Figure 2.10. Chemical structure of synthetic and natural polyelectrolytes.

The most widely known natural cationic polyelectrolytes are chitosan and cationic lignin (CATLIG).[162,163] In particular chitosan is derived from the deacetylation of chitin, which comes from wastes of fishery industries. Chitosan has a cationic charge when dissolved in acidic water and was used efficiently to enhance the sustainability of layer-by-layer coating processes. CATLIG is a derivative of kraft lignin, in which quaternary ammonium groups of glycidyl tetramethylammonium chloride (GTMAC) are added to lignin structure. The final product is lignin with cationic charge, with the zeta potential of +32 mV.

Both chitosan and CATLIG have been used to enhance the enzyme immobilization processes described in this thesis.

2.3.3 Bionanocatalysts: procedures and benefits

The field of bionanocatalysis has experienced a rapid growth due to recent advances in nanotechnology.[164] The bionanocatalysis born with the fusion of the enzyme immobilization strategy and the nanostructured materials.[165]

As natural biocatalysts, enzymes have been applied to practical use in medicine, biosensors and material science. Enzymes have the excellent role of catalyze the reactions with high specificity under mild conditions. Enzymatic catalysis continues to open new pathways to site and stereoselective transformation and synthesis of bioactive substances, fine chemicals, polymers and pigments. Expensive and rare enzymes are not favored to be used in industries in the free state as they are difficult to be separated from the products and consequently are lost after the first use. The enzyme immobilization procedures have the aim to enhance the stability of enzymes while maintaining the enzyme activity and easy recyclability under various conditions. Nanomaterials serve as excellent platform for enzyme immobilization because they offer the optimal equilibrium between the efficiency

of the biocatalyst (including surface area, minimized mass transfer processes, etc) and the effective enzyme loading.[166]

Lignin at nano-scale levels offers a sustainable and efficient platform for enzyme immobilization. The use of this renewable support is poorly emphasized in literature. Sipponen et al. [167] showed that adsorption on lignin solid carriers increases the activity and stability of lipases and cutinases. Other types of enzymes immobilized on lignin nanoparticles are described in the following chapters.

An innovative bionanotechnology approach involve the co-immobilization of two or more enzymatic cascade processes on lignin nanoparticles. This technology is of central relevance for the design of bio-transformations and of novel biosensoring technologies. The co-immobilization can be produced *via* five chemical approaches (**Figure 2.11**): (a) random co-immobilization, (b) sequential immobilization, (c) positional immobilization, (d) site-specific co-immobilization, and (e) scaffold-free cross-linking, which can be further divided into non-specific or controlled immobilization.[168,169]

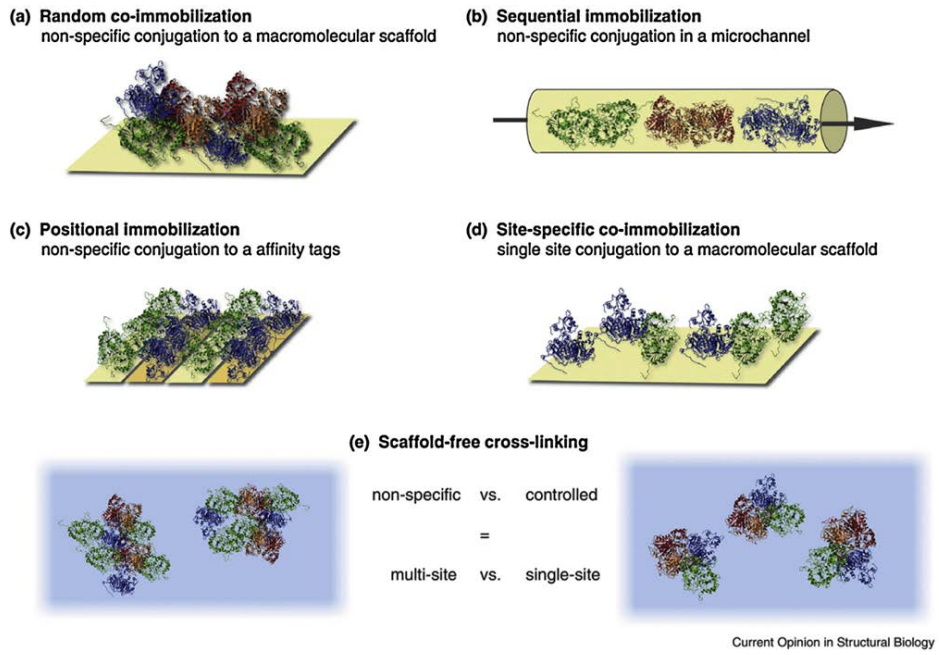

Figure 2.11 The main chemical approaches to immobilize multienzymatic complex.

In an ideal co-immobilization procedure, the enzymes are linked in a controlled and oriented manner. [170] It is reported that the use of natural lectins is beneficial for obtain a co-immobilization in an eco-friendly procedure. Lectins are defined as carbohydrate-binding proteins that can recognize specifically two or more glyco-enzymes.[171] For the oriented immobilization studies reported in this thesis, the lectin Concanavalin A (Con

A), originally extracted from the jack bean (*Canavalia ensiformis*), was selected as the optimal spacer. [171] Lectins are homotetramer, that specifically binds α-D-mannosyl and α-D-glucosyl residues in terminal position of ramified structures of β-glycans. Each subunit binds one metallic atom, usually Mn^{+} and Ca^{+}. The metals may directly stabilize the saccharide-binding residues in their active conformation and enhance the stability of glycoproteins.[172]

Apart from single enzymes or enzymatic cascade processes, other biological molecules can also be immobilized on lignin nanoparticles such as nucleic acids, antigens, peptides, and drugs. In this context further studies are required.

2.4 Layer-by-Layer preparation of microcapsules and nanocapsules of mixed polyphenols with high antioxidant and UV-shielding properties

2.4.1 Aim of work

Microcapsules and nanocapsules containing renewable materials have been prepared in order to explore innovative pharmaceutical and technological applications.[173] The main advantage of these devices resides in the high biocompatibility and in the emergence of specific scale-dimensional chemical and physical properties.[174,175] Present day, capsules containing only one type of polyphenol have been described, irrespective to the nature of the starting materials and to the specific preparation procedure. On the other hand, capsules of mixed polyphenols are expected to increase the physical and chemical properties with respect to their simple homo-polymer counterpart, as a consequence of possible synergistic effects between the different active components. The Layer-by-Layer (LbL) procedure, consisting on the sequential deposition of polyelectrolytes with opposite electrical charge, is a pivotal tool for the preparation of multicomponent devices,[176] allowing the assembly of different compounds by electrostatic, dipole-dipole, hydrogen bonds, and van der Waals interactions.[177] In these systems, one layer is responsible for the chemical and physical properties, while the remaining one is mainly involved in the stabilization of the overall structure. [178]

We studied the layer-by-layer preparation of microcapsules and nanocapsules of mixed polyphenols, sulfonate lignin (LS) and tannic acid (TA), using $MnCO_3$ and organosolv lignin nanoparticles as core templates, and polydiallyldimethylammonium chloride (PDDA) and chitosan (CH) as supporting layers. LS is a no toxic raw lignin produced in large amount during the sulfite pulping industrial process. The novel microcapsules and nanocapsules showed antioxidant activity, UV-shielding properties, and electrochemical responsiveness higher than that of the respective homo-polymer counterparts, confirming the beneficial role of the contemporary presence of two different polyphenols in enhancing both chemical, physical and biological properties. These devices are useful ingredients in different application fields, such as the preparation of bioplastics,[179] drug delivery technology[180] and sunscreen development in cosmetic and cosmeceutical formulations.[181]

2.4.2 Experimental Part

Materials

Tannic acid (TA, 90% pentagalloyl glucose, SigmaAldrich), chitosan (CH, low molecular weight) with 20% chitin units, sulfonate lignin calcium salt (LS, Mw ~18,000, average Mn ~2,500), organosolv lignin (OL), poly(diallyldimethylammonium chloride) (PDDA, 20%v/v water solution), poly(sodium 4-styrenesulfonate) (PSS), deuterated chloroform ($CDCl_3$), ethylenediaminetetraacetic acid (EDTA), 2-chloro-4,4,5,5-tetramethyl-1,3,2-dioxaphospholane, chrome (III) acetylacetonate, and 2,2-diphenyl-1-picrylhydrazyl (DPPH), were purchased from Sigma-Aldrich and were used without any further purification. Ascorbic acid (AA), 2,2'-Azino bis(3-ethylbenzothiazoline-6-sulfonic acid) (ABTS), boric acid (H_3BO_3), acetic acid (CH_3COOH), ortophosphoric acid 85% (H_3PO_4), potassium persulfate ($K_2S_2O_8$) and potassium chloride (KCl) were purchased from Sigma-Aldrich (Buchs, Switzerland). All solutions were prepared using Milli-Q water (ρ = 18.2 MΩ cm a 25 °C; TOC < 10 μg L−1, Millipore, Molsheim, France).

Preparation of microcapsules

The microcapsules were prepared by the LbL protocol, consisting in the sequential addition of polyelectrolytes with different electric charge to inorganic particles used as templates.[182] Briefly, the sodium acetate solution (0.5 mL, pH 5.0) of the appropriate polyphenol (1 mg/mL; LS or TA as negative charged layer), and of the appropriate polyelectrolyte (1 mg/mL; PDDA or CH as positive charged layers), were alternatively added to $MnCO_3$ particles suspension (20 mg suspended in 4.0 mL in sodium acetate solution pH 5.0) at room temperature. After 20 min, the solution was centrifuged (6000 rpm, 20 min) and the supernatant removed. Experiments were performed by deposition of three and five couple of layers. At the end, the microcapsules were $MnCO_3$ core was dissolved with EDTA (3 mL, 0.1M; pH 5) to yield empty microcapsules with general formula (X/Y)n, where X and Y are the different polyphenol and polyelectrolyte in the sequential deposition order with respect to the inorganic core, and "n" represents the total number of coupled layers. Microcapsules $(PDDA/LS)_3$ **1**, $(PDDA/LS)_5$ **2**, $(CH/LS)_5$ **3**, $(PDDA/TA)_5$ **4**, $(CH/TA)_5$ **5**, $(PDDA/TA/PDDA/LS)_5$ **6**, $(CH/TA/CH/LS)_5$ **7** and $(PDDA/LS+TA)_5$ **8** (where LS+TA is the mixture of sulfonate lignin and tannic acid in the 1:1 ratio) were prepared and successively characterized. Homo-polyphenol

microcapsules **1-5** were used as references for the mixed polyphenol systems **6-8** in the chemical and physical assays.

Preparation of nanocapsules

Nanocapsules were prepared by the dialysis protocol using nanoparticles of organosolv lignin (OL) as organic template.[134] Briefly, commercially available OL (20 mg) was dissolved in THF (20 mL), followed by filtration (0.45 μm syringe filter) and dialysis against deionized water for 24h at 25°C. The solution (1 mL; sodium acetate buffer pH 4.5) of the appropriate polyphenol (0.5 mg/mL; LS or TA as negative charged layer), and of the appropriate polyelectrolyte (0.5 mg/mL; PDDA or CH as positive charged layers), were alternatively added to 30 mL of previously prepared organosolv lignin nanoparticles (NOL) in sodium acetate buffer (0.1 mL/mg; sodium acetate buffer pH 4.5) at room temperature. After 20 min, the solution was centrifuged (6000 rpm, 20 min) and the supernatant removed. Experiments were performed by deposition of five couple of layers. The nanocapsules were rinsed with deionized water, recovered by centrifugation (6000 rpm, 20 min) and lyophilized to yield nanocapsules with general formula (X/Y)n, where X and Y are the different polyphenol and polyelectrolyte in the sequential deposition order with respect to the organic NOL ore, and "n" represents the total number of coupled layers. Nanocapsules NOL(CH/TA)$_5$ **9**, NOL(CH/LS)$_5$ **10** and NOL(CH/TA/CH/LS)$_5$ **11**, were prepared and characterized. Nanocapsules **10**-**11** were used as references for the mixed polyphenol system **9**. The mass percentage of polyphenols in microcapsules and nanocapsules has been evaluated by use of the Folin-Ciocalteu assay to measure the amount of polyphenol content in the residual solution after any layer deposition.[183] As reported in **Table 2**, microcapsules and nanocapsules showed a similar total amount of coated polyphenol.

Typically, the calibration curve was prepared using gallic acid solution as standard at different concentrations (20%, 40%, 60% and 80% from a 10 mg/mL starting solution). The samples were obtained from the residual solutions recovered during the layer-by-layer deposition, and were analyzed at the appropriate dilution factor after addition of 800 μL of $NaCO_3$ (5% water solution) and Folin (100 μL) reagent at 40 °C for 20 min. Finally, the samples were analyzed at 560 nm by UV-vis spectrophotometer. The total amount of polyphenols (mg of polyphenols for mg of capsules) was calculated as a difference between the starting amounts of polyphenol with respect to the recovered one in the residual solutions. Note that the various types of microcapsules and nanocapsules did not

released appreciable number of polyphenols in the solution after 7 days of storage in water (pH 7.0) at room temperature, as evaluated by UV-vis analysis (Folin-Ciocalteu assay). Similarly, the novel capsules showed mechanical stability as they retained the original spherical shape under similar experimental conditions in optical microscopy analysis (Leitz. Ergolux AMC).

Table 2. Total amount of polyphenols deposited in microcapsules and nanocapsules.

Entry	Sample	Adsorbed polyphenols (mg/mL)
1	$(PDDA/LS)_3$ **1**	0.45
2	$(PDDA/LS)_5$ **2**	0.47
3	$(CH/LS)_5$ **3**	0.51
4	$(PDDA/TA)_5$ **4**	0.46
5	$(CH/TA)_5$ **5**	0.52
6	$(PDDA/TA/PDDA/LS)_5$ **6**	0.52
7	$(CH/TA/CH/LS)_5$ **7**	0.55
8	$(PDDA/LS+TA)_5$ **8**	0.54
9	$NOL(CH/TA)_5$ **9**	0.58
10	$NOL(CH/LS)_5$ **10**	0.59
11	$NOL(CH/TA/CH/LS)_5$ **11**	0.69

[a]The amount of polyphenols is expressed as mg of adsorbed polyphenols for mg of each capsule. All experiments were conducted in triplicate.

Electron microscopy analysis

For Scanning Electron Microscopy (SEM), microcapsules **1**-**8**, and nanocapsules **9**-**11** were fixed with 3% glutaraldehyde in 0.1 M cacodylate buffer (pH 7.2), washed and post-fixed in OsO_4 (1% weight) in the same buffer at room temperature. Specimens were dehydrated in a graded ethanol series. They were then air dried, sputter-coated with gold in a Balzers MED 010 unit. The bservation was made by a JEOL JSM 6010LA electron microscope. For Transmission Electron Microscopy (TEM), nanocapsule **11** was fixed and dehydrated as described above and embedded in LRWhite resin (Multilab Supplies, Surrey, England) as a selected sample. The resin was polymerised in tightly capped gelatine for 48 h at 50°C. Thin sections were cut with Reichert Ultracut and LKB Nova ultra-microtomes using a diamond knife, collected on copper grids, stained with uranyl acetate and lead citrate, and observed with a JEOL 1200 EX II electron microscope. Micrographs were acquired by the Olympus SIS VELETA CCD camera equipped the iTEM software.

Phosphorus Nuclear Magnetic Resonance ^{31}P-NMR analysis

The qualitative and quantitative analysis of phenolic moieties in microcapsules and nanocapsules was determined by ^{31}P-NMR analysis.[184] Typically, the appropriate sample

(10 mg) was dissolved in pyridine/$CDCl_3$ (300 μL; 1.6/1.0 v/v), followed by addition of chrome (III) acetylacetonate solution 50 μL, 11.4 mg/ml) as relaxing agent. Then, the phosphitylation reagent 2-chloro-4,4,5,5- etramethyl-1,3,2-dioxaphospholane (200 μl) was added under magnetic stirrer and gentle heating at 45 °C for 2 hours. NMR analysis was performed in the presence of cholesterol as an internal standard on a Bruker 400MHz apparatus. The total amount of characteristic OH groups of polyphenols in microcapsules and nanocapsules was evaluated by comparing the ^{31}P NMR integral area of each specific signal with respect to standard reference. The ^{31}P NMR (ppm) characteristic range for any OH groups have been derived from data in the literature.[185,186]

Antioxidant activity

The antioxidant activity of selected microcapsules $(CH/LS)_5$ **3**, $(CH/TA/CH/LS)_5$ **7** and $(PDDA/LS+TA)_5$ **8**, and of nanocapsules NOL$(CH/LS)_5$ **10** and NOL$(CH/TA/CH/LS)_5$ **11**, was evaluated by the 2,2'-diphenyl picrylhydrazyl (DPPH) radical scavenging analysis.[187] using the same concentration of polyphenols (0.5 mg/mL). Briefly, the appropriate amount of the sample (depending on data in Table 4) was dissolved in EtOH 60% and added to freshly prepared DPPH solution (6 $x10^{-5}$ M in MeOH). The decrease in absorbance (517 nm) was determined at different times and concentrations until the reaction reached a plateau. The kinetic of the process was analyzed for each concentration tested, and the rate of DPPH remaining at the steady state was estimated. This value was used to calculate the IC_{50} (defined as the concentration of substrate in μg/mL that causes 50% loss of DPPH activity). The data were expressed as percentage of inhibition of the DPPH activity and were calculated according to the following equation: % inhibition of DPPH = {(Abs control - Abs sample)/Abs control} × 100 where "Abs control" is the absorbance of the DPPH solution without the sample.

UV shielding assay

The UV absorption properties of micro and nano-capsules, were spectrophotometrically determined by Varian Cary UV 50 scan using the same concentration of polyphenol (0.1 mg/mL). The analysis was carried out thought UV-vis scan using deionized H_2O suspension (pH 7) of the appropriate amount of sample (depending on data in **Table 2**) in quartz cuvette (3.0 mL), working in the range from 190 nm to 600 nm at 25°C under gentle stirring.

Electrochemical analyses

Cyclic voltammetry and amperometric experiments were performed by using a PGSAT204N potentiostat (Eco Chemie, The Netherlands) controlled by Nova 2.1 software (Eco Chemie, The Netherlands), using a conventional three-electrodes electrochemical cell equipped with a modified glassy carbon (GC) electrode as working electrode (d=3 mm, Cat. 6.1204.300, Metrohm, Herisau, Switzerland), and a saturated calomel electrode (SCE, 244 mV vs. NHE, Cat. 303/SCG/12, AMEL, Milano, Italy) and a glassy carbon rod electrode (d=2 mm, Cat. 6.1241.020, Metrohm, Herisau, Switzerland) as reference and counter electrodes, respectively. Cyclic voltammetry experiments were performed in 120 mM Britton-Robinson buffer pH 6.5 + 100 mM KCl containing 250 μM ABTS as mediator, while the pH experiments were performed by varying the pH of Britton-Robinson buffer in the range 2.5-7.5. Amperometric experiments were performed in 120 mM Britton-Robinson buffer pH 6.5 + 100 mM KCl injecting $ABTS^{+\bullet}$ radical solution (7mM) followed by sequential addition of ascorbic acid (AA) as antioxidant.

Electrode preparation

GC electrodes (d=3 mm, Cat. 6.1204.300, Metrohm, Herisau, Switzerland) were polished with alumina slurries (Al_2O_3, particle size of 0.3 and 0.05 μm) on cloth pads wet with Milli-Q water (SIEM, Bologna, Italy), thoroughly rinsed with Milli-Q water and further sonicated for 5 min between each polishing step. For the bio-modification, GC electrodes were modified by drop casting 5 μL of the appropriate sample (2 mg/mL). For each different modification, three replicates have been performed.

Amperometric antioxidant activity experiments

In order to prepare in situ the $ABTS^{+\bullet}$ radical cation, $K_2S_2O_8$ (140 mM, aqueous solution) was added to ABTS (2.5 mL; 7 mM, aqueous solution) at 4 °C for 8h. Afterwards, 1.0 mL of the so prepared solution was injected in 10 mL of 120 mM Britton-Robinson buffer pH 6.5 containing 100 mM KCl as supporting electrolyte. Next, 30 μL of 1 mM AA solution were sequentially injected. The potential applied for the analysis was 0.550 V vs. SCE.

2.4.3 Result and discussion

Preparation of microcapsules of mixed polyphenols

The LbL procedure for the preparation of microcapsules of mixed polyphenols is reported in **Figure 2.12**. LS and TA were used as negative charged polyelectrolytes, PDDA and CH as positive charged counterparts. We started with the deposition of the first positive layer in accordance with the slightly negative charge showed by the surface of $MnCO_3$ particles[148]. Microcapsules containing LS and TA alone, associated to PDDA, were also prepared as references.

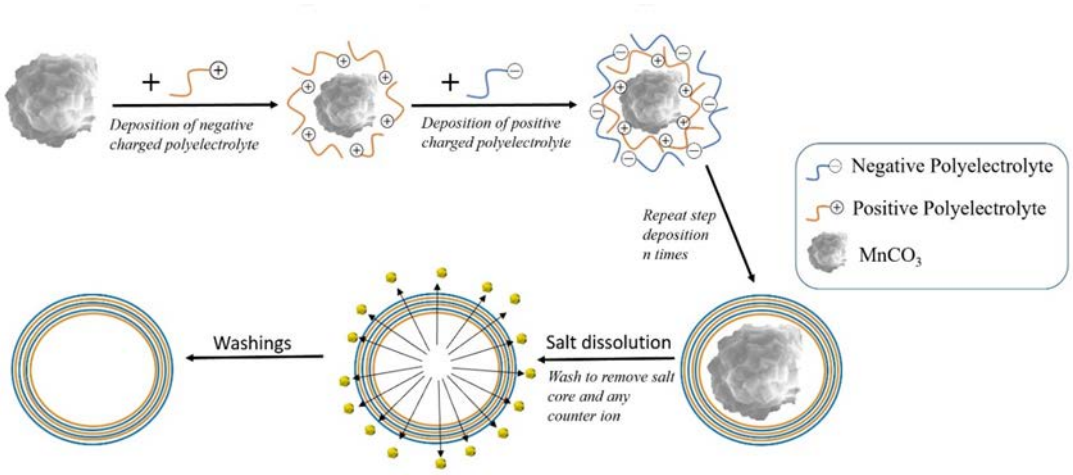

Figure 2.12. Procedure for the preparation of microcapsules of mixed polyphenols LS and TA using $MnCO_3$ particles as templates. Positive polyelectrolyte: PDDA or CH. Negative polyelectrolyte: LS and TA. The layer deposition was performed at pH 5.

As a general procedure, PDDA (0.5 mL, 1.0 mg/mL in sodium acetate buffer pH 5.0) was slowly added to a dispersion of MnCO3 particles in MilliQ-grade water at pH 5 to build up the first layer. The coated particles were treated under similar conditions with LS (0.5 mL, 1.0 mg/mL in sodium acetate buffer pH 5.0). Then, PDDA and LS layers were continuously built up in the same way as above, to yield (PDDA/LS)n, where "n" represents the number of the couple of the deposited layers. The scanning electron microscopy images (SEM) of (PDDA/LS)3 **1** and (PDDA/LS)5 **2**, are reported in **Figure 2.13**

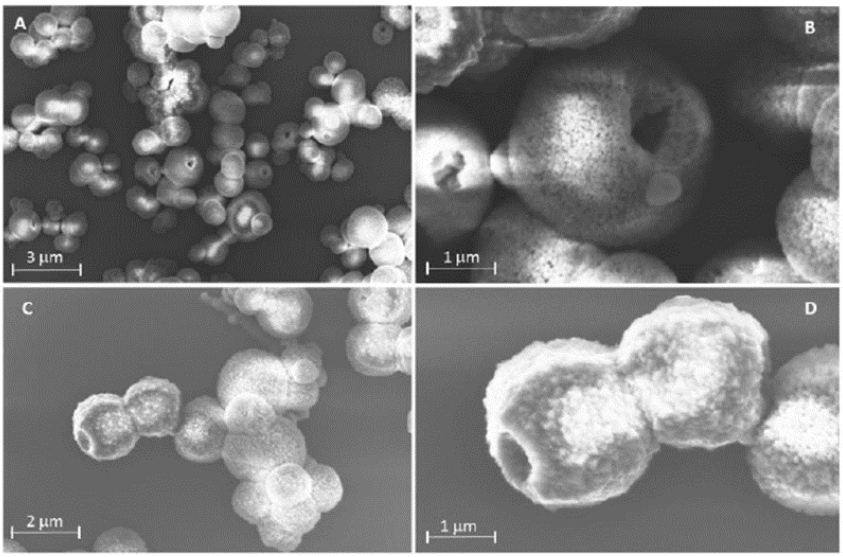

Figure 2.13. SEM image of (PDDA/LS)3 **1** (panels A and B) and (PDDA/LS)5 **2** (panels C and D).

The SEM image of $(PDDA/LS)_3$ **1** showed spheres of regular shape with an average diameter of 2.0±0.1 μm, some of which are characterized by an "open mouth" at the lateral side of the capsule, probably as a consequence of the rush out effect of the solvent in the interior of the sample during the drying conditions required for the microscopy analysis (**Figure 2.13**, panels A-B).[188] Examples of "open mouth" have been previously reported in the case of LS capsules prepared by precipitation of lignin from THF.[189] At a larger magnification, the surface of the capsules appeared as a roughly aggregate of small clumps (**Figure 2.13**, panel B). This morphology was found to be changed by increasing the number of the layers, as for $(PDDA/LS)_5$ **2**, in which case the clumps are associated to each other to form large homogeneous zones with a regular bee nest-like structure (**Figure 2.13**, panels C-D). Next, chitosan (CH, 0.5 ml, 1.0 mg/ml in sodium acetate buffer pH 5.0) was used as natural alternative to PDDA for the preparation of $(CH/LS)_5$ **3**, due to its high biodegradability and nontoxicity.[190,191] The SEM images of **3** showed microcapsules with an average diameter of the same order of magnitude than **2** (Figure **Figure 2.14**, panel A), characterized by an irregular surface. This morphology is different from that observed for microcapsules of CH alone, showing a homogeneous distribution of small globules (**Figure 2.14**, panel B). Again, an "open mouth" was observed in some of the detected capsules (**Figure 2.14**, panel C).

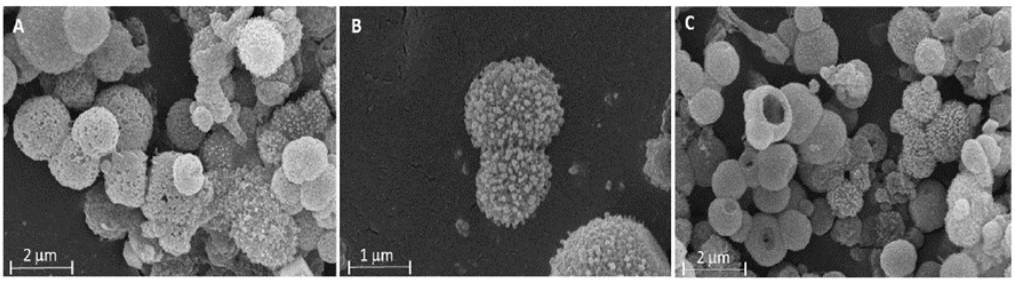

Figure 2.14. SEM image of (CH/LS)5 **3** (panel A and panel C). Panel B shows microcapsules of CH alone.

Microcapsules of TA alone, namely (PDDA/TA)$_5$ **4** and (CH/TA)$_5$ **5** (**Figure 2.15**, panels A-D), were prepared as references.[160] In this latter case, hydrogen bonding interactions were mostly responsible for the stability of the aggregate.[192.193] Microcapsules of **5** were spherically shaped with a regular distribution and homogeneous surface morphology, probably due to the formation of stable hydrogen bonding networks between the TA and CH layers.[194] Fragmented particles of **5** showed the presence of sub-structure motifs inside the external shell (**Figure 2.15**, see arrow).

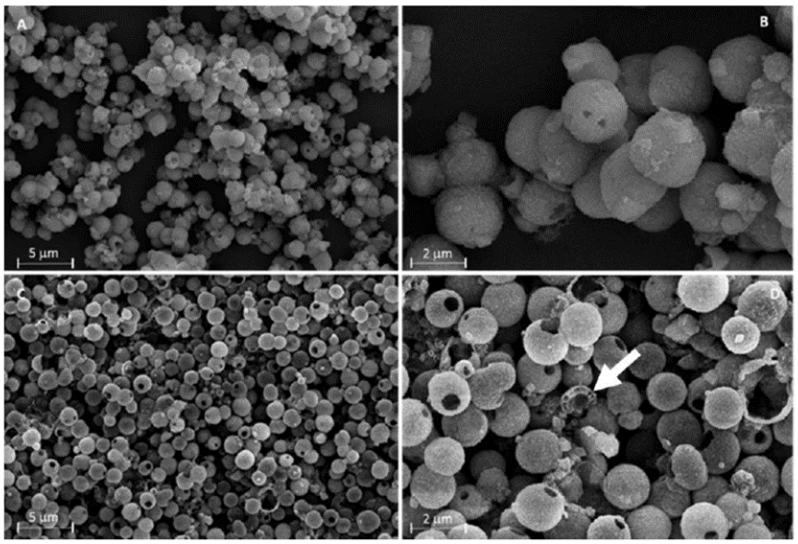

Figure 2.15. SEM image of (PDDA/TA)5 **4** (Panel A-B) and (CH/TA)5 **5** (Panel C-D).

Finally, we focused our attention on the preparation of microcapsules of mixed polyphenols containing both LS and TA, using PDDA as the support layer. Microcapsules (PDDA/TA/PDDA/LS)$_5$ **6** (with LS as the external layer) showed two main morphologies (**Figure 2.16**, panel A). The prevalent motif was a regular spherical shape (**Figure 2.16**, panel B), besides to a scratched motif (**Figure 2.16**, panel C). Probably, the presence of the scratched motif might be due to incomplete deposition of the PDDA layer. The

contemporary presence of LS and TA layers in **6** was confirmed by 31P-NMR analysis (see next).

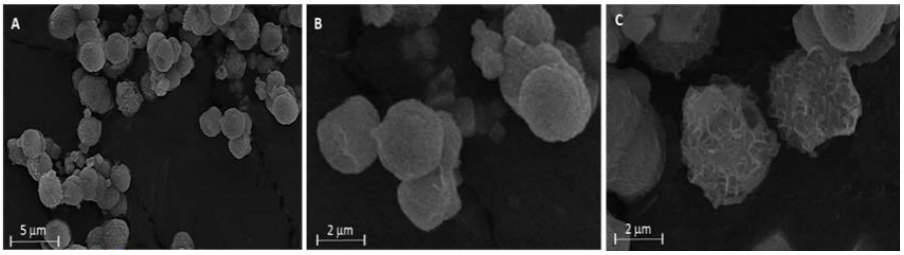

Figure 2.16. SEM images of (PDDA/TA/PDDA/LS)5 **6** at different magnification. Panel A: General particles view. Panel B: Detail of the predominant regular spherical shape motif. Panel C: Detail of the scratched surface motif.

Microcapsules $(CH/TA/CH/LS)_5$ **7**, bearing the CH layer instead of PDDA, were prepared in a similar way. The SEM analysis of **7** showed capsules with a regular spherical shape (**Figure 2.17**, panels A-B), characterized by well-defined networks.

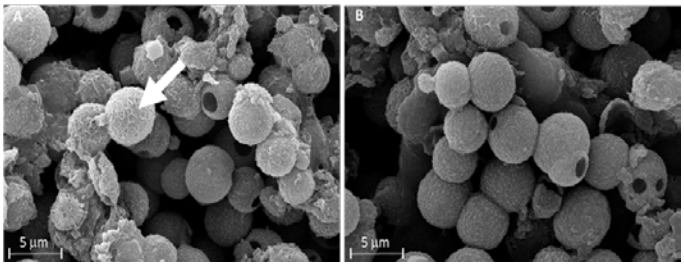

Figure 2.17 SEM images of $(CH/TA/CH/LS)_5$ **7** at different magnification.

Microcapsules containing the mixture of LS and TA (1:1 w/w ratio), namely $(PDDA/LS+TA)_5$ **8**, were also prepared as an alternative to the previously studied sequential deposition of the individual layers of the single polyphenols. In this latter case, spherical capsules formed large aggregates (**Figure 2.18**, panel A), with a pronounced film-like surface motif (Figure 2.12, panel B). These large aggregates were most probably produced as a consequence of the known coordination properties of the external layer of TA.

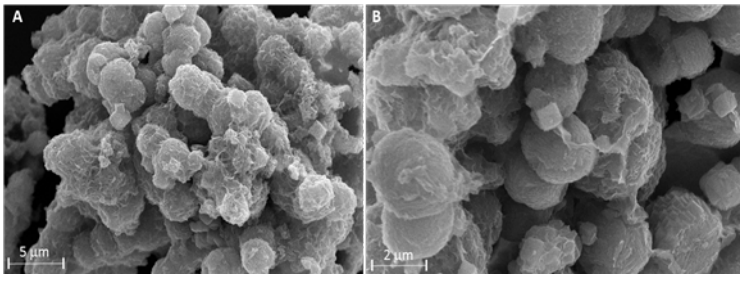

Figure 2.18. SEM images of (PDDA/LS+TA)5 **8** at different magnification. Panel A: large aggregates of partial fused spherical capsules. Panel B: magnification of the surface film-like motif..

Preparation of mixed LS and TA nanocapsules

The procedure for the preparation of nanocapsules of mixed polyphenols is reported in **Figure 2.19** (Panels A-B). Nanoparticles of organosolv lignin (NOL) were used as a template instead of $MnCO_3$. We started with the deposition of CH as positive charged counterpart, since NOL are characterized by a negative surface charge.

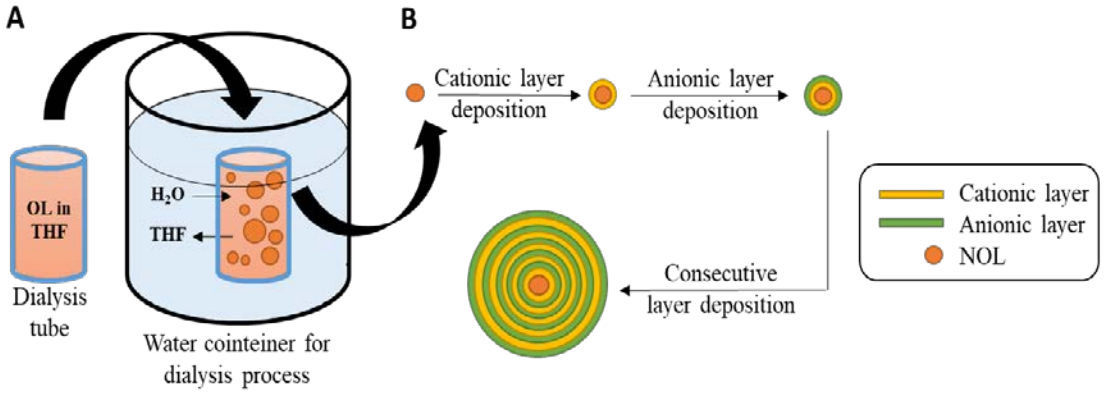

Figure 2.19. Preparation of mixed LS and TA nanocapsules. Panel A: Organosolv Lignin (OL) dissolved in THF was dialyzed against deionized water to yield NOL. Panel B: Preparation of NOL(CH/TA)5 **9**, NOL(CH/LS)5 **10** and NOL(CH/TA/CH/LS)5 **11**. Cationic layers: CH. Anionic layers: TA and LS.

Then, LS, CH and TA layers were continuously built up as previously described, to yield $NOL(X/Y)_n$, where "n" represents the number of couple of layers, while X and Y are the single polyphenol and polyelectrolyte components. In **Figure 2.20**, $NOL(CH/TA)_5$ **9** and $NOL(CH/LS)_5$ **10** showed capsules of regular spherical shape similar to that previously observed for **7**, the sample **10** being characterized by the highest size uniformity. A different morphology was observed in the case of the mixed polyphenol $NOL(CH/TA/CH/LS)_5$ **11** (**Figure 2.14**), which is characterized by a morphological structural motif similar to **7**, probably as a consequence of the presence of the same sequence of deposited layers (that is: TA, LS and CH).

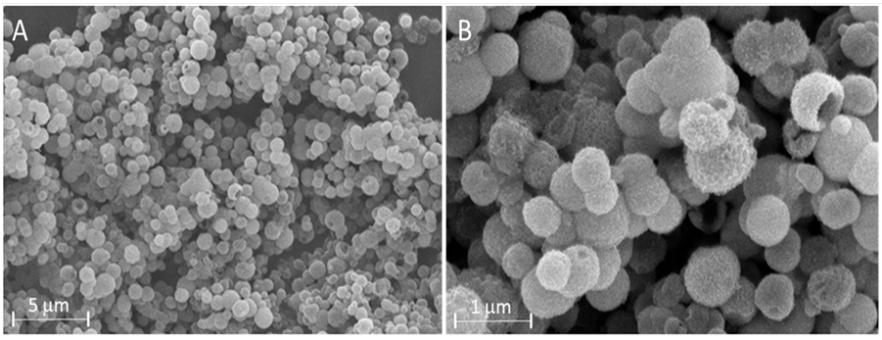

Figure 2.20. SEM images of NOL(CH/TA/CH/LS)5 **11** at different magnification. Quantitative 31P-NMR characterization of microcapsules and nanocapsules of mixed polyphenols

In order to verify the contemporary presence of the different polyphenol layers, capsules (CH/TA/CH/LS)$_5$ **7** and NOL(CH/TA/CH/LS) **11** were characterized by ^{31}P-NMR spectroscopy. PDDA containing capsules, e.g. (PDDA/TA/PDDA/LS)$_5$ **6**, were not analyzed due to the lack of PDDA signals in ^{31}P NMR analysis. Briefly, the samples were dissolved in pyridine/$CDCl_3$ (300 μL; 1.6/1.0 v/v) under sonication conditions and phosphitylated in situ with 2-chloro-4,4,5,5- tetramethyl-1,3,2-dioxaphospholane. The ^{31}P-NMR analysis of native LS, OL, TA, and CH were also performed as references (Figure **2.21**).

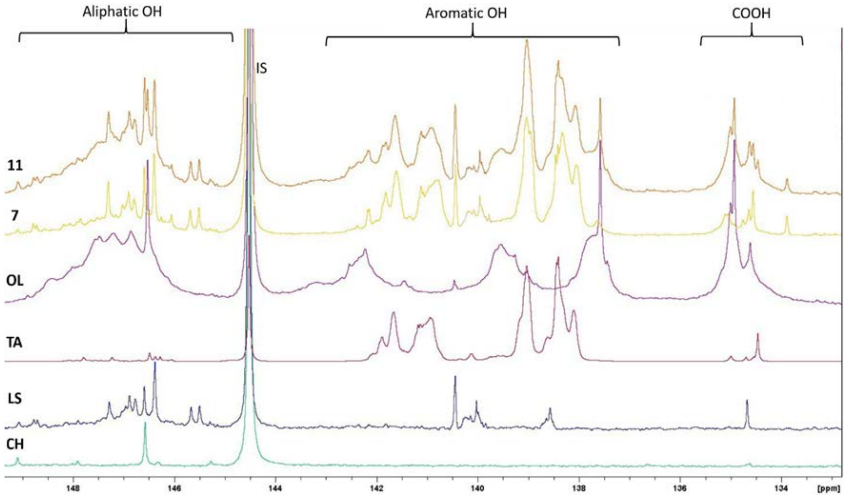

Figure 2.21. Quantitative 31P-NMR spectra and signal assignment of commercial CH, LS, OL and TA, and of capsules (CH/TA/CH/LS)5 **7** and NOL(CH/TA/CH/LS)5 **11** after dissolution in pyridine/CDCl3 (300 μL; 1.6/1.0 v/v) under sonication conditions and phosphitylation with 2-chloro-4,4,5,5-tetramethyl-1,3,2-dioxaphospholane. OL: Organosolv lignin; LS: Sulfonate lignin; TA: Tannic acid: CH: Chitosan. Typical lignin chemical shift (ppm): A) *para*-phenolic groups - 138.5-138.8 ppm; B) guaiacyl groups-138.7-140.1 ppm; C) condensed phenol groups-140.3-140.5 ppm; D) syringyl groups-142.0-144.0 ppm; E) aliphatic hydroxyl groups-146.0-149.0 ppm; F) carboxylic acids groups-134.0-135.5 ppm. Typical tannin chemical shift (ppm): A) *ortho*substituted phenol groups-138.0-138.7 ppm; B) catechol hydroxyl groups-138.8-139.4 ppm; C) *ortho*-disubstituted phenol groups (internal gallate units)-140.6-141.4 ppm; D) *ortho*-disubstituted phenol groups (external gallate units)-141.5-142.2 ppm.

LS, OL and TA showed characteristic ^{31}P-NMR signals in the range of 145-149 ppm, and 137- 142 ppm, respectively. These signals were also detected in the spectra of **7** and **11**. The spectrum of LS (**Figure 2.21**, blue-line) exhibited typical *para*-phenolic groups at 138.5-138.8 ppm, followed by guaiacyl groups in the range of 138.7-140.1 ppm, and condensed phenol units at 140.3-140.5 ppm. In a similar way, the spectrum of OL (**Figure 2.21**, purple-line) exhibited the *para*-phenolic groups at 137.3-138.0 ppm, followed by the guaiacyl groups in the range of 139.5-140.1 ppm, and the syringyl groups at 142.0-144.0 ppm. Both lignin samples showed aliphatic hydroxyl groups in the range of 146.0-149.0 ppm, and carboxylic acids groups at 134.0-135.5 ppm. The spectrum of TA (**Figure 2.21**, red-line) showed a different pattern. In particular, the *ortho*-substituted phenol and

the catechol hydroxyl groups were detected at 138.0-138.7 ppm, and 138.8-139.4 ppm respectively, while the *ortho*-disubstituted phenols were found at 140.6-141.4 ppm (internal gallate units), and at 141.5-142.2 ppm (external gallate units), respectively. In this latter case a low contribute of the aliphatic hydroxyl peaks was observed. Finally, CH showed signals only in the range of aliphatic hydroxyl groups. The most representative signals expected for LS and OL, and for TA, were clearly identified in the ^{31}P-NMR spectra of **7** and **11**, confirming the presence of the two polyphenols. **Table 3** reports the quantitative distribution of the phenolic and alcoholic functional groups (millimoles/gram) in the samples for which the spectra are displayed in **Figure 2.21**.

Table 3. Functional group distribution (mmol/gram) for LS, OL, TA, (CH/TA/CH/LS)5 **7** and NOL(CH/TA/CH/LS)5 **11.**[a]

sample	carboxylic acids	aliphatic-OH	phenolic -OH				
			Ortho-disubstituted -OH	Ortho-substituted -OH	Syringyl -OH	Guaiacyl	p-hydroxyl phenyl
11	3.97	6.89	4.92	6.71	2.89	2.21	7.21
7	1.98	3.81	4.71	6.57	-	1.29	0.95
LS	1.12	2.79	-	-	-	1.31	0.98
TA	0.92	0.75	4.51	6.23	-	-	-
OL	2.01	3.96	-	-	2.91	0.81	6.11

[a]Quantitative ^{31}P-NMR spectra were performed after dissolution of the sample in pyridine/$CDCl_3$ (300 μL; 1.6/1.0 v/v) under sonication conditions and phosphitylation with 2-chloro-4,4,5,5-tetramethyl-1,3,2-dioxaphospholane. OL: Organosolv lignin; LS: Sulfonate lignin; TA: Tannic acid.

Antioxidant activity and UV-absorbing properties of microcapsules and nanocapsules of mixed Polyphenols

Lignin and tannic acid are characterized by radical scavenging activity due to the presence of free phenolic groups which are able to capture the radical species by formation of stable phenoxy radicals. The presence of ortho-substituents in the aromatic ring, such as the methoxyl substituents of the guaiacyl and syringyl moieties, further increases the antioxidant activity by both steric hindering and resonance effects.[195] The antioxidant activity of selected microcapsules (CH/LS)$_5$ **3**, (CH/TA/CH/LS)$_5$ **7** and (PDDA/LS+TA)$_5$ **8**, and of nanocapsules NOL(CH/LS)$_5$ **10** and NOL(CH/TA/CH/LS)$_5$ **11**, was evaluated by the 2,2'-diphenyl picrylhydrazyl (DPPH) radical scavenging analysis. These microcapsules and nanocapsules have been selected in order to compare samples containing both polyphenols and having the same sequence in the layer composition. Moreover, sample **8** has been selected to evaluate the antioxidant effect of capsules containing both polyphenols in the same layer. Native LS and TA were also studied as references. The appropriate sample was suspended in EtOH and added to

standard DPPH solution. DPPH is a stable free radical, that is applied for the spectrophotometric evaluation of the radical scavenging ability of polyphenols. The decrease of DPPH absorbance (517 nm) was determined for each sample and the collected data were used to calculate the IC_{50} (defined as the μg/mL concentration of substrate that causes 50% loss of DPPH activity). **Figure 2.22** reports the percentage of DPPH radical scavenging activity and the IC_{50} value for the analyzed samples. As a general trend, the nanocapsules **10**-**11** showed antioxidant activity higher than microcapsules **3** and **7**-**8**. Moreover, the antioxidant activity of nanocapsules **10**-**11** was higher than that of native LS and TA. The higher antioxidant activity of **11** with respect to **7** is in accordance with the total amount of aromatic phenolic groups as measured by ^{31}P-NMR analysis, that is 23.94 (mmol/gram) for **11 v**ersus 13.52 (mmol/gram) for **7**, respectively (**Table 3**, entries 1 and 2). Nanoscale lignin showed highest antioxidant activity when compared to micro-scale lignin, probably due to a combination between the highest surface-area-to-volume ratio and the emergence of specific π-π interactions.[196] As a general trend, the capsules of mixed polyphenols were the most active antioxidants, showing an IC_{50} value of the same order of magnitude than that of standard food antioxidants, such as BHT and ascorbate (IC_{50} c.a. 10 μg). Irrespective to the scale dimension, the presence of TA always enhanced the antioxidant activity, probably as a consequence of the higher amount of ortho-substituted and ortho-disubstituted phenol moieties, as detected by ^{31}P-NMR analysis (**Table 3**, entry 4).

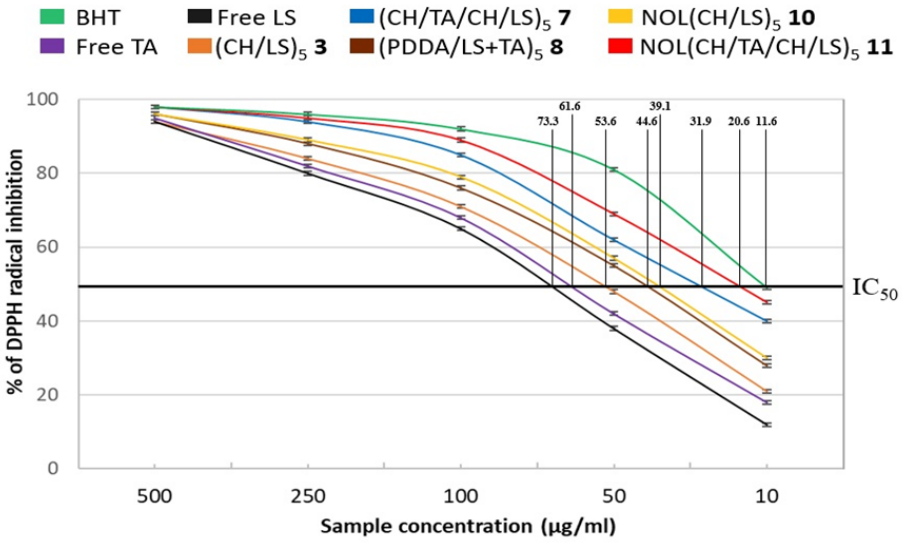

Figure 2.22. DPPH antioxidant scavenging activity of investigated microcapsules and nanocapsules presented as % of DPPH radicals inhibitions and IC50 values (μg/mL). Relative standard deviation was less than 3.0 %

The UV-absorbing ability of microcapsules $(CH/LS)_5$ **3**, $(CH/TA/CH/LS)_5$ **7** and $(PDDA/LS+TA)_5$ **8**, and of nanocapsules $NOL(CH/LS)_5$ **10** and $NOL(CH/TA/CH/LS)_5$ **11**, was determined by irradiation experiments in the energy range from 190 nm to 600 nm (from UV to visible regions) LS, TA and NOL were studied as references. As reported in **Figure 2.23**, microcapsules **3** and **7-8** showed a similar absorbance ability in the UV-C and UV-B regions.

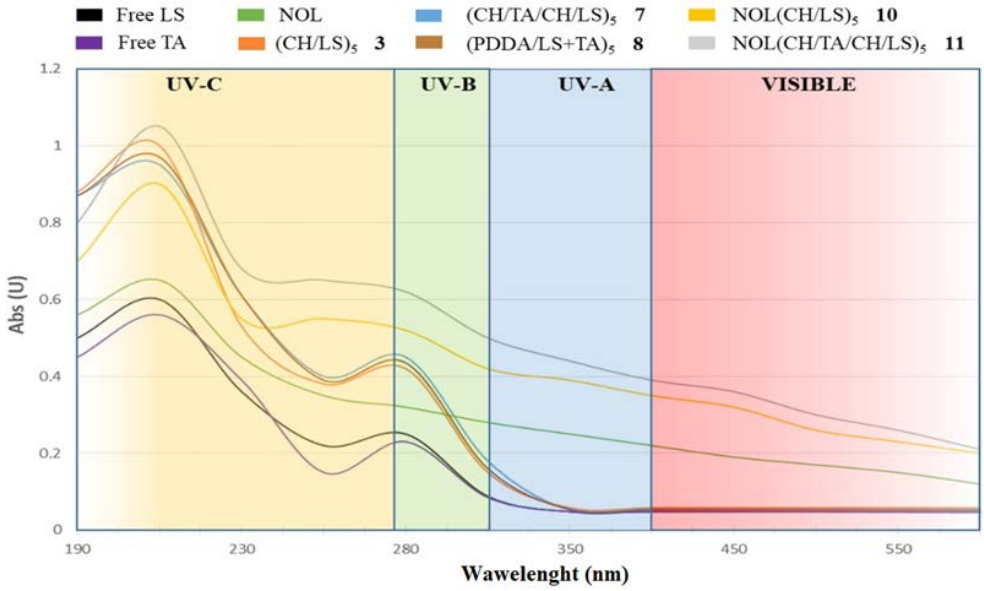

Figure 2.23. UV-Visible radiation absorbing capacity of investigated micro and nano-capsules.

Note that microcapsules **3** and **7-8** were more active than native LS and TA. As a general trend, nanocapsules **10** and **11** were photoabsorbers more efficient than **3** and **7-8**, sample **11** being the most active system. Moreover, nanocapsules **10** and **11** were more efficient than NOL. This effect was particularly pronounced in the UV-B and UV-A regions. The high UV-A absorption property of **10** and **11** is noteworthy, since native LS and TA, and the corresponding microcapsules, showed only a low absorbance capacity in this UV-region. Moreover, a bathochromic shift of the absorption peak at 280 nm (accredited to guaiacyl units and/or to unconjugated phenolic groups) [197] was observed for both microcapsules and nanocapsules in the following order: **11**>**10**>**7**,**8**>**3**. Previous studies showed that the lignin macromolecule is organized as a flat and disk-like aggregate in solution, [198] stabilized by π–π interactions between the aromatic rings[199,200,201]. Conferring an UV absorbing enhancement.[202] The bathochromic shift observed in microcapsules and nanocapsules has been related to formation of

J-aggregates in which the orientation of the adjacent aromatic rings is parallel to the longitudinal direction of the layer, following a head-to-tail like arrangement. A similar

bathochromic shift was also observed in the case of nanocapsules produced from Kraft lignin. The appreciable UV absorbing enhancement suggested that nanocapsules have stronger π-π interactions than microcapsules, while the order of the bathochromic shift previously reported highlight that capsules containing mixed polyphenols were more aggregated than the homo-polymeric counterpart.

Voltammetric and amperometric characterization of nanocapsules

Cyclic voltammograms (CVs) of NOL, NOL(CH/TA)$_5$ **9,** NOL(CH/LS)$_5$ **10**, and NOL(CH/TA/CH/LS)$_5$ **11** were performed, as selected examples, in the presence of ABTS (250 μM) in the Britton-Robinson buffer (pH 6.5, 120 mM) and KCl (100 mM) as supporting electrolyte (**Figure 2.24**). The CV at slow potential scan rate for the naked modified glassy carbon (GC) electrode (dotted black line) showed two stable and reversible redox couples, where the first anodic peak 0.5 V vs. SCE) is associated to the formation of the $ABTS^{+\bullet}$ radical cation, while the second peak (0.89 V vs. SCE) corresponds to the formation of the $ABTS^{2+}$bis-cation species. As reported in **Figure 2.24**, a remarkable increasing in the anodic peak current densities was observed in the presence of nanocapsules **9-11**, due to the reactions taking place between the two oxidized forms of ABTS and the lignin and tannic acid residues exposed on the surface of the nanocapsules.[203]

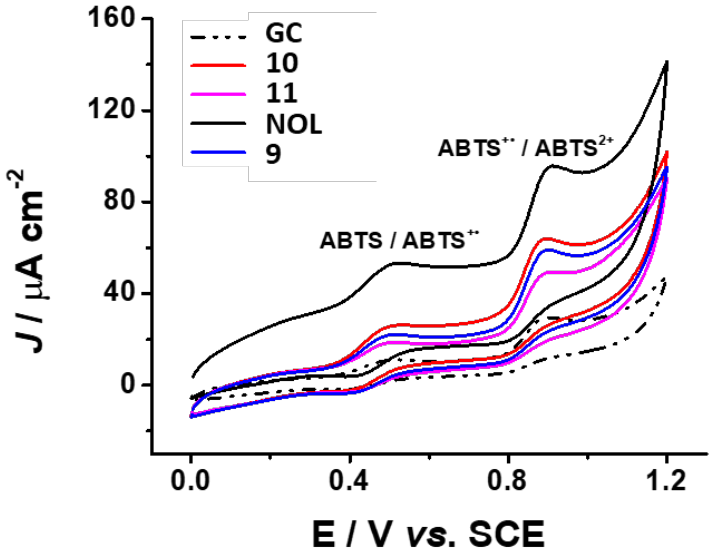

Figure 2.24. CVs performed with GCE (dash-dotted line), NOL (black line), NOL(CH/TA)5 **9** (bluline), NOL(CH/LS)5 **10** (red line), and NOL(CH/TA/CH/LS)5 **11** (purple line). Measurements were performed in 250 μM ABTS solution (120 mM Britton-Robinson buffer pH 6.5 containing 100 mM KCl as supporting electrolyte) at scan rate 20 mV s-1, T=25°C

In accordance with the DPPH antioxidant data previously reported, the polyphenol mixed nanocapsules NOL(CH/TA/CH/LS)$_5$ **11** showed an inhibitory activity against the electrochemical induced oxidation of ABTS (purple line) higher than that of its homo-polymer counterparts, NOL(CH/TA)$_5$ **9** (blu line) and NOL(CH/LS)$_5$ **10** (red line), respectively. The samples **9** and **10** were more effective than NOL as reference, confirming the beneficial role of the sequential deposition of the TA and LS layers on the antioxidant activity. Moreover, **9** showed lower oxidation current densities with respect to **10**, probably due to the higher amount of ortho-substituted and ortho-disubstituted phenolic moieties in TA with respect to LS (**Table 3**).[204]

The effect of the pH on the antioxidant activity of nanocapsules **9**-**11** was successively evaluated by analyzing the variation of the formal potential (E_0') of the system depending on the specific pH range applied. Cyclic voltammograms have been recorded at a scan rate of 50 mV s^{-1} under previously described experimental conditions. Nanocapsules retained their antioxidant activity in the pH range of 2.5-7.5 units, with the only exception of NOL(CH/TA)$_5$ **9**, which displayed the E_0' shifting versus pH only in the pH range of 4.5-7.5 units (**Figure 2.25**, panels A-D). Generally, nanocapsules showed a similar pH dependence being all slopes very close to -60 mV/pH, which s the calculated slope for $2H^+/2e^-$ redox processes in the reduction of quinone to hydroquinone, according to the Nernst equation.[205]

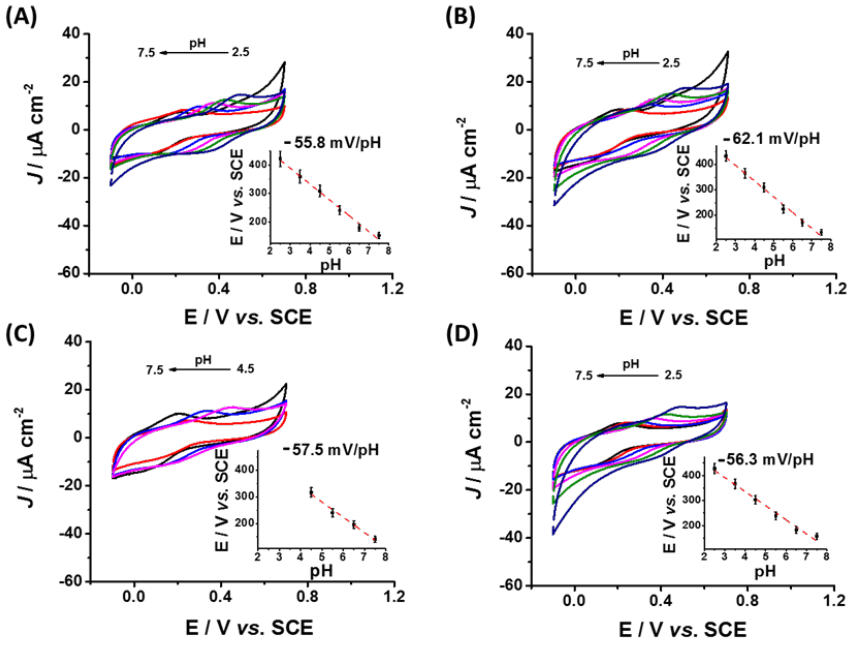

Figure 2.25. CVs of NOL (A), NOL(CH/TA)5 **9** (C), NOL(CH/LS)5 **10** (B), and NOL(CH/TA/CH/LS)5 **11** (D)**.** CVs were recorded in 120 mM Britton-Robinson buffer containing 100 mM KCl as supporting electrolyte in the range 2.5-7.5. Insets: linear dependence of the formal potential (E0') versus pH

Next, the ABTS+• scavenging activity of nanocapsules **9-11** was measured in comparison with ascorbic acid (AA) by amperometry analysis.[207] Amperograms of nanocapsules **9-11** were recorded at the applied potential +0.55 V vs. SCE (required for the oxidation of ABTS+•), followed by the addition of several aliquots of ascorbic acid (30 μL of 1.0 mM AA solution). The progressive decolouration of ABTS+• from blue-green to colourless was observed during the increase of the AA concentration. As a general trend, the oxidation current densities of ABTS+• decreased by increasing the AA concentration, confirming the radical scavenging activity of nanocapsules (**Figure 2.26,** panel A). In accordance with the previously reported voltammetric data, polyphenol mixed nanocapsules **11** were more effective than the corresponding homo-polymer counterparts **9-10**, showing the highest slope values (**Figure 2.26**, panel B). Again, LbL nanocapsules **9-11** were more active than simple NOL.

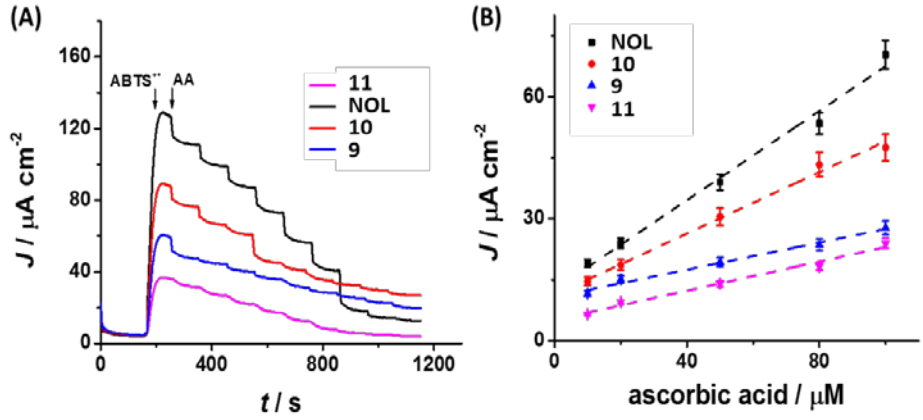

Figure 2.20. (A) Amperograms of NOL (black line), NOL(CH/TA)5 **9** (blu line), NOL(CH/LS)5 **10** (red line), and NOL(CH/TA/CH/LS)5 **11** (purple line). Measurements were performed in 120 mM Britton-Robinson buffer pH 6.5 containing 100 mM KCl as supporting electrolyte, adding 7 mM ABTS+• solution followed by several additions of AA. Experimental conditions: applied potential (Eapp): +0.55 V vs. SCE; stirring: 400 rpm ant T=25°C. **(B)** linear dependence of antioxidant activity on AA concentration.

Chapter 3
Biocatalysts

3.1 Functionalized Tyrosinase-Lignin Nanoparticles as Sustainable Catalysts for the Oxidation of Phenols

3.1.1 Aim of work

It is assumed that renewable materials might play a key role in Circular Economy due to their unique environmentally benign properties.[207] Lignin byproducts are low cost materials that perform as well as petroleum-derived counterparts, showing beneficial properties associated with their aromatic character, such as antioxidant activity,[208,209] UV-shielding protection,[210,211] anticorrosion effects,[212] and electrochemical responsiveness in both charge storage composites[213] and electrochemical sensors.[214] For this reason, lignin is emerging as a new and inexpensive raw material for the preparation of nanocapsules with increased chemical and physical properties,[215] due to the direct consequence of "size-effect" phenomena. These nanoparticles can be, in principle, useful polyphenol-based platforms for the immobilization of enzymes.[216,217] The supramolecular interaction between lignin and proteins has been studied in details, identifying lignin-binding peptide sequences of affinity[153] and analyzing the role that conformational changes of the polymer played in the molecular recognition process.[155] The folding structure of the protein, associated to the prevalence of Coulombic forces in non-ionic medium with respect to hydrogen bonding and hydrophobic polar type interactions, emerged as crucial parameters in the self-assembly of proteins on the lignin surface. Moreover, lignin showed high boosting activity towards copper oxidative enzymes, such as Lytic Polysaccharide MonoOxygenases (LPMOs), through long-range electron transfer mechanisms between the aromatic moieties and the metal atoms in the active site of the enzyme.[104] In this context, tyrosinase (EC 1.14.18.1) showed to further improve the LPMOs oriented boosting activity of lignin,[218] performing the ortho-hydroxylation of phenol moieties to corresponding low redox-potential catechol derivatives (1, 2-benzene diols; monophenolase activity).[219] Thus, lignin and tyrosinase cooperate in synergy to realize efficient oxidative processes. Tyrosinase has been widely studied because of its relevance in several applied areas, [220] showing better performances in industrial applications when used in the immobilized form, as a consequence of its reusability, enhanced stability, and easier purification procedures.[221]

In recent years, we described the preparation of heterogeneous catalysts for the synthesis of bioactive catechol derivatives by immobilization of tyrosinase on

microcapsules of the epoxy resin Eupergit[222] and in alternative, by Layer-by-layer coating on Multi Walled Carbon Nanotubes (MWCNTS).[223] These catalysts provided high catalytic efficiency in the synthesis of neuroactive 3,4-dihydroxyphenylalanine (DOPA)-containing peptides[224] and of lipophilic catechols with broad spectrum antiviral activity against both DNA and RNA viruses[225]. As a general trend, nanostructured catalysts showed greater activity, storage life, and reusability than the microcapsule counterparts.[226] This project describes the immobilization of tyrosinase from *Agaricus bisporus* (T3824, multimeric enzyme with H2L2-type structure)[227] in nanoparticles of organosolv lignin (OL)[228] by four different procedures, namely: i) encapsulation, ii) surface adsorption, iii) Layer-by-layer (LbL) coating, and iv) LbL coating in the presence of bovine serum albumin (BSA) and glutaraldehyde (GA). At difference from native lignin and other technical lignins, OL has a relatively low molecular weight and a distinct solubility in organic solvents.[229] The novel catalysts have been characterized regarding to their structural and kinetic properties, and they have been successively applied for the oxidation of selected phenols to corresponding bioactive catechols.

3.1.2 Experimental

Materials

Organosolv lignin (OL) were purchased from Chemical Point. Mushroom tyrosinase, bovine serum albumin (BSA), glutaraldehyde (GA), poly(diallyldimethylammonium chloride) (PDDA, 20% v/v water solution), 2-chloro-4,4,5,5-tetramethyl-1,3,2-dioxaphopholane, chrome (III) acetylacetonate; deuterated chloroform ($CDCl_3$), ascorbic acid, Bradford reagent, *L*-tyrosine, *para*-cresol, tyrosol, 4-hydroxyphenylacetic acid, 3-(4-hydroxyphenyl)propionic acid, catechol, potassium chloride (KCl) and organic solvents were purchased from Sigma–Aldrich and were used without any further purification. All experiments were done in triplicate using native and immobilized tyrosinase in Phosphate buffer saline (PBS).

Reactivity of tyrosinase with organosolv lignin

An appropriate amount of OL (70 mg) was treated with tyrosinase (1000 U) in PBS (5.0 mL, 0.1 M; pH 7) under dioxygen atmosphere at room temperature for 24 h. This mixture was acidified (pH 3, 1.0 M HCl) and successively centrifuged (6000 rpm, 20 min) to remove the supernatant.

The residue was rinsed with deionized water and then freeze-dried. The qualitative and quantitative analysis of alcoholic, acidic, and phenolic OH groups in the residual crude after tyrosinase treatment was determined by quantitative ^{31}P-NMR analysis.[230] Typically, the lignin sample (10 mg) was dissolved in pyridine/$CDCl_3$ (300 μL; 1.6/1.0 v/v), followed by addition of chrome (III) acetylacetonate solution (50 mL, 11.4 mg/ml) as relaxing agent. Then, the phosphitylation reagent 2-chloro-4,4,5,5-tetramethyl-1,3,2-dioxaphopholane (200 μl) was added under magnetic stirrer and gentle heating at 45 °C for 2 h. NMR analysis was performed in the presence of cholesterol as an internal standard on a Bruker 400MHz apparatus. Gel Permeation Chromatography (GPC) analysis of OL was carried out following the procedure of acetobromination.[231] Briefly, an appropriate amount of lignin sample (10 mg) was suspended in acetic glacial/acetyl bromide mixture (2.5 mL of 92:8 v/v) and stirred at room temperature. After 2 h the solvent was evaporated under vacuum and the residue was dissolved in THF (5 ml). The GPC analysis were performed using a Shimadzu LC 20AT liquid chromatograph with a SPD M2OA ultraviolet diode array (UV) detector at 280 nm.

*Preparation of catalyst **I***

The preparation of catalyst **I** required the encapsulation of tyrosinase within the OL nanoparticles. Briefly, an appropriate amount of tyrosinase (3.0 mg, 900 U/mg) was added to a solution of OL in THF (2.0 mg/mL, 7.5 mL) previously filtered by 0.45 μm filter membrane. The solution obtained was dialyzed against deionized MilliQ water (500 mL) for 24 h at 25°C under slow magnetic stirring, using Spectrapore™ dialysis membrane (3,5 kD MWCO). Catalyst **I** was recovered by centrifugation (20 min at 6000 rpm) and the surnatant was used for the calculation of the activity parameters. The catalyst was washed several times with PBS in order to ensure the complete removal of unbounded tyrosinase (as evaluated by the Bradford method).

*Preparation of catalyst **II***

Catalyst **II** was prepared by direct adsorption of tyrosinase on preformed OL nanoparticles prepared by the dialysis protocol. Briefly, OL solution (THF, 2 mg/mL) previously filtered by 0.45 μm filter membrane, was dialyzed against deionized water for 24h at 25°C with slow magnetic stirring, using Spectrapore™ dialysis membrane (3,5 kD MWCO). Finally, the OL nanoparticles obtained were centrifuged (20 min at 6000 rpm), washed with Milli-Q water and lyophilized. The appropriate amount of tyrosinase (3.0

mg, 900 U/mg), dissolved in sodium phosphate buffer PBS (3.0 mL, 0.1 M; pH 7), was added to a suspension of OL nanoparticles (15 mg) in PBS (15 mL) under orbital shaking at room temperature for 24 h. Catalyst **II** was recovered by centrifugation (20 min at 6000 rpm) and the surnatant was used for the calculation of activity parameters. The catalyst was washed several times with PBS in order to ensure the complete removal of unbounded tyrosinase (as evaluated by the Bradford method).

*Preparation of catalyst **III***

The OL nanoparticles were coated with PDDA applying the LbL procedure.[232] Briefly, a suspension (15 mL) of OL nanocapsules in MilliQ water (1mg/mL, pH 4.2) was added dropwise to PDDA solution (1mg/mL, Milli-Q water) under slow magnetic stirring. After 2 h, the final suspension was centrifuged in order to recover OL-PDDA nanoparticles followed by washing with Milli-Q water and lyophilization. Tyrosinase (3.0 mg, 900 U/mg) was added to a suspension of OL-PDDA nanoparticles (15 mg) in PBS (15 mL) under orbital shaking at room temperature for 24 h. Catalyst **III** was recovered by centrifugation (20 min at 6000 rpm) and the surnatant was used for the calculation of the activity parameters. The catalyst was washed several times with PBS in order to ensure the complete removal of unbounded tyrosinase (as evaluated by the Bradford method).

*Preparation of catalyst **IV***

The OL-PDDA nanoparticles were prepared as described above and then used in order to immobilize BSA and tyrosinase by crosslinking with GA. Briefly, tyrosinase (300 μL, 3.4 mg/ mL in PBS) and BSA (1.5 ml, 2.0 mg/mL) were added to OL-PDDA nanoparticles suspension (3.5 mg ml^{-1}, PBS 1.4 ml), and the mixture was shaken for 30 min at room temperature. Finally, GA (150 μl, 2.5% v/v water solution) was added and the mixture was shaken again at room temperature for 30 min and then at 4 °C overnight. Catalyst **IV** was recovered by centrifugation (20 min at 6000 rpm) and the surnatant was used for the calculation of activity parameters. The catalyst was washed several times with PBS in order to ensure the complete removal of unbounded tyrosinase (as evaluated by the Bradford method).

SEM caracterization

For Scanning Electron Microscopy (SEM), catalysts (**I-IV**), were fixed with 3% glutaraldehyde in 0.1 M cacodylate buffer (pH 7.2), washed and post-fixed in OsO_4 (1.0% in weight) in the same buffer at room temperature. The samples were dehydrated in

agraded ethanol series before the analysis. They were then ai dried and sputter-coated with gold in a Balzers MED 010 unit. The observation was made by a JEOL JSM 6010LA electron microscope.

DLS and Zeta potential

Measurements of particle size and Zeta potential were performed on freshly prepared aqueous suspensions (pH = 7) of OL nanoparticles and Catalyst **I-IV** dispersed in water were performed before and by dynamic light scattering (DLS) using a Zetasizer Nano ZS (Malvern Instruments, Malvern, UK) equipped with a He-Ne laser (633 nm, fixed scattering angle of 173°, 25°C). Prior to perform size measurements, suspensions were filtered with a 0.45-mm filter membrane. Measurements were performed at least in triplicate at room temperature (T=25°C).

Determination of the catalyst activity

The catalyst activity of the native and immobilized enzyme was determined by measuring the tyrosinase-catalyzed oxidation of L-tyrosine. The reaction was started by adding the substrate to the solution containing the appropriate amounts of the native enzyme, and in alternative, of catalysts **I−IV** in PBS under magnetic stirring. The initial rates were measured as the linear increase of the optical density at 475 nm, due to dopachrome formation. One unit of enzyme activity was defined as the increase in absorbance of 0.001 unit per minute at pH 7 and 25 °C, measured in a 3.0 mL reaction cuvette containing 0.83 mM of *L*-tyrosine and 67 mM PBS (pH 7.0). Spectrophotometric data were analyzed with Cary WinUV. All experiments were conducted in triplicate using free and immobilized tyrosinase.

Determination of the kinetic constants

Kinetic parameters, K_m, V_{max} and V_{max}/K_m, were determined spectrophotometrically by measuring the enzyme activity at different concentrations of *L*-Tyrosine (0.33–0.10 mM) and by plotting data in Lineweaver−Burk. All experiments were conducted in triplicate using native and immobilized tyrosinase. Reactions were carried out by means of the same procedure as for activity assay and measuring absorbance at 475 nm as described above.

Electrochemical characterization

Cyclic voltammetry experiments were performed by using a PGSAT204N potentiostat (Eco Chemie, The Netherlands) controlled by Nova 2.1 software (Eco Chemie, The Netherlands) with a conventional three-electrodes electrochemical cell equipped with a modified glassy carbon (GC) electrode as working electrode (d=3 mm, Cat. 6.1204.300, Metrohm, Herisau, Switzerland), a saturated calomel electrode (SCE, 244 mV vs. NHE, Cat. 303/SCG/12, AMEL, Milano, Italy) and a glassy carbon rod electrode (d = 2 mm, Cat. 6.1241.020, Metrohm, Herisau, Switzerland), as reference and counter electrodes, respectively. All electrochemical measurements were performed in 50 mM PBS buffer pH 6.5 plus 100 mM KCl containing 250 µM cathecol, used as electrochemical mediator. GC electrodes (d=3 mm, Cat. 6.1204.300, Metrohm, Herisau, Switzerland) were polished with alumina slurries (Al_2O_3, particle size of 0.3 and 0.05 µm) on cloth pads wet with Milli-Q water (SIEM, Bologna, Italy), thoroughly rinsed with Milli-Q water and further sonicated for 5 min between each polishing step. For the bio-modification, GC electrodes were modified by drop-casting 5 µL of sample OL nanoparticles (2 mg/mL), catalyst **I** (2 mg/mL), catalyst **II** (2 mg/mL), catalyst **III** (2 mg/mL), and catalyst **IV** (2 mg/mL), respectively. For each different modification, three replicates have been performed.

General procedure for the oxidation of phenols

As a general procedure, phenols **1-4** (0.02 mmol), tyrosinase (540 IU) and ascorbic acid (2 eq) were placed in PBS 5.0 mL (0.1 M; pH 7) at 25°C for 24 h, and the mixture was stirred under O_2 atmosphere. Oxidations were performed using homogeneous and heterogeneous conditions. The reactions were monitored by thin layer chromatography (TLC, n-hexane/EtOAc=2.0:1.0). After the disappearance of the substrate, the reaction mixture was acidified with a solution of HCl 2.0 M and extracted twice with EtOAc. The organic extracts were treated with a saturated solution of NaCl and dried over anhydrous Na_2SO_4, then filtered and concentrated under vacuum. In the case of immobilized enzyme, catalysts **I-IV** were recovered by centrifugation (6000 rpm) for 20 minutes and the solution was subjected to the same work up as described above. The residue was treated with pyridine, HMDS and TMCS (HMDS–TMCS, 2:1 v/v) under vigorous stirring at room temperature for 2 h. Products were identified by gas-chromatography associated to mass-spectrometry analysis (GC–MS). The analyses were performed by 450 GC-320 MS apparatus using a VF-5MS column and an isothermal temperature profile of

100 °C for 2 min, followed by a 10 °C/min temperature gradient to 280 °C for 25 mn. The injector temperature was 280 °C. Chromatography-grade helium was used as the carrier gas with a flow of 2.7 mL/min. Mass spectra were recorded with an electron beam of 70 eV.

3.1.3 Results and discussion

Reactivity of tyrosinase towards organosolv lignin (OL)

The reactivity of tyrosinase towards lignin is debated. Lignans, the secondary metabolites resembling the dimeric units of lignin, generally showed inhibitory activity against tyrosinase[233,234], and the catalytic effect of tyrosinase in the oxidation of milled wood lignin was found to be negligible with respect to that of laccase and horseradish peroxidase.[235] On the other hand, tyrosinase from *Agaricus bisporus* was reported to cleave the 4-*O*-5 and Cα-Cβ bonds of some representative dimeric lignin model compounds (4-phenoxylphenol and guaiacyl glycerol-β-guaiacylether)[236]. For this reason, we decided to study the reactivity of tyrosinase from *Agaricus bisporus* towards organosolv lignin (OL) before the immobilization procedures. OL (70 mg) was treated with tyrosinase (1000 U) in phosphate buffer (5.0 mL, 0.1 M; pH 7) under dioxygen atmosphere at room temperature.

After 24 h, the mixture was acidified (pH 3, 1.0 M HCl) and successively centrifuged (6000 rpm, 20 min) to remove the supernatant. The residue was washed with deionized water and freeze-dried to yield OL-tyr. A sample of OL, treated under similar experimental conditions in the absence of tyrosinase, was used as reference. The amount of characteristic OH groups in OL-tyr and OL samples was determined by quantitative ^{31}P NMR. Briefly, the samples were dissolved in pyridine/$CDCl_3$ (300 μL; 1.6/1.0 v/v) under sonication conditions and phosphitylated in situ with 2-chloro-4,4,5,5-tetramethyl-1,3,2-dioxaphopholane. **Table 4** shows the relevant experimental data collected. More specifically, aliphatic, condensed, guaiacylic, para-hydroxy phenyl, and acidic lignin OH groups were measured. Data are averages of three phosphitylation experiments. The ^{31}P-NMR data showed a modest decrease of the total phenolic OH and of the total OH groups after the enzyme treatment (11% and 9%, respectively), confirming the low reactivity of tyrosinase towards lignin.

Table 4. Functional OH distribution (mmol/gram) for parent OL and for OL-tyr after treatment with tyrosinase.[a]

Sample	Carboxylic acid	Aliphatic -OH	Condesed -OH	Para-hydroxy Phenyl -OH	Guaiacyl -OH	Total phenolic -OH	Total group -OH
OL	0.22	0.99	1.95	0.24	0.68	2.87	4.08
OL-tyr	0.19	0.97	1.79	0.17	0.59	2.55	3.71

[a]Quantitative ^{31}P-NMR spectra were performed after dissolution of the sample in pyridine/$CDCl_3$ (300 μL; 1.6/1.0 v/v) under sonication conditions and phosphitylation with 2-chloro-4,4,5,5-tetramethyl-1,3,2-dioxaphopholane. OL: original sample of organosolv lignin; OL-tyr: organosolv lignin after treatment with tyrosinase. [b]Maximum standard deviation: 2 x 10^{-2} mmol/gram. Maximum error: 1x10^{-2} mmol/gram.

Structural modifications in OL-tyr were further evaluated by Gel Permeation Chromatography analysis (GPC) of the residue. In **Table 5** are reported the weight average molecular weight (M_w), the number average molecular weight (M_n) and the polydispersity (M_w/M_n) of OL-tyr compared to parent OL. Tyrosinase treatment induced an appreciable increase in the M_w and M_n values.

Table 5. M_w, M_n and M_w/M_n of OL tyr compared with the parent OL.

Sample	**M_w**	**M_n**	**M_w/M_n**
OL	154.670[a]	15.104	10.2
OL-tyr	202.828	18.803	18.8

[a]Analyses were repeated in triplicate.

Thus, in our hand tyrosinase showed a low reactivity towards OL, affording a modest decrease of the total amount of phenolic OH, associated with a modest, although if significant, increasing in the weight average molecular weight of the polymer, probably as a consequence of oxidative coupling processes.[237]

Encapsulation and direct adsorption procedures

Alkali Lignin nanoparticles have been previously reported as containers for drug delivery systems.[238,239] The encapsulation procedure consisted in the formation of nanoparticles by slow solvent exchange in the presence of the bioactive principle to be immobilized, such as resveratrol, sorafenib, benzazulene and ibuprofen.[240] Lignin nanoparticles showed high antioxidant protective effect, successfully releasing the bioactive principle in the cell. A similar procedure was applied in the encapsulation of dyes.[241] We decided to apply this procedure for the encapsulation of tyrosinase in OL nanoparticles. Tyrosinase (3.0 mg, 900 U/mg) was added to a solution of OL in THF (2.0 mg/mL, 7.5 mL) at room temperature, and the solution was dialyzed against MilliQ water (500 mL) for 24 h. During the slow exchange of the solvent, the lignin molecules interacted together to close the nanoparticles, tyrosinase being entrapped inside their

empty core cavity. At the end, the encapsulated tyrosinase system (catalyst **I**) was recovered by centrifugation and washed to remove the excess of the enzyme (**Figure 3.1**, pathway A). Scanning electron microscopy (SEM) images of catalyst **I** are reported in **Figure 3.2**.

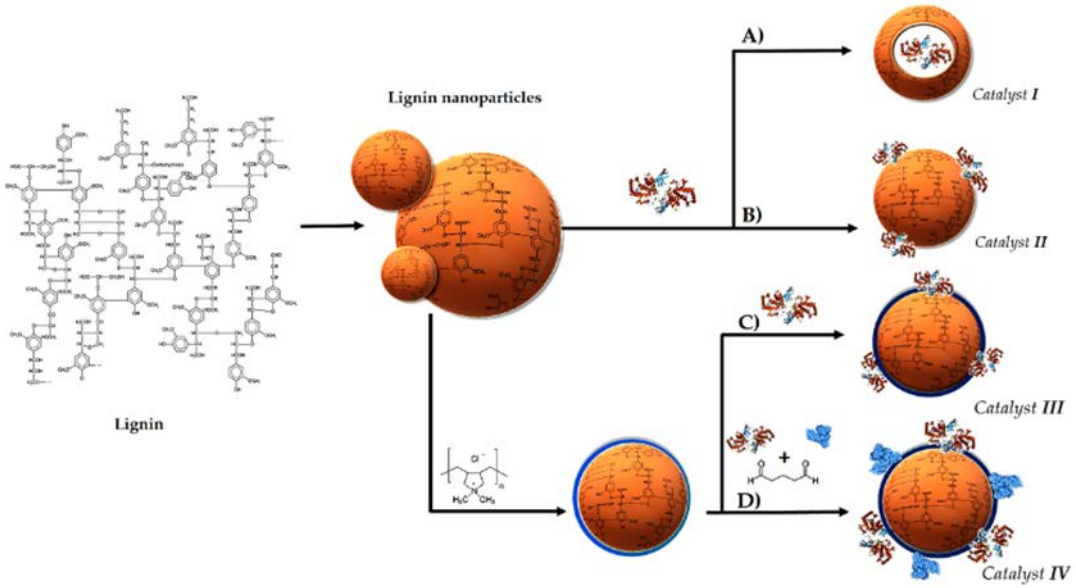

Figure 3.1. Schematic representation for the preparation of catalysts **I-IV**.

The SEM image of catalyst **I** showed spheres of regular shape (**Figure 3.2**, panel A) with an average diameter of 0.19±0.01 μm, as evaluated by Dinamic Light Scattering (DLS) analysis (**Figure 3.3**).

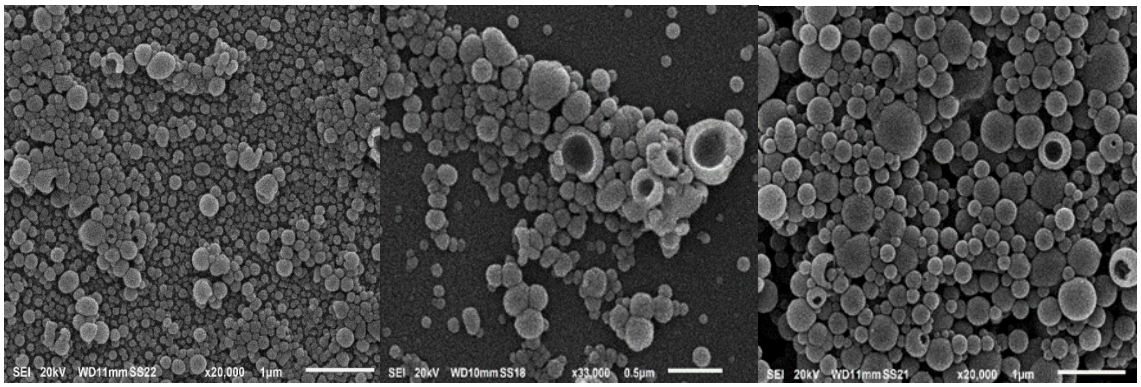

(a) (b) (c)

Figure 3.2. SEM images of catalyst **I** and catalyst **II**. (**a**) General overview of catalyst **I**; (**b**) Selected magnification of catalyst **I;** (**c**) General overview of catalyst **II.**

Fragmented particles were characterized by the presence of empty cavity (**Figure 3.2**, panel B). The presence of the enzyme in catalyst **I** was observed by confocal analysis using a tyrosinase previously marked with Fluorescein isothiocyanate (FITC).[242] As reported in (**Figure 3.4**, panel A), catalyst **I** showed the expected green signal inside nanoparticles. The entrapment of tyrosinase was further confirmed measuring the value

of the Zeta potential of the particle surface, that was found to be very similar to the value obtained for the parent OL nanoparticles (**Figure 3.5**).

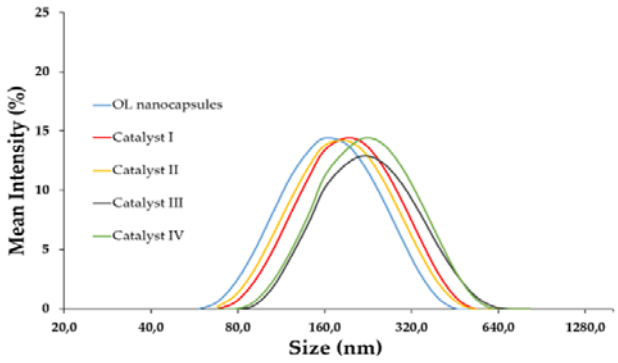

Figure 3.3. Particle diameter distributions of OL nanocapsules and Catalyst **I-IV**

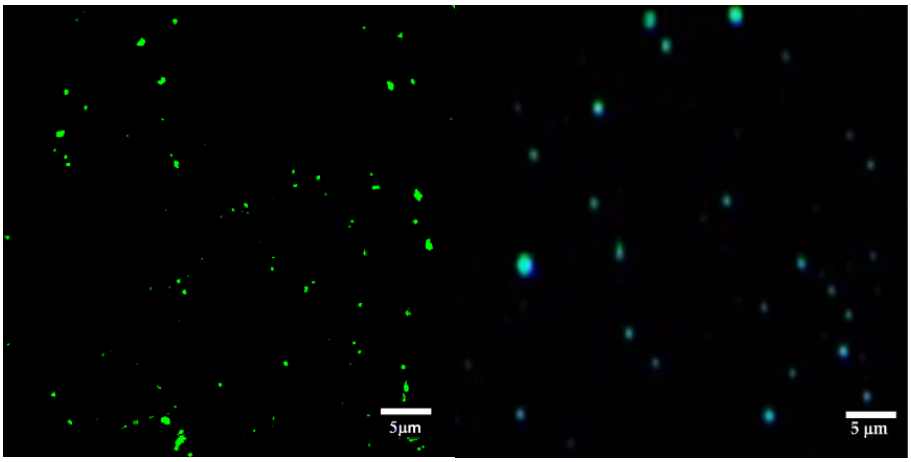

Figure 3.4. Confocal images of (**a**) Catalyst **I**; (**b**) Catalyst **II**.

As an alternative, catalyst **II** was prepared by direct adsorption of tyrosinase on preformed OL nanoparticles (**Figure 3.1**, pathway B). Briefly, tyrosinase (3 mg, 900 U/mg) dissolved in sodium phosphate buffer PBS (3.0 mL, 0.1 M; pH 7) was added to a suspension of OL nanoparticles (15 mg) in PBS (15 mL) under orbital shaking at room temperature overnight. Catalyst **II** was recovered after centrifugation and rinsed with PBS to remove the excess of the enzyme. (**Figure 3.6**, panel C) reports the SEM image of particles of catalyst **II,** characterized by an average diameter of 0.20±0.01 µm (Figure 2.23). The confocal image of catalyst **II** (**Figure 3.4**, panel B), performed in the presence of the marked enzyme, showed a relatively weak green fluorescence signal only on the surface of nanoparticles (the background azure emission of the core being associated to the known auto-fluorescence of lignin.[243] Moreover, the Zeta potential of catalyst **II**

varied with respect to parent OL nanoparticles (**Figure 3.5**). hese data confirmed that the adsorption of tyrosinase was limited to the surface of the nanoparticles.

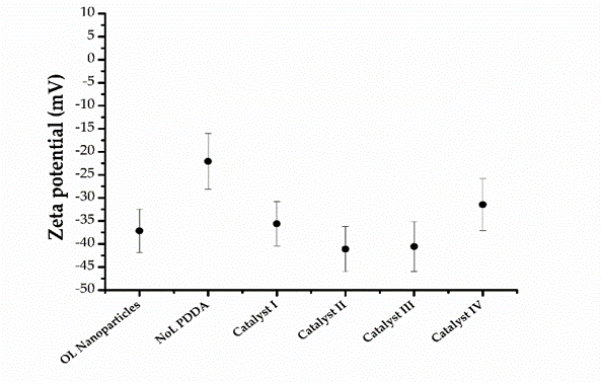

Figure 3.5 Zeta potential values of OL nanoparticles, OL PDDA nanoparticles and catalysts **I-IV.**

Layer-by-layer immobilization procedure

The LbL procedure, based on the consecutive deposition of alternatively charged polyelectrolytes onto an appropriate support, protects enzymes from denaturing agents and allows regulation of the permeability towards small substrates, which can cross the multilayer and react with the catalytic site.[244] The use of the LBL procedure for the immobilization of tyrosinase from *Agaricus bisporus* on Multiwalled Carbon Nanotubes (MWCNTs) has been previously reported to increase the activity of the enzyme. Since lignin nanoparticles are characterized by a negative value of the Zeta potential (-42 mV at pH 4.2), we started by the deposition of a first positive charged layer of polydiallyldimethylammonium chloride (PDDA), able to efficiently interact with the lignin surface by cation-π interactions.[245] Briefly, a suspension (15 mL) of OL nanoparticles in MilliQ water (1.0 mg/ml, pH 4.2) was added dropwise to PDDA solution (1.0 mg/mL, Milli-Q water) under slow magnetic stirring for 2 h. The deposition of the PDDA layer was monitored by UV-visible analysis, following the appearance of typical peak at 276 nm, which corresponds to the shift of the characteristic PDDA B-band after adsorption on lignin. This result was further confirmed by the Zeta potential analysis (**Figure 3.5**), the system reaching the value of -22 mV. Tyrosinase (3 mg, 900 U/mg) was then added to OL/PDDA nanoparticles (PBS; 3mL) to yield catalyst **III** (**Figure 3.1**, pathway C). Scanning electron microscopy (SEM) image of catalyst **III** (**Figure 3.6**, panel A) showed regular spherical particles with a wrinkled surface and an average diameter of 0.22±0.02 μm. Catalyst **III** showed a Zeta potential value of -40 mV (**Figure 3.5**)

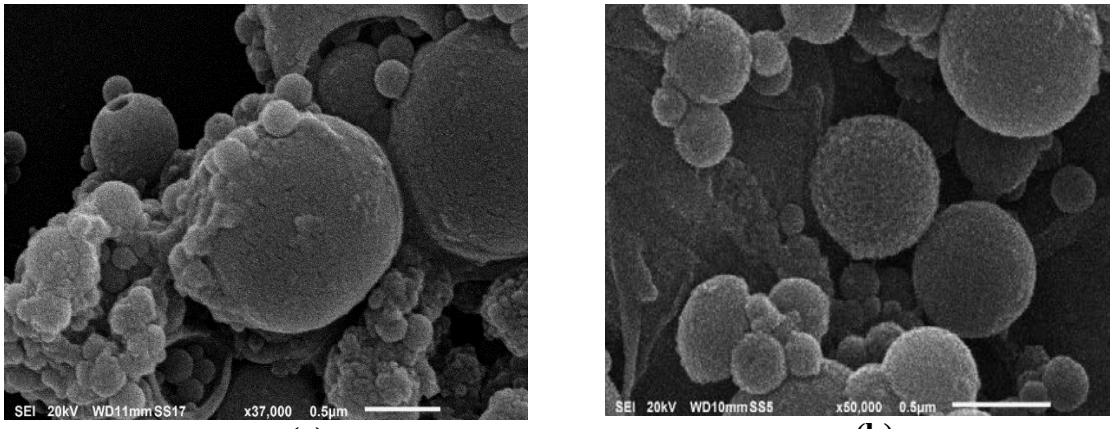

(**a**) (**b**)

Figure 3.6. SEM images of catalyst **III** in the first panel (**a**) and of catalyst **IV** in the second panel (**b**).

Finally, we applied the glutaraldehyde (GA)-assisted co-immobilization of tyrosinase in the presence of Bovine Serum Albumin (BSA).[246] As a general trend, the immobilization efficiency of tyrosinase is dependent upon the number of the enzyme molecules loaded on the selected surface. The enzyme strives for the greatest surface coverage, leading to conformational changes that could influence the activity. BSA performs as an inert protein with an isoelectric point close to that of tyrosinase, to partially reduce the amount of surface area available for the enzyme, while GA forms a protective three-dimensional network. Briefly, the suspension of OL/PDDA nanoparticles (3.5 mg/mL) in PBS (1.4 mL) was added to tyrosinase (300 μL, 3.4 mg/mL in PBS) and BSA (1.5 ml, 2.0 mg/mL) under gentle shaken for 30 min at room temperature. Finally, GA (2.5% v/v water solution) was added to yield catalyst **IV** (**Figure 3.1**, pathway D). **Figure 3.6** (panel B) reports the SEM image of catalyst **IV**. The surface of catalyst **IV** appeared as a roughly aggregate of small clumps with an average diameter of 0.22±0.02 μm (Figure 3.3) and a value of the Zeta potential of -32 mV, that is significantly different from that previously measured for catalyst **III**.

*Activity parameters of catalysts **I-IV***

The Tyrosinase (Tyr) activity was determined by the dopachrome assay[247] following the oxidation of L-tyrosine at 475 nm, the enzyme unit being defined in terms of the increase in absorbance of 10^{-3} unit/min at 25 °C in 0.1M phosphate buffer (pH 7.0). The immobilization and activity yields were evaluated as reported in equations 1 and 2, respectively.

$$\text{Activity (units/mg)} = U_x/W_{support} \quad (1)$$

$$\text{Activity yield (\%)} = [U_x/(U_a - U_r)] \times 100 \quad (2)$$

$$\text{Immobilization yield (\%)} = [(U_a - U_r)/U_a] \times 100 \quad (3)$$

Where U_a is the total activity (units) of the enzyme added to the solution and U_r is the residual activity (units) evaluated by the dopachrome method in the washing solutions.

As reported in **Table 6**, catalysts **III-IV** showed a value of the immobilization yield higher than that of catalysts **I-II**, suggesting a better performance of the LbL procedure in the immobilization of tyrosinase with respect to encapsulation and direct adsorption processes (entries 3-4 versus entries 1-2). The activity yield followed a similar trend. Note that catalyst **IV** was characterized by the highest value of the activity yield confirming the beneficial role of BSA and GA in the retention of the tyrosinase catalytic performance after the immobilization process. The activity of catalyst **II-IV** was comparable to that previously reported tyrosinase based nanocatalysts.[248]

Table 6. Activity parameters of catalysts **I-IV.**

Entry	Catalyst	Immobilization yield %	Activity yield %[a]	Activity (units/mg)[b]
1	**I**	69	34	6.8
2	**II**	71	31	6.2
3	**III**	90	42	8.4
4	**IV**	87	58	11.6

[a] The activity of native tyrosinase, evaluated by the dopachrome method, was 900 units/mg of enzyme.
[b]The enzyme loading is referred to the percentage of the initial tyrosinase supported on the catalyst.

Cyclic voltammetry analysis

Cyclic voltammograms (CVs) of catalysts **I-IV** were recorded at 25°C in comparison with parent OL nanoparticles as a reference. The analyses were carried out in 250 µM catechol solution (PBS buffer, 50 mM; pH 6.5), in the presence of KCl (100 mM) as supporting electrolyte. Irrespective to the catalysts studied, the electrocatalytic wave in CVs started in the correspondence of the formal potential ($E^{0'}$) of catechol (0.190 V) measured *versus* Saturated Calomel Electrode (SCE). Data are reported in Figure 2.27 (panels A-D; catalysts are marked by a red line, while the reference is reported as black line). As a general pattern, the CVs confirmed the previously observed trend for the activity parameters (Table 8). In particular, the CV of catalyst **I** (**Figure 3.7**, panel A) showed a well-defined electrocatalytic wave starting from 0.190 V *vs*. SCE and rising up to -20 µA cm^{-2} at -0.2 V *vs*. SCE. This data indicated that tyrosinase retained an

appreciable electrocatalytic activity also in the encapsulation state. Catalyst **II** (**Figure 3.7**, panel B) was characterized by a weakly electrocatalytic responsiveness (electrocatalytic wave from 0.190 V *vs*. SCE to -4 µA cm^{-2} at -0.2 V *vs*. SCE), in accordance with the low activity yield previously measured (**Table 6**, entry 2). Afterwards, the electrocatalytic responsiveness of catalyst **III** was found to be increased (electrocatalytic wave from 0.190 V *vs*. SCE to -30 µA cm^{-2} at -0.2 V *vs*. SCE). Finally, catalyst **IV** showed the highest electrocatalytic wave compared to the other catalysts starting from 0.190 V *vs*. SCE to -56 µA cm^{-2} at -0.2 *vs*. SCE.

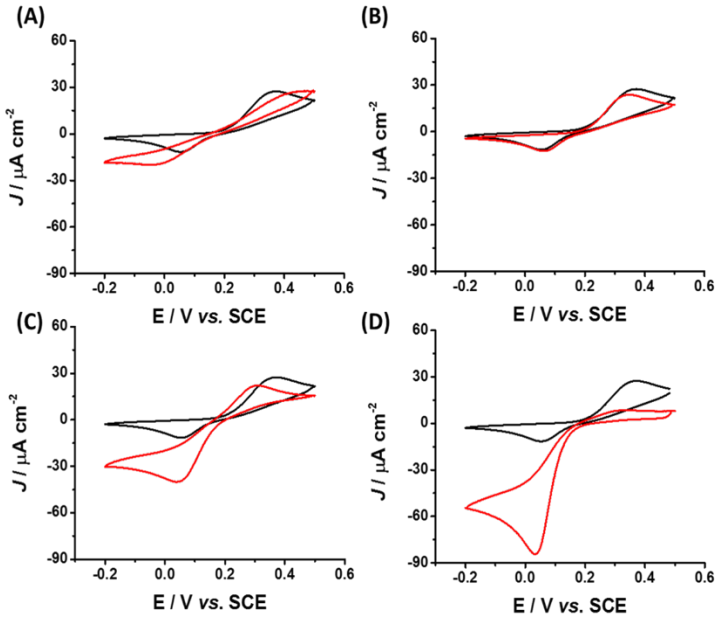

Figure 3.7. Cyclic voltammograms of OL nanocapsules (black line, A-D), Catalist **I** (red line, A), Catalyst **II** (red line, B), Catalyst **III** (red line, C) and Catalyst **IV** (red line, D) performed in 250 µM catechol solution (50 mM PBS buffer pH 6.5 + 100 mM KCl) at scan rate 5 mV s^{-1}.

*Kinetic properties of catalysts **I-IV** and synthesis of catechol derivatives*

Catalysts **I–IV** were characterized for their kinetic properties using L-Tyrosine (in the range 0.33–0.1 mM) as substrate and plotting data to a double reciprocal Lineweaver–Burk plot (**Table 7**). Data for native Tyrosinase are also reported as a reference (**table 7**, entry 1). Irrespective from the procedures used for the immobilization, V_{max} decreased and K_m increased for supported tyrosinase, which led to a partial reduction in the catalytic efficiency with respect to free enzyme. Similar trends in K_m and V_{max} values have been reported for tyrosinase immobilized on other carriers, they being attributed to mass transfer limitation processes.[249]

Table 7. Kinetic parameters of Tyr and catalysts **I-IV**.

Entry	Catalyst	K_m (mM)	$V_{max} \times 10^{-3}$ (ΔAbs min μg_{enzyme})$^{-1}$	V_{max}/K_m ($x10^{-3}$)
1	Tyr	0.18	6.02	33.44
2	**I**	0.51	3.40	6.77
3	**II**	0.67	1.14	1.70
4	**III**	0.37	3.89	10.51
5	**IV**	0.25	4.10	16.40

All experiments were conducted in triplicate using free and immobilized tyrosinase. Average errors in kinetic parameters were 2–4% for Km and 1–3% for Vmax. L-Tyrosine was used as substrate.

Catalysts **III**-**IV** showed a higher rate and catalytic efficiency than catalysts **I**-**II** (**Table 7**, entries 4-5 versus entries 2-3), confirming the beneficial role of the LbL. Note that catalyst **I** was more active than catalyst **II** (**Table 7**, entry 2 versus entry 3), probably as a consequence of conformational changes occurring when the enzyme was directly adsorbed on the surface of the OL nanoparticles.

The synthetic versatility of catalysts **I**-**IV** was then evaluated in the oxidation of a panel of selected phenols **1**−**4** (**Figure 3.8**) to obtain the corresponding catechol derivatives **5**-**8**, including bioactive hydroxytyrosol[250] **6**, and 3,4-dihydroxydihydrocinnamic acid **8**.[251]

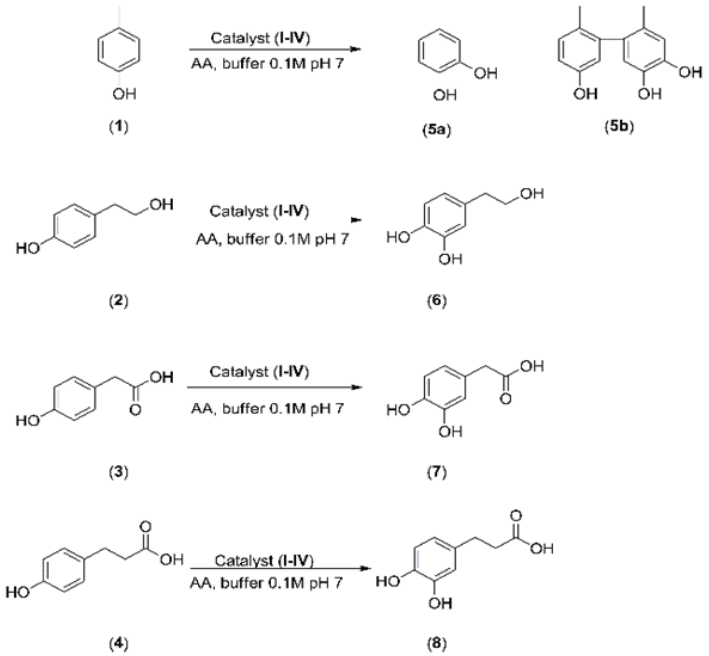

Figure 3.8. Oxidation of phenols **1**–**4** with catalysts **I**–**IV.**

Catechols are characterized by several biological activities and are well recognized as antioxidant compounds.[252] The biotechnological potential of tyrosinase in the synthesis of catechols has received a great degree of attention because they are difficult to obtain under environmentally friendly conditions by means of traditional chemical procedures.[253] As a general procedure, phenols **1**-**4**, catalysts **I-IV** (540 units), and ascorbic acid AA (2.0 equiv) were stirred in PBS (0.1 M, pH 7.0, 5.0 mL) at room temperature, under a dioxygen atmosphere (O_2). Ascorbic acid was used as an internal reducing agent to avoid the polymerization of the quinone intermediates.[254] As a general trend, catalysts **I-IV** were able to oxidize phenols to corresponding catechols from moderate to high yield. No oxidation was observed in the presence of OL alone. Irrespective from the experimental conditions, catalysts **III** and **IV** were more reactive than catalyst **II**, affording the desired catechol in acceptable yields. The oxidations were very selective, catechol derivatives being the only isolated products besides to unreacted substrate. In the case of catalyst **I**, a lower selectivity was observed, since catechols were detected only in low yield with respect to the total conversion of substrate (**Table 8**, entry 2-5).

Table 8. Oxidation of Phenols **1**−**4** with Native Tyrosinase and Catalysts **I-IV**.

Entry	Catalyst	Substrate	Product(s)	% Conversion	%Yield
1	Tyr	1	5a	99	98
2	**I**	1	5a[5b]	91	20
3	**II**	1	5a	40	39
4	**III**	1	5a	59	59
5	**IV**	1	5a	75	75
6	Tyr	2	6	96	96
7	**I**	2	6	35	25
8	**II**	2	6	20	18
9	**III**	2	6	38	37
10	**IV**	2	6	46	46
11	Tyr	3	7	77	77
12	**I**	3	7	18	7
13	**II**	3	7	15	15
14	**III**	3	7	21	20
15	**IV**	3	7	28	28
16	Tyr	4	8	78	78
17	**I**	4	8	34	12
18	**II**	4	8	30	30
19	**III**	4	8	57	56
20	**IV**	4	8	67	65

The oxidation was performed on 0.02 mmol of substrate with the appropriate catalyst (540 units) in PBS (0.1 M pH 7) at 25°C under O_2 atmosphere for 24 h.

The low mass balance was probably due to over-oxidation processes, as confirmed by the isolation of a product of oxidative coupling, compound **5b**, in the oxidation of *para*-cresol **1** (Table 10, entry 2). Moreover, the low yield observed in the oxidation of phenol **3** (**Table 8**, entries 11-15) was probably ascribable to the known inhibitory activity reported for this compound against tyrosinase.[255] Recycling experiments proceeded with success in the oxidation of phenol **1**, as a selected example. After the first oxidation, catalysts **I-IV** were recovered by centrifugation, washed, and reused with fresh substrate. As shown in **Table 9**, catalysts **I-IV** were used for at least 5 cycles with only a slight decrease of activity.

Table 9. Recycling of catalyst **I-IV** in the oxidation of *para*-cresol **1.**

Entry	Run	Catalyst I (Yield %)	Catalyst I (Yield %)	Catalyst III (Yield %)	Catalyst IV (%Yield)
1	**1**	20	39	59	75
2	**2**	20	39	59	75
3	**3**	15	32	51	70
4	**4**	11	27	46	67
5	**5**	9	21	42	61

Reusability is expressed as the yield in % of catechol **5a** obtained by oxidation of 1 with catalyst **I-IV**.

3.2 Layer by layer supported laccase on lignin nanoparticles catalyzes the selective oxidation of alcohols to aldehydes

3.2.1 Aim of work

The physical and chemical properties of lignin are modified during the transition from the natural amorphous state to micro- and nano-scaled devices, as a consequence of the formation of π-interactions between the aromatic moieties.[256,258] Procedures for the preparation of lignin nanoparticles with increased UV- absorption capacity and radical scavenger activity by solvent exchange,[258] and layer by layer (LbL)[259] technologies are reported,[260] encompassing the use of raw materials, at both laboratory and pilot scales.[135]

Laccase (EC 1.10.3.2, *p*-diphenol: dioxygen oxidoreductase) [261] catalyzes the reduction of dioxygen to water[262] by the use of different clusters of copper atoms, indicated as T1–T3. Clusters T2 and T3 participate directly in dioxygen reduction,[263] while T1 transfers electrons from the substrate to the tri-nuclear cluster.[264] This enzyme has been successfully applied in bioremediation,[265] organic synthesis,[266] wood pulp bleaching and biorefinery.[267,268] Low molecular weight redox mediators increase the reactivity of laccase acting as electron shuttles from the enzyme active site to the bulk of

the solution.[269,270] Among the immobilization procedures reported for laccase,[271–272] the use of nano-scaled supports has been reviewed, highlighting the advantage of a high surface area, biocompatibility, and mechanical resistance.[273,274] In particular, favorable electrochemical properties emerged in the oxidation of alcohols to aldehydes after immobilization of laccase on multi walled carbon nanotubes (MWCNTS).[244] Environmentally friendly synthesis of aldehydes is required to avoid the low selectivity and toxicity of organometallic species and inorganic oxidants.[275,276] Lignin is a suitable support for the immobilization of oxidative enzymes due to its electro-chemical responsiveness.[277,278] For example, the association between lignin and laccase (or other polyphenol oxidases) can boost the activity of lytic polysaccharide mono-oxygenase (LPMO) in delignification processes, as a consequence of the formation of low molecular weight lignin derivatives (LMWLD).[105] In this latter case, LMWLD worked in synergy with traditional redox mediators.[106] The boosting effect was also observed at the nano-scale level, the activity of tyrosinase (EC 1.14.18.1)[279] being enhanced after immobilization of the enzyme on organosolv lignin nanoparticles (NOL).[280] NOL stabilized and reinforced against solvent dissolution after treatment with laccase, thanks to the occurrence of oxidative coupling reactions.[281] The LbL coating of lignin nanoparticles with lipase and cutinase was also reported.[167] We describe here the immobilization of laccase from *Trametes versicolor* (EC 1.10.3.2) on NOL by encapsulation, physical adsorption, and LbL procedures.[282]

Laccase preserved the catalytic activity and kinetic properties after the immobilization, showing pseudo direct electron transfer (pseudo-DET) and mediated electron transfer (MET)[262] mechanisms. The LbL procedure was more efficient than physical adsorption and encapsulation, favoring the selective 2,2,6,6-tetramethylpiperidin-1-yl- oxyl (TEMPO) mediated oxidation of alcohols to aldehydes. TEMPO was more efficient than other possible redox mediators, such as 2,2′-azino-bis 3-ethylbenzthiazoline-6-sulfonic acid) (ABTS), *N*-hydroxy-benzotriazole (HOBT), vanillin and syringaldehyde. The catalytic activity and morphological integrity were retained for six runs. Among the novel catalysts, LbL based systems showed a reactivity and selectivity comparable to native laccase[283] and higher than other catalysts in which laccase was immobilized on silica, [284] suggesting the possibility of a specific boosting effect exerted by the electro- chemically active lignin support.

3.2.2 Experimental part

Materials

Organosolv lignin (OL) was furnished by Chemical Point (Ger- many). Laccase (1.04 U mg^{-1}), Bradford reagent, polydiallyldimethylammonium chloride) PDDA (20% v/v water solution), 2,2-azinobis-(3-ethylbenzothiazoline-6-sulfonic acid) (ABTS), 2,2,6,6-tetramethyl-1-piperidinyloxy (TEMPO), *N*-hydroxybenzotriazole (HOBt), vanillin, syringaldehyde, boric acid (H_3BO_3), orthophosphoric acid (H_3PO_4), acetic acid (CH_3-COOH), potassium perchlorate ($KClO_4$), glutaraldehyde (GA), tetrahydrofuran (THF) and bovine serum albumin (BSA) were purchased from Sigma-Aldrich (St. Louis, MO, USA). All exper- iments were done in triplicate using native and immobilized laccase in sodium acetate buffer (Na-acetate buffer 0.1 M pH 5.0). Solutions were prepared by using Milli-Q water (ρ = 18.2 MΩ cm a 25 °C; TOC < 10 μg L^{-1}, Millipore, Molsheim, France). The cationization reaction of OL to yield cationic lignin (CATLIG) was performed as follows: lignin organosolv (10 mg ml^{-1}; 0.1 M) in NaOH was treated with glycidyl tetramethyl ammonium chloride (20 mg) at 60 °C for 2 h, under magnetic stirring. reaction product was dialyzed for 24 h against deionized H_2O using Spectrapore™ dialysis membrane (3.5 kDa MWCO). ^{31}P NMR analysis of CATLIG confirmed the structure of the expected product (**Figure 3.9**).[163]

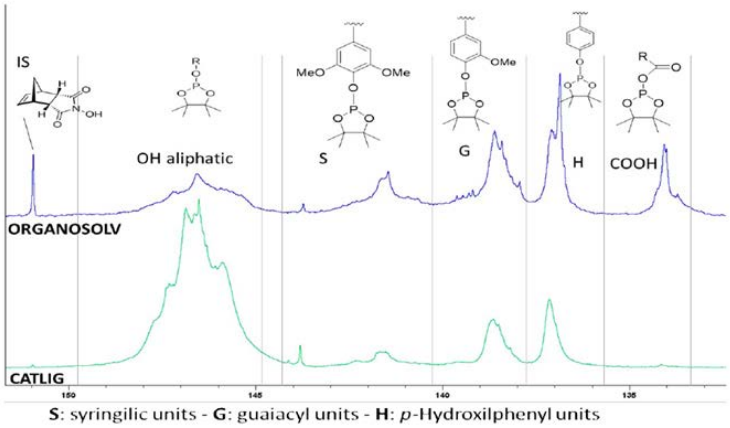

Figure 3.9. ^{31}P NMR analysis of phosphitylated lignin organosolv and cationic lignin (CATLIG) in presence of internal standard (N-hydroxy-5-norbornene-2,3-dicarboxylic acid imide).

*Encapsulation procedure. Catalyst **I***

A solution of organosolv lignin OL (2.0 mg mL^{-1} in 1.2 mL of THF/H_2O 5:1 v/v) was added to an aqueous solution (3.8 mL) of laccase (3.0 mg mL^{-1}, 1.04 U mg^{-1}) under magnetic stirring. Lignin nanoparticles NOL formed instantaneously. Catalyst **I** was recovered from residual H_2O by centrifugation (20 min at 6000 rpm) after removal of

THF. The loading factor and activity parameters were evaluated by analyzing the residual aqueous solution. Catalyst **I** was washed several times with sodium acetate buffer (0.1 M) and lyophilized.

*Physical adsorption procedure. Catalyst **II***

A solution of organosolv lignin OL (2.0 mg mL^{-1} in 1.2 mL of THF/H_2O 5:1 v/v) was added to Milli-Q water (in 3.8 mL) under gentle magnetic stirring followed by centrifugation (20 min at 6000 rpm) to afford NOL. Next, laccase (2.0 mg, 1.04 U mg^{-1}) in sodium acetate buffer (1.0 mL, 0.1 M; pH 5.0) was added to NOL (10 mg) in the same buffer (15 mL) under orbital shaking at room temperature for 24 h. Catalyst **II** was recovered by centrifugation (20 min at 6000 rpm) and the residual solution was used for the evaluation of the loading factor and activity parameters. Catalyst **II** was washed several times with sodium acetate buffer (0.1 M) and lyophilized.

*Layer by layer procedure. Catalysts **III–V***

Catalyst **III**. NOL in Milli-Q water (15 mL; 1 mg mL^{-1}, pH 4.2) were added dropwise to a PDDA water solution (1 mg mL^{-1}) under gentle magnetic stirring at room temperature. After 2 h, the suspension was centrifuged and washed with Milli-Q water to afford the NOL–PDDA intermediate. Laccase (2.0 mg, 1.04 U mg^{-1}) dissolved in sodium acetate buffer (1.0 mL, 0.1 M; pH 5.0) was added to NOL–PDDA (10 mg) in the same buffer (15 mL) under orbital shaking at room temperature for 24 h. Catalyst **III** was recovered by centrifugation (20 min at 6000 rpm) and the residual solution was used for the evaluation of the loading factor and activity parameters. Catalyst **III** was washed several times with sodium acetate buffer (0.1 M) and lyophilized.

Catalyst **IV**. Laccase (2.0 mg, 1.04 U mg^{-1}) and bovine serum albumin (BSA, 2.0 mg) were added to NOL–PDDA (4 mg mL^{-1}) in sodium acetate buffer (3 mL, 0.1 M), and the mixture was shaken at room temperature for 30 min. GA (150 μL, 2.5% v/v water solution) was added to the suspension and the mixture was shaken again at room temperature for 30 min, and then at 4 °C overnight. Catalyst **IV** was recovered by centrifugation (20 min at 6000 rpm) and the residual solution was used for the evaluation of the loading factor and activity parameters. Catalyst **IV** was washed several times with sodium acetate buffer (0.1 M) and lyophilized.

Catalyst **V**. NOL in Milli-Q water (20 mg mL^{-1}, pH 4.2) were added dropwise to a CATLIG water solution (1 mg mL^{-1}, 15 mL) under gentle magnetic stirring at room

temperature. After 2 h, the final suspension was centrifuged and washed with Milli-Q water to afford the NOL–CATLIG intermediate. Laccase in sodium acetate buffer (2.0 mg, 1.04 U mg^{-1}, 1.0 mL) was added to NOL–CATLIG (10 mg) in the same buffer (15 mL) under orbital shaking at room temperature for 24 h. Catalyst **V** was recovered by centrifugation (20 min at 6000 rpm) and the residual solution was used for the evaluation of the loading factor and activity parameters. Catalyst V was washed several times with sodium acetate buffer (0.1 M) and lyophilized.

Morphological characterization

Scanning electron microscopy (SEM) was conducted using a JEOL JSM 6010LA electron microscope (Tokyo, Japan). As a general procedure, catalysts **I–V** were treated with GA (3.0%) in cacodylate buffer (0.1 M, pH 7.2), followed by treatment with osmium-tetroxide (OsO_4, 1.0% w/w) in the same buffer at room temperature. Ethanol (EtOH) was used for the dehydration of the samples before the analysis. The samples were air dried, and sputter-coated with gold in a Balzers MED 010 unit.

ATR-IR characterization

Attenuated total reflection Fourier transform infrared (ATR- IR) spectroscopic analysis was carried out with a PerkinElmer (Spectrum One) spectrometer equipped with an UATR unit cell. IR spectra were recorded by averaging 32 scans, with a resolution of 4 cm^{-1}.

Enzyme activity assay

2,2′-azino-bis 3-ethylbenzothiazoline-6-sulfonic acid) diammonium salt (ABTS) was used for the enzyme activity evaluation.[285] Briefly, the absorbance of the cation radical of ABTS (sodium acetate buffer solution, 5 mM, 3.0 mL) was measured at 420 nm (ε_{420} = 36 000 M^{-1} cm^{-1}) in the presence of different concentrations of laccase. One unit of laccase activ- ity is defined as the amount of enzyme that catalyzes the transformation of ABTS (1.0 μmol) in the mixture (200 μL) at 25 °C for 1.0 min.

Kinetic parameters

The Michaelis–Menten constant (K_m) and catalytic constant (K_{cat}) have been determined by standard ABTS procedure as previously reported, using different concentrations of ABTS (125–5000 μM) in sodium acetate buffer (pH 5.0). Lineweaver–Burk plots were drawn from the initial rates obtained at various ABTS concentrations,

while the amount of enzyme was kept constant. The values have been calculated by the use of the GraphPad software.

Electrochemical characterization

Electrochemical analyses of the samples were carried out using a PGSTAT204N potentiostat (Eco Chemie, Nova 2.1 software). Three electrodes were used, a glassy carbon (GC) electrode (working electrode, d = 3 mm, Metrohm), a saturated calomel electrode (reference electrode, SCE, 244 mV *vs.* NHE, AMEL), and a glassy carbon rod electrode (counter electrode, d = 2 mm, Metrohm). Cyclic voltammetry measurements were performed in two different ways: pseudo-direct electron transfer (pseudo- DET): 120 mM Britton–Robinson (B–R) buffer pH 5.5 and 100 mM $KClO_4$; mediated electron transfer (MET): 120 mM Britton–Robinson (B–R) buffer pH 5.5 and 100 mM $KClO_4$ containing 500 μM ABTS. Catalysts I–V (2 mg mL^{-1}) in Britton– Robinson (B–R) buffer (5 μL) were immobilized on GC electrodes by a drop-casting procedure. NOL were used as a reference under similar loading conditions.

Oxidation of alcohols: general procedure

Aliphatic and aromatic alcohols, benzyl alcohol **1**, 4-methoxybenzyl alcohol **2**, 4-chlorobenzyl alcohol **3**, cinnamyl alcohol **4** and geraniol **5** (20 mM), the catalyst (0.65 U) and TEMPO (6.0 mM) were placed in sodium acetate buffer (1.0 mL, 0.1 M, pH 5.0) under an O_2 atmosphere and vigorous stirring conditions at room temperature. The oxidation of alcohol **3** was also performed with ABTS, HOBT, vanillin, and syringaldehyde, as alternative redox mediators. After the disappearance of the substrate, the catalyst was recovered by filtration, and the residual mixture was extracted with ethyl acetate (EtOAc) (10 ml × 3 times). The organic layer was washed with NaCl (saturated solution) and dried (anhydrous Na_2SO_4). Gas chromatography–mass spectrometry (GC-MS) was performed on a Varian 450GC-320 MS apparatus (electron beam of 70 eV) using an SPB column (25 m × 0.25 mm, 0.25 mm film thickness), a helium flow of 1.0 mL min^{-1}, an injector temperature of 280 °C, and an isothermal profile at 70 °C for 2.0 min, followed by 10 °C min^{-1} up to 280 °C for 25 min. Acetophenone was used as an internal standard.

Catalyst recycling

The reusability of catalysts **III** and **IV** was evaluated analyzing the oxidation of 4-methoxybenzyl alcohol (20 mM) in the presence of TEMPO under previously reported conditions. After 16 h, the catalyst was recovered by centrifugation and reused for six runs.

3.2.3 Results and discussions

*Encapsulation procedure. Catalyst **I***

Laccase was encapsulated by applying a slight modification of a reported solvent exchange procedure. Briefly, organosolv lignin (OL, 2.0 mg) in a tetrahydrofuran THF/water mixture (1.2 mL, 5:1 v/v) was quickly added to laccase in water (3.0 mg mL^{-1}, 1.04 U mg^{-1}, 3.8 mL) under gentle magnetic stirring at room temperature (**Figure 3.10**, pathway A). Lignin nanoparticles (NOL) formed instantaneously. During the addition, the polar chemical groups (alcohols and carboxylic acid moieties) of lignin are exposed toward water, the resting one being organized inside the aggregation. Hollow spherical particles are then produced for the encapsulation of laccase.[286,287] Catalyst **I** was recovered after evaporation of THF, washed with sodium acetate buffer (0.1 M) and lyophilized. The residual solution was used for the evaluation of the loading factor and activity parameters (see the next section). A similar encapsulation procedure has been reported for the delivery of drugs,[288] pesticides,[289] genetic material,[290] and food additives.[291,292] The SEM image of catalyst **I** confirmed the formation of nanoparticles with an average diameter of 0.22 ± 0.01 μm (**Figure 3.11**, panel B). The SEM image of empty NOL is also reported as a reference (**Figure 3.11**, panel A).

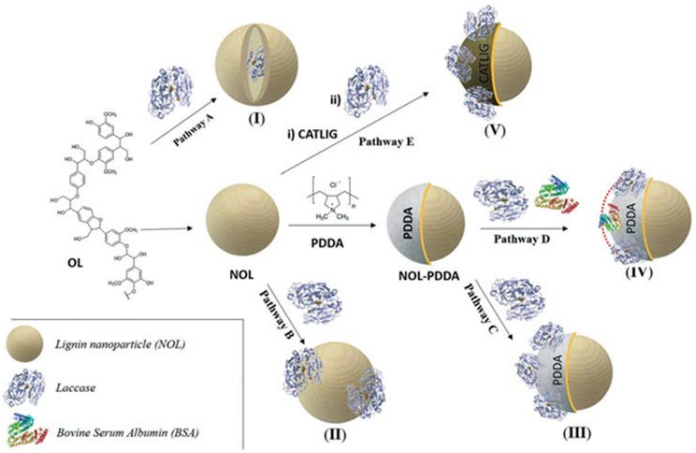

Figure 3.10 Schematic representation for the preparation of catalysts **I**–**V**. Encapsulation (pathway A), physical adsorption (pathway B) and layer by layer (pathways C–E) immobilization procedures.

*Adsorption procedure. Catalyst **II***

Catalyst **II** was prepared by adsorption of laccase on the surface of NOL. The interaction between lignin and proteins is reported,[153] histidine, proline, and serine residues showing the highest affinity.Aromatic and charged amino acids also proved to be essential for the adsorption, as confirmed by the value of their binding energy.[293] Undesired denaturation of the protein may inhibit the accessibility of amino acids to the lignin surface.[294] As a general procedure, laccase (2.0 mg, 1.04 U mg^{-1}) was added to NOL in sodium acetate buffer (10 mg, 15 mL) under orbital shaking at room for 24 h (**Figure 3.10**, pathway B). Catalyst **II** was recovered by centrifugation and washed with sodium acetate buffer (0.1 M) to remove the excess of the enzyme. The SEM image of catalyst **II** showed particles with an average diameter of 0.20 ± 0.01 μm (**Figure 3.11**, panel C). Some of the particles were characterized by an "open mouth" as a consequence of the fast-internal removal of the solvent under the drying conditions.[160] The "open mouth" morphology was reported also in the preparation of NOL by precipitation procedures.[295]

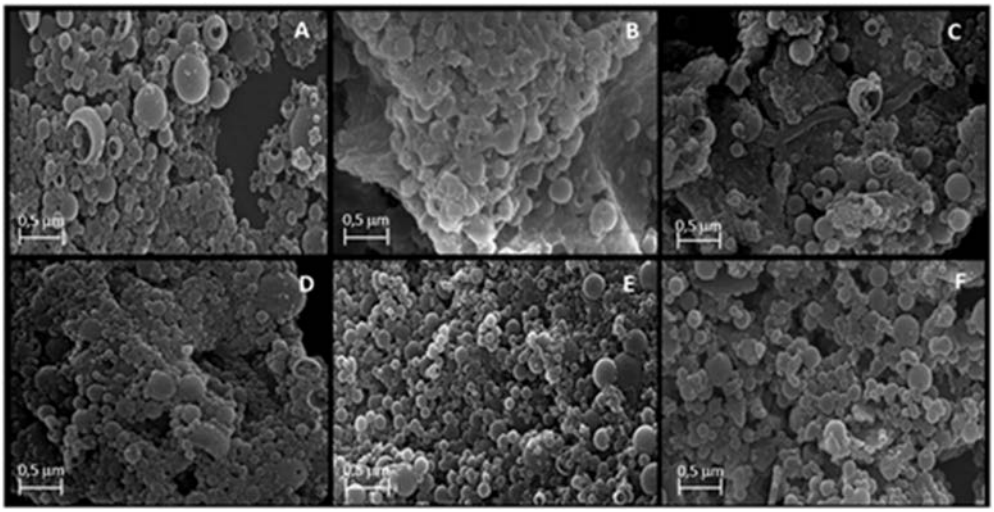

Figure. 3.11 SEM images of catalysts **I–V**. Panel A: NOL. Panel B: Catalyst **I** obtained by encapsulation of laccase inside NOL. Panel C: Catalyst **II** obtained by physical adsorption of laccase on pre-formed NOL. Panel D: Catalyst **III** obtained by deposition of laccase on NOL–PDDA. Panel E: Catalyst **IV** obtained by application of the glutaraldehyde (GA) assisted co-immobilization procedure in the presence of bovine serum albumin (BSA). Panel F: Catalyst **V** obtained by deposition of laccase on NOL–CATLIG.

*Layer by layer procedure. Catalysts **III–V***

The LbL procedure was realized by the sequential deposition of polyelectrolytes with opposite electrical charges. The layers applied in this process are responsible for the chemical and physical properties of the system, as well as for the stabilization of the overall structure. NOL showed a negative value of the Z potential (−42 mV at pH 4.2),

which favored the cation–π interactions with positively charged polyelectrolytes. Poly(diallyl dimethyl ammonium chloride) (PDDA), and as an alternative, the cationic form of lignin (CATLIG), were used as positively charged polyelectrolytes (**Figure 3.10**, pathway C). Briefly, NOL in deionized water (15 mL; 1 mg mL^{-1}, pH 4.2) were added dropwise to PDDA (1.0 mg mL^{-1}, deionized water) to afford the NOL/PDDA intermediate. Next, NOL–PDDA (10 mg, 15 mL) was treated with laccase (2.0 mg, 1.04 U mg^{-1}) in the same buffer under orbital shaking at room temperature for 24 h to yield catalyst **III**. The SEM image of catalyst **III** is reported in **Figure 3.11** (panel D). As an alternative, the glutaraldehyde (GA)-assisted co- immobilization procedure, in the presence of bovine serum albumin (BSA), was applied. This procedure optimizes the immobilization process avoiding conformational changes of the enzyme due to its tendency to cover the greatest surface area of the support. BSA performs as an inert spacer reducing the surface area available for laccase, while the GA cross-linking creates a protective three-dimensional film (**Figure 3.10**, pathway D). Laccase (2.0 mg) and BSA (2.0 mg) were added to NOL–PDDA (4 mg mL^{-1}, 3 mL) in sodium acetate buffer (0.1 M), followed by addition of GA (150 μL, 2.5% v/v water solution) at room temperature for 30 min, and then at 4 °C overnight, to yield catalyst **IV** (**Figure 3.11**, panel E). Finally, catalyst **V** was prepared under the experimental conditions previously reported for catalyst **III** (Figure 3.10, pathway E), using CATLIG instead of PDDA. **Figure 3.11** (panel F) shows a SEM image of catalyst **V**.

*Attenuated total reflectance Fourier transform infrared analysis of catalysts **I–V***

The attenuated total reflectance Fourier transform infrared (ATR-FTIR) spectra of catalysts **I–V** are reported in **Figure 3.12**. The ATR-FTIR spectrum of NOL is also reported as a reference. NOL showed all characteristic IR signals expected for lignin at 1420–1450 cm^{-1} (aromatic ring and C–H bonds), 1522 cm^{-1} (aromatic ring), 1600 cm^{-1} (aromatic ring and conjugated C=O), 2910 cm^{-1} (C–H bonds), and 3400 cm^{-1} (ali- phatic and phenolic units).[296]

Irrespective of the immobilization procedure, catalysts **I–V** showed two novel IR signals at 1690 cm^{-1} and 3050 cm^{-1}, respectively, corresponding to C=O stretching (amide I band) and N–H bending (amide II band) vibrations typical of proteins. These values are in accordance with data reported for the ATR-FTIR analysis of laccase after immobilization on silica, [297] or alternatively, after adsorption on gold nanoparticles.[298]

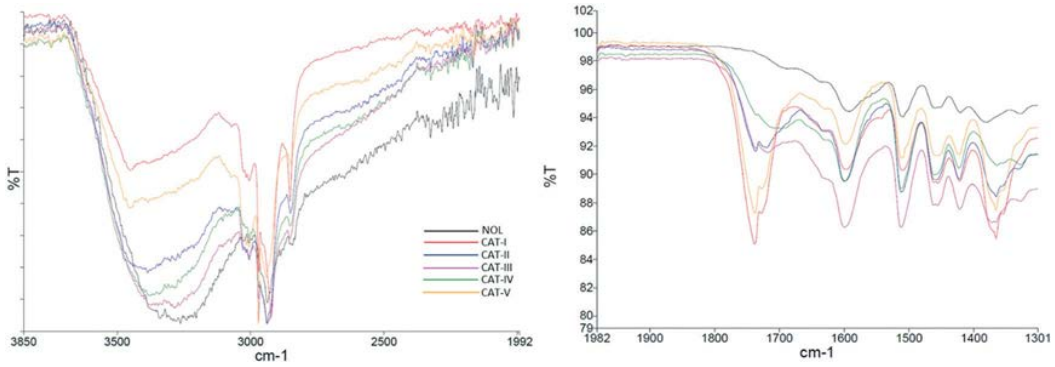

Figure 3.12. ATR-FTIR spectra of catalysts **I–V**. Signals at 1690 cm^{-1} and 3050 cm^{-1}, corresponding to C=O stretching (amide bond) and N–H vibration (amide I band), respectively, were characteristic of laccase

*Activity parameters of catalysts **I–V***

The activity parameters of catalysts **I–V** were determined by the 2,2-azinobis-(3-ethylbenzothiazoline-6-sulfonic acid) (ABTS) assay. The formation of the ABTS cation radical was detected at 420 nm (ε_{420} = 36 000 M^{-1} cm^{-1}). The activity, activity yield, and immobilization yield were evaluated using eqn (1)–(3), respectively:

$$\text{Activity (units per mg)} = U_x/W_{support} \quad (1)$$

$$\text{Activity yield (\%)} = [U_x/(U_a - U_r)] \times 100 \quad (2)$$

$$\text{Immobilization yield (\%)} = [(U_a - U_r)/U_a] \times 100 \quad (3)$$

In eqn (1)–(3), U_a represents the total activity (units) of laccase added to the solution, U_r is the residual activity (units) in the washing solution, and U_x is the activity of the enzyme after immobilization (the enzyme unit was defined as the increase in the absorbance of 10^{-3} unit per min at 25 °C in 0.1 M Na-acetate buffer). As reported in **Table 10**, the immobilization yield of catalysts **III–V** was higher than that of catalysts **I–II**, indicating that the LbL procedure was the most efficient method for the immobilization of laccase (**Table 10**, entries 3 and 4 *versus* entries 1 and 2). The activity yield followed a similar trend. Note that the activity parameters of catalysts **III–V** were similar to those previously reported after the immobilization of laccase on electrochemical active multi walled carbon nanotubes (MWCNTs). They were of the same order of magnitude as those showed by the native enzyme (**Table 10**, entry 6).

Table 10 Activity parameters of catalysts **I–V**

Entry	Catalyst	Loading[a]	Activity yield%[b]	Activity (U mg^{-1})	Immobilization yield%[c]
1	I	5.1	5.6	0.12	6.0
2	II	31.6	20.6	0.31	25.8
3	III	69.4	65.4	0.71	64.1
4	IV	72.1	65.7	0.59	66.6
5	V	60.6	54.1	0.56	55.2
6	Laccase	—	—	1.07	—

[a] The loading value was expressed as the percentage of immobilized laccase with respect to the starting enzyme. [b] Calculated as in eqn (2).[c] Calculated as in eqn (3).

*Cyclic voltammetry and amperometric analysis of catalysts **I–V***

These analyses were designed to evaluate the electrocatalytic mechanism of laccase after the immobilization, considering both pseudo direct electron transfer (pseudo-DET) and mediated electron transfer (MET) mechanisms.[299] Cyclic voltammograms (CVs) have been recorded in Britton–Robin- son buffer (120 mM, pH 5.5) and $KClO_4$ (100 mM) with a scan rate of 5 mV s^{-1} at room temperature, from the reported EONSET value to 0 V (vs. SCE).

Pseudo direct electron transfer (pseudo-DET) mechanism

No electrocatalytic effect was detected for catalyst **I** (**Figure 3.13**, panel A, red line) when compared to NOL (**Figure 3.13**, panel A, black line), as a consequence of the impossibility for laccase to interact with the surface of the electrode after the encapsulation procedure.[300] On the other hand, the pseudo-DET mechanism was operative in the case of catalyst **II** (electrocatalytic wave starting at EONSET = 0.398 V and rising up to −23 μA cm^{-2}), highlighting the electrochemical responsiveness of absorbed laccase (**Fig. 3.13**, panel B, red line). Afterwards, the presence of PDDA in catalyst **III** further increased the electrocatalytic responsiveness of the enzyme (electrocatalytic wave starting at EONSET = 0.320 V and rising up to −35 μA cm^{-2}) (Figure **3.13**, panel C, red line). The interaction between PDDA and laccase may be responsible for the increased electron transfer properties.[301] This result is in accordance with the higher activity parameters of catalyst **III** with respect to catalysts **I** and **II** (**Table 10**).

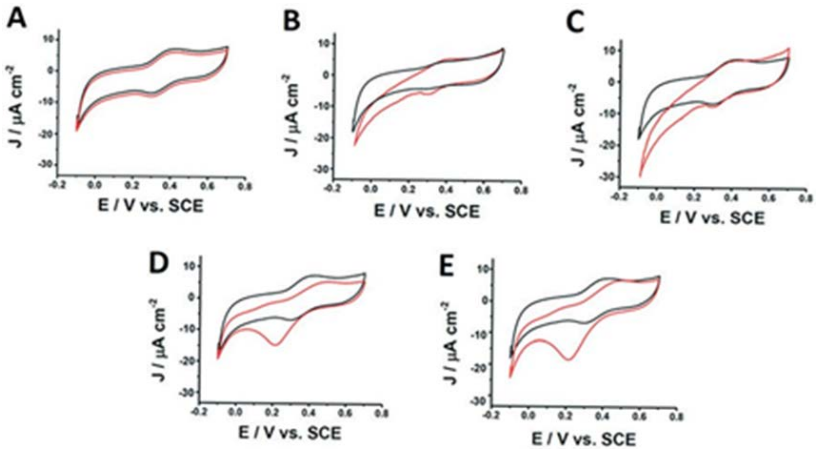

Figure 3.13 Cyclic voltammetry analysis of catalysts **I–V** under pseudo-DET conditions. NOL is indicated by the black line, catalysts **I–V** by the red line. Panel A: Catalyst **I**. Panel B: Catalyst **II**. Panel C: Catalyst **III**. Panel D: Catalyst **IV**. Panel E: Catalyst **V**. The analyses were performed in Britton–Robinson buffer (120 mM, pH 5.5) and KClO4 (100 mM) with a scan rate of 5 mV s−1 at room temperature.

Catalyst **IV** showed an electrocatalytic wave starting at EONSET = 0.290 V and rising up to −18 µA cm^{-2}, suggesting a detrimental effect on the electron transfer process by the (GA)-assisted BSA co-immobilization procedure (**Figure 3.13**, panel D, red line). Finally, catalyst **V** showed an intermediate behavior, being characterized by an electrocatalytic wave starting at EONSET = 0.315 V and rising up to −25 µA cm^{-2} (**Figure 3.13**, panel E, red line).

Mediated electron transfer (MET) mechanism

The cyclic voltammograms of catalysts **I–V** were repeated in the presence of ABTS as a redox mediator, in order to evaluate the role of the MET mechanism in the activity of immobilized laccase. Catalyst **I** showed a clear electrocatalytic wave starting at EONSET = 0.398 V and rising up to −110 µA cm^{-2} (**Figure 3.14**, panel A, red line). Two electrocatalytic peaks were expected for the ABTS/$ABTS^{\bullet+}$ and quinone/hydroquinone (QH_2/Q) redox couples, this latter transformation occurring on the lignin surface. The presence of only one electrocatalytic peak in the analysis of catalyst **I** (**Figure 3.14**, panel A, red line) was a consequence of the similar values of the formal potential for the two aforementioned redox processes. The electrocatalytic wave of catalyst **I** started approximately at the formal potential of ABTS, and no other contributions were observed, confirming the diffusion of ABTS through the NOL surface to reach the T1 cluster of the enzyme. The low electrocatalytic performance of catalyst **I** was probably due to the reported poor diffusion of O_2 through NOL.[301] These results are in accordance with the higher barrier properties and lower vapor permeability of agar composites containing an increasing amount of lignin,[302] as further confirmed by permeability data of NOL.[303]

Catalyst **II** presented an electrocatalytic wave starting at EONSET = 0.6 V and rising up to −147 μA cm^{-2}. In this latter case, the two expected electrocatalytic peaks were observed, corresponding to the MET mechanism operated by ABTS (electrocatalytic wave starting at EONSET = 0.6 V *vs.* SCE) and the pseudo-DET mechanism operated by laccase (catalytic wave starting at EONSET = 0.32 V *vs.* SCE) (**Figure 3.14**, panel B, red line).

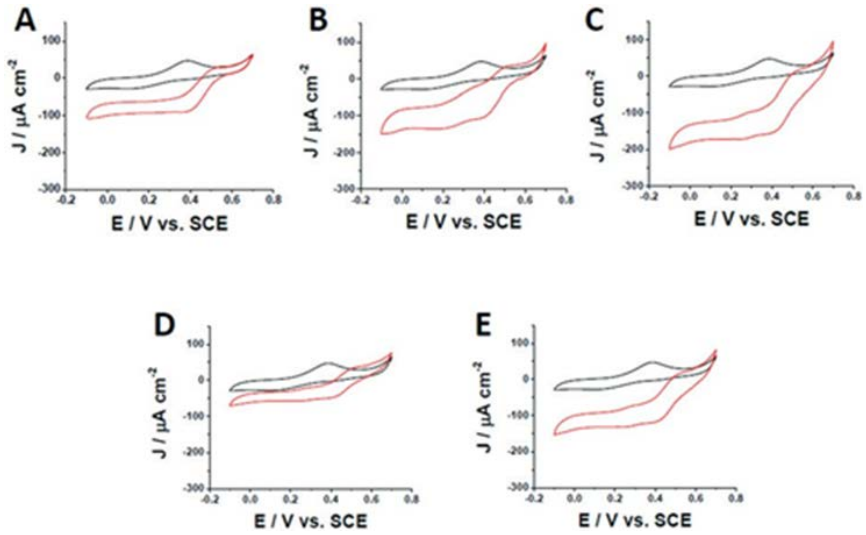

Figure 3.14 Cyclic voltammetry analysis of catalysts **I–V** under MET conditions. NOL is indicated by the black line, catalysts **I–V** by the red line. Panel A: Catalyst **I.** Panel B: Catalyst **II**. Panel C: Catalyst **III**. Panel D: Catalyst **IV**. Panel E: Catalyst **V**. The analyses were performed in Britton– Robinson buffer (120 mM, pH 5.5) and $KClO_4$ (100 mM) in the presence of ABTS (500 μM) with a scan rate of 5 mV s−1 at room temperature

Catalyst **III** showed the highest electrocatalytic responsive ness (electrocatalytic wave starting at EONSET = 0.6 V and rising up to −193 μA cm^{-2}) (**Figure 3.14**, panel C, red line). Again, both MET (catalytic wave starting at EONSET = 0.6 V *vs.* SCE) and pseudo-DET (catalytic wave starting at EONSET = 0.32 V *vs.* SCE) mechanisms were operative. Catalyst **IV** was less effective than catalyst **III** under MET conditions, showing a slight electrocatalytic wave starting at EONSET = 0.580 V and rising up to −78 μA cm^{-2} (**Figure 3.14**, panel D, red line). Finally, catalyst **V** showed an electrocatalytic wave starting at EONSET= 0.620 V and rising up to −157 μA cm^{-2} at 0 V *vs.* SCE (**Figure 3.14**, panel E). In the latter two cases, it was still possible to observe both contributions of MET and pseudo-DET mechanisms.

*Amperometric determination of the kinetic parameters of catalysts **I–V***

Amperograms of catalysts **I–V** were recorded by applying a fixed potential of −0.050 V (*vs.* SCE) and injecting 25 μM of ABTS every 40 s. The kinetic parameters J_{max} and Km_{app} are reported in **Table 11**. Amperograms of catalysts **I–V** are reported in **Figure**

3.15 (panel A). **Figure 3.15** also displays (panel B) the fitting of the data by using the Michaelis–Menten kinetic model. The J_{max} values showed the following trend: catalyst I< II< V < IV < III. The Km_{app} values seem to be quite similar except for the case of catalyst **I**, which was characterized by the highest value.

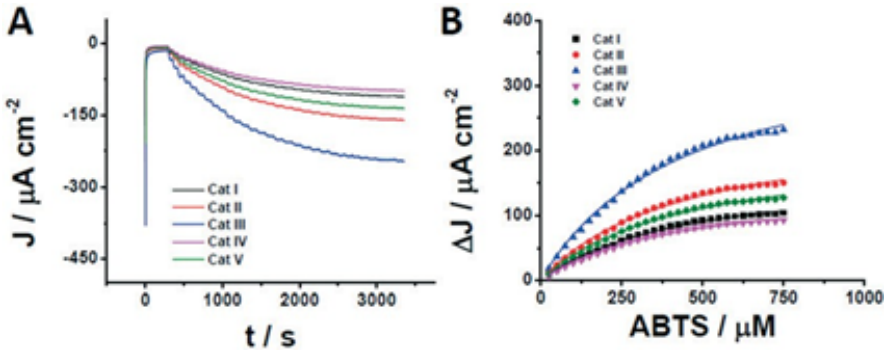

Figure 3.15 Amperograms of catalyst **I** (black), catalyst **II** (red), catalyst **III** (blue), catalyst **IV** (purple), and catalyst **V** (green) are reported in panel A. The fitting of the data by using Michaelis–Menten kinetic model are reported in panel B. The analyses were recorded by applying a fixed potential Eapp = −0.050 V vs. SCE under constant stirring (400 rpm). ABTS (25 µM) was injected every 40 s.

Table 11 Amperograms of catalysts **I–V** were recorded by applying a fixed potential of −0.050 V (vs. SCE) and injecting 25 µM ABTS every 40 s

Entry	Catalysts	J_{max} (µA cm^{-2})	K_M^{app} (mM)
1	**I**	152.4 ± 3.5	0.67 ± 0.05
2	**II**	171.5 ± 3.9	0.44 ± 0.02
3	**III**	381.0 ± 8.7	0.36 ± 0.03
4	**IV**	247.7 ± 5.7	0.38 ± 0.03
5	**V**	209.6 ± 4.8	0.32 ± 0.04

*Spectroscopic determination of the kinetic parameters of catalysts **I–V***

Kinetic parameters of catalysts **I–V** were further characterized by the ABTS procedure (ABTS in the range of 0.33–0.5 mM), plotting the data to a double reciprocal Lineweaver–Burk plot (**Table 12**). Data for native laccase were used as a reference. Irrespective of the immobilization procedure, V_{max} decreased and K_m increased after immobilization of laccase, as a consequence of partial reduction in the catalytic efficiency with respect to the native enzyme. Similar trends in K_m and V_{max} have been reported for laccase when immobilized on other carriers, due to mass transfer limitation processes.[304] Catalyst **III–V** showed a higher rate and catalytic efficiency with respect to catalysts **I–II** (**Table 12**, entries 3–5 *versus* entries 1 and 2), confirming the beneficial role of the LbL procedure. Kinetic parameters determined by the ABTS procedure were similar to those previously obtained by amperometric determination. As a general trend, Km_{app} values (**Table 11**) were higher than K_m values (**Table 12**).

Table 12 Kinetic parameters of catalysts **I–V**[a]

Entry	Catalyst	K_m (mM)	$V_{max} \times 10^{-3}$ (ΔAbs min $\mu g_{enzyme})^{-1}$	V_{max}/K_m ($\times 10^{-3}$)	K_{cat} (s^{-1})
1	**I**	1.9 ± 0.001	99 ± 2	0.1	4 ± 8.2
2	**II**	0.23 ± 0.002	501 ± 12	2.39	41 ± 1.1
3	**III**	0.16 ± 0.001	1525 ± 21	9.53	89 ± 1.9
4	**IV**	0.17 ± 0.002	1245 ± 19	7.32	70 ± 2.0
5	**V**	0.17 ± 0.003	1191 ± 18	6.71	64 ± 1.4
6	Laccase	0.13 ± 0.002	1980 ± 29	15.23	98 ± 1.7

[a] Kinetic parameters were measured by the use of the ABTS procedure (ABTS in the range of 0.33–0.5 mM), plotting the data to a double reciprocal Lineweaver–Burk plot. All experiments were conducted in triplicate using free and immobilized laccase.

*Oxidation of alcohols **1–5***

A panel of aromatic and unsaturated alcohols, benzyl alcohol **1**, 4-methoxy benzyl alcohol **2**, 4-chloro benzyl alcohol **3**, cinnamyl alcohol **4** and geraniol **5**, were oxidized in order to evaluate the synthetic relevance of catalysts **I–V**. The aromatic alcohols **1**, **2** and **4** show a gradual decrease in the value of the redox potential, while alcohol **3** is a poor substrate for laccase, due to the presence of an electron withdrawing chlorine substituent in the *para*-position of the aromatic ring. The reactions were performed in the presence of 2,2,6,6- tetramethyl-1-piperidinyloxy (TEMPO) as a redox mediator.[305] TEMPO forms an oxoammonium ion intermediate that reacts with the substrate, followed by a comproportionation process.[306] Briefly, the appropriate alcohol (20 mM) and TEMPO (6.0 mM) were treated with catalysts **I–V** (0.65 U) in sodium acetate buffer (3.0 mL, 0.1 M, pH 5.0) at room temperature for 24 h. The reaction with native laccase was also performed as a reference. In the absence of TEMPO, compounds **1–5** were not oxidized.[307] Similarly, NOL alone were not reactive. Irrespective of experimental conditions, the oxidation of compounds **1–5** afforded the corresponding aldehydes 6–10 with high selectivity as the only recovered products (**Figure 3.16** and **Table 13**).

The selective oxidation of alcohols to aldehydes is an important synthetic transformation that usually requires organ- ometallic species with a high environmental impact.[308] The following order of reactivity was observed: catalyst **III** > **IV** > **V** > **II**, catalyst **I** being almost unreactive. This order of reactivity is in accordance with the activity and kinetic parameters previously reported, as well as with the electrochemical responsiveness of the catalysts. Catalysts **III** and **IV** showed a reactivity similar to, or higher than, native laccase, affording the corresponding aldehydes in quantitative yield, the oxidation of alcohol **1** being the only observed exception (**Table 13**, from entry 2 to

entry 6). It is worth noting that catalysts **I–V** were more selective than native laccase in the oxidation of recalcitrant 4-chloro benzyl alcohol **3**, in which case both aldehyde 8 and carboxylic acid 11 were synthesized (**Table 13**, entry 13 *versus* entries 16–18). Moreover, catalysts **III** and **IV** showed a reactivity and selectivity in the oxidation of **3** higher than covalently immobilized laccase on silica nanoparticles under similar experimental conditions. In this latter case, aldehyde 8 and carboxylic acid 11 have been reported in 22% and 50% yield, respectively.

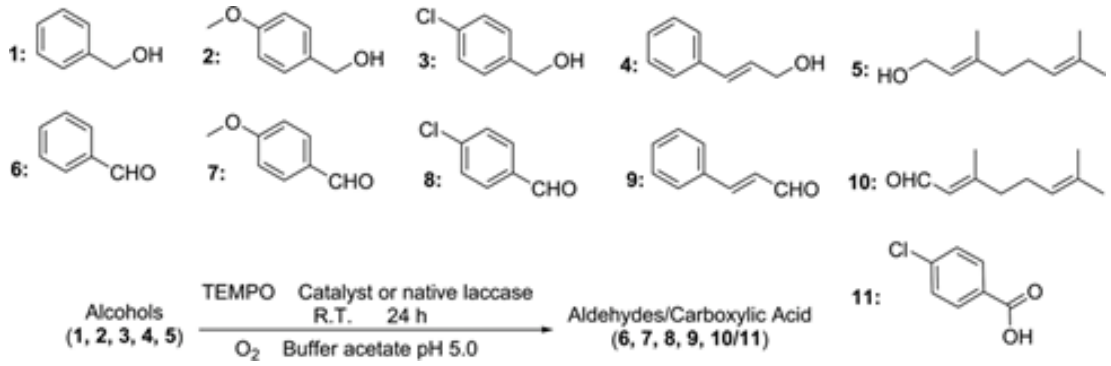

Figure 3.16 Application of catalysts **I–V** or native laccase in the oxidation of alcohols 1–5 to the corresponding aldehydes 6–10.

able 13 Oxidation of alcohols 1–5[a]

Entry	Catalyst	Substrate	Product(s)	% yield[b]
1	Laccase	1	6	96
2	**I**	1	6	0.5
3	**II**	1	6	3.5
4	**III**	1	6	85.0
5	**IV**	1	6	61.1
6	**V**	1	6	40.2
7	Laccase	2	7	>99
8	**I**	2	7	1.5
9	**II**	2	7	22.1
10	**III**	2	7	>99
11	**IV**	2	7	>99
12	**V**	2	7	98
13	Laccase	3	8(11)	66(23)[c]
14	**I**	3	8	4.5
15	**II**	3	8	6.3
16	**III**	3	8	99
17	**IV**	3	8	95
18	**V**	3	8	36.5
19	Laccase	4	9	97
20	**I**	4	9	1.1
21	**II**	4	9	49.8
22	**III**	4	9	>99
23	**IV**	4	9	>99
24	**V**	4	9	84.1
25	Laccase	5	10	93
26	**I**	5	10	1.2

27	**II**	5	10	35.4
28	**III**	5	10	>99
29	**IV**	5	10	>99
30	**V**	5	10	55.6

[a] Reaction conditions: the appropriate alcohol (20 mM), catalysts **I–V** (0.65 U) and TEMPO (6 mM) were suspended in 0.1 M sodium acetate buffer pH 5 (3.0 mL) and vigorously stirred at room temperature for 24 h. All experiments were conducted in triplicate. Native laccase was used as a reference. [b] The yield was evaluated by GC-MS analysis using acetophenone as an internal standard. [c] Compound 11 was observed only in the case of the reaction with native laccase as a reference.

The reusability of catalysts **III** and **IV** was evaluated in the oxidation of compound **2**. The experiment was performed by using the recovered catalyst for six runs (**Figure 3.17**). As a general trend, catalyst **IV** retained a reactivity higher than **III**, showing *ca.* 50% conversion of substrate at the sixth run, thus resulting in the most stable system. Moreover, at the sixth run catalysts **III** and **IV** lost more than 30% of their activity with respect to the initial activity. In accordance with previously reported data, the decrease in the activity of laccase could be ascribed to inactivation[309] and leaching of laccase during the successive runs.[310]

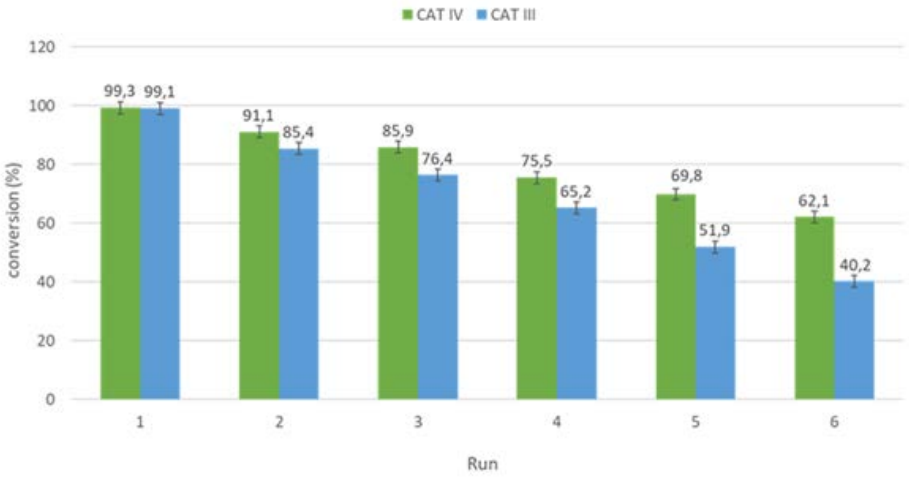

Figure 3.17 Conversion (%) of compound 2 after 6 runs. Compound 2 (20 mM) was oxidized with catalysts **III** and **IV** (0.65 U) and TEMPO (6.0 mM) under previously reported experimental conditions. The standard deviation was less than 3%. Results are the mean of three different experiments.

Note that the SEM image of catalyst **IV** after the end of the analysis showed the complete integrity of the support (**Figure 3.18**).

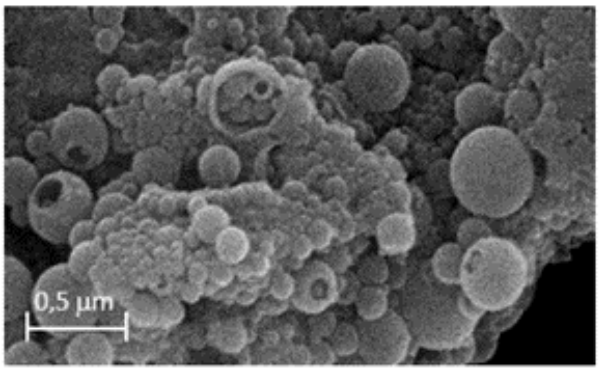

Figure 3.18. SEM analysis of catalyst **IV** after the sixth run of oxidation of alcohol 3. The analysis showed a complete integrity of the support.

Finally, the oxidation of the less reactive alcohol **3** with catalyst **III** was repeated in the presence of redox mediators characterized by a reaction mechanism different than TEMPO, such as ABTS, [311] HOBt, [312] and two natural secondary fungal metabolites, namely, vanillin and syringaldehyde, involved in the activity of oxidoreductases.[313,314] Reactions were performed by treating 3 (20 mM) with catalyst **III** (0.65 U) and the appropriate redox mediator (6 mM) in sodium acetate buffer (3.0 mL, 0.1 M, pH 5.0) at room temperature for 24 h. As reported in **Table 14** TEMPO showed the highest yield of aldehyde 8 with respect to other mediators. Among the novel redox mediators studied, vanillin showed the highest yield of aldehyde 8, confirming its natural role as an electron shuttle for laccase.

Table 14 Oxidation of compound 3 with catalyst **III** in the presence of different redox mediators

Entry	Redox mediator	Yield[a,b] (%)
1	TEMPO[c]	>99
2	ABTS[d]	15.1
3	HOBt[e]	23.5
4	Vanillin	38.9
5	Syringaldehyde	29.2

[a] All experiments were conducted in triplicate. [b] The yield was evaluated by GC-MS analysis using acetophenone as an internal stan- dard. [c] (2,2,6,6-Tetramethylpiperidin-1-yl)oxidanyl. [d] 2,2-Azinobis-(3-ethylbenzothiazoline-6-sulfonic acid). [e] *N*-Hydroxybenzotriazole.

3.3 Oxidative bio-desulfurization by nanostructured peroxidase mediator system

3.3.1 Aim of work

Many efforts are devoted to removing recalcitrant aromatic sulfur compounds from liquid fuel oil, as a consequence of the application of the international legislation for the protection of the environment from the emission of sulfur oxides.[315] Among new technologies, oxidative desulfurization (ODS) [316,317] has gained growing interest thanks to the development of selective and efficient catalytic procedures for the extraction of sulfur contaminants, even when they are present in the liquid fuel oil in a very low amount.[318] Analysis and review of the application of metal-based heterogeneous nano-catalysts in ODS procedures,[319-322] as well as the role played by different primary oxidants in the desulfurization process,[323,324] are reported in the literature,[325] hydrogen peroxide (H_2O_2) emerging as a well-recognized green reagent.[326,327] As an alternative, H_2O_2 and dioxygen can be activated in bio-desulfurization processes by use of microorganisms[328,330] or crude and purified enzymes, including laccase,[331] laccase mediator system (LMS),[332] hemoglobin,[333] lignin peroxidase,[334] manganese peroxidase,[335] microperoxidase-1,[336] chloroperoxidase,[337] lactoperoxidase[338] and horseradish peroxidase [339,340] assisted by ultrasound treatment.[341] These procedures avoid the leaching of active species from metal oxides and organometallic reagents and are effective at low pressure and temperature in a large range of pH values.[342] Moreover, the use of enzymes makes the overall treatment greener. Despite the efforts to optimize the efficacy of bio-desulfurization processes, only a few examples of immobilization protocols are reported, limited to the use of mesoporous Santa Barbara Amorphous silica SBA-16 and zeolite Al-MCM-41,[343] sol-gel supports[344] at the micro-scale and single-walled carbon nanotubes[345] and (1D)-γ-Al_2O_3 nanorods[346] at the nano-scale. The immobilization of enzymes is of practical relevance since it reduces the protein denaturation and improves activity, stability and selectivity, favoring the use of the bio-catalyst for more treatments.[347] The aforementioned projects report that nanoparticles of lignin (LNPs), show improved antioxidant and UV-absorbing properties. LNPs are easily obtained by the layer-by-layer technology, and used as a renewable platform for the immobilization of oxidative enzymes, such as laccase and tyrosinase. In particular, LNPs

showed specific boosting activity for laccase by long-range electron transfer (pseudo-DET) and mediated electron transfer (MET) mechanisms between the structurally oriented aromatic groups in the polymer and the enzyme.[348] In order to further improve nano-catalysis in bio-desulfurization processes, we report here the immobilization of horseradish peroxidase (HRP) on LNPs by the layer-by-layer procedure and the application of the novel nano-biocatalysts in the H_2O_2 oxidation of dibenzothiophene (DBT) as a well-recognized model of ODS. The use of concanavalin A (Con A) for the controlled orientation of HRP on the surface of LNPs,[349] associated to the presence of a multiple layered structure of cationic polyelectrolytes poly(diallyl-dimethylammonium chloride) PDDA and cationic lignin CATLIG, were found to be crucial elements for the optimal removal of DBT.

3.3.2 Experimental part

Materials

Organosolv lignin (OL) and kraft lignin (KL) were obtained from chemical point and stora enso, respectively. Horseradish peroxidase (HRP, 173 U/mg), concanavalin A (ConA) from *Canavalia ensiformis* (Jack bean) type VI, poly(diallyldimethylammonium chloride) PDDA (20% *v/v* water solution), Bradford reagent, 2,2-azinobis-(3-ethylbenzothiazoline-6-sulfonic acid) (ABTS), hydrogen peroxide (H_2O_2, 35 wt%), dibenzothiophene (DBT), veratryl alcohol (VA),1-hydroxybenzotriazole (HoBt) from Sigma–Aldrich (St. Louis, MO, USA), were used without any further purification. Triplicate experiments with native and immobilized peroxidase were performed in Na-acetate buffer (0.1 M, pH 5.0) or phosphate buffer saline (PBS, 0.1 M, pH 8.0). Milli-Q water (ρ = 18.2MΩ cm a 25 °C; TOC < 10 μg L^{-1}, Millipore, Molsheim, France) was used as solvent. CATLIG was prepared from kraft lignin (10 mg/ml; 0.1 M) in NaOH, by treatment with glycidyl tetramethyl ammonium chloride (20 mg) at 60 °C for 2 h under magnetic stirring. The crude was purified by dialysis with Spectrapore™ membrane (24 h, 3.5 kD MWCO). A Hewlett Packard 6890 with a FID (Flame ionization detector) and a 30 m × 0.32 mm × 0.25 mm column (cross-linked with 5% phenyl methyl siloxane) was used for the GC-MS determinations (He carrier gas). Mass-spectrometry was performed by 450 GC-320 MS apparatus (VARIAN, Palo Alto, CA, USA) by comparison with commercial samples. *n*-Hexadecane was used as internal standard. The product yield was referred to converted substrate.

*Preparation of Cat **I-II***A solution of organosolv lignin OL or kraft lignin (KL) (2.0 mg in 1.2 mL of THF/H_2O 5:1 v/v) was added to Milli-Q water (in 3.8 mL) to afford OL-LNPs and KL-LNPs. Concanavalin A (0.5 mg) in PBS (1.0 mL, 0.1 M; pH 7.3) was added to OL-LNPs and KL-LNPs (1.5 mg) in PBS (1.0 mL) and the dispersion was sonicated for 5 min to yield OL/Con A and KL/Con A, followed by addition of HRP (0.1 mg, 18 U/mg) in PBS (0.1 mL, 0.1M; pH 7.3) under orbital shaking at 4 °C for 24 h. Cat **I-II** were isolated by centrifugation (20 min at 6000 rpm) and the residual solution was evaluated for the immobilization yield and activity parameters. Finally, cat **I-II** were washed with sodium phosphate buffer (1.0 mL, 0.1 M; pH 7.3) and lyophilized.

*Preparation of Cat **III-V** and Cat **IV-VI***

Cat **III** and **V** carrying out PDDA as cationic polyelectrolyte were prepared in a similar way**.** OL-LNPs and KL-LNPs (15 mL Milli-Q water; 1.0 mg/mL, pH 4.2) were treated with PDDA (1.0 mg/mL, Milli-Q water) under magnetic stirring at 25 °C for 2 h. OL–PDDA or KL-PDDA intermediates were isolated by centrifugation and freeze dry. A PBS suspension (1.0 mL) of OL-PDDA and KL-PDDA (1.5 mg,) was treated with Concanavalin A (0.5 mg) in PBS (1.0 mL, 0.1 M; pH 7.3) and sonicated for 5 min to yield OL-PDDA/Con A and KL-PDDA/Con A, followed by addition of HRP (0.1 mg, 18 U/mg) in PBS (0.1 mL, 0.1M; pH 7.3) under orbital shaking at 4 °C for 24 h. Cat **III-V** were obtained by centrifugation (20 min at 6000 rpm) and the residual solution evaluated for the immobilization yield and activity parameters. Cat **III-V** were washed with PBS (1.0 mL, 0.1 M; pH 7.3) and lyophilized before the use. Cat **IV-VI** were prepared in a similar way, treating OL-LNPs and KL-LNPs (20 mg/mL, pH 4.2; Milli-Q water) with CATLIG (1 mg/mL, 15 mL; water solution) at 25 °C for 24 h to yield OL–CATLIG and KL-CATLIG intermediates. Next, these intermediates were reacted with concanavalin A (0.5 mg) in PBS (1.0 mL, 0.1 M; pH 7.3) for 5 min, followed by addition of HRP (0.1 mg, 18 U/mg) in PBS (0.1 mL, 0.1M; pH 7.3) at 4 °C for 24 h to afford **cat V-VI** after centrifugation (20 min at 6000 rpm).

*Preparation of Cat **VII-X***

In order to prepare **cat VII-IX** with PDDA-Con A/HRP as a double layer, the procedure described above was repeated under similar experimental conditions. Briefly,cat **III-V** in Milli-Q water (1.0 mL; 1.5 mg/mL) were treated with PDDA (1.0 mg/mL, water solution) at 4 °C for 2 h, followed by addition of concanavalin A (0.5 mg)

in PBS (1.0 mL, 0.1 M; pH 7.3; for 1.0 h) and HRP (0.1 mg, 18 U/mg) in PBS (0.1 mL, 0.1M; pH 7.3) at 4 °C for 24 h, to yield cat **VII-IX** after centrifugation (20 min at 6000 rpm). Cat **VIII-X** were prepared by cat **IV-VI** (20 mg/mL, pH 4.2) to a CATLIG water solution (1.0 mg/mL, 15 mL) at 4 °C for 2 h, followed by addition of concanavalin A (0.5 mg) in PBS (1.0 mL, 0.1 M; pH 7.3) and HRP (0.1 mg, 18 U/mg) in PBS (0.1 mL, 0.1M; pH 7.3) at 4 °C for 24 h to afford cat **VIII-X** after centrifugation (20 min at 6000 rpm).

Scanning Electron Microscopy Analysis

The Field emission scanning electron microscopy (FESEM) (Carl Zeiss Microscopy GmbH) of cat **I-X** was acquired on FESEM ZEISS GeminiSEM500, operated at 5 kV after drop 20 µl (with deionized water) of biocatalyst dispersion on specimen stubs, air dried and coated with gold by sputtering with AGAR (Auto Sputter Coater). Before the observations, the sample received a deposition of chromium thin film (5 nm) by sputter coating using a QUORUM Q 150T ES plus coater.

Synthesis of FITC-Labeled HRP and Laser Confocal Microscopy

The procedure of fluorescent labelling of HRP was performed as described in literature. Briefly, HRP (20 mg) was solubilized in 4.0 mL of sodium bicarbonate buffer (pH 9.2, 50 mM). FITC (2mg) in 400 µL of dimethyl sulfoxide (DMSO) was added to HRP solution dropwise in the dark. Unreacted dye was removed through overnight dialysis using Spectra pore dialysis membrane (3.5 kD MWCO) against ammonium chloride (NH_4Cl). ZEISS LSM-710 NLO confocal system (Carl Zeiss Microscopy GmbH) equipped with a Plan Apochromat 100X/1.40 oil DIC M 27 objectives was used for laser confocal microscopy at the excitation wavelengths for FITC-HRP/Con A complex (488 nm).

ATR-IR Characterization

Lignin nanoparticles coated with Con A were analyzed by attenuated total reflection Fourier transform infrared (ATR-IR) spectroscopic (PerkinElmer Life and Analytical Sciences, Bridgeport Avenue,Milford, CT, USA) using a PerkinElmer (Spectrum One) spectrometer (UATR unit cell) averaging 32 scans (resolution of 4 cm^{-1}).

*Activity Parameters of Cat **I-X***

The ABTS test was used for the determination of the enzymatic activity of HRP and **cat I-X** [50] by following the cation radical absorption (sodium acetate buffer solution, 0.1 M, pH 5, 3.0 mL) at 415 nm ($\varepsilon 420 = 36\,000\ M^{-1}\ cm^{-1}$) at different concentrations of HRP. In a typical experiment, the appropriate biocatalyst (18 U in acetate buffer solution, 0.1 M, pH 5, 3.0 mL), corresponding to c.a. 1.0 mg of LNPs), was added to a acetate buffer solution (0.5 mM) of ABTS and 0.3% of H_2O_2. One unit activity of HRP is the amount of enzyme that transforms 1.0 μmole of H_2O_2 per minute at pH 5 at 25 °C.

*Kinetic Data of Cat **I-X***

Kinetic data (K_m and V_{max}) were collected by using different concentrations of ABTS (0.3–20 mM) in sodium acetate buffer (pH 5) with HRP concentration (18 U) and H_2O_2 dose (0.3%) kept constant. Lineweaver–Burk plots furnished the initial velocities (1/V vs. 1/[S]), K_m and V_{max} being calculated as intercepts at the cartesian axes, respectively. Kinetic data were analyzed by GraphPad software in triplicate, using native and immobilized HRP.

*Oxidation of DBT with cat **I-X** and Redox Mediator Systems.*

As a general procedure, DBT (10 mg) was dissolved in a solution of *n*-hexane (4 ml) and PBS (0.1M pH 8, 4mL) and left under magnetic stirring. The appropriate amount (18 U/mg) of Cat (**I-X**) were added to the biphasic dispersion, that was heated at 45 °C and H_2O_2 (4.0 equiv) was added in seven steps to avoid the inactivation of HRP. In alternative, the oxidation of DBT was performed with HoBt and VA as redox mediators. The formation of DBTO in the polar phase was monitored by thin layer chromatography (TLC, n-hexane/EtOAc = 3.0:7.0). The reaction was conducted for two hours, after this time, cat **I-X** were centrifuged (6000 rpm) for 20 min and the buffer and organic layers were analyzed by gas-chromatography associated to mass-spectrometry (GC-MS) (VARIAN, Palo Alto, CA, USA))in order to evaluate the conversion of DBT. Next, the polar phase was evaporated under reduced pressure and DBTO was collected and analyzed by GC-MS. LNPs alone were unreactive.

3.3.3 Results and discussions

Preparation of Nanobiocatalysts

LNPs were prepared starting from two raw polyphenols with different hydrophobicity organosolv lignin (OL) and kraft lignin (KL) by use of the nanoprecipitation procedure. The immobilization of HRP on OL-LNPs and KL-LNPs is schematically represented in **Figure 3.19**.

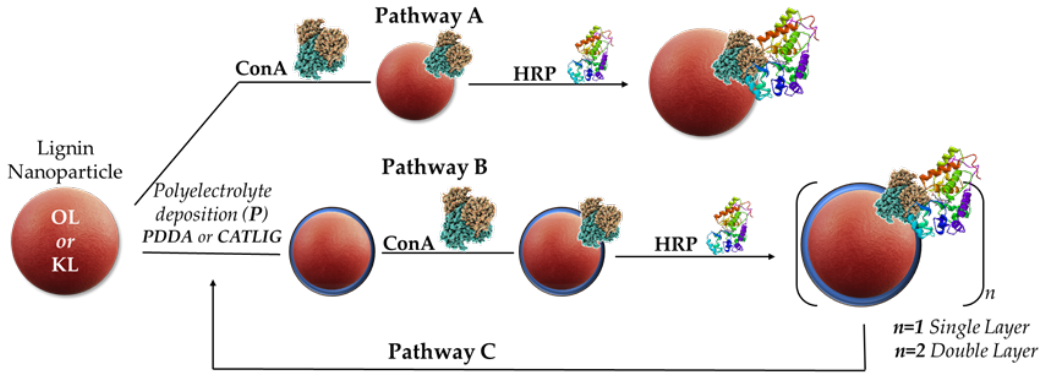

n	P	OL	KL
-	-	Cat I	Cat II
1	PDDA	Cat III	Cat V
1	CATLIG	Cat IV	Cat VI
2	PDDA	Cat VII	Cat IX
2	CATLIG	Cat VIII	Cat X

Figure 3.19. Preparation of biocatalysts **I-X**. Pathway A: Direct adsorption of Con A on nanoparticles of lignin (LNPs) followed by immobilization of horseradish peroxidase (HRP). Pathway B: Layer-by-layer mediated adsorption of Con A; n is the number of layers and P indicates the type of cationic polyelectrolyte. Pathway C: Repeated cycle of deposition of the polyelectrolyte, Con A and HRP.

The site-specific immobilization and spatial orientation of HRP on the surface of the support is an essential parameter to avoid the random distribution of the enzyme, which is responsible for undesired conformational modification and shielding of the active site.[350] Con A, a homo-tetramer protein with ζ-potential of −14 mV [351] and specific molecular recognition properties for glycoproteins, selectively recognize HRP preserving the enzyme from denaturation.[352] On the basis of these data, OL-LNPs and KL-LNPs were functionalized with Con A and successively loaded with HRP. Briefly, the appropriate LNPs (1.5 mg) dispersed in buffer (1.0 mL; 0.1 M PBS, pH 7.3) were treated with a freshly prepared PBS solution of Con A (0.5 mg/mL) followed by the addition of HRP (18 units) at 5 °C to yield OL-Con A/HRP cat **I** and KL-Con A/HRP cat **II** (Scheme 1, Pathway A). The effective loading of Con A on OL-LNPs and KL-LNPs was confirmed

by the presence of the FT-IR vibrational mode at c.a. 1644 cm^{-1} corresponding to the amide I (C=O) band characteristic of the Con A structure (**Figure 3.20**). Furthermore, the formation of the complex between immobilized Con A and HRP was detected by confocal analysis of cat **I** as representative sample after the fluorescein isothiocyanate (FITC) labeling (**Figure 3.21**). Panel A: HRP showed a green fluorescence signal; Panel B: Magnification of the emission sites).

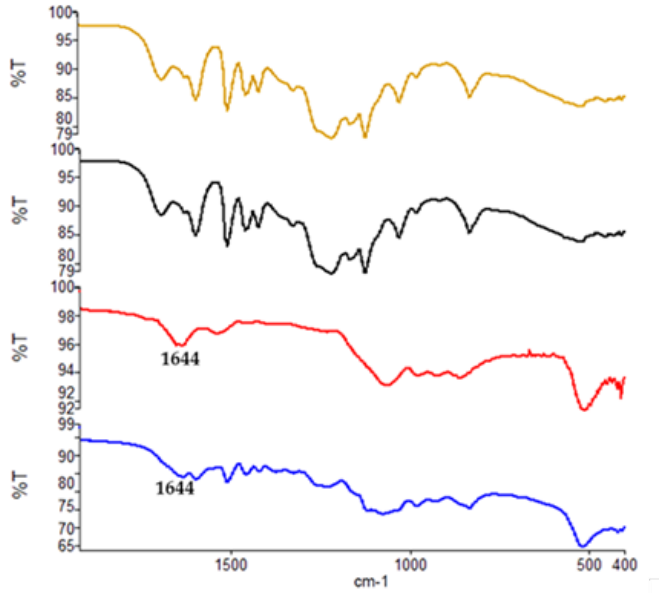

Figure 3.20. FT-IR analysis of Con A after deposition on organosolv lignin (OL)-LNPs (red line) and kraft lignin (KL)-LNPs (blue line). The FT-IR spectra of native OL-LNPs and KL-LNPs (yellow line and black line) are reported as references. The amide I (C=O) stretching band typical of the Con A structure is located at c.a. 1644 cm^{-1}.

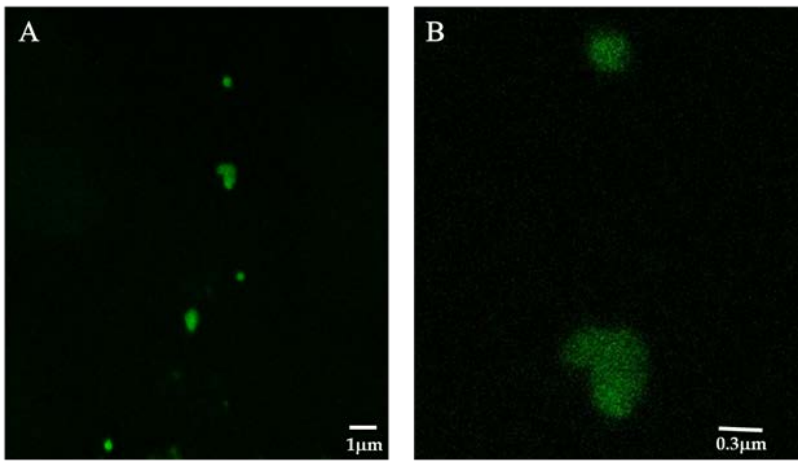

Figure 3.21. Confocal image of **cat I** (Panel **A**) after fluorescein isothiocyanate (FITC) labeling and magnification of the emission site (Panel **B**).

As an alternative, Con A was adsorbed on OL-LNPs and KL-LNPs after the initial deposition of a cationic polyelectrolyte layer of PDDA or CATLIG. In this latter case

NPs (1.5 mg) dispersed in buffer (1.0 mL; 0.1 M PBS, pH 7.3) were coated with the appropriate polyelectrolyte followed by treatment with PBS solution of Con A (0.5 mg/mL) and addition of HRP (18 units) to yield OL-PDDA-ConA/HRP cat **III**, OL-CATLIG-ConA/HRP cat **IV**, KL-PDDA-ConA/HRP cat **V** and KL-CATLIG-ConA/HRP cat **VI** (Scheme I, Pathway B). The procedure was repeated under similar experimental conditions for the deposition of a second layer of polyelectrolyte, Con A and HRP, to

afford OL-(PDDA-ConA/HRP)2 cat **VII**, OL-(CATLIG-ConA/HRP)2 cat **VIII**, KL-(PDDA-ConA/HRP)2 cat **IX** and KL-(CATLIG-ConA/HRP)2 cat **X** (**Figure 3.19**, Pathway C). The morphological characterization of cat **I-X** performed by Scanning Electron Microscopy (SEM) analysis is reported in **Figure 3.22** and **Figure 3.23**, respectively. Irrespective from the experimental conditions, the LNPs retained their original regular spherical shape after the deposition procedure. Note that the surface of biocatalysts is characterized by a corona-like structural motif that is reported to be characteristic for the deposition of Con A.[354]

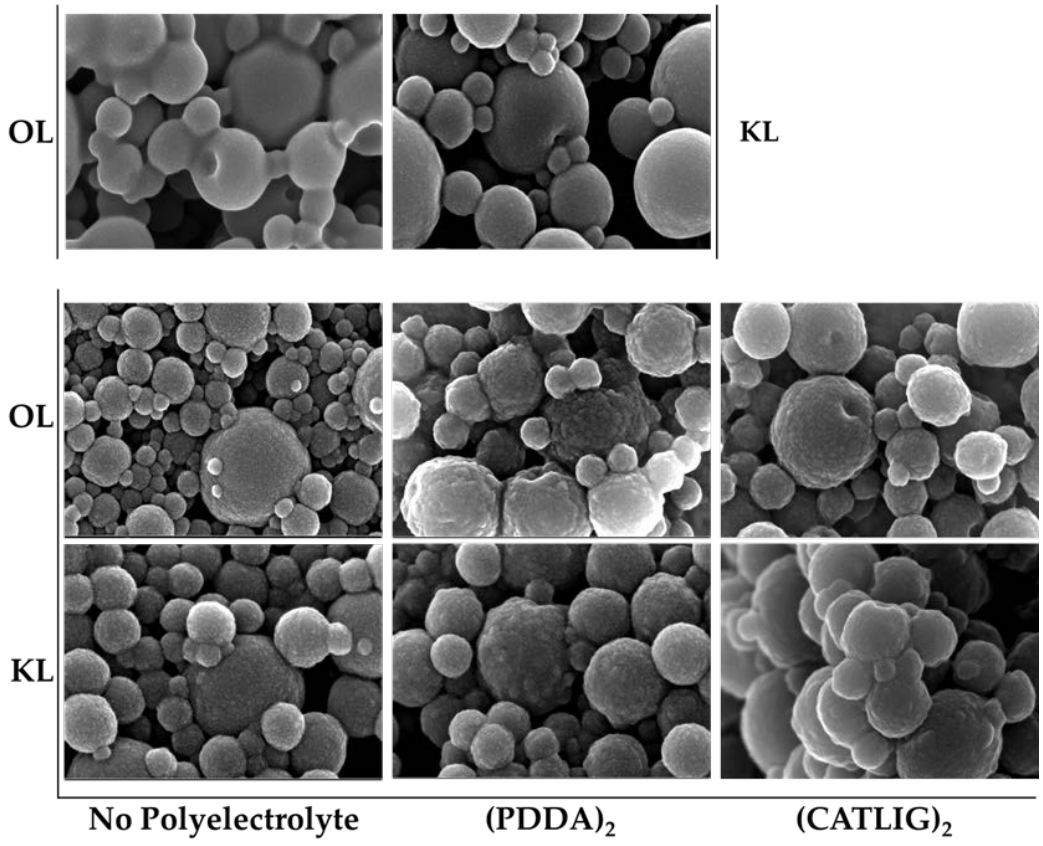

Figure 3.22 Upper panel: Scanning Electron Microscopy (SEM) images of OL-LNPs and KL-LNPs. Lower panel: SEM images of **cat I-II** and **cat VII-X**, separately. The n index in subscript of the parenthesis represents the number of cyclic depositions of polyelectrolyte, Con A and HRP. The corona-like motif present on the surface of nanoparticles is characteristic of the deposition of Con A as the external layer.

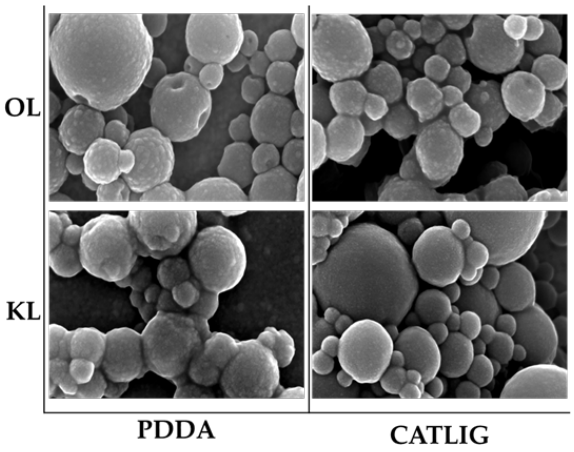

Figure 3.23. Upper panel: SEM images of **cat III-IV**. Lower panel: SEM images of **cat V-VI**.

*Activity Parameters and Kinetic Data of Biocatalysts **I–X***

The activity parameters of **cat I–X** were measured through the standard 2,2'-azinobis-(3-ethylbenzothiazoline-6-sulfonic acid) (ABTS) test, consisting in the detection of the ABTS cation radical at 415 nm ($\varepsilon 420 = 36\,000\ M^{-1}\ cm^{-1}$). The activity, activity yield and immobilization yield were determined using Equations 1–3, respectively:

$$\text{Activity (units per mg)} = U_x/W_{support} \quad (1)$$

$$\text{Activity yield (\%)} = [U_x/(U_a - U_r)] \times 100 \quad (2)$$

$$\text{Immobilization yield (\%)} = [(U_a - U_r)/U_a] \times 100 \quad (3)$$

Where U_a is the total activity (units) of HRP, U_r is the residual activity (units) in the solution and U_x is the activity of HRP after immobilization (the enzyme unit is the increase in the absorbance of 10^{-3} unit per min at 25 °C in 0.1 M Na-acetate buffer, pH 5). The presence of the cationic polyelectrolyte layer favors the immobilization yield of Con A/HRP on LNPs, PDDA and CATLIG showing a similar efficacy (**Table 15**, entries 3–4 and 7–8 versus entries 5–6 and 9–10). Moreover, the immobilization yield was increased by increasing the total number of layers. The activity yield of HRP was found to be dependent on the specific nature of LNPs in the absence of polyelectrolyte. Cat **I** showed an activity yield significantly lower than cat **II** (**Table 15**, entry 1 versus entry 2), suggesting that the different hydrophobicity and elemental composition of OL with respect to KL was a relevant parameter in tuning the efficacy of the Con A immobilization, probably due to dissociation of its dimeric sub-units.[355] This hypothesis is in accordance with the reported hydrophilicity character of Con A layers.[356] The presence of PDDA and CATLIG generally increased the activity yield, the overall effect being more pronounced in the case of OL (**Table 15**, entry 1 versus entries 3–4) relative

to KL (**Table 15**, entry 2, versus entries 5–6). As a general trend, the activity yield was increased by increasing the number of the total layers, KL based biocatalysts being generally the most active systems (**Table 15**, entries 9-10 versus entries 5–6).

Table 15. Activity parameters and kinetic data of **cat I–X**. [1.]

Entry	Lignin/P	Cat	Immobilization Yield%	Activity Yield %	Activity (U/mg)	K_m (mM)	V_{max} (μM/s)
1	OL	**I**	45	21	3.78	12.5	0.26
2	KL	**II**	53	63	11.34	11.3	0.28
3	OL/PDDA	**III**	56	43	7.74	9.9	0.30
4	OL/CATLIG	**IV**	57	64	11.52	9.7	0.33
5	KL/PDDA	**V**	62	72	12.96	9.8	0.32
6	KL/CATLIG	**VI**	64	86	15.48	9.4	0.34
7	$OL/(PDDA)_2$	**VII**	68	75	13.50	8.3	0.34
8	$OL/(CATLIG)_2$	**VIII**	69	76	13.68	8.1	0.36
9	$KL/(PDDA)_2$	**IX**	72	84	15.12	8.2	0.34
10	$KL/(CATLIG)_2$	**X**	73	85	15.30	7.9	0.35
11	None	**HRP**	-	-	18.00	9.5	0.35

[1] ABTS in the range of 0.3–20 mM. Data were elaborated by a double reciprocal Lineweaver–Burk plot. The experiments were carried out in triplicate. Average errors in kinetic parameters were 2–4% for K_m and 1–3% for V_{max}.

Kinetic parameters of cat **I–X** are reported in **Table 15** (entries 1–10), using native HRP as a reference (**Table 15**, entry 11). The biocatalyst carrying out the cationic polyelectrolyte layer showed K_m and V_{max} values comparable to that of native HRP irrespective from the lignin type (**Table 15**, entries 3–10 versus entry 11). In this latter case, the systems coated with PDDA where characterized by K_m and V_{max} values slightly higher than that measured for the CATLIG counterpart. Moreover, the K_m values decreased (and V_{max} increased) by increasing the total number of the layers (**Table 15**, entries 7–10 versus entries 3–6). In the absence of the cationic polyelectrolyte higher value of K_m were always observed (**Table 15**, entries 1–2). Other supports showed a similar trend, [357] indicating a reduction of the catalytic efficiency due to mass transfer imitation processes[358] and restriction of the mobility of the enzyme.[359]

*Oxidation of DBT with cat **I–X***

As a general procedure, DBT (10 mg, 0.05 mmol) and the appropriate biocatalyst (18 U/mg) in *n*-hexane (4 mL) and phosphate buffer saline PBS (0.1M pH 8, 4mL) were treated with H_2O_2 (4.0 equiv) at 45 °C for 2 h. The addition of the primary oxidant was performed in more steps to avoid the inactivation of HRP. In alternative, hydroxybenzotriazole HoBt (20 μg, 1.0×10^{-3} mmol) and veratryl alcohol VA (18 μg, 1.0×10^{-3} mmol) were used as redox mediators. Low molecular weight redox mediators

are electron shuttles for the peroxidase, [360] showing beneficial effect on the overall catalytic activity.[361] HoBt and VA have a similar mechanism for the redox transfer process, encompassing the radical hydrogen abstraction (HAT) pathway.[362] The oxidation with native HRP and with H_2O_2 in the absence of the enzyme were performed as references. No oxidation of DBT occurred without the enzyme. Irrespective from the experimental conditions, the reaction was very selective to yield the dibenzothiophene sulfone (DBTO) as the only recovered product (**Table 16**).

Table 16. Application of cat **I-X** in the oxidation of dibenzothiophene (DBT) as a model of oxidative desulfurization (ODS).

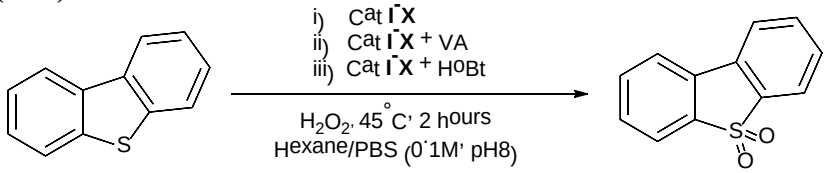

DBT DBTO

Entry	Lignin/P	Cat	Redox Mediator [1]	Conversion (%)	Yield (%) [2]
1	OL	**I**	none	18	>99
2	KL	**II**	none	22	>99
3	OL/PDDA	**III**	none	20	>99
4	OL/CATLIG	**IV**	none	23	>99
5	KL/PDDA	**V**	none	30	>99
6	KL/CATLIG	**VI**	none	32	>99
7	OL/(PDDA)$_2$	**VII**	none	35	>99
8	OL/(CATLIG)$_2$	**VIII**	none	36	>99
9	KL/(PDDA)$_2$	**IX**	none	37	>99
10	KL/(CATLIG)$_2$	**X**	none	38	>99
11	None	**HRP**	none	78	>99
12	OL	**I**	VA	25	>99
13	OL	**I**	HoBt	34	>99
14	KL	**II**	VA	32	>99
15	KL	**II**	HoBt	46	>99
15	OL/PDDA	**III**	VA	28	>99
17	OL/PDDA	**III**	HoBt	33	>99
18	OL/CATLIG	**IV**	VA	31	>99
19	OL/CATLIG	**IV**	HoBt	36	>99
20	KL/PDDA	**V**	VA	43	>99
21	KL/PDDA	**V**	HoBt	52	>99
22	KL/CATLIG	**VI**	VA	44	>99
23	KL/CATLIG	**VI**	HoBt	53	>99
24	OL(PDDA)$_2$	**VII**	VA	54	>99
25	OL(PDDA)$_2$	**VII**	HoBt	64	>99
26	OL(CATLIG)$_2$	**VIII**	VA	55	>99
27	OL(CATLIG)$_2$	**VIII**	HoBt	65	>99
28	KL(PDDA)$_2$	**IX**	VA	53	>99
29	KL(PDDA)$_2$	**IX**	HoBt	64	>99

30	KL(CATLIG)$_2$	**X**	VA	54	>99
31	KL(CATLIG)$_2$	**X**	HoBt	65	>99
32	KL(CATLIG)$_2$	**X**	HoBt	64 (Run no.1)[3]	>99
33	KL(CATLIG)$_2$	**X**	HoBt	60 (Run no.2)	>99
34	KL(CATLIG)$_2$	**X**	HoBt	58 (Run no.3)	>99
35	KL(CATLIG)$_2$	**X**	HoBt	42 (Run no.4)	>99
36	KL(CATLIG)$_2$	**X**	HoBt	45 (Run no.5)	>99
37	None	**HRP**	VA	55	>99
38	None	**HRP**	HoBt	70	>99

[1]**Cat I-X** (18 U/mg of HRP), 4.0 equiv. of H_2O_2, n-hexane, PBS (0.1 M, pH 8) with two redox mediators: Veratryl alcohol (VA) and 1-Hydroxybenzotriazole (HoBt) at 45 °C. [2] The yield is referred to converted substrate. [3] **Cat X** was recovered by centrifugation and used in the following runs.

The conversion of DBT with cat **I-X** was lower than that obtained with HRP in the absence of the redox mediators, probably as a consequence of the occurrence of mass-transfer limitation processes associated to the heterogeneous system. Double layered systems cat **VII-X** were the most effective biocatalysts irrespective from the lignin type and the nature of the polyelectrolyte layer. In this latter case, conversion values in the range of 35–38% were observed (**Table 16**, entries 6–10). Better results were obtained using the redox mediators (38–65% conversion range), HoBt performing better than VA. This different behavior is probably due to the reported lower redox-potential value of HoBt with respect to VA, favoring the oxidation of the substrate . The conversion of DBT with double layered cat **VII-X** was of the same order of magnitude as that obtained with HRP and both VA and HoBt (**Table 16**, entries 24–31 versus entries 37–38). The efficacy of the KL based biocatalysts was higher than the OL counterpart, while any specific effect was observed in relation to the nature of the polyelectrolyte layer, the performance of PDDA and CATLIG being similar. Note that the general efficacy of native HRP was decreased in the presence of VA (**Table 16**, entry 37 versus entry 11) and was only slightly increased with HoBt (**Table 16**, entry 38 versus entry 11), suggesting the benign effect of redox mediators in the desulfuration activity of HRP after the immobilization process.

The reusability of cat **X** was evaluated, as a representative sample, analyzing the oxidation of DBT for more runs. The experiment was performed by recovery of the biocatalyst and reuse for five runs under reported experimental conditions (**Table 16**, entries 32–36). As a general trend, **cat X** showed 45% conversion of substrate at the five run, suggesting the relative stability of the system.

Chapter 4
Bioinks

4.1 Enzyme-lignin nanocapsules are sustainable catalysts and vehicles for the preparation of unique polyvalent bioinks

4.1.1 Aim of the work

Over the last years, increased legislative attention and safety burden, as well as environmental concerns, oriented traditional printing ink formulations towards the use of renewable resources with reduced or absent environmental impact.[363] Bio-inks might not only limit dependency on fuel-oil, but they also can drive the development of novel technological applications.[364] Ink formulations are usually composed by four type of ingredients, namely pigment, vehicle and binder, additive and solvent.[365] Moreover, depending on the specific application and on the viscosity of the binder, no additional solvent might be necessary, leading to solvent free ink.[366] Water can be used as sustainable solvent in environmental friendly ink formulations.[367] Tall oil rosin (colophony) ,[368] soybean and edible vegetable oils,[369] frying oils,[370] karanja oil,[371] abietic acid polymers,[372] and polysaccharides [373] have all been used as binders to replace fuel-oil derived synthetic materials. Unfortunately, drawbacks are envisaged in the application of these bio-binders, since they are in competition with food production, demanding toxic additives to improve rheological properties.[374]

Lignin, the main by-product of pulp and paper industry and of bio-refinery processes, is a sustainable binder due to its favorable physical-chemical properties associated to low cost and easy availability .[375] Lignin is a highly branched polyphenolic polyether consisting of oligomeric sub-units produced by radical polymerization of monolignols, *para*-coumaryl alcohol, coniferyl alcohol and sinapyl alcohol. This polymer shows antioxidant activity, UV-shielding protection, anticorrosion effects, and electrochemical responsiveness . Amine salts of Kraft lignin are additives in water-based pigments, acting both as grinding agents for the pigment in the formulation, and as binder in the printing processes.[70] Moreover, organosolv lignin has been applied as filler in different ink formulations, improving the viscosity of the medium,[71] as well as in sustainable formaldehyde resins.[376] In a similar way, nitrate alkaline lignin esters,[72] carboxylate softwood lignin,[377] and acetylated lignin[378] have been used as binders in ink formulations. Nanoparticles and nanocapsules of lignin showed innovative pharmaceutical and technological applications. Nano-scaled binders are of relevant interest, since they can penetrate easily into the structure of bulky paper promoting the rate of biodegradation.[379]

For this reason, sub-micron Kraft lignin particles have been applied as binders in novel water ink formulations [380]. The main advantage of lignin nanodevices resides in the high biocompatibility, in the possibility to be degraded by microorganisms and in the emergence of novel scale-dimensional chemical and physical properties.

Improved UV-shielding properties and antioxidant activities emerged during the preparation of organosolv lignin and lignosulphonate nanocapsules by a template Layer by Layer approach, (see **Chapter 2**) consisting on the alternative deposition of polyelectrolytes of different electrical charge. Lignin nanodevices have been used as support for the immobilization of enzymes (see **Chapter 3**), including tyrosinase and laccase. In this latter case, they showed capacity to improve the enzymatic activity by boosting effect and by direct and mediated electron transfer processes. Tyrosinase and laccase catalyze the preparation of several pigments and dyes under natural or synthetic procedures.[382] Thus, lignin nanocapsules functionalized with oxidative enzymes can perform as biocatalyst for the synthesis of the pigment, and as vehicle, binder, and additive for the newly synthesized pigment. Here we describe the use of lignin nanocapsules loaded with tyrosinase from *Aspergillus niger* and, in alternative, with laccase from *Trametes versicolor*, for the efficient "in situ" polymerization of appropriate chemical precursors to afford a large panel of pigments. The pigments resulted to be stably linked to the support affording a large panel of colored nanocapsules to be used as a unique polyvalent bio-ink.

4.1.2 Experimental part

Materials

Organosolv lignin (OL) was purchased from Chemical Point (Oberhaching, Germany). Tyrosinase from *Aspergillus niger* (1000 U/mg), laccase from *Trametes versicolor* (1.07 U/mg), Bradford reagent, poly(diallyldimethylammonium chloride) (PDDA, 20%v/v water solution), chitosan (CH, low molecular weight) with 20% chitin units, melanin, 2,2-azinobis(3-ethylbenzothiazoline-6-sulfonic acid) (ABTS), L-tyrosine, L-DOPA, epicatechin, catechol, 4-amino benzoic acid, hydroquinone, 3-aminobenzoic acid, resorcinol, and *para*-phenylenediamine were purchased from Sigma–Aldrich (St. Louis, MO, USA), and were used without any further purification. All experiments were repeated in triplicate using native and immobilized tyrosinase or laccase in phosphate buffer saline (PBS 0.1 M pH 7) or sodium acetate buffer (Na-acetate buffer 0.1 M pH 5),

respectively. Solutions were prepared using Milli-Q water (ρ = 18.2 MΩ cm a 25 °C; TOC < 10 μg $L^{-1,}$ Millipore, Molsheim, France).

Preparation of nanocapsules by a template-based Layer-by-Layer procedure

Nanocapsules were prepared by applying a modified version of the Layer-by-Layer (LbL) procedure using organosolv lignin (OL) as template. Briefly, commercially available OL (20 mg) was dissolved in THF (20 mL), followed by filtration (0.45 μm syringe filter) and dialysis against deionized water, for 24h at 25°C. The suspension (15 mL) of OL nanocapsules in MilliQ water (1 mg/ml; pH 4.2) was added dropwise to PDDA or CH solution (1.0 mg/mL, MilliQ water) under slow magnetic stirring. After 2 h, the final suspension was centrifuged (6000 rpm, 20 min) and the supernatant removed. The nanocapsules were rinsed with deionized water, recovered by centrifugation (6000 rpm, 20 min) and lyophilized to yield OL/PDDA and OL/CH intermediates, respectively.

Procedure for the loading of tyrosinase

The reactivity of tyrosinase towards lignin is reported[42]. As a general trend, tyrosinase showed negligible activity towards lignin modification[48]. Tyrosinase from *Aspergillus niger* (1.0 mg, 900 U/mg) was added to a suspension of OL-PDDA (100 mg), or in alternative, to OL/CH (100 mg), in the appropriate buffer (100 mL) under orbital shaking for 24h at 25°C. OL/PDDA/tyrosinase (**I**) and OL/CH/tyrosinase (**II**) were recovered by centrifugation (20 min at 6000 rpm). Compounds (**I**) and (**II**) were washed several times with PBS in order to ensure the complete removal of unbounded enzyme (as evaluated by the Bradford method). The recovered solution was used for the evaluation of the activity parameters.

Procedure for the loading of laccase

Laccase from *Trametes versicolor* (20 mg, 1.07 U/mg) was added to a suspension of OL-PDDA (100 mg), or in alternative, to OL/CH, in Na-acetate buffer (100 mL) under orbital shaking for 24h at 25°C. OL/PDDA/laccase (**III**), and OL/CH/laccase (**IV**), were recovered by centrifugation (20 min at 6000 rpm). Compounds (**III**) and (**IV**) were washed several times with Na-acetate buffer in order to ensure the complete removal of unbounded enzyme (as evaluated by the Bradford method). The recovered solution was used for the evaluation of the activity parameters.

Determination of the kinetic parameters

Kinetic parameters of compounds (**I-II**) (K_m, V_{max}, and V_{max}/K_m) were determined spectrophotometrically by measuring the activity of immobilized tyrosinase at different concentrations of L-tyrosine (0.33–0.10 mM) using the dopachrome method. As a general procedure, the reaction was started by adding L-tyrosine to PBS solution (0.1 M, pH 7) containing the appropriate amount of compounds (**I**) and (**II**) (0.1 mg). The initial rates were measured in a 3.0 mL reaction cuvette as linear increase of the optical density (475 nm) at 25°C under magnetic stirring.

Kinetic parameters of compounds (**III**) and (**IV**) were determined by measuring the activity of immobilized laccase at different concentrations of ABTS (0.1–5 mM). Briefly, the reaction was started by adding ABTS to compounds (**III**) and (**IV**) (0.1 mg) in Na-acetate solution (0.1 M pH 5). The initial rates were measured in a 3.0 ml reaction cuvette as the linear increase of the optical density at 436 nm at 25°C under magnetic stirring. The data were analyzed by a double reciprocal Lineweaver–Burk plot. Spectrophotometric data were obtained by using a Cary WinUV (AGILENT, Santa Clara, CA, USA). All experiments were conducted in triplicate using free and immobilized tyrosinase and laccase.

Determination of activity parameters.

The activity parameters of tyrosinase were determined by measuring the tyrosinase catalyzed oxidation of L-tyrosine by the dopachrome method. As a general procedure, the reaction was started by adding L-tyrosine (0.83 mM) to PBS solution (67 mM, pH 7) containing the appropriate amount (from 45 to 100 units) of samples **(I-II)** (from 0.045 to 0.1 mg). The initial rates were measured in a 3.0 mL reaction cuvette as the linear increase of the optical density (475 nm) at 25 °C under magnetic stirring. One unit of enzyme activity was defined as the increase in absorbance of 0.001 unit per minute at pH 7 and 25 °C. Spectrophotometric data were analyzed with Cary WinUV. All experiments were conducted in triplicate. The activity parameters of samples **(III-IV)** were assayed by using the 2,2'-azino-bis (3-ethylbenzothiazoline-6-sulfonic acid) diammonium salt (ABTS) procedure. ABTS (5 mM), sodium acetate buffer (2.0 mL, pH 5.0), and the sample solution (200 μL) were used as standard solution. The formation of the cation radical was detected by measuring the increase of absorbance at 436 nm. One unit of laccase activity has been defined as the amount of enzyme that catalyzed the oxidation of 1.0 μmol of ABTS in 200 μL reaction mixture at 25 °C during 1.0 min.

Dynamic light scattering

Measurements of particle size and Zeta potential were performed on freshly prepared aqueous suspensions (pH = 7) of OL nanocapsules and compounds (**I**-**II**) were dispersed in water by dynamic light scattering (DLS) using a Zetasizer Nano ZS (Malvern Instruments, Malvern, UK) apparatus, equipped with an He-Ne laser (633 nm, fixed scattering angle of 173°, 25°C). Prior to perform size measurements, the suspensions were filtered with a 0.45 μm filter membrane. Measurements were performed in triplicate at room temperature (T = 25 °C).

Procedure for the pigmentation of lignin nanocapsules functionalized with tyrosinase

As a general procedure, OL/CH/tyrosinase (**II**) (1.0 mg/mL) was suspended in PBS buffer (pH 7, 0.1 M) in the presence of L-DOPA PBS solution (2 mM) and the suspension was stirred for 2 hours at 25°C under oxygen atmosphere. The black suspension was centrifuged (6000 rpm, 20 min) and the supernatant removed. Nanocapsules were rinsed three times with KOH (1.0 M) in order to ensure the complete removal of unbounded melanin, followed by washing with deionized water up to neutral pH. Next, nanocapsules were recovered by centrifugation (6000 rpm, 20 min) and lyophilized to yield compound (**V**). The amount of unbounded melanin in the KOH solution was evaluated spectrophotometrically by comparing the OD at 470 nm of unknown sample with a standard melanin (1mg/ml) . All measurements were done in triplicate. The disappearance of L-DOPA during the reaction was monitored by gas-chromatography associated to mass-spectrometry (GC-MS). The analyses were performed by 450 GC-320 MS apparatus using a VF-5MS column and an isothermal temperature profile of 100 °C for 2 min, followed by a 10 °C/min temperature gradient to 280 °C for 25 min. The injector temperature was 280 °C. Chromatography-grade helium was used as the carrier gas with a flow of 2.7 mL/min. Mass spectra were recorded with an electron beam of 70 eV.

Procedure for the pigmentation of lignin nanocapsules functionalized with laccase

As a general procedure, OL/CH/Laccase (**IV**) (1.0 mg/ml) was suspended in Na-acetate buffer (pH 5, 0.1M) in the presence of the appropriate substrate (2.0 mM) in 0.1 M sodium-acetate buffer (pH 5.0), containing 2% (*v/v*) absolute ethanol. The suspension was stirred for 24 hours at 25°C under oxygen atmosphere. The final suspension was centrifuged (6000 rpm, 20 min) and the supernatant removed. The product was rinsed three times with MilliQ water (10 mL) in order to ensure the complete removal of

unbounded pigment. Residual traces of unreacted substrate were monitored by GC-MS. Irrespective to experimental conditions, the quantitative conversion of the substrate was observed.

The colored nanocapsules were recovered by centrifugation (6000 rpm, 20 min) and lyophilized to yield compounds (**VIII**), (**IXa-IXb**), (**Xa-Xb**), and (**XIa-XIb**). The formation of the epicatechin polymer with OL/CH/Laccase (**IV**) was evaluated spectrophotometrically in the range of 250–300nm at different reaction times (1 h, 2 h and 6 h) using epicatechin monomer as standard.

Electron microscopy analysis

For Scanning Electron Microscopy (SEM), compounds (**V-VIII**), (**IXa-IXb**), (**Xa-Xb**), and (**XIa-XIb**) were fixed with 3% glutaraldehyde in 0.1 M cacodylate buffer (pH 7.2), washed and post-fixed in OsO_4 (1% weight) in the same buffer at room temperature. Specimens were dehydrated in a graded ethanol series. They were then air dried, sputter-coated with gold in a Balzers MED 010 unit. The observation was made by a JEOL JSM 6010LA electron microscope. For Transmission Electron Microscopy (TEM), nanocapsules were placed on formvar–carbon-coated grids and allowed to be adsorbed for 60 s. Excess liquid was gently removed from each droplet with a strip of filter paper. Processing for negative staining was carried out by placing a drop of negative stain (2%uranyl acetate in distilled water) on the specimen grids, followed by quick blotting. This step was repeated a second time on a new drop of negative staining solution and prolonged for 60 s. Nanocapsules were observed with a JEOL 1200 EX II electron microscope. Micrographs were acquired by the Olympus SIS VELETA CCD camera equipped the iTEM software.

FTIR Characterization

Attenuated total reflection infrared (ATR-IR) spectroscopic analyses were performed, at room temperature, with a Perkin–Elmer Spectrum One spectrometer equipped with an ATR-IR cell. IR spectra were recorded by averaging 32 scans, with a resolution of 4 cm^{-1}.

EPR analysis

EPR spectra of solid samples were recorded in a CW (Continuous wave) X-band (9GHz) at room temperature with a Bruker E580 Elexsys Series using the Bruker ER4122SHQE cavity. The 1mm diameter quartz capillaries were filled in with the

samples and they were placed into a suprasil tube of 3.5 mm internal diameter. Experimental conditions for acquisition were: 9.87 GHz microwave frequency, 0.1mT modulation amplitude and 2mW microwave power.

Characterization of color parameters after pigmentation of lignin nanocapsules

Color parameters were measured through X-Rite CA22 reflectance spectrophotometer according to the CIE L*a*b* color system (ISO 11664-4). In this system, the coordinate L* describes the lightness, while the coordinates a* and b* describe the chromatic coordinates on the green-red and blue-yellow axes, respectively. The characteristics of the color measuring instrument are the following: light source D65; standard observer 10°; fixed geometry of measurement 45°/0°; spectral range 400-700 nm; spectral resolution 10 nm; aperture size 4 mm. For each sample three measurements were performed, and then average values and standard deviations were calculated. Data are reported as L*, a*, b*, and reflectance spectra in the visible range.

Effect of alkaline treatment and of Ultraviolet photo-irradiation on the color strength and fastness properties

The effect of UV irradiation, on the color change of compounds (**V**) and (**VIII**) in lyophilized powder (60 mg) on a glass slide (size 25 mm × 75 mm) support was performed by UVA and UVB light irradiation, which was provided by UV LAMP 300 W (ULTRAVITALUX, UVA power 13.6 W and UVB power 3.0 W). After 2 or 24 h of light irradiation the compounds (**V**) and (**VIII**) were collected for the characterization of color parameters using the untreated compounds as reference.

As reported in literature, the effect of the treatment with NaOH (1.0 M) on the color change of compound (**V**) was performed by using a slightly modified procedure.[382] After 2 or 24 h of NaOH (1.0 M) treatment the final suspension was centrifuged (6000 rpm, 20 min) and the supernatant removed. The compound (**V**) was lyophilized for the characterization of color parameters using the untreated compound **V** as reference.

4.1.3 Results and discussions

Preparation of lignin nanocapsules and their loading with tyrosinase and laccase

Functionalized lignin nanocapsules supporting tyrosinase and laccase have been prepared by a modified version of the Layer-by-Layer (LbL) procedure (**Figure 4.1**,

pathway A), consisting in the consecutive deposition of alternatively charged polyelectrolytes onto the appropriate support. The coating protects the enzyme from denaturing agents and allow regulation of the permeability towards small substrates. Briefly, nanocapsules of organosolv lignin (OL) were obtained by dialysis of a lignin tetrahydrofuran (THF) solution against deionized water. The OL nanocapsules were used as a template for the sequential deposition of positively charged poly (diallyl dimethylammonium chloride (PDDA) and negatively charged tyrosinase from *Aspergillus niger*. Kinetic parameters of OL/PDDA/tyrosinase (**I**) (K_m, V_{max} and V_{max}/K_m), determined by measuring the enzyme activity at different concentrations of L-tyrosine, were found to be in agreement with data previously reported in **chapter 3** (**Table 17**, entry 1), confirming the effective loading of the enzyme.

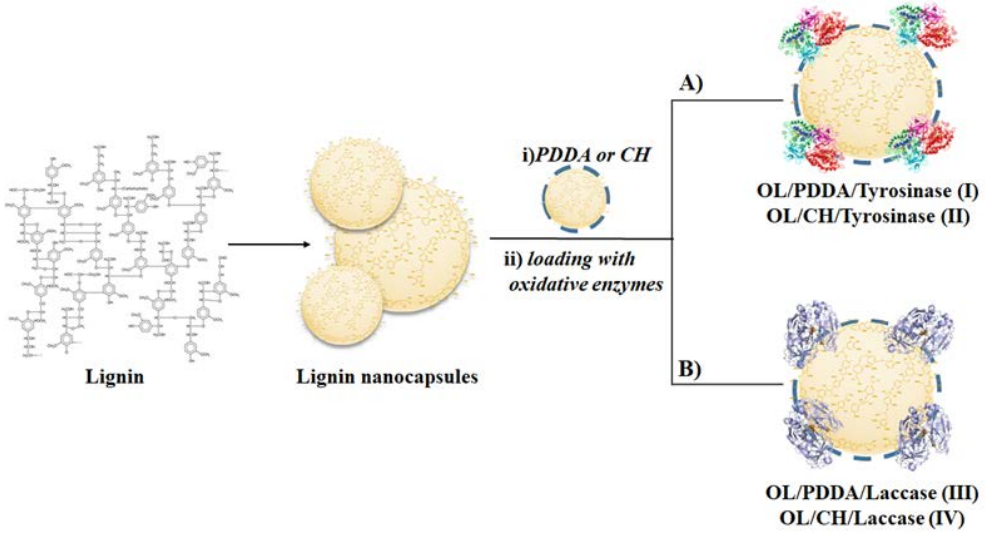

Figure 4.1. Structure model of lignin, and schematic preparation of functionalized lignin nanocapsules supporting tyrosinase and laccase. PDDA and CH were used as positively charged polyelectrolytes. Tyrosinase from *Aspergillus niger*, and laccase from *Trametes versicolor*, are negatively charged at the operative pH. The consecutive deposition of alternatively charged polyelectrolytes was performed on the surface of organosolv lignin nanocapsules.

Table 17.
Kinetic parameters of functionalized lignin nanocapsules (**I-IV**).

Entry	Sample	K_m (mM)	V_{max} (X 10^{-3})[c] (ΔAbs min μg enzyme)	V_{max}/K_m X 10^{-3}	Immobilization Yield (%)[d]
1	**(I)[a]**	0.37	3.89	10.51	90.0
2	**(II)[a]**	0.36	3.88	10.77	89.5
3	**(III)[b]**	0.17	1245	7323	64.1
4	**(IV)[b]**	0.16	1240	7750	62.3

[a] Tyrosinase based system. L-tyrosine was used as a substrate.
[b] Laccase based system. ABTS was used as a substrate.
[c] V_{max} represents the maximum rate achieved by the system, at a saturating substrate concentration. The Michaelis constant K_m is the substrate concentration at which the reaction rate is half of V_{max}. All experiments were conducted in triplicate. Average errors in kinetic parameters were 2–4% for Km, and 1–3% for Vmax.
[d] Immobilization yield (%) = [(Ua − Ur)/Ua] ×100. Ua is the total activity (units) of the enzyme added to the solution, and Ur is the residual activity (units) in the washing solutions.

Chitosan (CH), a linear polysaccharide composed of randomly distributed β-(1,4)-D-glucosamine and *N*-acetyl-D-glucosamine units, was successfully used as biodegradable and no toxic alternative to PDDA to yield OL/CH/tyrosinase (**II**). As reported in **Table 17** (entry 2), the kinetic parameters of OL/CH/tyrosinase (**II**) were of the same order of magnitude than that of OL/PDDA/tyrosinase (**I**).

The scanning electron microscopy (SEM) image of compound (**II**) showed nanoparticles with a regular spherical shape and an average diameter of 0.22±0.02 μm (**Figure 4.2**). Dinamic Light Scattering (DLS) analysis of compounds (**I-II**) is reported in **Figure 4.3**.

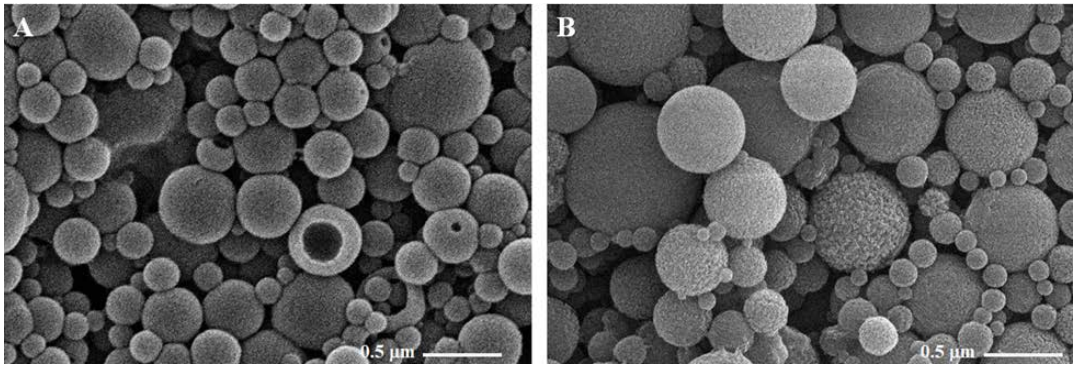

Figure 4.2. SEM images of lignin nanocapsules. Panel A: organosolv lignin nanocapsules. Panel B: OL/CH/tyrosinase (**II**).

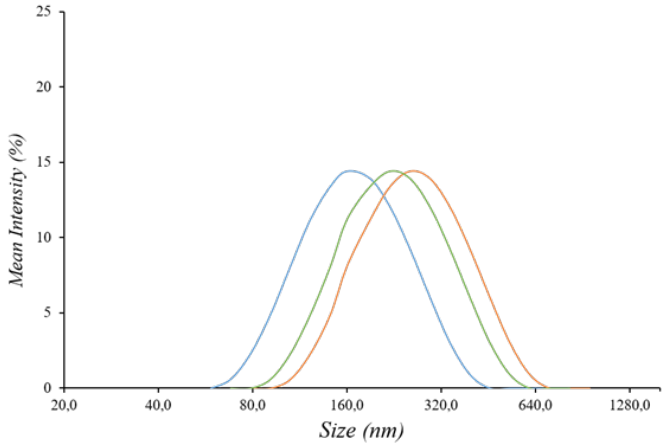

Figure 4.3. Size distribution and polydispersity index (PDI) of OL nanocapsules (blue line, PDI=0.349), compound (**I**) (red line, PDI=0.353), and compound (**II**) (orange line, PDI=0.382).

In order to improve the range of catalytic activity, laccase from *Trametes versicolor* was used instead of tyrosinase as a negative layer to yield OL/PDDA/laccase (**III**) and OL/CH/laccase (**IV**), respectively (**Figure 4.1**, pathway B). Kinetic parameters of compounds (**III**) and (**IV**) are reported in **Table 17** (entries 3 and 4). Compounds (**III**) and (**IV**) showed kinetic parameter higher than that measured for similar catalysts previously produced by LbL immobilization of laccase on Multi Walled Carbon

Nanotubes (MWCNTs)[383]. SEM images of compounds (**III**) and (**IV**) are in **Figure 4.4**. The immobilization yield of samples (**I**-**IV**) was evaluated as reported in the following equation (**Table 17**):

$$\text{Immobilization yield (\%)} = [(Ua - Ur)/Ua] \times 100$$

Where Ua is the total activity (units) of the enzyme added to the solution, and Ur is the residual activity (units) in the washing solutions.

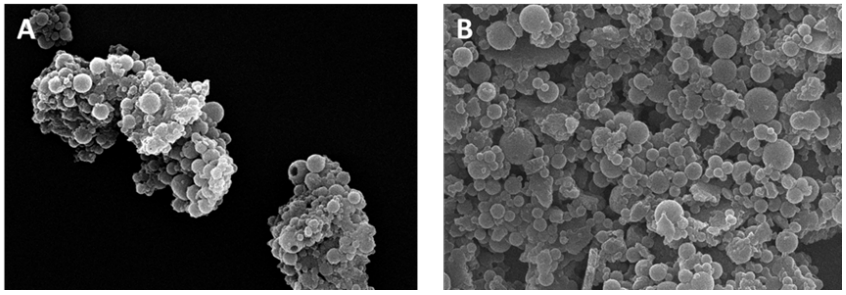

Figure 4.4 SEM images of OL/PDDA/laccase (III) (Panel A) and of OL/CH/laccase (IV) (Panel B)

Procedure for the pigmentation of lignin nanocapsules functionalized with tyrosinase

Tyrosinase (EC 1.14.18.1) catalyzes the conversion of L-tyrosine, and L-3,4-dihydroxyphenylalanine (L-DOPA), to melanin,[384] which is a black pigment widely used in bio-ink formulations.[385] The mechanism for the synthesis of melanin, especially for the most common variant, eumelanin, is reviewed.[386] It comprises the formation of colored reactive intermediates such as dopachrome, followed by sequential oxidative coupling reactions.

Eumelanin is usually represented as a complex structure with oligomeric chain lengths of up to a few tenth of monomers and variable chemical composition.[387] Synthetic melanin is mostly reported as amorphous solid without distinctive particles, [388] although some evidences exist that spherical particles can be produced from synthetic sources under controlled conditions.[389] In this latter case, a three-fold aggregation of oligomers, based on π-stacking interactions, have been proposed.[390]

With the aim to synthesize melanin on the surface of lignin nanocapsules, we decided to use OL/CH/tyrosinase (**II**) as a representative sample, being this nanodevice composed by bio-based ingredients. OL/CH/tyrosinase (**II**) (1.0 mg/mL) was suspended in PBS buffer (pH 7, 0.1 M) in the presence of L-DOPA (10 mg), and the suspension was stirred at 25°C under oxygen atmosphere. The system showed a red coloration, probably due to

the formation of the dopachrome intermediate, followed by the appearance of the characteristic black coloration of melanin. L-DOPA was completely converted after 2.0 h of reaction time (as evaluated by gas-chromatography associated to mass spectroscopy analysis) to yield black lignin nanocapsules (**V**). Nanocapsules (**V**) retained the black coloration after treatment with KOH (1.0 M, 3 x 1.0 mL), suggesting a stable linkage between newly synthesized melanin and the lignin support (**Figure 4.5**, pathway A). Lignin nanocapsules were stable during the KOH treatment, in accordance with previously reported data on the increased stability of lignin nanoparticles at high pH value, as a consequence of the structuring process.[391] Moreover, the alkaline stability of lignin nanoparticles was found to be significantly improved after chemical grafting with dopamine, due to cross-linking reticulation reactions.[392] Tyrosinase catalyzes the oxidative coupling between phenolic units (even when sterically hindered) by formation of reactive quinone intermediates,[393] that can diffuse towards chitin layer to lignin in accordance with results previously reported on the diffusion- and reaction rate-limited redox processes mediated by quinones through bilayer lipid membranes.[394]

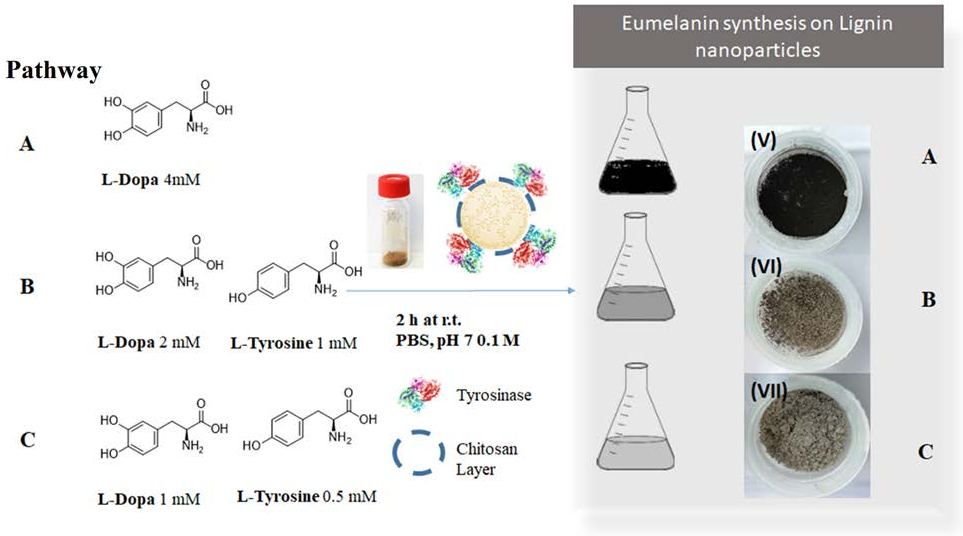

Figure 4.5. Schematic representation of the synthesis and subsequent deposition of melanin in the reaction of OL/CH/tyrosinase (**II**) with L-DOPA and L-DOPA/L-tyrosine mixtures, respectively. Different shades of gray were obtained depending on the L-DOPA/L-tyrosine ratio.

This reaction mechanism might be responsible for the formation of covalent bonds between the phenolic units of lignin and the growing melanin oligomers, assuring the observed stability of the black pigment on the surface of compound (**V**). π-Stacking interactions between the aromatic moieties of the lignin and melanin may be also responsible for the stability of the nanodevice.[395]

TEM and SEM investigations of compound (**V**) (**Figure 4.5** and **Figure 4.6**, respectively) showed the deposition of distinguishable agglomerates of melanin on the surface of

lignin. The irregular shape of these agglomerates, as highlighted by the TEM analysis, suggested the presence of a variable number of superimposed layers of amorphous melanin. Note that spherical nanoparticles of melanin have been previously obtained using tyrosinase adsorbed on an inert glass surface, in which case interactions were not operative between melanin and the support.[396]

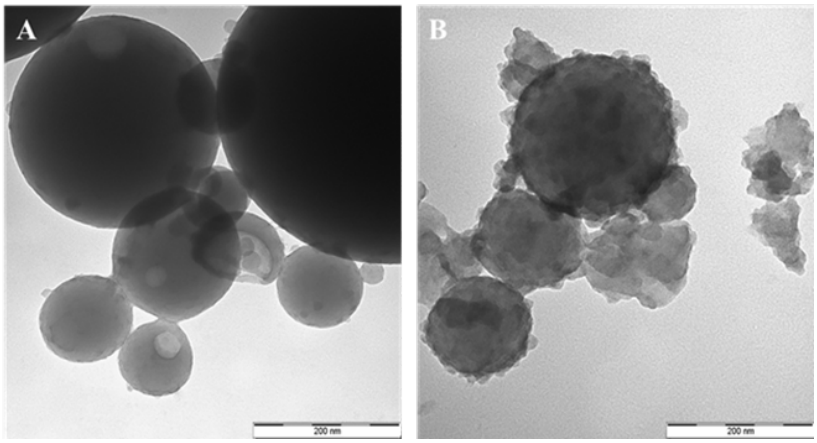

Figure 4.5. TEM images of lignin nanocapsules. Panel A: Organosolv lignin nanocapsules. Panel B: Black lignin nanocapsules (**V**). Agglomerates of amorphous melanin are clearly evident on the surface of lignin.

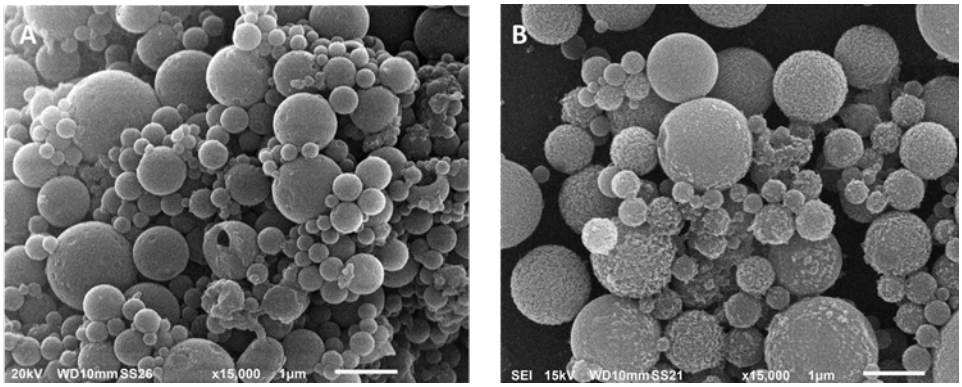

Figure 4.6 SEM images of lignin nanocapsules. Panel A: Organosolv lignin nanocapsules. Panel B: Black lignin nanocapsules (**V**)

Moreover, the internal spherical shape of compound (**V**) was similar to that of compound (**II**), indicating that the L-DOPA polymerization process was limited to the surface of lignin (**Figure 4.5**, panel A versus panel B).

Characterization of the melanin pigment and production of the gray color

The UV−vis-spectra of the KOH solution recovered during the preparation of compound (**V**) was similar to that of the standard (**Figure 4.7**), confirming the synthesis of the melanin pigment. The amount of unbounded melanin was measured by comparing the OD at 470 nm with respect to standard sample[35]. As reported in **Figure 4.8**, 0.2

mg/mL of unbounded melanin were detected, indicating that c.a. 0.8 mg of melanin were retained per 10 mg of compound (**V**).

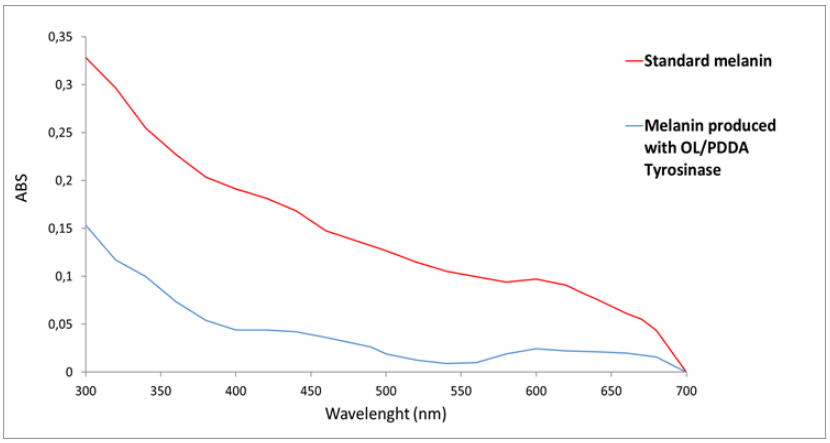

Figure 4.7. Comparison between the UV−vis-spectra of the KOH solution recovered during the preparation of compound (**V**) and the standard sample. Blue line: UV−vis-spectra of unbonded melanin produced by polymerization of L-DOPA in the presence of OL/PDDA/tyrosinase (**II**). Red line: UV−vis-spectra of standard melanin.

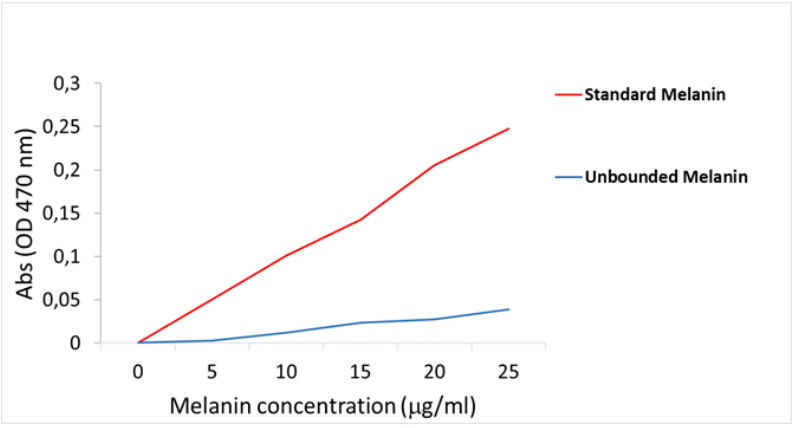

Figure 4.8 Melanin concentration after the work-up in KOH solution. Commercial melanin was used as reference.

The ATR-FTIR-spectra of compound (**II**) showed the vibration bands for the most frequent monomeric sub-units in melanin, 5,6-dihydroxyindole (DHI) and 5,6-dihydroxyindole-2-carboxylic acid (DHICA), respectively. However, the signal of the carboxylic acid (COOH, 1038 cm^{-1}) was not found in the standard, indicating a lower DHICA content in the reference sample of melanin (**Figure 4.9**, Panel A).

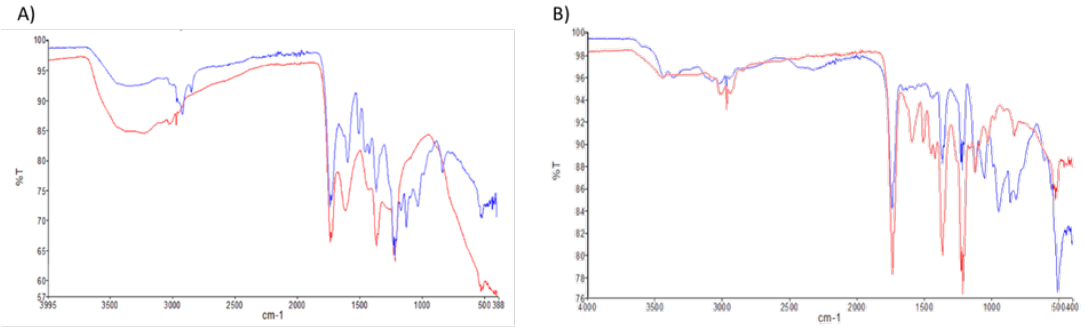

Figure 4.9. Panel A: ATR-FTIR-spectra of melanin recovered from the KOH solution (blue line), and standard melanin (red line). Band assignment: 3196 cm^{-1} OH-, NH- and water (broad signal); 1700 cm^{-1} quinone (C=O stretching); 1606 cm^{-1} indole (ring vibration); 1440 cm^{-1} pyrrole (C=C stretching); 1250 cm^{-1} pyrrole (N-C stretching); 1038 cm^{-1} COOH pyrrole (DHICA monomer). Panel B: ATR-FTIR-spectra of OL/PDDA/tyrosinase (**II**) (red line), and compound (**V**) (blue line). The band at 1038 cm^{-1} COOH in compound (**V**), corresponding to the pyrrole group (DHICA monomer), is characteristic of the melanin structure.

The vibrational bands of melanin were also detected in the ATR-FTIR-spectrum of compound (**V**) (**Figure 4.9**, Panel B), showing the characteristic COOH absorption band, associated to the pyrrole group (DHICA monomer), at 1038 cm^{-1}.

The presence of the melanin pigment in sample (**II**) was definitely proved by first-derivative Electron Paramagnetic Resonance (EPR) analysis (**Figure 4.10**, **Table 18**, entry 2), which showed the characteristic melanin EPR signal at a *g* factor of 2.0041[397-398].

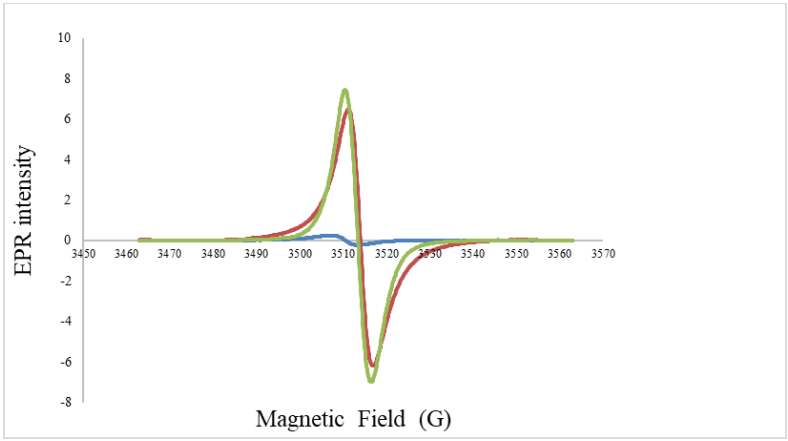

Figure 4.10. The first-derivative EPR analysis of sample (**V**). Red line: standard melanin. Green line: sample (**V**). Blue line: OL nanocapsules.

Next, experiments using L-DOPA in the presence of different concentrations of L-tyrosine were performed in order to tune the shade of the melanin pigment.[399]

When L-DOPA (2.0 mM) was reacted with L-tyrosine (1.0 mM and 0.5 mM, respectively) in the presence of compound (**II**) under previously reported conditions,

lignin nanocapsules (**VI**) and (**VII**), characterized by two different shade of gray, were obtained. The lighter shade of gray was observed in the presence of the lower amount of L-tyrosine (**Figure 4.5**, pathways B and C), suggesting the possible control of the shade simply by varying the ratio between the reagents. The effective presence of melanin in compounds (**VI**) and (**VII**) was demonstrated by first-derivative EPR experiments, in which the characteristic signal of melanin was observed at *g* factor of 2.0042 and 2.0038, respectively (**Table 18**, entries 3 and 4). Probably, the gray color was a consequence of a low concentration of the pigment.

Table 18. Mean values of *g*-factor of samples (**V**-**VII**).

Entry	Sample	*g* factor [a]
1	Standard melanin	2.0036
2	sample (**V**)	2.0041
3	sample (**VI**)	2.0042
4	sample (**VII**)	2.0038

[a] The error on the *g* factors was ±0.0001

Procedure for the pigmentation of lignin nanocapsules functionalized with laccase

Laccase (EC 1.10.3.2, p-diphenol: dioxygen oxidoreductase) is a multicopper enzyme that catalyzes the oxidation of four molecules of substrate through the direct reduction of dioxygen (O_2).[400] The industrial interest in the application of laccase lies in the low substrate selectivity, high value of catalytic constants, and high thermal resistance.[401] Immobilized laccase has been also used in the chemistry of lignin.[402] Laccase efficiently catalyzes the polymerization of phenol derivatives to form pigments in dyeing processes and formulations.[403] In this latter case, a large panel of color and a wide range of shade have been obtained by using heteropolymer synthesis.[404] For example, mixture of natural compounds belonging to the flavonoids family have been successfully applied to give rise to yellow, orange and dark brown colored heteropolymers.[405]

When the flavonoid epicathechin (2.0 mM) was treated with OL/CH/laccase (**IV**) (1.0 mg/mL) in Na-acetate buffer (0.1 M, pH 5) at room temperature under dioxygen atmosphere, the yellow-like colored lignin nanocapsules (**VIII**) were obtained (**Figure 4.11**, pathway A). The color was retained after washing with Na-acetate buffer, suggesting the occurrence of stable interactions between the epicatechin polymer and lignin. This result is in accordance with data previously reported on the laccase mediated grafting-process of flavonoids on cotton fibers.[406] The mechanism for the laccase

mediated formation of covalent linkages between raw lignin and flavonoids is reviewed, including the formation of C-C and C-O covalent bonds.[407]

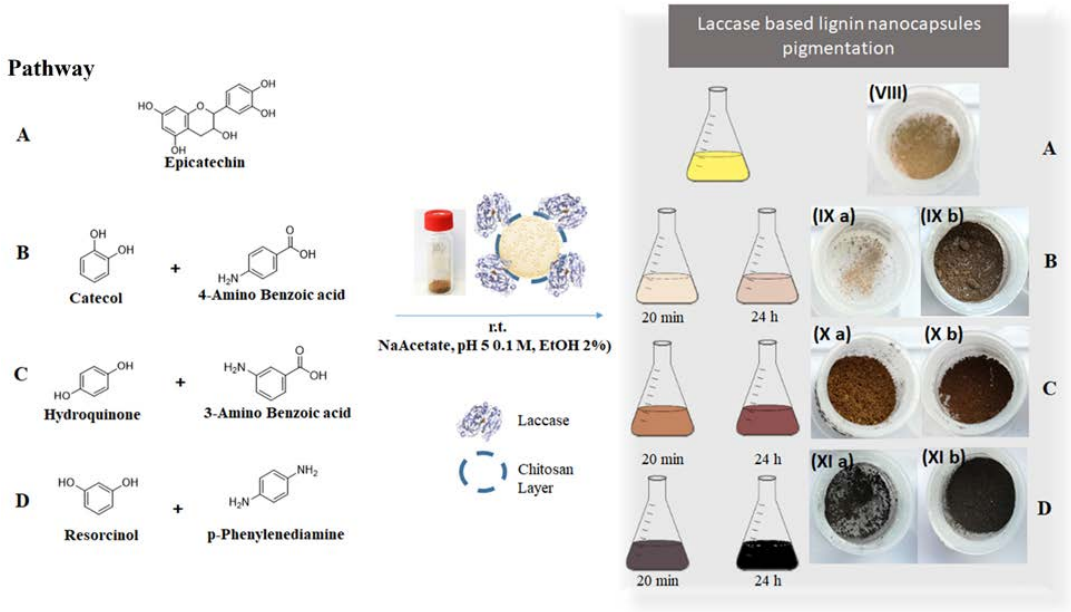

Figure 4.11. Schematic representation of the synthesis and subsequent deposition of pigments during the reaction of OL/CH/laccase (**IV**) with phenol derivatives.

The SEM image of compound (**VIII**) showed spherical capsules with an average diameter of 0.33±0.02 μm (**Figure 4.12**, Panel A), while in the TEM analysis the presence of the epicatechin layer surrounding the lignin capsule was highlighted (**Figure 4.12**, Panel B).

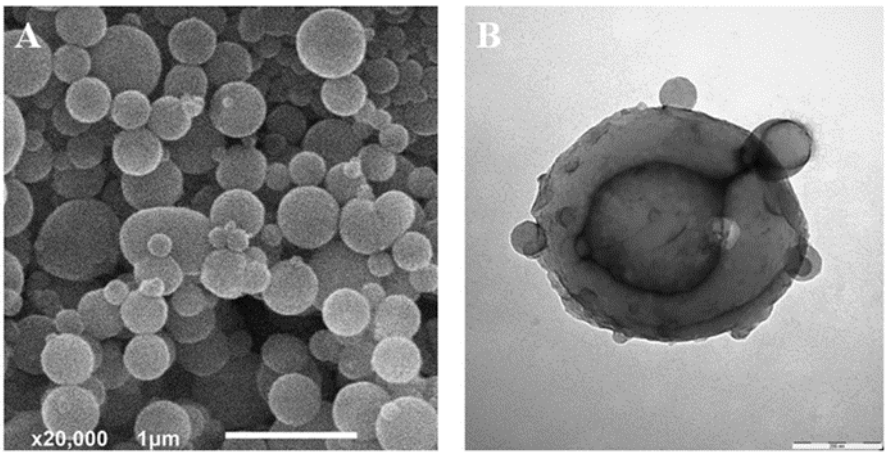

Figure 4.12. Panel A: SEM image of the yellow-like lignin nanocapsules (**VIII**). Panel B: TEM image of the yellow-like lignin nanocapsules (**VIII**).

The formation of the epicatechin polymer was monitored by UV-visible titration at different reaction times (**Figure 4.13**). Epicatechin showed a major absorption band in the range of 250–300nm. The addition of OL/CH/laccase (**IV**) afforded the decrease of the initial absorption band, with the contemporary formation of a new peak in the 325–

800 nm range (with a maxima at 392 nm), corresponding to expected epicatechin polymer.

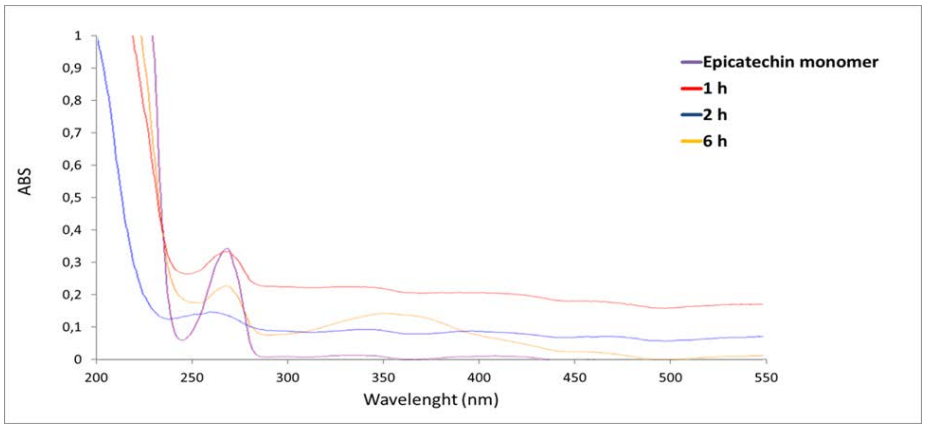

Figure 4.13. UV-visible titration of the reaction between OL/CH/laccase (**IV**) and epicatechin. Newly synthesized epicatechin polymer showed a characteristic absorption peak in the 325–800 nm range.

The ATR-FTIR spectra of compound (**VIII**) confirmed the modification of lignin during the reaction with epicatechin, as evidenced by the disappearance and attenuation of some of the main absorption bands characteristic of lignin (1738 cm^{-1}, 1364 cm^{-1} and 1217 cm^{-1}) (**Figure 4.14**, Panel A). Moreover, the spectra showed the expected absorption bands, including the OH stretching (3400 – 3100 cm^{-1}), C = C stretching (1600 cm^{-1}), and C – O stretching (1150 – 1010 cm^{-1}) [79].

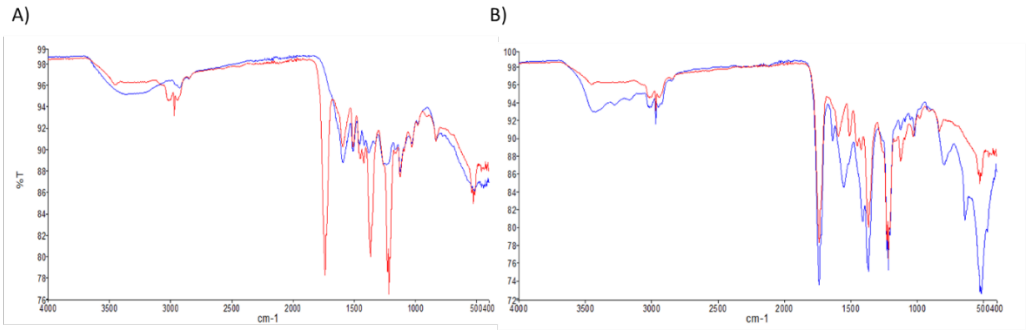

Figure 4.14. ATR-FTIR spectra of compounds (**VIII**) and (**IXa**). Panel A (red line): absorption bands of compound (**IV**). Panel A (blue line): absorption bands of compound (**VIII**). Panel B (red line): absorption bands of compound (**IV**). Panel B (blue line): Absorption bands of compound (**IXa**). Characteristic adsorption bands of the amino-benzoic scaffold were found at 760 cm^{-1}, 860 cm^{-1}, 1490 cm^{-1}, 1600 $cm^{-1}$and 1640 cm^{-1}, respectively.

A larger panel of colours was obtained by reaction of compound (**IV**) with mixtures of phenol derivatives. The treatment of catechol (1.0 mM) and 4-amino-benzoic acid (0.5 mM) with compound (**IV**) afforded pink-like colored lignin nanocapsules (**IXa-b**), whose shade intensity was found to be dependent from reaction time, the darker shade corresponding to the higher value of reaction time (**Figure 4.11**, pathway B). The

presence of catechol/4-amino-benzoic acid heteropolymer on the lignin surface of nanocapsules (**IXa**) was confirmed by the TEM analysis (**Figure 4.15**).

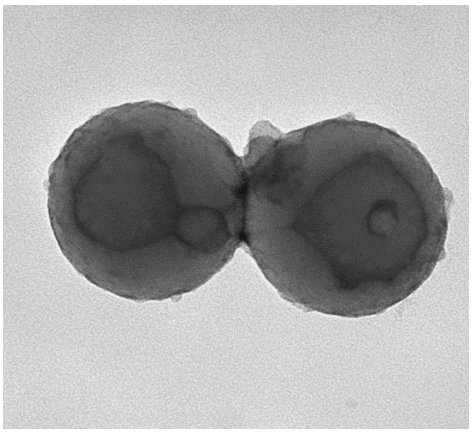

Figure 4.15. TEM image of nanocapsules (**IXa**).

ATR-FTIR spectrum of compound (**IXa**) showed typical signals for the amino-benzoic scaffold associated to the formation of the catechol/4-amino-benzoic acid heteropolymer, including frequency at 760 cm^{-1}, 860 cm^{-1}, 1490 cm^{-1}, 1600 $cm^{-}1$, and 1640 cm^{-1} [408] (**Figure 4.14**, Panel B).

Red/brown-like lignin nanocapsules (**Xa-b**), and grey/black lignin nanocapsules (**XIa-b**), have been obtained by the co-polymerization of hydroquinone (1.0 mM) with 3-amino benzoic acid (0.5 mM) (**Figure 4.11**, pathway C), and of resorcinol (1.0 mM) with *para*-phenylenediamine (0.5 mM) (**Figure 4.11**, pathway D), respectively. Again, the darker shade of the colour was obtained in the correspondence of the highest reaction time. Pigments were found to be stably linked to lignin, confirming the formation of covalent linkages between the colored heteropolymer and the support.

Unexpectedly, reactions of compound (**IV**) produced also pigments that were un-bonded to lignin. For example, 2-amino-3-methoxy benzoic acid (**Figure 4.16**, pathway A), 2-methoxy hydroquinone (**Figure 4.16**, pathway B), and the mixture of 4-hydroxy-benzoic acid with ABTS (**Figure 4.16**, pathway C), or in alternative, the mixture of 4-methyl-amino benzoic acid with 4-methoxy-phenol (**Figure 4.16**, pathway D), afforded orange, yellow, blue and violet pigments that were lost during the work-up of the reaction.

These data suggested that catechol or hydroquinone moieties were necessary for the formation of a stable linkage between the pigment and lignin. Probably, the higher reactivity of these derivatives with respect to simple phenols in the oxidative cross-

coupling process may be responsible for the observed results.[409] This hypothesis is in accordance with the role that quinone derivatives play in the covalent grafting of lignin.[410]

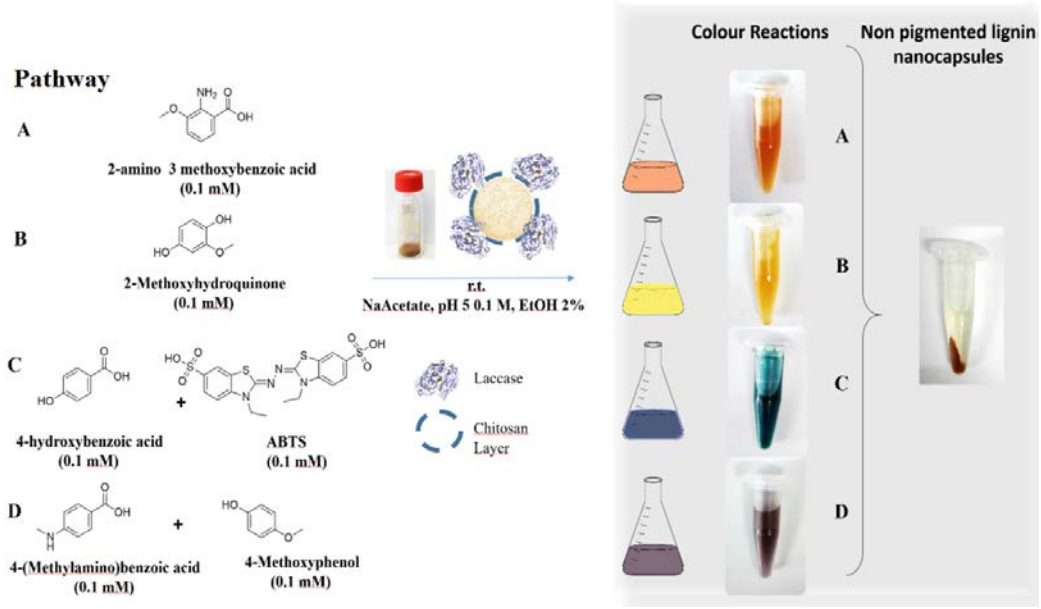

Figure 4.16 Unproductive OL/CH/laccase (**IV**) catalyzed polymerization of phenol derivatives 2-amino-3-methoxy benzoic acid (pathway A), 2-methoxy hydroquinone (pathway B), and of mixture of 4-hydroxy-benzoic acid with ABTS (pathway C), or 4-methyl-amino benzoic acid with 4-methoxy-phenol (pathway D). After the reaction the orange, yellow, blue and violet pigments were not retained on the surface of the lignin nanocapsules.

Characterization of color parameters after pigmentation of lignin nanocapsules

The characterization of the color parameters of compounds (**V-VIII**), (**IXa-b**), (**Xa-b**) and (**XIa-b**) has been performed by reflectance spectrophotometry (**Figure 4.17** panel A) using the CIE L*a*b* system (**Figures 4.17** panel B and C). The reflectance spectrum and the values of chromatic coordinates indicated for the reference lignin nanocapsules a yellowish color (average value of b* equal to 23.3).[411] Compound (**V**) confirmed a black-grey color having low reflectance in the visible spectrum and low values of the chromatic coordinates. Similar trend was observed in compounds (**XIa**) and (**XIb**), that exhibited, in respect to compound (**V)**, only a slightly higher values of lightness.

Lignin nanocapsules (**VI**) and (**VII**) showed constant values in the reflectance spectrum along the entire visible range, confirming the light grey color of these samples. The two different grey shades were also documented by color measurements: compound (**VI**) showing the higher value of lightness and the lower value of b* with respect to compound (**VII).**

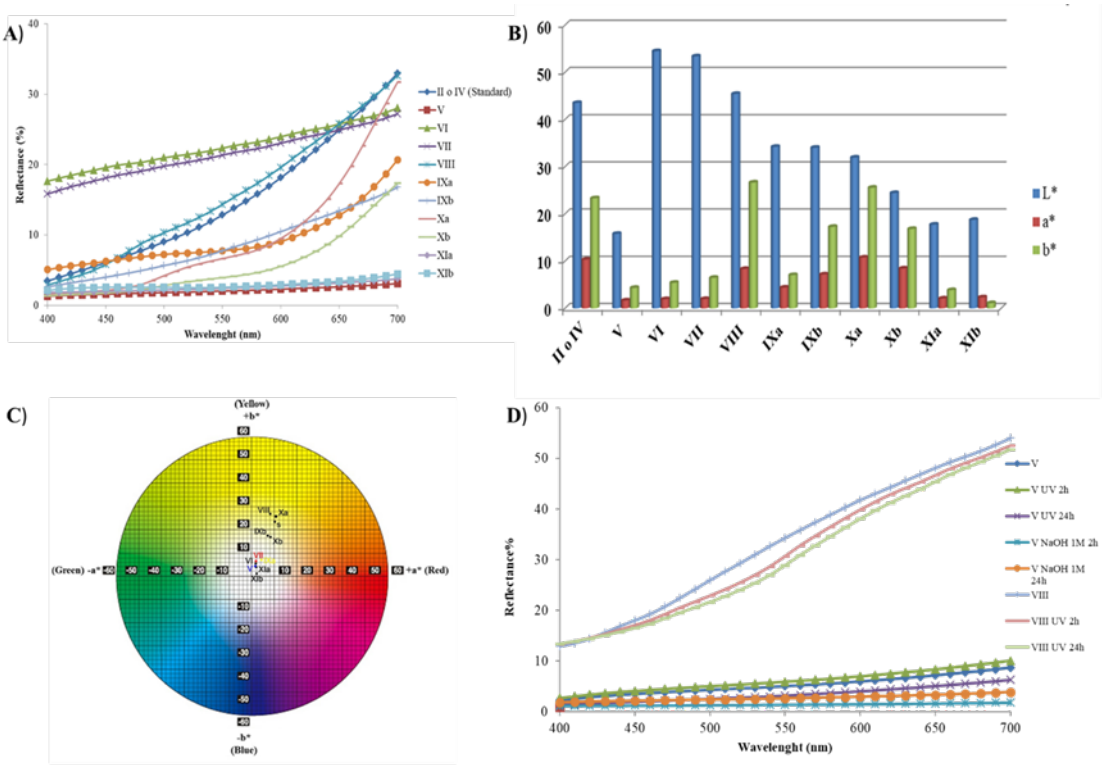

Figure 4.17. Panel A: Reflectance spectra of colored lignin nanocapsules (**V-VIII**), (**IXa-b**), (**Xa-b**) and (**XIa-b**). Panel B: CIE L*a*b* parameters of colored lignin nanocapsules (**V-VIII**), (**IXa-b**), (**Xa-b**) and (**XIa-b**). Panel C: Chromatic diagram for a*b* parameters of colored lignin nanocapsules (**V-VIII**), (**IXa-b**), (**Xa-b**) and (**XIa-b**). Acronym S is for standard compounds (**II**) and (**IV**). Panel D: Reflectance spectra of compound (**V**) and (**VIII**) after UV irradiation and treatment with NaOH of compound (**V**).

Compound (**VIII**) exhibited a reflectance spectrum similar to that of compounds (**II**) and (**IV**), with a clear dominance of yellow, as showed by the b* value. Compounds (**IXa-b**) showed a different trend in the reflectance spectra and in the values of chromatic coordinates a* and b*, whereas the values of L* were the same for the two samples. In particular, compound (**IXb**) has a higher value of b* indicating a yellow dominant of the color, on the other hand, sample (**IXa**) is located very close to the center of the chromatic diagram, i.e. the grey scale axis.

Compounds (**Xa**) and (**Xb**) exhibited the typical reflectance spectra of orange-red color with a rapid increase of reflectance in the red portion of the visible range at 650-700 nm, especially highlighted in the case of compound (**Xb**).

Effect of ultraviolet photo-irradiation and alkaline treatment on the color strength and fastness properties

The effect of UV photo-irradiation on the color strength and light fastness properties was evaluated in the case of compounds (**V**) and (**VIII**) as representative examples of black colored and yellow-like colored nanoparticles. Color strength and light fastness are

important physical properties for the quality, weather resistance, and applications of the inks. Alkaline medium and artificial and natural light may cause most pigments to degrade resulting in color change. The light fastness of inks is important especially in tattoo, in packaging and in printing industries.[412] Light fastness refers to the resistance of a color to fading under the sunlight radiation. The effect of UV irradiation on the color change of compounds (**V**) and (**VIII**) is reported in **Figure 4.17** (panel D) and **Table 19**. The color changes were defined as both variation of the single chromatic coordinates and total color variation (ΔE*). ΔE*is the geometrical distance between two points in the CIE L*a*b* colorimetric space and is calculated according to equation (1):

(1) $\Delta E^* = \sqrt{\{(\Delta L^*)^2 + (\Delta a^*)^2 + (\Delta b^*)^2\}}$

Samples (V) and (VIII) showed only a slight color variation after 2 h of UV irradiation as indicated by the ΔE* value (**Table 19**, entries 2 and 7). A value of ΔE* close to 2 is considered imperceptible by human eye, the perceptible variation being observed only at ΔE* value close to 5.[413] Interestingly, the sample (**V**) showed a darker black color (that is a decrease of L*) after 24 h of irradiation (**Table 19**, entry 3), suggesting the occurrence of a further polymerization process, probably involving semiquinoid-type free radical species, able to increase the π-conjugation degree of the sample.[414] In the case of sample (**VIII**) only a modest ΔE* variation was observed after 24 h, encompassing the decrease of L* (darkening), the increase of a* (reddish trend), and the decrease of b* (yellowish trend) (**Table 19**, entry 8).

Table 19. Variations of the chromatic coordinates L*, a*, b* and total color change (ΔE*) of compound (**V**) and (**VIII**).

Entry	Compounds	Treatment	L*,[a]	a*	b*	ΔL*	Δa*	Δb*	ΔE*,[b]
1	**V**	none	27.2	2.89	8.69				
2	**V**	UV 2h	29.5	3.04	9.15	2.26	0.15	0.47	2.31
3	**V**	UV 24h	21.1	4.00	10.0	-6.11	1.11	1.31	6.35
4	**V**	NaOH 1M 2h	12.1	0.89	2.08	-15.1	-1.99	-6.61	16.6
5	**V**	NaOH 1M 24h	18.7	1.67	4.04	-8.5	-1.22	-4.65	9.77
6	**VIII**	none	65.08	5.98	25.59				
7	**VIII**	UV 2h	62.78	9.12	23.85	-2.30	3.14	-1.74	4.26
8	**VIII**	UV 24h	61.41	9.79	22.78	-3.67	3.81	-2.81	5.99

[a]L* describes the lightness while a* and b* describe the chromatic coordinates on the green-red and blue yellow axes, respectively. [b] ΔE* is defined as reported in equation (1).

The treatment of the sample (**V**) with NaOH as selected example produced a great variation of color after 2 h, mainly due to the change of L* value, in association with a slight decrease of b* (**Table 19**, entry 4). The resulting color was darker than the reference, and completely black having lost the b* contribute. The reflectance spectrum further supports this assessment (**Figure 4.17**). Note that, a lower value of ΔE* was observed after 24h of treatment (**Table 19**, entry 5). This reaction pattern can be explained assuming that NaOH can initially favor the complete polymerization of melanin quinones intermediates by a general alkaline catalysis,[415] followed by degradative pathway of lignin for longer reaction time

Chapter 5
Biosensors

5.1 Lignin nanoparticles are renewable and functional platforms for the concanavalin A oriented immobilization of glucose oxidase-peroxidase in cascade bio-sensing

5.1.1 Aim of the work

The reciprocal orientation of the active site in the cascade is an important feature to control the overall activity of the enzymatic system.[416] For this reason, specific molecular spacers and linkers are used [417,418] for orienting the enzymes in the proper way.[419]

Here we report that LNPs are green and suitable platform for the immobilization of the enzymatic cascade of Horseradish Peroxidase (HRP) and Glucose Oxidase (GOX) [420,421] in biosensing applications.[422-423] To the best of our knowledge, only examples of the use of hybrid systems encompassing unstructured lignin and metal oxides have been previously reported for the immobilization of GOX.[424,425] The correct orientation of the two enzymes during the immobilization process was obtained by the use of the lectin Concanavalin A (Con A), able to selectively interact with the carbohydrate part of both HRP and GOX.[426] Since the carbohydrate component of glycoproteins is usually far from the active site of the enzyme, the use of Con A ensures the retention of the enzymatc activity, sometimes enhancing the performance of the system. [427-428] The effectiveness of Con A in the immobilization of HRP alone on LNPs has been reported in **Chapter 3**, focusing on bio-desulfurization processes. The overall immobilization procedure of the enzymatic cascade was based on two different approaches: i) direct adsorption on the surface of LNPs; ii) layer by layer (LbL) mediated adsorption in the presence of cationic polyelectrolytes including poly (diallyl dimethylammonium chloride) (PDDA), chitosan (CH) and cationic lignin (CATLIG). These polyelectrolytes have been selected on the basis of their previous application in the coating of LNPs, two of them (PDDA and CH) being also reported in the formation of aggregates with Con A.[429,430] CATLIG is the cationic form of lignin with relevant application in the stabilization of pickering emulsions and in the immobilization of different enzymes. Förster resonance energy transfer (FRET) measurement [431] confirmed the co-immobilization of HRP and GOX on LNPs, the two enzymes being located at the optimal distance. The application of natural and renewable polyelectrolytes CH and CATLIG is in accordance with the development of a full green system. LNPs showed a boosting effect in the electrocatalytic activity of the enzymatic cascade as evaluated by cyclic voltammetry analysis. The biosensing application of immobilized HRP/GOX enzymatic

cascade has been measured by the colorimetric detection of β-D-glucose using two chromogenic substrates, 2,2'-azinobis-(3-ethylbenzothiazoline-6-sulfonic acid) (ABTS) and dopamine. The limit of detection (LOD) was found to be better than, or comparable to, that previously reported for other HRP/GOX immobilized systems.

5.1.2 Experimental part

Materials

rganosolv lignin (OL), were purchased from Chemical Point (Oberhaching, Germany). Glucose oxidase (GOX, from *Aspergillus niger*, 160 kDa, catalytic activity according to producer specification is 100–250U/mg), horseradish peroxidase (HRP, from *Armoracia Rusticana*, 44 kDa, catalytic activity according to producer specification is 173 U/mg), concanavalin A (Con A, from *Canavalia ensiformis*, Jack bean type VI), poly(diallyldimethylammonium chloride) PDDA (20% v/v water solution), chitosan (CH, low molecular weight, 75-85% deacetylated degree, 50-190 KDa), were purchased Sigma-Aldrich. Cationic lignin (CATLIG) was prepared from organosolv lignin (10 mg/ml; 0.1 M) in NaOH, by treatment with glycidyl tetramethyl ammonium chloride (20 mg) at 60 °C for 2 h under magnetic stirring. The crude was purified for 24 hours by dialysis with Spectrapore™ membrane (3.5 kDa molecular weight cut off). Bradford reagent, 2,2-azinobis-(3-ethylbenzothiazoline-6-sulfonic acid) (ABTS) and β-D-glucose were purchased from Sigma-Aldrich. L-dopamine were purchased from TCI Europe. All experiments were performed in phosphate buffer saline (PBS, 0.1 M, pH 7.3 or pH 8.0), or sodium acetate buffer (0.1 M, pH 5.0 or pH 6.0), prepared by using Milli-Q water (ρ = 18.2MΩ cm a 25 °C; TOC < 10 μg L−1, Millipore, Molsheim, France).

*Procedure for the preparation of **Bio I***

Lignin nanoparticles (LNPs) were prepared from organosolv lignin (OL) by using the nanoprecipitation procedure. Briefly, a solution of OL (2.0 mg in 1.2 mL of tetrahydrofuran (THF)/H_2O 2:1 v/v) was added to Milli-Q water (3.8 mL) to yield LNPs. The LNPs dispersion was concentrated using a rotary evaporator in order to remove the organic solvent, frozen and lyophilized. LNPs (1.5 mg) in PBS (1.0 mL) were treated with Con A (0.5 mg) in PBS (1.0 mL, 0.1 M; pH 7.3) in order to obtain the LNPs/Con A intermediate. LNPs/Con A was added to a solution of HRP (0.12 mg/mL) and GOX (0.25 mg/mL) in PBS (1.0 mL, 0.1M; pH 7.3) and left under orbital shaking at 4°C for 24 h. LNPs/Con A/HRP-GOX **Bio I** was isolated by centrifugation (20 min at 6000 rpm), washed with sodium phosphate buffer (1.0 mL, 0.1 M; pH

7.3) and lyophilized, while the residual solution was evaluated for the immobilization yield and activity parameters.

*Procedure for the preparation of **Bio II-IV***

LNPs/polyelectrolyte intermediates were prepared by treatment of LNPs (1.0 mL Milli-Q water; 1.0 mg/mL) with the appropriate amount of poly(diallyldimethylammonium chloride) (PDDA), chitosan (CH), or cationic lignin (CATLIG) (1.0 mg/mL, 0.5 mg/mL, and 0.1 mg/mL, respectively), in deionized water (1.0 mL) at 25 °C under orbital shaking for 2 hours. The corresponding LNPs/PDDA, LNPs/CH and LNPs/CATLIG were isolated by centrifugation and lyophilized. Concanavalin A was adsorbed on the surface of the appropriate LNPs/polyelectrolyte (1.5 mg) in PBS (1.0 mL) by treating with Con A (0.5 mg) in PBS (1.0 mL, 0.1 M; pH 7.3) in order to obtain LNPs/polyelectrolyte/Con A intermediates.

LNPs/polyelectrolyte/Con A was added to a solution of HRP (0.12 mg/mL) and GOX (0.25 mg/mL) in PBS (1.0 mL, 0.1M; pH 7.3) and left under orbital shaking at 4°C for 24 h. **Bio II-IV** were isolated by centrifugation (20 min at 6000 rpm), washed with sodium phosphate buffer (1.0 mL, 0.1 M; pH 7.3) and lyophilized, while the residual solution was evaluated for the immobilization yield and activity parameters.

Bradford assay

The loading of Con A on LNPs (defined as % in weight of Con A per mg of LNPs) obtained during the different procedures was evaluated by the Bradford assay of the appropriate residual solution. The Con A concentration was calculated spectrophotometrically at 595 nm by using the Bradford reagent and bovine serum albumin as reference protein.

Activity and kinetic parameters

The ABTS spectrophotometric assay was used for the determination of the enzymatic activity of ConA/HRP-GOX and **Bio I-IV** by following the absorbance at 415 nm (ε_{415} = 36 000 M^{-1} cm^{-1}) for 10 minutes. In a typical experiment, ConA/HRP-GOX and **Bio I-IV** (0.1 mg in PBS, 0.1 M, pH 7.0, 3.0 mL), were added to ABTS (0.5 mM) and β-D-glucose (100 mM). The activity unit of HRP in the enzymatic cascade was considered as the amount of enzyme able to transforms 1.0 μmole of H_2O_2 *per* min at pH 7 at 25°C. Kinetic parameters (K_m, V_{max}, and K_{cat}) were determined by measuring the activity at different concentrations of β-D-glucose (0−100 mM) using the ABTS assay. As a general procedure, the reaction was started by adding

β-D-glucose to PBS solution containing the appropriate amount of the sample (0.1 mg in PBS, 0.1 M, pH 7.0, 3.0 mL). The data were analysed by Lineweaver–Burk plots, the initial velocities (1/V vs. 1/[S]) and K_m and V_{max} being calculated as intercepts at the cartesian axes, respectively. The Michaelis–Menten constant and the turnover number have been calculated performing the analysis in triplicate by the use of the GraphPad software.

Temperature and pH stability and reusability assay

Temperature and pH stability, and reusability assay were performed by using a slightly modified procedure of the ABTS spectrophotometric test. In particular, the temperature stability was determined by adding **Bio I** and **Bio III-IV** (0.1 mg in PBS, 0.1 M, pH 7.0, 3.0 mL) to a solution of ABTS (0.5 mM) and β-D-glucose (100 mM) in an oil bath at 60°C and monitoring the absorbance at 415 nm for 10 minutes. For the pH stability, the appropriate amount of Bio I and Bio III-IV (0.1 mg) was added to buffer solution (3.0 mL) at different pH values (sodium acetate buffer 0.1 M, t pH 5.0 and at pH 6.0, PBS 0.1 M at pH 7.3 and at pH 8.0), containing the appropriate solution of ABTS (0.5 mM) and β-D-glucose (100 mM). The production of the cation radical of ABTS was monitored at 415 nm for 10 minutes at 25°C. The reusability of **Bio I** and **Bio III-IV** was performed under the experimental condition described above. At the end of the transformation, **Bio I** and **Bio III-IV** were recovered by centrifugation and washed three times with deionized water in order to eliminate the residual ABTS. After all, **Bio I** and **Bio III-IV** were reused with fresh glucose/ABTS solution for five consecutive runs.

*Electrochemical characterization of **Bio I**, ConA/HRP-GOX, LNPs/HRP-GOX*

The immobilization procedure for the development of modified glassy carbon electrodes (GCE) with **Bio I**, Con A/HRP-GOX and LNPs/HRP-GOX was performed by a sequential layer-by-layer drop-casting procedure. In particular, for **Bio I**, a three step drop casting procedure was performed as follow: LNPs (15 µl, 1.5 mg/mL) in PBS (50mM, pH 7.0) was sonicated for 5 minutes, the dispersion was drop-cast onto the (GCE) and let it dry for 20 minutes. Successively, a solution of Con A (15 µL, 0.5 mg/mL) was drop-cast onto the electrode surface and let it dry for 20 minutes. The electrode was then rinsed with PBS 50 mM pH 7.0. Finally, HRP (15 µL, 0.12 mg/mL) and GOX (15 µL, 0.25 mg/mL) in PBS (50mM, pH 7.0), was drop-cast onto the electrode surface and let it dry for 30 minutes. The electrode surface was then rinsed with PBS. The GCE/ConA/HRP-GOX system was prepared under the experimental conditions previously reported for **Bio I** without the LNPs drop-casting. The GCE/LNPs/HRP-

GOX system was prepared under the experimental conditions previously reported for **Bio I** without the ConA drop-casting. The voltammetric experiments were performed at room temperature in PBS (50mM, pH 7.0), using hydroquinone solution (H_2Q), as the electroactive mediator (1.0 x 10^{-4} M, PBS, 50 mM; pH 7.0), in the absence and presence of β-D-glucose (1.0 x 10^{-2} M) and in a potential range between -0.5 and 0.5 V at a scan rate of 100 mV s^{-1}. All electrochemical measurements were carried on with a PGSAT204N potentiostat (Eco Chemie, Utrecht) controlled by the Nova 2.1 software with a conventional three electrodes configuration. A saturated calomel electrode (SCE, 244 mV vs. NHE, Cat. 303/SCG/12, AMEL, Milan, Italy) as reference, a glassy carbon rod electrode (d=2mm, Cat. 6.1241.020, Metrohm, Herisau, Switzerland) as counter and a glassy carbon (GC) as working electrode (d=3 mm, Cat. 6.1204.300, Metrohm, Herisau, Switzerland). Before functionalization, GCE was polished for 10 minutes using alumia slurries with two different particle size (0.3 μm / 0.05 μm) using cloth pads wet with Milli-Q water, rinsed with Milli-Q water, and further sonicated for 5 min between each polishing step.

*Colorimetric performance of **Bio I** and **Bio III-IV***

The colorimetric analysis was performed by using different concentrations of β-D-glucose (from 4.0 μM to 2000 μM) into cuvettes containing the appropriate amount of **Bio I** and **Bio III-IV** (1.0 mg, in PBS 0.1 M, pH 7.0, 3.0 mL) and ABTS (0.5 mM, 0.1 mL) or L-dopamine (0.5 mM, 0.1 mL) as chromogenic substrates. After 30 minutes under magnetic stirring at 25°C the dispersion was photographed with a digital camera and the corresponding absorption spectra were measured by a UV−vis spectrophotometer (Varian Cary® 50 UV-Vis) setting the wavelength at 415 nm and 700 nm for ABTS and L-dopamine, respectively.

ATR FT-IR analysis

LNPs/Con A and LNPs/polyelectrolyte/Con A samples were analyzed by attenuated total reflection Fourier transform infrared (ATR-IR) spectroscopic using a PerkinElmer (Spectrum One) spectrometer (UATR unit cell) averaging 32 scans (resolution of 4 cm^{-1}).

Scanning electron microscopy

The field emission scanning electron microscopy (FESEM) of **Bio I-IV** was acquired on FESEM ZEISS GeminiSEM500, operated at 5 kV after drop 20 μl (with deionized water) of sample dispersion on specimen stubs, air dried and coated with gold by sputtering with AGAR

(Auto Sputter Coater). Before the observations, the sample received a deposition of chromium thin film (5 nm) by sputter coating using a QUORUM Q 150T ES plus coater.

Confocal Laser microscopy, FRET.

Procedure for the labeling of HRP and GOX

The synthesis of FITC-labeled HRP was performed by using 20 mg of HRP dissolved in 4.0 mL of Na_2CO_3-$NaHCO_3$ buffer (pH=9.0, 50 mM). Fluorescein isothiocyanate in DMSO (5 mg/mL, 0.4 mL) was added dropwise. The solution was left under magnetic stirring for 4 h at 25°C in dark condition. After the incubation time, the solution of HRP-FITC was quenched with NH_4Cl (50 mM, 0.4 mL) and left under magnetic stirring for 1 h at 25°C in dark condition. Next, the solution was dialyzed against phosphate buffer (pH 7.0, 50 mM) using Spectra pore dialysis membrane (3.5 kD MWCO) for 5 days at 4 °C in dark condition, in order to remove the unreacted fluorescent dye. Finally, FITC-HRP was washed with deionized water and lyophilized. With the same procedure, Rhodamine B isothiocyanate was used to label GOX.

The confocal images of **Bio IV** were obtained by ZEISS LSM-710 NLO confocal system equipped with a Plan Apochromat 100X/1.40 oil DIC M 27 objectives was used for laser confocal microscopy.

Calculation of the FRET effect

The corrected FRET (F_c) and the FRET efficiency (N_{FRET}) are expressed by the following equations:

$$F_c = F_f - \left[\frac{F_d}{D_d} \times D_f\right] - \left[\frac{F_a}{A_a} \times A_f\right] \qquad (1)$$

$$N_{FRET} = \frac{F_c}{\sqrt{D_f \, x \, A_f}} \qquad (2)$$

Where F, D and A are acronyms for FRET, donor and acceptor channels, respectively, and the subscripts "f", "d" and "a" represent the FRET, donor and acceptor samples, respectively. The spectral bleed-through for donor (F_d/D_d) and acceptor (F_a/A_a) was calculated from donor-only and acceptor-only samples, respectively. Data of F_f, F_d/D_d, D_f, F_a/A_a and A_f are reported in Table S 4.

The distance between donor and acceptor moieties was calculated from N_{FRET} using the following equation:

$$N_{FRET} = \frac{R_0^6}{R_0^6 + r^6} \qquad (3)$$

The N_{FRET} has a strong dependence from the Förster distance (R_0) and the physical distance separating the donor and acceptor moieties (R). R_0 is a characteristic feature of each donor and acceptor FRET-pair and can be estimated basing on equation (2). This value is generally comprised in the range between 3.0 nm and 10 nm. R_0 for the pairs of FITC and rhodamine was found to be 5.8 nm. The average distance *r* of HRP from GOX was found to be 7.0 nm.

5.1.3 Results and discussions

Procedure for the immobilization of HRP and GOX on LNPs

LNPs have been prepared starting from commercially available organosolv lignin by applying the nanoprecipitation procedure. Briefly, a solution of the raw lignin in tetrahydrofuran (THF) was rapidly added to deionized water with instantaneous formation of the nanoparticles. The immobilization procedure of HRP and GOX is reported in **Figure 5.1**. In the first case (pathway A), Con A from jack beans (*Canavalia ensiformis*) was adsorbed on the surface of LNPs by treating the nanoparticles (1.5 mg/mL) in sodium phosphate buffer (PBS, 1.0 mL; pH 7.3, 0.1 M) with different concentration of Con A (from 0.2 mg/mL to 1.0 mg/mL) in the same buffer (1.0 mL) at 25 °C. The tetrameric configuration of Con A necessary for the molecular recognition of glycoproteins was preserved by buffering the pH of the system (pH 7.3).

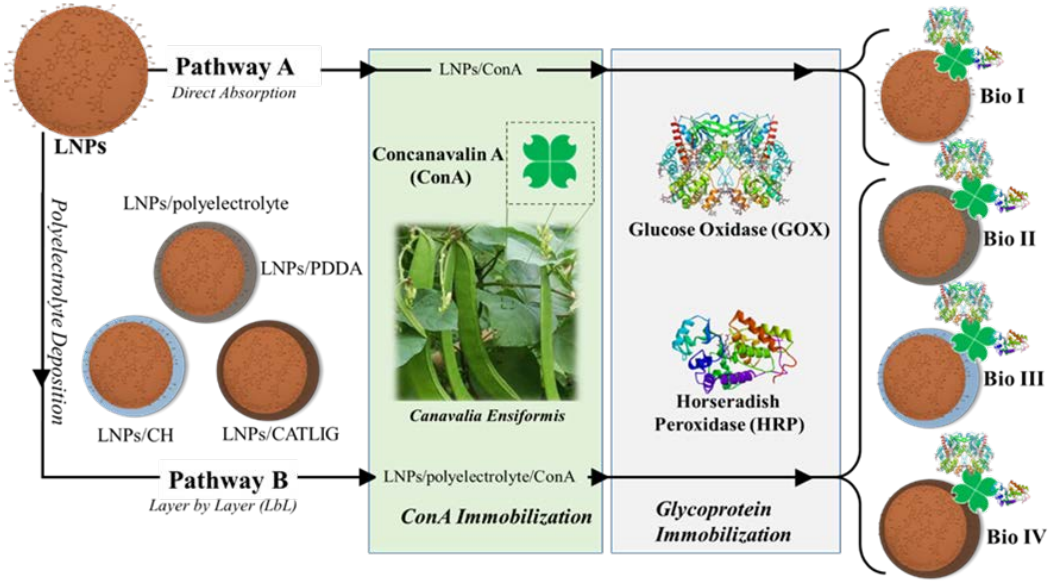

Figure 5.1 Schematic representation of the immobilization of HRP and GOX on LNPs. Pathway A: direct adsorption on the surface of LNPs; Pathway B: layer by layer (LbL) mediated adsorption in the presence of different cationic polyelectrolytes. Grey color: PDDA; Azure color: CH; Dark brown color: CATLIG.

The efficacy of the adsorption of Con A was evaluated by the Bradford assay on the residual solution after removal of the nanoparticles. The interaction between lectins and polyphenols is reported, mainly focusing on their relevance for nutraceutical aspects.[432] The loading factor (% in weight) of Con A on LNPs is reported in **Figure 5.2**. The highest efficacy in the immobilization process was obtained starting from 0.5 mg/mL of Con A (**Figure 5.2**, green line).

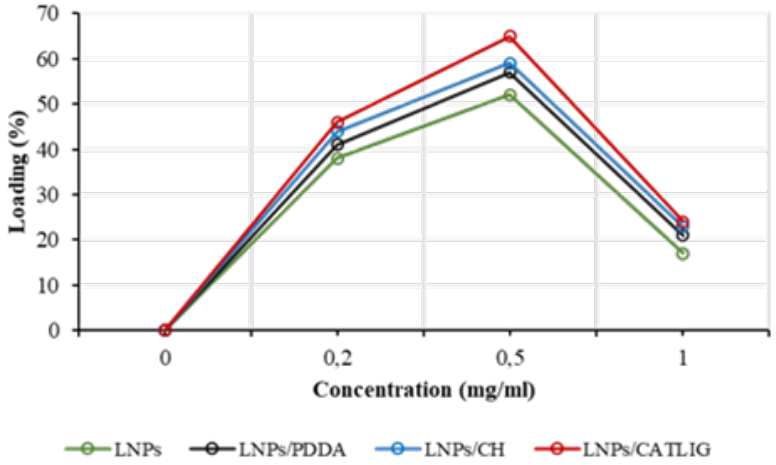

Figure 5.2. Loading of Con A on LNPs during different adsorption procedures. The loading factor is defined as % in weight of Con A per mg of LNPs. LNPs, LNPs/PDDA, LNPs/CH or LNPs/CATLIG intermediates are represented with a color code (green line, black line, blue line and red line, respectively). All experiments were conducted in triplicate. The average error in protein concentration parameters is c.a. 1.2%.

Attenuated total reflection Fourier transform infrared (ATR FT-IR) analysis confirmed the effectiveness of the immobilization of Con A on LNPs, as shown by the appearance of the amide I band in the spectrum (1.644 cm^{-1}) associated to the characteristic stretching amide vibrational mode (amide II band) (**Figure 5.3**). The LNPs/Con A intermediate (1.5 mg/mL) in PBS (1.0 mL) was treated with HRP (2.5 mg/mL) and GOX (5.0 mg/mL) in PBS (20 μL) at 4.0 °C, applying the optimal HRP/GOX ratio value previously reported for the co-immobilization of the two enzymes on Con A in homogeneous conditions[433] to yield LNPs/Con A/HRP-GOX system **Bio I.**

As an alternative, LNPs were coated with cationic polyelectrolyte to favor the electrostatic interaction with negative charged Con A (ζ-potential, -14 mV)[434] (**Figure 5.1**, pathway B). LNPs (1.0 mg/mL) in deionized water (1.0 mL) were treated with the appropriate polyelectrolyte poly (diallyl dimethylammonium chloride) (PDDA), chitosan (CH), and cationic lignin (CATLIG) (1.0 mg/mL, 0.5 mg/mL, and 0.1 mg/mL respectively), in deionized water (1.0 mL) at 25 °C under orbital shaking. The optimal

concentration of the polyelectrolyte was selected on the basis of previous data reported in **chapters 3** and **4.**

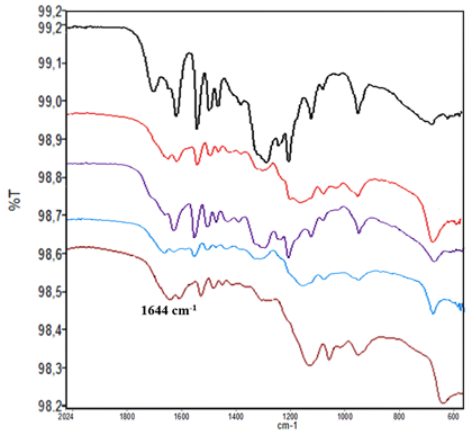

Figure 5.3. ATR FT-IR analysis of LNPs/Con A and LNPs/polyelectrolyte/Con A samples. LNPs alone: black line; LNPs/Con A: red line; LNPs/PDDA/Con A: purple line; LNPs/CH/Con A: azure line; LNPs/CATLIG/Con A: brown line. The presence of Con A was associated to the appearance of the amide I band in the spectrum (c.a. 1.644 cm^{-1}).

The intermediates, LNPs/PDDA, LNPs/CH and LNPs/CATLIG (1.5 mg/mL) in PBS (1.0 mL) were added with different concentration of Con A (from 0.2 mg/mL to 1.0 mg/mL) in the same buffer (1.0 mL) at 25 °C. The highest loading values were obtained in the presence of 0.5 mg/mL of Con A irrespective to the nature of the polyelectrolyte (**Figure 5.2**), CATLIG being the best support for all of the tested concentrations. Dynamic light scattering (DLS) data for original LNPs, LNPs/CATLIG and LNPs/CATLIG/ConA, as selected examples, are reported in **Figure 5.4.**

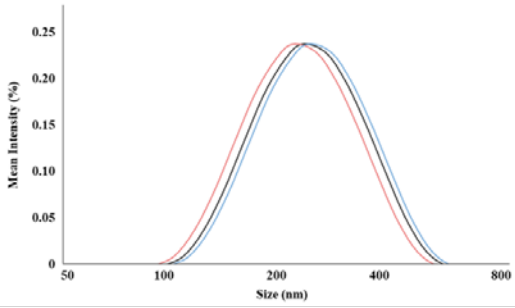

Figure 5.4 Size distribution of LNPs (Red line, 219 nm), LNPs/CATLIG (Black line, 234 nm) and LNPs/CATLIG/ConA (Blue line, 244 nm)

LNPs showed an average size of diameter of 219 nm. After the deposition of CATLIG the diameter value was slightly increased to 234 nm, reaching the value of 244 nm in the presence of ConA. This trend was in accordance with previous reported data.[435]The optimal value of concentration of Con A was then selected for the further study. The presence of the polyelectrolyte generally increased the efficacy of the Con A

loading. ATR FT-IR analysis of LNPs/polyelectrolyte/Con A intermediates confirmed the presence of Con A (**Figure 5.3**) (ATR FT IR spectra of LNPs/polyelectrolyte intermediates are reported in **Figure 5.5**).

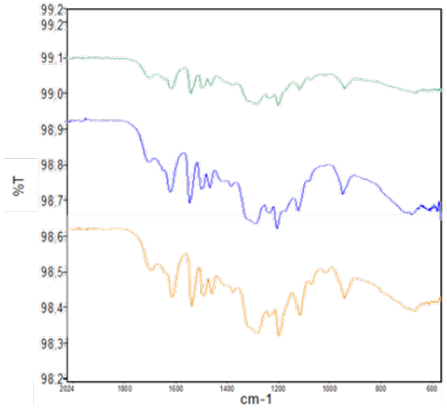

Figure 5.5 ATR FT-IR analysis of LNPs/PDDA (azure line), LNPs/CH (blue line) and LNPs/CATLIG (orange line)

The successive treatment of LNPs/polyelectrolyte/Con A intermediates (1.5 mg/mL) in PBS (1.0 mL) with HRP (2.5 mg/mL) and GOX (5.0 mg/mL) in PBS (20 μL) at 4.0 °C afforded LNPs/PDDA/Con A/HRP-GOX **Bio II**, LNPs/CH/Con A/HRP-GOX **Bio III**, and LNPs/CATLIG/Con A/HRP-GOX **Bio IV**, respectively (**Figure 5.1**). The scanning electron microscopy images of **Bio I-IV** are reported in **Figure 5.6** (panels A-F). **Bio I-IV** showed a regular spherical shape after the deposition procedure. The magnification of **Bio I** and **Bio IV** highlight the typical corona-like structural motif associated to Con A.[427]

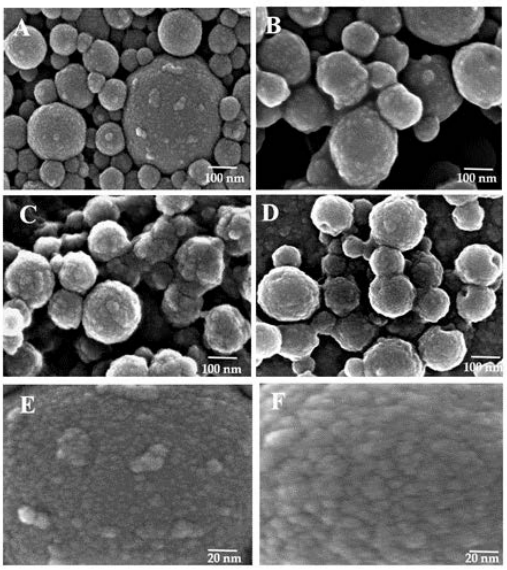

Figure 5.6. Scanning electron microscopy images of **Bio I** (panel A), **Bio II** (panel B), **Bio III** (panel C), and **Bio IV** (panel D). Panel E and panel F: magnification (x 800 K) of **Bio I** and **Bio IV**, respectively.

Activity Parameters and Kinetic Data of Bio I–IV

The activity parameters and kinetic data of **Bio I–IV** are reported in **Table 20**. The data were recorded following the activity of HRP as a quantitative marker of the overall enzymatic cascade process, firstly activated by the GOX oxidation of β-D-glucose to β-D-glucone lactone with concomitant production of hydrogen peroxide (H_2O_2). The efficacy of HRP in the reduction of H_2O_2 was then measured by the 2,2'-azinobis-(3-ethylbenzothiazoline-6-sulfonic acid) (ABTS) assay, following the concentration of the corresponding ABTS radical cation (415 nm) at 25 °C, and working at the optimal pH value for the activity of both HRP and GOX (pH 7.0).[436] The selection of HRP as representative component of the HRP-GOX cascade system is widely reported, the two enzymes having similar reaction rates.The activity yield and immobilization yield were determined using equations 1–2, respectively:

$$\text{Activity yield (\%)} = [U_x/ (U_a - U_r)] \times 100 \quad (1)$$

$$\text{Immobilization yield (\%)} = [(U_a - U_r)/U_a] \times 100 \quad (2)$$

Where U_a is the total activity (units) of co-immobilized HRP, U_r is the residual HRP activity (units) in the solution and U_x is the activity of HRP after the co-immobilization process (the enzyme unit is the increase in the absorbance of 10^{-3} unit per min at 25 °C in 0.1 M PBS). Notably, the random immobilization of HRP and GOX on LNPs without the use of Con A, both in the presence or in the absence of the polyelectrolyte, afforded systems deprived of any catalytic activity (reported in **Table 21**).

Table 21. Immobilization and activity yield of enzymatic cascade systems produced by the random immobilization of HRP and GOX on the surface of LNPs.

Entry	Sample[a]	Immobilization Yield (%)[b]	Activity Yield (%)[b]
1	LNPs/HRP-GOX	64	0.3
2	LNPs/PDDA/HRP-GOX	45	0.7
3	LNPs/CH/HRP-GOX	54	1.2
4	LNPs/CATLIG/HRP-GOX	61	1.4

[a] The immobilization procedure was performed in the presence or in the absence of polyelectrolyte layer.

This result is in accordance with previously reported data on the relevance of the spatial distribution for the catalytic activity of the enzymes during the immobilization processes.[437-440] The cationic polyelectrolyte layers favored the Con A mediated immobilization yield of HRP and GOX (Table 22, entries 3-5 versus entry 2), CATLIG

being the most effective polyelectrolyte (**Table 22**, entry 5 versus entries 3–4). As a general trend, the polyelectrolyte layer increased the activity yield, with the only exception of PDDA. The overall effect was more pronounced in the case of CATLIG (Table 22, entry 5). The kinetic data (K_m, V_{max}, and K_{cat}) of **Bio I-IV** have been compared with the performance of the two enzymes loaded on Con A under similar experimental conditions but in the absence of LNPs (ConA/HRP-GOX). As reported in Table 22, **Bio IV** showed always the highest V_{max} and K_{cat} values (Table 22, entry 5 versus entries). Moreover, **Bio I** and **Bio III** were characterized by V_{max} values similar to Con A/HRP-GOX, having a lower K_{cat}. Finally, **Bio II** was the lowest active system. Note that, in the case of layered samples, better results were obtained with polyelectrolytes characterized by a ζ-potential value comprised between +20 mV and +10 mV (CATLIG and CH, respectively).[441,442] Apparently, the higher value of the ζ-potential reported for PDDA (+ 40 mV)[443] was detrimental for the overall activity of the system. Probably, the catalytic efficiency of **Bio I-IV** was dependent on the modality of the loading of Con A, due to the occurrence of supramolecular interactions tuning the optimal tetrameric configuration of the lectin. In accordance with this hypothesis, the effect of cationic polyelectrolytes in the stability and aggregation behavior of Con A has been reported in relation to the formation of amyloid fibrils, [444,445] able to control the transition of Con A from the optimal β-sheet configuration to less effective α-helices.[446] The alteration of the β-sheet configuration might be also responsible for the lower activity of **Bio I** with respect to Con A/HRP-GOX, since it is reported that low molecular weight polyphenols interact with Con A by H-bonding and hydrophobic forces at the rigid β-sheet responsible for the stabilization of the canonical tetrameric structure.[447]

Table 22. Activity and kinetic parameters of **Bio I-IV**[a]

Entry	Sample	Immobilization Yield (%)	Activity Yield (%)	K_m (mM)[c]	V_{max} (μmol L^{-1} s^{-1})[c]	K_{cat} (s^{-1})[c]
1	Con A/HRP-GOX[b]	-	-	17.26	0.12	594
2	**Bio I**	88	52	8.72	0.10	563
3	**Bio II**	91	51	4.77	0.07	284
4	**Bio III**	93	55	8.30	0.13	576
5	**Bio IV**	96	61	4.85	0.15	652

[a] **Bio I**: LNPs/ConA/HRP-GOX; **Bio II**: LNPs/PDDA/ConA/HRP-GOX; **Bio III**: LNPs/CH/HRP-GOx; **Bio IV**: LNPs/CATLIG/HRP-GOX. [b]Con A/HRP-GOX was used as reference.[49] [c] Kinetic data (K_m, V_{max} and K_{cat}) were analyzed by GraphPad software. Average errors in kinetic parameters were 2–4% for K_m, 1–3% for V_{max} and 1-2% for K_{cat} .The experiments were carried out in triplicate.

Temperature and pH stability, and reusability assay

The temperature and pH stability, and reusability assay, were evaluated for the most active **Bio I** and **Bio III-IV**. The activity yield for the selected samples was measured at 60 °C and at different pH values (from pH 5 to pH 8). Data are reported in **Table 23** and

Figure 5.7, respectively. The systems showed a high thermal stability (from 85% to 99% of retained activity, respectively), **Bio IV** being the most stable device (**Table 23**, entries 1-3). As reported in **Figure 5.7**, irrespective from the experimental conditions, the optimal value of the activity yield was observed in the range of pH value between 6.0 and 7.5, the highest performance being always obtained at pH 7.3. Again, **Bio IV** performed as the best system. The time stability of the most active system **Bio IV** was evaluated by measuring the activity of the system after 30 days of storage in PBS solution at 5°C. Under these experimental conditions, **Bio IV** retained the original activity (**Table 23**, entry 3). The reusability of **Bio I** and **Bio III-IV** was then evaluated by recovering the sample at the end of the oxidation, followed by washing and successive new runs. The systems maintained a significative activity yield after five runs (**Table 23**, reusability expressed in % with respect to the initial value), the better result being obtained with Bio IV (52% of the initial activity).

Table 23 Activity retained after different temperature condition and reusability test of **Bio I-III** and **IV**

Entry	Sample	Activity Yield (%)						
		25 °C	60°C	Reusability (%)[a]				
				run 1	run 2	run 3	run 4	run 5
1	**Bio I**	52	44	42	31	28	25	23
2	**Bio III**	55	53	44	39	34	31	30
3	**Bio IV**	61 (60)[b]	60	59	57	55	54	52

[a] The experiment was performed by recovery of **Bio I** and **Bio III-IV** analyzing their reuse for five runs with freshly prepared glucose and ABTS solutions in PBS (pH 7.0, 0.1 M). [b]Activity of **Bio IV** after 30 days of storage in PBS solution at 5°C

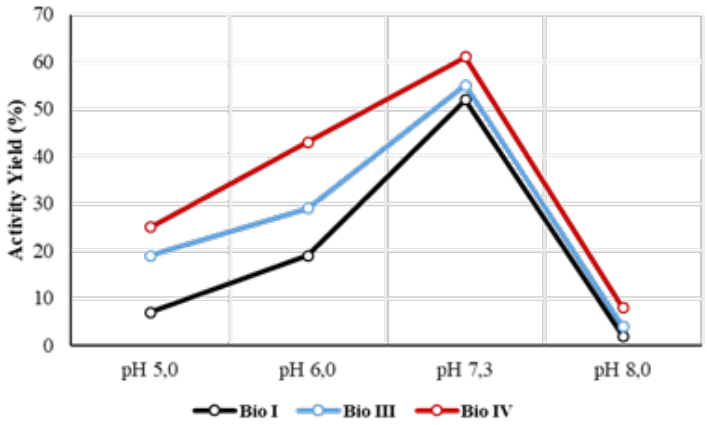

Figure 5.7. pH stability of **Bio I** and **Bio III-IV**. The pH range was controlled by sodium acetate buffer (pH 5.0-6.0) and PBS (pH 7.3-8.0). The pH stability of **Bio I** and **Bio III-IV** are represented with a color code (black line, azure line and red line, respectively). All experiments were conducted in triplicate- The average error in activity yield calculation is c.a. 1.5%.

Electrochemical characterization

Bio I was analyzed by cyclic voltammetry (CV) as a representative example to elucidate the role of Con A in the electrocatalytic activity of the enzymatic cascade after

the immobilization on LNPs. The electrochemical behavior of original LNPs in **Figure 5.8** was in accordance with data previously reported.[448,449]

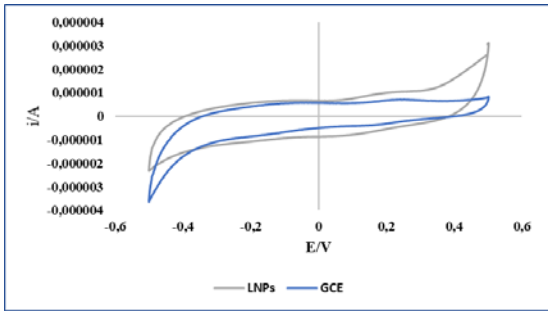

Figure 5.8: Cyclic voltammetry analysis of LNPs compare to GCE alone. LNPs and GCE (blue line and grey line, respectively).

The experiments were performed in hydroquinone solution (H_2Q) as electroactive mediator (1.0 x 10^{-4} M, PBS, 50 mM; pH 7.0), in the absence and presence of glucose (1.0 x 10^{-2} M) (the detailed procedure is reported in the experimental part). Cyclic voltammograms (CVs) have been recorded with a glassy carbon electrode (GC) reproducing **Bio I**, as shown in **Figure 5.9** (panel C). The overall bioelectrode performance was regulated by the oxidation of H_2Q to 1,4-benzoquinone on the electrode surface, following the cascade reaction of HRP and GOX. The schematic representation of the enzymatic transformations occurring at the surface of the GC electrode is reported in **Figure 5.9** (panel A). Con A/HRP-GOX (panel B) and LNPs/HRP-GOX (panel C) have been used as references. The electrochemical response of each system was compared with that obtained in the absence of glucose, corresponding to the cyclic voltammograms of H_2Q alone (black curves, panels B and C). The voltammetry curves of LNPs/HRP-GOx and **Bio I** in the absence of glucose showed a similar behavior, **Bio I** showing a slightly higher electrochemical responsiveness. The cyclic voltammogram of Con A/HRP-GOX with H_2Q solution showed an irreversible behavior as highlighted by the separation between the cathodic and anodic peaks (c.a. 360 mV; panel B, black curve). However, in the presence of LNPs/HRP-GOX and **Bio I** the electrochemical behavior appeared to be more reversible, with a peak-to-peak potential separation of about 150 mV, indicating the occurrence of a quasi-reversible two-electron transfer reaction (panel C, black curve). The anodic and cathodic peak currents were linearly related to $\nu^{1/2}$, thus meaning a typical diffusion-controlled process (data not shown). The diffusion coefficient (D) was calculated to be 5.2×10^{-4} cm^2 s^{-1}, higher than that reported in the literature for a bare glassy carbon electrode.[450] Hence, LNPs increased the electrochemical performance

independently from the presence of Con A. This result can be ascribed to the electrochemical responsiveness of LNPs, which allows a better electron transfer mechanism at the electrode surface.[451] Successively, the electrocatalytic activity of the three systems was studied by adding glucose. The Con A/HRP-GOX showed a clear electrocatalytic responsiveness in the presence of glucose, confirming the retained activity of HRP and GOX after immobilization of Con A (**Figure 5.9**, panel B. red curve).

The beneficial role of Con A was further highlighted by the comparison of the CVs of **Bio I** and LNPs/HRP-GOX (**Figure 5.9**, panel C). In this latter case, the presence of Con A assured the highest electrocatalytic effect (blue curve), a slight electrochemical responsiveness being observed for the LNPs/HRP-GOX counterpart (orange curve). Note that LNPs played a boosting effect in the activity of the overall system, the CV of **Bio I** showed an electrocatalytic effect higher than simple Con A/HRP-GOX (**Figure 5,9**, panel C versus panel B). Boosting effect exerted by lignin on the activity of oxidases are reported in **Chapter 3**. Probably, this effect may be due to the improved stability of the system, even if the amplification of the electrochemical signal by electron transfer processes occurring in the aromatic structure of LNPs cannot be completely ruled out.

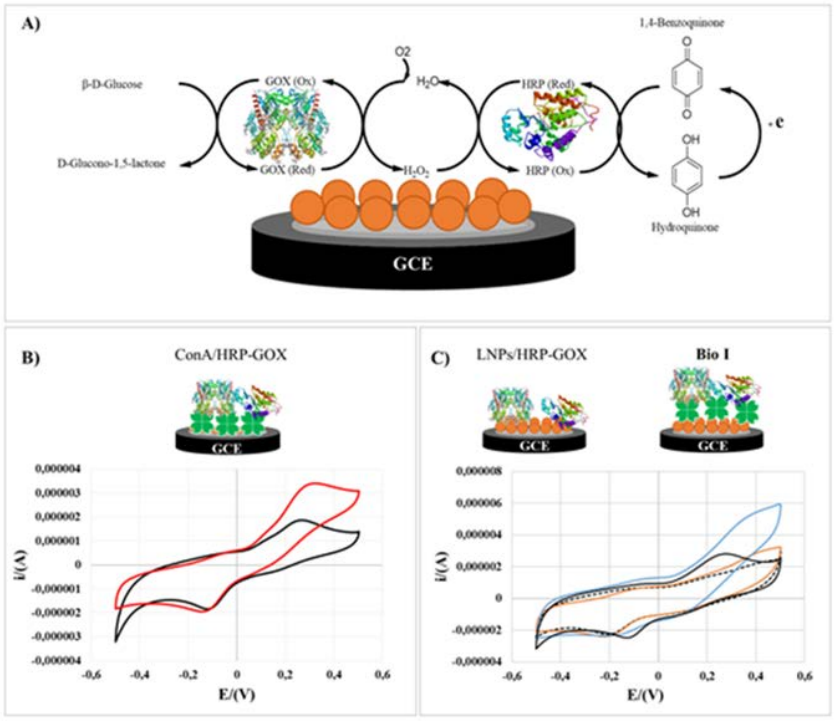

Figure 5.9 Cyclic voltammetry analysis of Con A/HRP-GOX compared to **Bio I** and the random immobilization of HRP and GOX on LNPs without the use of Con A. Panel A: reaction scheme of cascade reaction. Panel B: Con A/HRP-GOX and hydroquinone in absence and in presence of glucose (black line and red line, respectively). Panel C: LNPs/HRP-GOX and hydroquinone in absence and in presence of glucose (black dashed line and orange line, respectively) and **Bio I** and hydroquinone in absence and in presence of glucose (black line and blue line, respectively).

Förster resonance energy transfer (FRET) analysis

The spatial distance between HRP and GOX in the most active **Bio IV** was determined by confocal laser scanning microscopy (CLSM) analysis associated to Forster resonance energy transfer (FRET) effect (**Figure 5.10**, panel A-D). FRET signal in CLSM occurs between two proximately located fluorophores via non-radiative dipole-dipole coupling as a consequence of the energy transfer between a donor and an acceptor dye in close proximity (3-10 nm).[452] The application of the FRET analysis in the study of bio-molecular conformation, protein-protein interaction and molecular motor devices has been reported. [453,454] In the case of **Bio IV**, HRP was labeled with fluorescein isothiocyanate (FITC) as donor, while GOX was labeled with rhodamine B (RhoB) and worked as the acceptor counterpart.[455] The labelling procedure of HRP and GOX is reported in expertimental part. The effective presence of FITC-HRP in **Bio IV** was detected in the donor channel mode at 490 nm (**Figure 5.10** panel A, green fluorescence signal), while that of RhoB-GOX was detected in the acceptor channel mode at 560 nm (**Figure 5.10** panel B, red fluorescence signal). The effective co-localization of HRP-GOX in **Bio IV** was highlighted by the presence of the merged fluorescent signal (**Figure 5.10**, panel C). The original and corrected FRET signals of **Bio IV** (**Figure 5.10**, panel D and panel E, respectively) were used to calculate the average distance between the donor and the acceptor moieties. HRP and GOX were located at the distance of 7.0 nm, a value that is comprised in the range of reported optimal distances for the activity of the enzymatic cascade. [456]

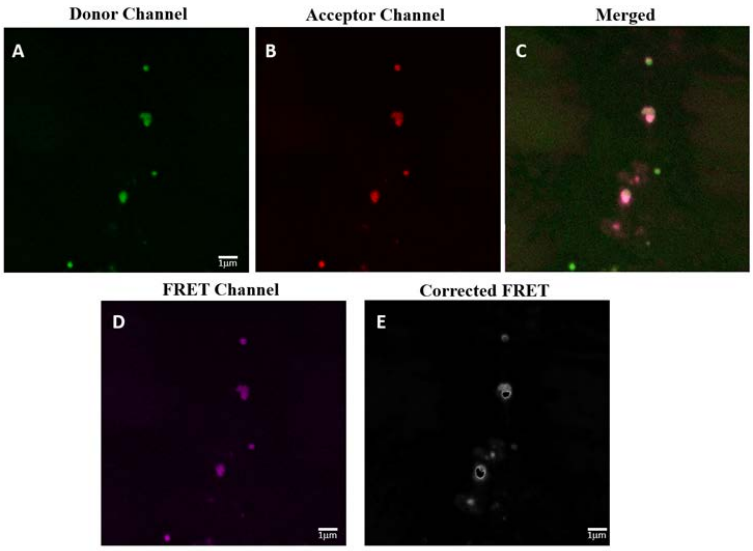

Figure 5.10. Laser confocal scanning microscopy of **Bio IV**. Panel A: HRP labelled with FITC in the donor channel at 490 nm (green pixels). Panel B: GOX labelled with RhoB in the acceptor channel at 560 nm (red pixels). Panel C: merged fluorescence effect. Panel D: original FRET signal. PANEL E: corrected FRET signal.

Evaluation of Bio I and Bio III-IV as colorimetric biosensor

The performance of **Bio I** and **Bio III-IV** as colorimetric biosensors was first evaluated by using the ABTS assay. Briefly, the appropriate sample (1.0 mg) in PBS (0.1 M, pH 7, 3.0 mL) was treated with ABTS (0.5 mM, 0.1 mL) in the presence of different concentrations of β-D-glucose (from 4.0 μM to 2000 μM). The absorbance of the ABTS radical cation produced during the HRP-GOX oxidation was monitored at 415 nm after 30 min at 25°C. The data of the most active **Bio IV** are reported in **Figure 5.11**, corresponding data for **Bio I** and **Bio III** are in **Figure 5.12**. The homogeneous HRP-GOX mixture (same ratio value than that used for the bio systems) and Con A/HRP-GOX were used as references. The color of the solution changed significantly during the addition of β-D-glucose from pale azure to deep blue and dark indigo (**Figure 5.11**, panel B).

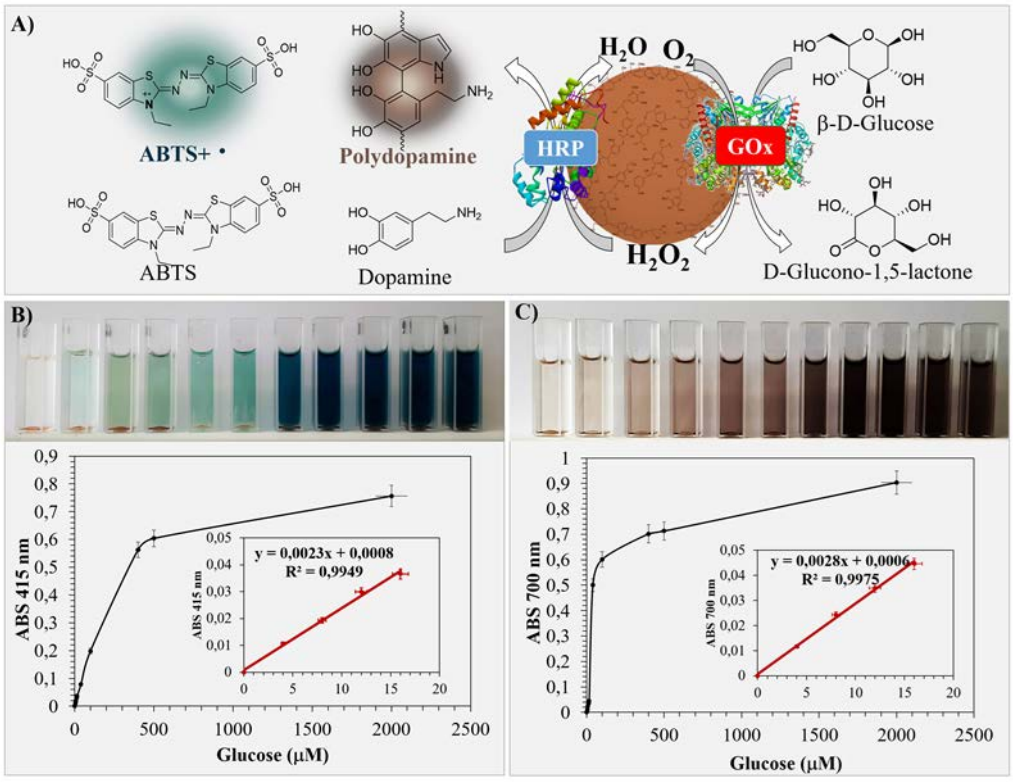

Figure 5.11. ABTS and dopamine colorimetric assay of **Bio IV.** Panel A: schematic representation of the cascade oxidation of β-D-glucose by **Bio IV** in the presence of ABTS or dopamine. The structure of the chromogenic products is reported with a different color code. Panel B: color change variation and absorbance trend (415 nm) during the ABTS assay. Panel C: color change variation and absorbance trend (700 nm) during the dopamine assay. Linear trends and correlation coefficient values are magnified in both panels. The error bars indicate the standard deviation of three replicate of the measurement.

The variation of the absorbance with respect to β-D-glucose concentration was used for the determination of the limit of detection (LOD), taking into account the linear part of the curve.[456]

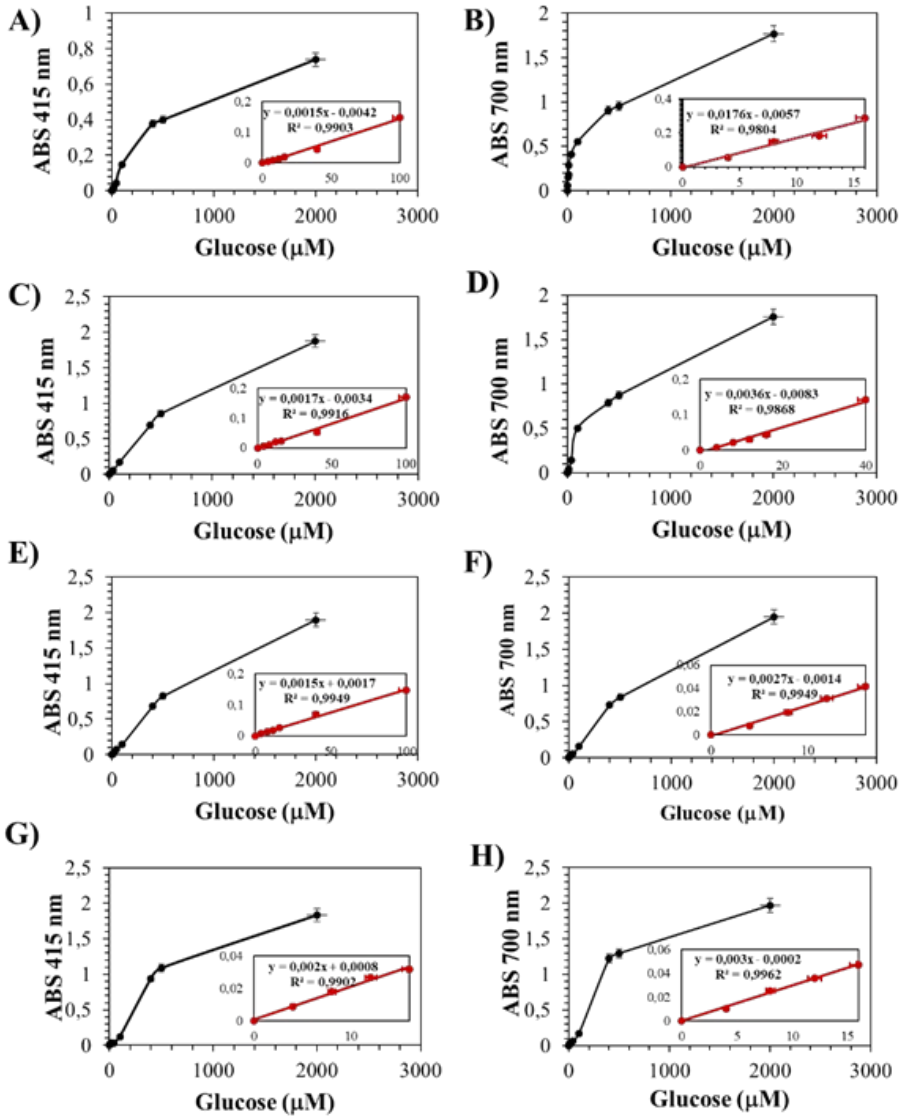

Figure 5.12. Limit of detection (LOD) of HRP-GOX, ConA/HRP-GOX, and Bio I and Bio III devices. absorbance trend during ABTS (415 nm) and dopamine (700 nm) colorimetric assay of HRP-GOX, Con A/HRP-GOX, and **Bio I** and **Bio III**. Linear trends and correlation coefficient values are magnified in all panels. Panel A absorbance trend during ABTS assay of HRP-GOX. Panel B: absorbance trend during dopamine assay of HRP-GOX. Panel C: absorbance trend during ABTS assay of Con A/HRP-GOX. Panel D: absorbance trend during dopamine assay of Con A/HRP-GOX. Panel E: absorbance trend during ABTS assay of **Bio I**. Panel F: absorbance trend during dopamine assay of Bio I. Panel G: absorbance trend during ABTS assay of **Bio III**. Panel H: absorbance trend during dopamine assay of **Bio III**. The error bars indicate the standard deviation of three replicate of the measurement.

The linear trend of **Bio IV** was found to be comprised between 4.0 µM and 16 µM, corresponding to a linear correlation coefficient R^2= 0.9949 and a LOD value of 1.21 µM (**Table 24**, entry 5). **Bio IV** showed a LOD value lower than **Bio I**, **Bio III** and references (**Table 24**, entry 5 versus entries 1-4). This result confirmed the relevance of the ordered deposition of the two enzymes on the lignin platform. Note that the shape of **Bio IV** particles was unchanged after the biosensing application, as evaluated by SEM analysis (**Figure 5.13**).

Table 24. Limit of detection value (LOD) for **Bio I** and **Bio III-IV**.

Entry	Sample	LOD(μM)[a]	
		ABTS	Dopamine
1	HRP-GOX[b]	5.43	2.39
2	Con A/HRP-GOX	5.10	3.25
3	**Bio I**	3.90	1.20
4	**Bio III**	1.71	1.14
5	**Bio IV**	1.21	0.85

[a] The LOD was evaluated as reported in literature.[b] Homogeneous HRP-GOX mixture (same ratio value than that used for the Bio systems).

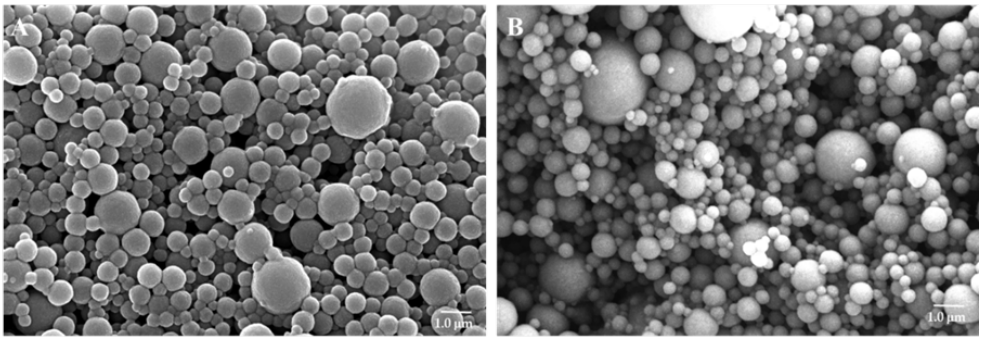

Figure 5.13: Scanning electron microscopy image (SEM) of **Bio IV** after biosensing performance with chromogenic substrates. Panel A SEM image of **Bio IV** after biosensing performance with ABTS. Panel B SEM image of **Bio IV** after biosensing performance with L-dopamine.

As an alternative, the LOD was evaluated by following the oxidation of L-dopamine as a natural chromogenic compound. The oxidation of L-dopamine by HRP and H_2O_2 to yield black poly-dopamine in quantitative yield has been reported.[457] In this latter case the LOD was found to be significantly lower than that obtained with other standard chromogenic compounds.[458] The oxidation of L-dopamine with **Bio IV** was performed under the experimental conditions previously reported for ABTS. The colorimetric variation during the addition of β-D-glucose and the respective absorbance values at 700 nm are in **Figure 5.11** (panel C) (LOD values of **Bio I** and **Bio III** are in **Table 24**, the corresponding absorbance curves are in **figure 5.12**). As reported in **Table 24**, **Bio IV** showed lower LOD value with respect to the ABTS assay. Again, the LOD of **Bio IV** was lower than that of **Bio I** and **Bio III**, and of the two reference systems (**Table 24**, entry 5 versus entries 1-4).

Conclusions

Bionanotechnologies based on the application of micro- and nanoparticles of polyphenols are of large industrial interest for the design of novel biobased materials with antioxidant and UV-protecting properties, as well as for the construction of biocatalysts, bio-based inks and biosensors. The renewable and biodegradable devices prepared with the layer-by-layer technology have been successfully applied in the food packaging, in the development of high technological fibers and in the metal surface coatings, as well as in environmentally friendly sensoring, and biomedical applications. In this context, nanocapsules of mixed polyphenols which are characterized by the sequential deposition of sulfonate lignin and tannic acid, showed the advantage of an increased antioxidant, UV protecting effect, and electrochemical responsiveness with respect to the homopolymer counterpart, as a consequence of the synergist effects between the two polymeric components. It is interesting to note that the antioxidant activity and UV-protecting properties of nanocapsules of mixed polyphenols were finely tuned by the specific order of the layers of the components. In fact, nanocapsules of the PDDA/LS+TA type, in which the polyphenols are mixed together to form a single disordered layer, is lesser active than the sequential and alternate coating of layers of any single polyphenol. In this latter case, the orientation of the adjacent aromatic rings is parallel to the longitudinal direction of the layer, following a head-to-tail-like arrangement. Since the redox and UV-absorbing properties of polyphenols strictly depends on their aggregation state ("exciton" theory"), it is reasonable to suggest that the structural order of the polyphenol aggregation is the key parameter for the emergence of synergistic effects. As a general trend, the reduction of the dimensional scale of the nanocapsules improved both the antioxidant activity and the UV-protecting effects. These data highlight the relevant role of mixed polyphenol layers to increase the antioxidant and UV-protecting properties.

Organosolv lignin nanoparticles was shown to be an efficient and renewable support for the immobilization of tyrosinase. Phosphorus-based Nuclear Magnetic Resonance (^{31}P-NMR) and GPC analysis demonstrated the stability of lignin towards the phenoloxidase activity of tyrosinase. Among the different procedures applied for the preparation of the catalysts, the layer-by-layer deposition of PDDA on pre-formed lignin nanoparticles, followed by the deposition of tyrosinase and BSA, yielded the most active catalyst for the oxidation of phenols to corresponding catechols. The layer-by-layer

procedure performed better than the direct adsorption and encapsulation of tyrosinase on lignin nanoparticles.

Several procedures have been developed for the immobilization of laccase from *Trametes versicolor* on lignin nanoparticles. The layer-by -layer procedure showed again higher activity and kinetic parameters, as well as reactivity performances, with respect to alternative physical adsorption and encapsulation processes. The reactivity observed for the novel biocatalysts was confirmed by electrochemical and amperometric analyses. In this latter case, pseudo-DET and MET mechanisms were operative depending on the specific experimental conditions. Laccase immobilized on lignin nanoparticles catalyzed the selective oxidation of alcohols to the corresponding aldehydes by using TEMPO as a redox mediator. TEMPO was more efficient than other possible low molecular weight redox mediators. The laccase/lignin nanoparticle devices showed higher reactivity and selectivity when compared to laccase covalently immobilized on silica, suggesting a specific boosting effect exerted by lignin on the activity of the enzyme. Biocatalysts retained their activity for at least six runs, preserving the morphological integrity of the lignin nanoparticle. The increased stability and the high activity of laccase LbL functionalized lignin nanoparticles make these systems an attractive entry for novel biotechnological applications.

Nanoparticles of lignin were effective functional and natural platforms for the immobilization of the HRP/Con A complex. In this process, the hydrophobicity of the support was a crucial parameter, OL favoring the dissociation of Con A into the two un-effective sub-unit components. KL was the most efficient support. Thanks to the selective supramolecular interaction between Con A and the oligosaccharide part of HRP, that is located far from the active site of the enzyme, the overall activity of the system was generally retained after the immobilization. The presence of the cationic polyelectrolyte layer increased the overall stability and activity of the biocatalyst, PDDA and CATLIG showing a similar behavior. In addition, multi-layered systems performed better than the single layered counterpart, confirming the beneficial effect of the layered structure in preserving the enzyme from possible denaturation processes. On the other hand, some mass-transfer limitation occurred in the biphasic medium PBS/n-hexane during the oxidation of DBT. This kinetic limitation was solved through the use of redox mediators that enhanced the efficacy of the biocatalyst acting as redox shuttles between the active site of HRP and the bulk of the solution. Irrespective from the experimental conditions, DBTO was obtained as the only recovered product, highlighting the high reactivity and

selectivity of HRP and making easier the successive extraction of the polar end product from the oil phase. The possibility of removing DBT with efficacy similar to native HRP, associated to the general green property of the system at relative low temperature (45 °C), room pressure and recyclability, makes HRP/Con A an effective tool in bio-desulfurization ODS processes.

In the case of bioink based on functionalized lignin nanocapsules, the synthesis of the pigment was catalyzed by LbL-immobilized tyrosinase and laccase, with the lignin scaffold performing as the vehicle and binder of the pigment. L-DOPA, L-tyrosine, epicatechin, and other phenol derivatives were used as reactants to afford a large panel of pigments. When tested together, a mixture of phenols afforded different colors, with the specific shade depending upon both the reaction time and the ratio between the two reactants. Pigments were found to be linked to lignin, suggesting the formation of covalent bonds between the pigment and the support. The presence of the catechol or hydroquinone moiety in the substrate was essential for the stability of the ink. Oxidative coupling processes occurring through reactive quinone intermediates were probably responsible for this effect. The pigmentation process does not modify the spherical shape of lignin nanocapsules, and the pigment was mainly deposited on the surface of lignin, probably in the proximity of immobilized enzymes. Black bioinks characterized by low values of reflectance were obtained. Black ink, two shades of gray and yellow inks were resistant to ultraviolet photoirradiation. In the case of the black color, the darkness increased during the exposition time. Exposure to ultraviolet radiation usually induces the modification of melanin, suggesting the occurrence of a protective effect, probably due to the known UV shielding capacity of lignin at the nanoscale level. The black pigment was also resistant to alkaline treatment, retaining a black coloration darker than the reference, even for prolonged reaction time. The very fact that the pigment is confined on the surface of lignin nanocapsules, which can act contemporary as vehicle, additive, and binder for the pigment, encourages the use of this procedure for the preparation of unique polyvalent bioinks.

Finally, lignin nanoparticles proved to be an efficient green platform for the immobilization of HRP and GOX mediated by Con A. The activity and kinetic parameters of the HRP–GOX enzymatic cascade were controlled by the specific nature of the cationic polyelectrolyte layer able to modify the aggregation stability of the tetrameric sub-units of Con A, CATLIG being the best performing polyelectrolyte. In this latter case, the optimal distance of 7.0 nm was measured between immobilized HRP and GOX by

F¨orster resonance energy transfer (FRET) effect. Cyclic voltammetry analysis confirmed the critical role played by Con A in the electrochemical responsiveness of the systems, associated to a boosting effect exerted by LNPs probably due a better electron transfer mechanism occurring at the electrode surface. The efficacy of novel immobilized Con A/HRP–GOX systems in the oxidation of β-D-glucose was tested by colorimetric assay, using ABTS and dopamine as chromogenic substrates. The lowest LOD values were obtained in the presence of CATLIG as cationic polyelectrolyte layer. The comparison of the LOD value obtained with the CATLIG based biosensor with that of other reference systems showed that a LOD value (0.85 mM) is better than, or comparable to, that previously reported for other heterogeneous HRP–GOX immobilized systems. The fact that a full renewable nanoplatform composed by lignin (organosolv and CATLIG) and Con A can efficiently support the HRP–GOX enzymatic cascade maintaining the catalytic activity open a new entry for a green and biodegradable family of biosensors useful for bio-catalytic and environmentally friendly applications.

References

1. Clark, J. From waste to wealth using green chemistry: The way to long term stability. Curr. Opin. Green Chem. **2017**, 8, 10–13.
2. Clark J.H. Green chemistry: today (and tomorrow). Green Chem. **2006**, 8, 17–21
3. Ragauskas A.J, Williams C.K., Davison B.H., Britovsek G., Cairney J., et al. The path forward for biofuels and biomaterials. Science **2006**, 311, 484–89
4. Bilal, M., Wang, Z., Cui, J., Ferreira, L. F. R., Bharagava, R. N., & Iqbal, H. M. N. Environmental impact of lignocellulosic wastes and their effective exploitation as smart carriers – A drive towards greener and eco-friendlier biocatalytic systems. Science of The Total Environment, **2020**. 722, 137903.
5. Bilal, M., Iqbal, H. M. N. Ligninolytic Enzymes Mediated Ligninolysis: An Untapped Biocatalytic Potential to Deconstruct Lignocellulosic Molecules in a Sustainable Manner. Catalysis Letters. **2020**, 150(2), 524–543.
6. Asgher, M., Ijaz, A., Bilal, M. Lignocellulose-degrading enzyme production by Pleurotus sapidus WC 529 and its application in lignin degradation. Turkish Journal of Biochemistry **2016**, 41 (1), 26–36.
7. Gregoire, C. E., & Bain, R. L. Technoeconomic analysis of the production of biocrude from wood. Biomass and Bioenergy, **1994**, 7(1-6), 275–283.
8. Pettersen, R. C. The Chemical Composition of Wood. In The Chemistry of Solid Wood. Advances in Chemistry Series 207; Rowell, R. M., Ed.; American Chemical Society: Washington D.C., **1984**; pp 115−116.
9. Asgher, M., Ahmad, Z., Iqbal, H.M.N. Alkali and enzymatic delignification of sugarcane bagasse to expose cellulose polymers for saccharification and bio-ethanol production. Ind. Crop. Prod. **2013**, 44, 488–495.
10. Asgher, M., Bashir, F., Iqbal, H.M.N. A comprehensive ligninolytic pre-treatment approach from lignocellulose green biotechnology to produce bio-ethanol. Chem. Eng.Res. Des. **2014**, 92 (8), 1571–1578.
11. Moreno, A., & Sipponen, M. H. Lignin-based smart materials: a roadmap to processing and synthesis for current and future applications. Materials Horizons, **2020**. 7(9), 2237–2257.
12. M. Kleinert, T. Barth, Towards a lignocellulosic biorefinery: Direct one-step conversion of lignin to hydrogen-enriched biofuel Energy Fuels, **2008**, 22, 1371–1379.
13. Ragauskas, A. J., Beckham, G. T., Biddy, M. J., Chandra, R., Chen, F., Davis, M. F., Wyman, C. E. Lignin Valorization: Improving Lignin Processing in the Biorefinery. Science, **2014**, 344(6185), 1246843–1246843.
14. McCoy, M. Has lignin's time finally come? Chemical & Engineering News, **2016**, 94(39), 35-38.
15. Johansen, G. L. Lignin first: the Borregaard approach to lignocellulosic sugars and bioethanol. In EU-India Conference on Advanced Biofuel, **2018**, New Dehli (pp. 6-8).
16. Dessbesell, L., Paleologou, M., Leitch, M., Pulkki, R., Xu, C. Global lignin supply overview and kraft lignin potential as an alternative for petroleum-based polymers. Renewable and Sustainable Energy Reviews, **2020**, 123, 109768.
17. Caño-Delgado A., Penfield S., Smith C., Catley M., Bevan M. Reduced cellulose synthesis invokes lignification and defense responses in Arabidopsis thaliana. Plant J **2003**, 34, 351–362.
18. Ralph J., Lundquist K., Brunow G., Lu F., Kim H., Schatz P.F., Marita J.M., Hatfield R.D., Ralph S.A., Christensen J.H., et al. Lignins: natural polymers from oxidative coupling of 4-hydroxyphenylpropanoids. Phytochem Rev 2004, 3, 29–60.
19. Simon, J. P., Eriksson, K. E. L. Computational Studies of the Three-Dimensional Structure of Guaiacyl ß-O-4 Lignin Models. Holzforschung-International Journal of the Biology, Chemistry, Physics and Technology of Wood, **1998**, 52(3), 287-296.
20. Stomberg, R., Hauteville, M., Lundquist, K. Studies on lignin model compounds of the β-O-4 type: crystal structures of threo-1-(4-hydroxy-3, 5-dimethoxyphenyl)-2-(2-methoxyphenoxy)-1, 3-propanediol and 3-hydroxy-1-(4-hydroxy-3, 5-dimethoxyphenyl)-2-(2-methoxyphenoxy)-1-propanone-methanol (1/1). Acta chemica Scandinavica. Series B. Organic chemistry and biochemistry, **1998**, 42(10), 697-707.
21. Faulon, J.-L., Hatcher, P. G. Is There Any Order in the Structure of Lignin? Energy & Fuels, **1994** 8(2), 402–407.
22. Kennedy, J. F. Lignin: Properties and materials. Edited by Wolfgang G. Glasser and Simo Sarkanen, ACS Symposium Series No. 397, American Chemical Society, Washington, DC, Polymer International, **1991**. 24(2), 125–126.
23. Tronchet M., Balagué C., Kroj T., Jouanin L., Roby D. Cinnamyl alcohol dehydrogenases C and D, key enzymes in lignin biosynthesis, play an essential role in disease resistance in Arabidopsis. Mol Plant Pathol **2010**, 11, 83–92
24. Bonawitz, N. D., Chapple, C. The Genetics of Lignin Biosynthesis: Connecting Genotype to Phenotype. Annual Review of Genetics, **2010**, 44(1), 337–363.
25. Novo Uzal E., Gómez Ros L.V., Pomar F., Bernal M.A., Paradela A., Albar J.P., Ros Barceló A. The presence of sinapyl lignin in Ginkgo biloba cell cultures changes our views of the evolution of lignin biosynthesis. Physiol Plant **2009** 135, 196–213.
26. Rohde A, Morreel K, Ralph J, Goeminne G, Hostyn V, Molecular phenotyping of the pal1 and pal2 mutants of Arabidopsis thaliana reveals far-reaching consequences on phenylpropanoid, amino acid, and carbohydrate metabolism. Plant Cell. **2004**, 16:2749–71.
27. Ralph J. Lignins: natural polymers from oxidative coupling of 4-hydroxyphenylpropanoids. Phytochem. Rev. **2004**, 3:29–60.

28. Nakashima J., Chen F., Jackson L., Shadle G., Dixon R.A. Multi-site genetic modification of monolignol biosynthesis in alfalfa (Medicago sativa): effects on lignin composition in specific cell types. New Phytol **2008** 179 738–750).
29. Chapple C. Molecular-genetic analysis of plant cytochrome P450-dependent monooxygenases. Annu Rev Plant Physiol Plant Mol Biol **1998**, 49, 311–343.
30. Achnine L, Blancaflor EB, Rasmussen S, Dixon RA. () Colocalization of l-phenylalanine ammonia-lyase and cinnamate 4-hydroxylase for metabolic channeling in phenylpropanoid biosynthesis. Plant Cell **2004**, 16, 3098–3109
31. Bajwa, D. S., Pourhashem, G., Ullah, A. H., & Bajwa, S. G. A concise review of current lignin production, applications, products and their environmental impact. Industrial Crops and Products, **2019**, 139, 111526.
32. Zoghlami, A., Paës, G. Lignocellulosic Biomass: Understanding Recalcitrance and Predicting Hydrolysis. Frontiers in Chemistry, **2019**, 7.
33. Constant, S., Wienk, H. L. J., Frissen, A. E., Peinder, P. de, Boelens, R., van Es, D. S.,Bruijnincx, P. C. A. New insights into the structure and composition of technical lignins: a comparative characterisation study. Green Chemistry, **2016**, 18(9), 2651–2665.
34. Tuck, C. O., Perez, E., Horvath, I. T., Sheldon, R. A., Poliakoff, M. Valorization of Biomass: Deriving More Value from Waste. Science, **2012**, 337(6095), 695–699.
35. Li, T., Takkellapati, S. The current and emerging sources of technical lignins and their applications. Biofuels, Bioproducts and Biorefining, **2018**, 12(5), 756-787.
36. Crestini, C., Lange, H., Sette, M., Argyropoulos, D. S. On the structure of softwood kraft lignin. Green Chemistry, **2017**, 19(17), 4104-4121.
37. Vishtal, A. G., Kraslawski, A. Challenges in industrial applications of technical lignins. BioResources, **2011**, 6(3), 3547-3568.
38. Jiménez, L., De la Torre, M. J., Maestre, F., Ferrer, J. L., Pérez, I. Organosolv pulping of wheat straw by use of phenol. Bioresource Technology, **1997**, 60(3), 199-205.
39. Restolho, J. A., Prates, A., de Pinho, M. N., Afonso, M. D.. Sugars and lignosulphonates recovery from eucalyptus spent sulphite liquor by membrane processes. Biomass and Bioenergy, **2009**, 33(11), 1558-1566.
40. Kaur, H., Dutt, D., & Tyagi, C. H. Optimization of soda pulping process of ligno-cellulosic residues of lemon and sofia grasses produced after steam distillation. BioResources, **2011**, 6(1), 103-120.
41. Pye, E. K., & Lora, J. H. The AlcellTM process: a proven alternative to kraft pulping. Tappi journal, **1991**, 74(3), 113-118.
42. Laurichesse, S., Avérous, L. Chemical modification of lignins: Towards biobased polymers. Progress in Polymer Science, **2014**, 39(7), 1266–1290.
43. A. Agrawal, N. Kaushik, and S. Biswas, Derivatives and Applications of Lignin – An Insight, Sci. Tech. J. **2014**,1 (7), 30
44. J. Wang, Y. Deng, Y. Qian, et al., Reduction of lignin color via one-step UV irradiation Green Chem. **2016**, 18, 695.
45. Ajao, O., Jeaidi, J., Benali, M., Restrepo, A., El Mehdi, N., & Boumghar, Y. Quantification and Variability Analysis of Lignin Optical Properties for Colour-Dependent Industrial Applications. Molecules, **2018** 23(2), 377.
46. Azadfallah, M., Mirshokraei, S. A., & Latibari, A. J. Photodegradation of Acidolysis Lignin from BCMP. Molecules, **2008**, 13(12), 3129-3139.
47. S. Y. Lin, Process for reduction of lignin color, US Pat, US4184845, 1980.
48. Zhang, H., Yu, B., Zhou, W., Liu, X., Chen, F. High-value utilization of eucalyptus kraft lignin: Preparation and characterization as efficient dye dispersant. International journal of biological macromolecules, **2018**, 109, 1232-1238.
49. Zhang, H., Liu, X., Fu, S., & Chen, Y. High-value utilization of kraft lignin: Color reduction and evaluation as sunscreen ingredient. International journal of biological macromolecules, **2019**, 133, 86-92.
50. Saritha, V., Maruthi, Y. A., & Mukkanti, K. Biological decolourization of higher concentrations of synthetic lignin by native fungi. J. Environ. Resour. Manag, **2010**, 1, 1-4.
51. Wang, J., Deng, Y., Qian, Y., Qiu, X., Ren, Y., & Yang, D. Reduction of lignin color via one-step UV irradiation. Green Chemistry, 18(3), **2016**, 695-699.
52. Mazzanti, V., & Mollica, F. A Review of Wood Polymer Composites Rheology and Its Implications for Processing. Polymers, **2020**, 12(10), 2304.
53. Nguyen, N. A., Barnes, S. H., Bowland, C. C., Meek, K. M., Littrell, K. C., Keum, J. K., & Naskar, A. K. A path for lignin valorization via additive manufacturing of high-performance sustainable composites with enhanced 3D printability. Science Advances, **2018**, 4(12), eaat4967.
54. Lewis, N. G., and Lantzy, T. R. (1989). “Chapter 2. Lignin in adhesives, in adhesives - from renewable resources,” in ACS Symposium Ser. No. 385, eds R. H. Hemingway and A. H. Conner (Washington, DC: American Chemical Society), 13–26
55. Glasser, W. G. (2000). “Chapter 9. Classification of lignin according to chemical and molecular structure,” in Lignin – Historical, Biological, and Materials Perspectives, No. 742. ACS Symposium Series, eds W. G. Glasser, R. A. Northey, and T. P. Schultz (Washington, DC: American Chemical Society), 216–238.
56. .Glasser, W. G.About Making Lignin Great Again—Some Lessons From the Past. Frontiers in Chemistry, **2019**, 7.
57. Polat, Y., Stojanovska, E., Negawo, T. A., Doner, E., & Kilic, A. Lignin as an Additive for Advanced Composites. Green Energy and Technology, **2016**, 71–89.
58. Sarika, P. R., Nancarrow, P., Khansaheb, A., & Ibrahim, T. Bio-Based Alternatives to Phenol and Formaldehyde for the Production of Resins. Polymers,**2020**, 12(10),
59. Scott G The role of antioxidants in polymer conservation. S Afr J Chem **1970**, 32:137–145.

60. Yang, J., Ching, Y., Chuah, C. Applications of Lignocellulosic Fibers and Lignin in Bioplastics: A Review. Polymers, **2019**, 11(5), 751.
61. González Sánchez C, Alvarez LA, Micromechanics of lignin/polypropylene composites suitable for industrial applications. Angew Makromol Chem. **1999**, 272:65–70.
62. Satheesh Kumar MN, Mohanty AK, Erickson L, Misra M. Lignin and its applications with polymers. J Biobased Mater Bioenergy, **2009**, 3:1–24.
63. Stiubianu G, Cazacu M, Cristea M, Vlad A, Polysiloxane-lignin composites. J Appl Polym, **2009**, Sci 113:2313–2321.
64. Gadioli R, Waldman WR, De Paoli MA, Lignin as a green primary antioxidant for polypropylene. J Appl Polym Sci.**2016**.
65. Dias OAT, Negrão DR, Silva RC, Funari CS, Cesarino I, Leao AL Studies of lignin as reinforcement for plastics composites. Mol Cryst Liq Cryst **2016**, 628:72–78
66. Diop A, Mijiyawa F, Koffi D, Kokta BV, Montplaisir D, Study of lignin dispersion in low-density polyethylene. J Thermoplast Compos Mater, **2015**, 28:1662–1674
67. Song, P., Cao, Z., Meng, Q., Fu, S., Fang, Z., Wu, Q.,Ye, J.Effect of Lignin Incorporation and Reactive Compatibilization on the Morphological, Rheological, and Mechanical Properties of ABS Resin. Journal of Macromolecular Science, Part B, **2012**, 51(4), 720–735.
68. Spiridon, I., Leluk, K., Resmerita, A. M., & Darie, R. N. Evaluation of PLA–lignin bioplastics properties before and after accelerated weathering. Composites Part B: Engineering, **2015**, 69, 342–349.
69. Spiridon, I., & Tanase, C. E. Design, characterization and preliminary biological evaluation of new lignin-PLA biocomposites. International Journal of Biological Macromolecules, **2018**, 114, 855–863.
70. Schilling, P. Lignin Amine Salt-Based Binders for Water-Based Black Ink Formulations. US Patent US05188665; Westvaco Co.,1993.
71. Belgacem, M. N.; Blayo, A.; Gandini, A. Organosolv lignin as a filler in inks, varnishes and paints. Ind. Crops Prod. **2003**, 18, 145−153
72. Caes, B.; Rivas, M.; Noirot, P. A. Printing Ink with Nitrates Lignin Ester As binder component. WO 2015/062910 A1, 2015.
73. Glasser, W. G. "Chapter 4. Cross-linking options for lignins," in Adhesives From Renewable Resources, No. 385. ACS Symposium Series, eds R. W. Hemingway and A. H. Conner (Washington, DC: American Chemical Society), **1989**, 43–54.
74. Glasser, W. G., Loos, R., Cox, B., and Cao, N. Melt-blown compostable polyester films with lignin. TAPPI J. **2017**, 16, 111–121.
75. Ponomarenko, J., Lauberts, M., Dizhbite, T., Lauberte, L., Jurkjane, V., Telysheva, G. Antioxidant activity of various lignins and lignin-related phenylpropanoid units with high and low molecular weight. Holzforschung, **2015**, 69(6), 795–805.
76. Teacă, C.-A., Roşu, D., Bodîrlău, R., and Roşu, L. "Structural changes in wood under artificial UV light irradiation determined by FTIR spectroscopy and color measurements - A brief review," BioRes. **2013**, 8(1), 1478-1507.
77. Ponomarenko, J., Dizhbite, T., Lauberts, M., Volperts, A., Dobele, G., & Telysheva, G. Analytical pyrolysis–a tool for revealing of lignin structure-antioxidant activity relationship. Journal of Analytical and Applied Pyrolysis, **2015**, 113, 360–369.
78. Qin, Z., Liu, H.-M., Gu, L.-B., Sun, R.-C., & Wang, X.-D. Lignin as a Natural Antioxidant: Property-Structure Relationship and Potential Applications. Reactive and Functional Polymers Volume One,**2020**, 65–93.
79. J. L. Espinoza-Acosta, P. I. Torres-Ch´avez, B. Ram´ırez-Wong, C. M. L´opez-Saiz and B. Montano-Leyva, Antioxidant, antimicrobial, and antimutagenic properties of technical lignins and their applications, BioResources, **2016**, 11, 5452–5481.
80. Vinardell, M. P., Ugartondo, V., Mitjans, M. Potential applications of antioxidant lignins from different sources. Industrial Crops and Products, **2008**, 27(2), 220–223.
81. Gordobil, O., Herrera, R., Yahyaoui, M., İlk, S., Kaya, M., & Labidi, J. Potential use of kraft and organosolv lignins as a natural additive for healthcare products. RSC Advances, **2018**, 8(43), 24525–24533.
82. Sadeghifar, H., & Ragauskas, A. Lignin as a UV Light Blocker—A Review. Polymers, **2020**, 12(5), 1134.
83. Gonzaga, E. R. Role of UV light in photodamage, skin aging, and skin cancer: Importance of photoprotection. American Journal of Clinical Dermatology, **2009**, 10(Suppl. 1), 19–24.
84. Nichols, J.A.; Katiyar, S.K. Skin photoprotection by natural polyphenols anti-inflammatory: Antioxidant and DNA repair mechanisms. Arch. Dermatol. Res. 2010, 302, 71–83.
85. Hanson, K.M.; Gratton, E.; Bardeen, C.J. Sunscreen enhancement of UV-induced reactive oxygen species in the skin. Free Radical. Biol. Med. **2006**, 41, 1205–1212.
86. Hattori, H.; Ide, Y.; Sano, T. Microporous titanate nanofibers for highly efficient UV-protective transparent coating. J. Mater. Chem. A 2014, 2, 16381–16388.
87. Gerlock, J.L.; Kucherov, A.V.; Smith, C.A. Determination of active HALS in automotive paint systems II: HALS distribution in weathered clearcoat/basecoat paint systems. Polym. Degrad. Stab. 2001, 73, 201–210.
88. Girois, S.; Delprat, P.; Audouin, L.; Verdu, J. Kinetic study of the photostabilisation of polypropylene films by anhydroxyphenylbenzotriazole. Polym. Degrad. Stab. **1999**, 64, 107–114.
89. Qian Y., Qiu X., and Zhu S. Sunscreen Performance of Lignin from Different Technical Resources and Their General Synergistic Effect with Synthetic Sunscreens ACS Sustainable Chem. Eng. **2016**, 4, 4029-4035.

90. Jarzycka, A.; Lewinska, A.; Gancarz, R.; Wilk, K.A. Assessment of extracts of Helichrysum arenarium Crataegus monogyna Sambucus nigra in photoprotectiveUVAand UVB; photostability in cosmetic emulsions. J. Photochem. Photobiol. B **2013**, 128, 50–57.
91. Liu, D., Li, Y., Qian, Y., Xiao, Y., Du, S., & Qiu, X. Synergistic antioxidant performance of lignin and quercetin mixtures. ACS Sustainable Chemistry & Engineering, **2017**, 5(9), 8424–8428.
92. Milczarek, G.; Nowicki, M. Carbon nanotubes/kraft lignin composite: Characterization and charge storage properties. Mater. Res. Bull. 2013, 48, 4032–4038.
93. Thakur, V.K.; Thakur, M.K.; Raghavan, P.; Kessler, P. Progress in Green Polymer Composites from Lignin for Multifunctional Applications: A Review. ACS Sustain. Chem. Eng. 2014, 2, 1072–1092.
94. Admassie, S., Ajjan, F. N., Elfwing, A., Inganäs, O. Biopolymer hybrid electrodes for scalable electricity storage. Materials Horizons, **2016**, 3(3), 174–185.
95. Ajjan, F. N., Jafari, M. J., Rębiś, T., Ederth, T., Inganäs, O. Spectroelectrochemical investigation of redox states in a polypyrrole/lignin composite electrode material. Journal of Materials Chemistry A, **2015**, 3(24), 12927–12937.
96. Leguizamon, S., Díaz-Orellana, K. P., Velez, J., Thies, M. C., Roberts, M. E. High charge-capacity polymer electrodes comprising alkali lignin from the Kraft process. Journal of Materials Chemistry A, 2015, 3(21), 11330–11339.
97. Milczarek, G. Lignosulfonate-Modified Electrode for Electrocatalytic Reduction of Acidic Nitrite. Electroanalysis, **2008**, 20(2), 211–214.
98. haleawlert-umpon, S., Berthold, T., Wang, X., Antonietti, M., Liedel, C. Kraft Lignin as Electrode Material for Sustainable Electrochemical Energy Storage. Advanced Materials Interfaces, **2017**, 4(23), 1700698.
99. Milczarek, G. Preparation, characterization and electrocatalytic properties of an iodine|lignin-modified gold electrode. Electrochimica Acta, **2009**, 54(11), 3199–3205.
100. Degefu, H., Amare, M., Tessema, M., & Admassie, S. Lignin modified glassy carbon electrode for the electrochemical determination of histamine in human urine and wine samples. Electrochimica Acta, **2014**, 121, 307–314.
101. Milczarek, G. Lignosulfonate-Modified Electrodes: Electrochemical Properties and Electrocatalysis of NADH Oxidation. Langmuir, **2009**, 25(17), 10345–10353.
102. Lu, H., Cornell, A., Alvarado, F., Behm, M., Leijonmarck, S., Li, J. Lindbergh, G. Lignin as a Binder Material for Eco-Friendly Li-Ion Batteries. Materials, **2016**, 9(3), 127.
103. Zhu, J., Yan, C., Zhang, X., Yang, C., Jiang, M., Zhang, X. A sustainable platform of lignin: From bioresources to materials and their applications in rechargeable batteries and supercapacitors. Progress in Energy and Combustion Science, **2020**, 76, 100788.
104. Westereng, B.; Cannella, D.; Agger, J.W.; Jørgensen, H.; Andersen, M.L.; Eijsink, V.G.H.; Felby, C. Enzymatic cellulose oxidation is linked to lignin by long-range electron transfer. Sci. Rep. **2015**, 5, 18561.
105. Frommhagen, M.; Mutte, S.K.; Westphal, A.H.; Koetsier, M.J.; Hinz, S.W.A.; Visser, J.; Vincken, J.-P.; Weijers, D.; van Berkel, W.J.H.; Gruppen, H.; et al. Boosting LPMO-driven lignocellulose degradation by polyphenol oxidase-activated lignin building blocks. Biotechnol. Biofuels **2017**, 10, 121.
106. L. Brenelli, F. M. Squina, C. Felby and D. Cannella,Laccase-derived lignin compounds boost cellulose oxidative enzymes AA9 Biotechnol. Biofuels, 2018, 11, 1.
107. Chen, T., Li, M., Liu, J. π–π Stacking Interaction: A Nondestructive and Facile Means in Material Engineering for Bioapplications. Crystal Growth & Design, **2018**, 18(5), 2765–2783.
108. Chipot, C.; Jaffe, R.; Maigret, B.; Pearlman, D. A.; Kollman, P. A. J. Am. Chem. Soc. **1996**, 118, 11217-11224
109. Reddy, A. S.; Vijay, D.; Sastry, G. M.; Sastry, G. N. J. Phys. Chem. B **2006**, 110, 2479-2481.
110. Headen TF, Howard CA, Skipper NT, Wilkinson MA, Bowron DT, Soper AK. Structure of pi-pi interactions in aromatic liquids. J Am Chem Soc. **2010** Apr 28;132(16):5735-42.
111. Wang, Y., Zhang, W., Li, Y., Ye, L., Yang, G. X-ray Crystal Structure of Gallium Tris- (8-hydroxyquinoline): Intermolecular π−π Stacking Interactions in the Solid State. Chemistry of Materials, **1999**, 11(3), 530–532.
112. Tsuzuki, S., Honda, K., Uchimaru, T., Mikami, M., Tanabe, K. Origin of Attraction and Directionality of the π/π Interaction: Model Chemistry Calculations of Benzene Dimer Interaction. Journal of the American Chemical Society, **2002**, 124(1), 104–112.
113. Narten, A. H. X-ray diffraction pattern and models of liquid benzene. The Journal of Chemical Physics, 67(5),**1977**, 2102.
114. Sinnokrot, M. O., & Sherrill, C. D. Unexpected Substituent Effects in Face-to-Face π-Stacking Interactions. The Journal of Physical Chemistry A, **2003**, 107(41), 8377–8379.
115. Mikulski, D., Eder, K., & Molski, M. Quantum-chemical study on stacking interactions between bioactive polyphenols (trans-resveratrol, trans-piceatannol) and ribonucleosides. Insight into minimum energy geometries of π–π stacked systems. Computational and Theoretical Chemistry, **2014**, 1046, 118–125.
116. James, T. H. (1977). The Theory of the Photographic Process, Macmillan, New York.
117. Ruwoldt, J. A Critical Review of the Physicochemical Properties of Lignosulfonates: Chemical Structure and Behavior in Aqueous Solution, at Surfaces and Interfaces. Surfaces, **2020**, 3(4), 622–648.
118. Ma, Z., Liu, C., Niu, N., Chen, Z., Li, S., Liu, S., & Li, J. Seeking Brightness from Nature: J-Aggregation-Induced Emission in Cellulolytic Enzyme Lignin Nanoparticles. ACS Sustainable Chemistry & Engineering, **2018**, 6(3), 3169–3175.
119. Xu, F., Testoff, T. T., Wang, L., & Zhou, X. Cause, Regulation and Utilization of Dye Aggregation in Dye-Sensitized Solar Cells. Molecules, **2020**, 25(19), 4478.

120. DiLabio, G. A., & Johnson, E. R.. Lone Pair−π and π−π Interactions Play an Important Role in Proton-Coupled Electron Transfer Reactions. Journal of the American Chemical Society, **2007**, 129(19), 6199–6203.
121. Batra, A., Kladnik, G., Vázquez, H., Meisner, J. S., Floreano, L., Nuckolls, C., Venkataraman, L. Quantifying through-space charge transfer dynamics in π-coupled molecular systems. Nature Communications,2012, 3. RSC advance referenza 13
122. Mishra, P.K.; Wimmer, R. Aerosol assisted self-assembly as a route to synthesize solid and hollow spherical lignin colloids and its utilization in layer by layer deposition. Ultrason. Sonochem. **2017**, 35, 45–50.
123. Xiong, F.; Han, Y.; Wang, S.; Li, G.; Qin, T.; Chen, Y.; Chu, F. Preparation and formation mechanism of size-controlled lignin nanospheres by self-assembly. Ind. Crops Prod. **2017**, 100, 146–152.
124. Salentinig, S.; Schubert, M. Softwood Lignin Self-Assembly for Nanomaterial Design. Biomacromolecules **2017**, 18, 2649–2653.
125. RAY, P. C., YU, H., FU, P. P. Toxicity and Environmental Risks of Nanomaterials: Challenges and Future Needs. Journal of Environmental Science and Health, **2009**, Part C, 27(1), 1–35.
126. Rahman, O. ur, Shi, S., Ding, J., Wang, D., Ahmad, S., Yu, H. Lignin nanoparticles: synthesis, characterization and corrosion protection performance. New Journal of Chemistry, **2018**, 42(5), 3415–3425.
127. Myint, A. A., Lee, H. W., Seo, B., Son, W.-S., Yoon, J., Yoon, T. J. Lee, Y.-W.. One pot synthesis of environmentally friendly lignin nanoparticles with compressed liquid carbon dioxide as an antisolvent. Green Chemistry, **2016**, 18(7), 2129–2146.
128. Iravani, S., Varma, R. S. Plant-Derived Edible Nanoparticles and miRNAs: Emerging Frontier for Therapeutics and Targeted Drug-Delivery. ACS Sustainable Chemistry & Engineering, **2019**, 7(9), 8055–8069.
129. Low, L. E., Teh, K. C., Siva, S. P., Chew, I. M. L., Mwangi, W. W., Chew, C. L., … Tey, B. T. Lignin nanoparticles: The next green nanoreinforcer with wide opportunity. Environmental Nanotechnology, Monitoring & Management, **2021**, 15, 100398.
130. Nypel¨o, T.E., Carrillo, C.A., Rojas, O.J.. Lignin supracolloids synthesized from (W/ O) microemulsions: use in the interfacial stabilization of Pickering systems and organic carriers for silver metal. Soft Matter **2015**, 11, 2046–2054.
131. Nair, S.S., Sharma, S., Pu, Y., Sun, Q., Pan, S., Zhu, J.Y., Deng, Y., Ragauskas, A.J.,. High shear homogenization of lignin to nanolignin and thermal stability of nanolignin-polyvinyl alcohol blends. ChemSusChem **2014**, 7, 3513–3520.
132. Gilca, I.A., Popa, V.I., Crestini, C., Obtaining lignin nanoparticles by sonication. Ultrason. Sonochem. **2015**, 23, 369–375.
133. Frangville, C., Rutkevi˘cius, M., Richter, A.P., Velev, O.D., Stoyanov, S.D., Paunov, V.N.. Fabrication of environmentally biodegradable lignin nanoparticles. ChemPhysChem **2012**,13, 4235–4243.
134. Lievonen, M.; Valle-Delgado, J.J.; Mattinen, M.-L.; Hult, E.-L.; Lintinen, K.; Kostiainen, M.A.; Paananen, A.; Szilvay, G.R.; Setälä, H.; Österberg, M. A simple process for lignin nanoparticle preparation. Green Chem. **2016**, 18, 1416–1422.
135. Leskinen, T., Smyth, M., Xiao, Y., Lintinen, K., Mattinen, M.-L., Kostiainen, M. A., Österberg, M.. Scaling Up Production of Colloidal Lignin Particles. Nordic Pulp & Paper Research Journal, **2017**, 32(4), 586–596.
136. Vitale, S. A., & Katz, J. L. Liquid Droplet Dispersions Formed by Homogeneous Liquid−Liquid Nucleation: "The Ouzo Effect." Langmuir, **2003**, 19(10), 4105–4110.
137. Ganachaud, F., Katz, J. L. Nanoparticles and Nanocapsules Created Using the Ouzo Effect: Spontaneous Emulsification as an Alternative to Ultrasonic and High-Shear Devices. ChemPhysChem, **2005**, 6(2), 209–216.
138. Lepeltier, E., Bourgaux, C., & Couvreur, P. Nanoprecipitation and the "Ouzo effect": Application to drug delivery devices. Advanced Drug Delivery Reviews, **2014**, 71, 86–97.
139. D. Horn, J. Rieger, Organic nanoparticles in aqueous phase, Angew. Chem. 40, **2001**, 4330–4361.
140. J. Aubry, F. Ganachaud, J.P. Cohen-Addad, B. Cabane, Nanoprecipitation of polymethylmethacrylate by solvent shifting: 1. Boundaries, Langmuir 25, **2009**, 1970–1979.
141. E. Matijevic, Uniform inorganic colloid dispersions. Achievements and challenges, Langmuir 10 (1994) 8–16.
142. Chen, L., Shi, Y., Gao, B., Zhao, Y., Jiang, Y., Zha, Z., … Gong, L. Lignin Nanoparticles: Green Synthesis in a γ-Valerolactone/Water Binary Solvent and Application to Enhance Antimicrobial Activity of Essential Oils. ACS Sustainable Chemistry & Engineering, **2019**, 8(1), 714–722.
143. B.K. Johnson, R.K. Prud'homme,Mechanism for rapid self-assembly of block copolymer nanoparticles, Phys. Rev. Lett. 91 (**2003**) 118302.
144. J. Molpeceres, M. Guzman, M.R. Arberturas, M. Chacon, L. Berges, Application of central composite designs to the preparation of polycaprolactone nanoparticles by solvent displacement, J. Pharm. Sci. 85 (**1996**) 206
145. Conner, C. G., Veleva, A. N., Paunov, V. N., Stoyanov, S. D., Velev, O. D. Scalable Formation of Concentrated Monodisperse Lignin Nanoparticles by Recirculation-Enhanced Flash Nanoprecipitation. Particle & Particle Systems Characterization, **2020**, 37(7), 2000122.
146. Ajdary, M., Moosavi, M. A., Rahmati, M., Falahati, M., Mahboubi, M., Mandegary, A., . Varma, R. S. Health concerns of various nanoparticles: a review of their in vitro and in vivo toxicity. *Nanomaterials*, **2018**, (9), 634.
147. Imlimthan, S., Correia, A., Figueiredo, P., Lintinen, K., Balasubramanian, V., Airaksinen, A. J., .Sarparanta, M. Systematic in vitro biocompatibility studies of multimodal cellulose nanocrystal and lignin nanoparticles. *Journal of Biomedical Materials Research Part A*, **2019**,*108*(3), 770-783.
148. Siddiqui, L., Bag, J., Seetha, Mittal, D., Leekha, A., Mishra, H, Talegaonkar, S. Assessing the potential of lignin nanoparticles as drug carrier: Synthesis, cytotoxicity and genotoxicity studies. International Journal of Biological Macromolecules, **2020**, 152, 786–802.

149. Yiamsawas, D., Baier, G., Thines, E., Landfester, K., & Wurm, F. R. Biodegradable lignin nanocontainers. RSC Adv., **2014**, 4(23), 11661–11663.
150. Chung, Y.-L., Olsson, J. V., Li, R. J., Frank, C. W., Waymouth, R. M., Billington, S. L., & Sattely, E. S. A Renewable Lignin–Lactide Copolymer and Application in Biobased Composites. ACS Sustainable Chemistry & Engineering, **2013**, 1(10), 1231–1238.
151. Rahman, M. M., Tsukamoto, J., Rahman, M. M., Yoneyama, A., Mostafa, K. M. Lignin and its effects on litter decomposition in forest ecosystems. Chemistry and Ecology, **2013**, 29(6), 540-553.
152. Peng, Z., Peralta, M. D. R., Cox, D. L., Toney, M. D. Bottom-up synthesis of protein-based nanomaterials from engineered β-solenoid proteins. PLOS ONE, **2020**, 15(2), e0229319.
153. Yamaguchi, A., Isozaki, K., Nakamura, M., Takaya, H., & Watanabe, T. Discovery of 12-mer peptides that bind to wood lignin. Scientific Reports, **2016**, 6(1).
154. Salas, C., Rojas, O. J., Lucia, L. A., Hubbe, M. A., & Genzer, J. On the surface interactions of proteins with lignin. *ACS applied materials & interfaces*, **2013**, *5*(1), 199-206.
155. Leskinen, T., Witos, J., Valle-Delgado, J. J., Lintinen, K., Kostiainen, M., Wiedmer, S. K., .Mattinen, M. L. Adsorption of proteins on colloidal lignin particles for advanced biomaterials. *Biomacromolecules*, **2017**. *18*(9), 2767-2776.
156. Richter, A. P., Bharti, B., Armstrong, H. B., Brown, J. S., Plemmons, D., Paunov, V. N., ... & Velev, O. D. Synthesis and characterization of biodegradable lignin nanoparticles with tunable surface properties. *Langmuir*, **2016**, *32*(25), 6468-6477.
157. Ball, V.; Bernsmann, F.; Betscha, C.; Maechling, C.; Kauffmann, S.; Senger, B.; Voegel J.C.; Schaaf, P.; Benkirane-Jessel N. Polyelectrolyte multilayer films built from poly(L-lysine) and a two-component anionic polysaccharide blend. Langmuir **2009**, 25, 3593-6000.
158. Cuomo, F.; Lopez, F.; Ceglie, A. Templated globules — applications and perspectives Adv. Colloid Interface Sci. **2014**, 205, 124–133.
159. Luo, H.; Shen, Q.; Ye, F.; Cheng, Y.F.; Mezgebe, M.; Qin, R.J. *Structure and properties of layer-by-layer self-assembled chitosan/lignosulfonate multilayer film.* Mater. Sci. Eng., C. **2012**, 32, 2001–2006.
160. Shutava, T.; Prouty, M.; Kommireddy, D.; Lvov, Y. pH Responsive Decomposable Layerby-Layer Nanofilms and Capsules on the Basis of Tannic Acid. Macromolecules, **2005**, 38, 2850– 2858.
161. Österberg, M., Sipponen, M. H., Mattos, B. D., & Rojas, O. J. Spherical lignin particles: a review on their sustainability and applications. *Green Chemistry*,**2020**, *22*(9), 2712-2733.
162. Zou, T., Sipponen, M. H., & Österberg, M. Natural shape-retaining microcapsules with shells made of chitosan-coated colloidal lignin particles. *Frontiers in chemistry*, **2019**, *7*, 370.
163. Sipponen, M. H., Smyth, M., Leskinen, T., Johansson, L. S., & Österberg, M. All-lignin approach to prepare cationic colloidal lignin particles: stabilization of durable Pickering emulsions. *Green Chemistry*, **2017**, *19*(24), 5831-5840.
164. De Jesús Rostro-Alanis, M., Mancera-Andrade, E. I., Patiño, M. B. G., Arrieta-Baez, D., Cardenas, B., Martinez-Chapa, S. O., & Saldívar, R. P. Nanobiocatalysis: Nanostructured materials – a minireview. Biocatalysis, **2016**, 2(1), 1–24.
165. Palonen, H.; Tjerneld. F.; Zacchi, G.; Tenkanen, M. Adsorption of Trichoderma reesei CBH I and EG II and their catalytic domains on steam pretreated softwood and isolated lignin. J. Biotechnol. **2004**, 107, 65-72.
166. Gupta, M. N., Kaloti, M., Kapoor, M., & Solanki, K. Nanomaterials as matrices for enzyme immobilization. *Artificial Cells, Blood Substitutes, and Biotechnology*, **2011**, *39*(2), 98-109.
167. Mika Henrikki Sipponen, Muhammad Farooq, Jari Koivisto2, Alessandro Pellis , Jani Seitsonen and Monika Österberg. *Spatially confined lignin nanospheres for biocatalytic ester synthesis in aqueous media*. NATURE COMMUNICATIONS | (**2018)** 9:2300
168. Qingzhi Ji, Bochu Wang, Jun Tan, Liancai Zhu, Liuying Li. Immobilized multienzymatic systems for catalysis of cascade reactions. Process Biochemistry 51 **2016**, 1193–1203.
169. Andrij Kuzmak, Sheiliza Carmali, Eric von Lieres, Alan J. Russell& Svyatoslav Kondrat. Can enzyme proximity accelerate cascade reactions? SCIENTIFIC REPOrTS , **2019**, 9:455.
170. Irlanda Lagarda-Diaz, Ana Maria Guzman-Partida and Luz Vazquez-Moreno. Legume Lectins: Proteins with Diverse Applications. Int. J. Mol. Sci. **2017**, 18, 1242.
171. M. SALEEMUDDIN and QAYYUM HUSAIN. Concanavalin A: A useful ligand for glycoenzyme immobilization--a review. Enzyme Microb. Technol., **1991**, vol. 13, April.
172. R. Victor Rebois, Peter Schuck and John K. Northup. Elucidating Kinetic and Thermodynamic Constants for Interaction of G Protein Subunits and Receptors by Surface Plasmon Resonance Spectroscopy. Methods in Enzymology Volume 344, **2002**.
173. Ghosh, S. K. Functional Coatings: By Polymer Microencapsulation; Wiley-VCH, **2006**; pp 128.
174. McShane, M. J.; Lvov, Y. M. Dekker Encyclopedia of Nanoscience and Nanotechnology; Marcel, **2004**; pp 1−16.
175. (Moon, R. J.; Martini, A.; Nairn, J.; Simonsen, J.; Youngblood, J. Cellulose nanomaterials review: structure, properties and nanocomposites. Chem. Soc. Rev. **2011**, 40, 3941−3994.
176. Cuomo, F.; Lopez, F.; Ceglie, A. Templated globules applications and perspectives Adv. Adv. Colloid Interface Sci. **2014**,205, 124−133.
177. Laugel, N.; Betscha, C.; Winterhalter, M.; Voegel, J. C.; Schaaf, P.; Ball, V. Relationship between the growth regime of polyelectrolyte multilayers and the polyanion/polycation complexation enthalpy. J.Phys. Chem. B **2006**, 110, 19443−19449.

178. Luo, H.; Shen, Q.; Ye, F.; Cheng, Y. F.; Mezgebe, M.; Qin, R. J. Structure and properties of layer-by-layer self-assembled chitosan/ lignosulfonate multilayer film. Mater. Sci. Eng., C **2012**, 32, 2001−2006.
179. Tian, D.; Hu, J.; Bao, J.; Chandra, R. P.; Saddler, J. N.; Lu, C. Lignin valorization: lignin nanoparticles as high-value bio-additive for multifunctional nanocomposites. Biotechnol. Biofuels **2017**, 10, 192−203.
180. Figueiredo, P.; Ferro, C.; Kemell, M.; Liu, Z.; Kiriazis, A.; Lintinen, K.; Florindo, H. F.; Yli-Kauhaluoma, J.; Hirvonen, J.; Kostiainen, M. A.; Santos, H. A. Functionalization of carboxylated lignin nanoparticles for targeted and pH-responsive delivery of anticancer drugs. Nanomedicine **2017**, 12, 2581−2596.
181. Qian, Y.; Qiu, X.; Zhu, S. Lignin: a nature-inspired sun blocker for broad-spectrum sunscreens. Green Chem. **2015**, 17, 320−324.
182. Zhu, H.; Stein, E. W.; Lu, Z.; Lvov, Y. M.; McShane, M. J. Synthesis of Size-Controlled Monodisperse Manganese Carbonate Microparticles as Templates for Uniform Polyelectrolyte. Chem. Mater. **2005**, 17, 2323−2328.
183. Safdar, M. N.; Kausar, T.; Jabbar, S.; Mumtaz, A.; Ahad, K.; Saddozai, A. A. Extraction and quantification of polyphenols from kinnow (Citrus reticulate L.) peel using ultrasound and maceration techniques. J. Food Drug Anal **2017**, 25, 488−500.
184. Granata, A.; Argyropoulos, D. S. 2-Chloro-4,4,5,5-tetramethyl- 1,3,2-dioxaphospholane, a Reagent for the Accurate Determination of the Uncondensed and Condensed Phenolic Moieties in Lignins. J. Agric. Food Chem. **1995**, 43, 1538−1544.
185. Melone, F.; Saladino, R.; Lange, H.; Crestini, C. Tannin Structural Elucidation and Quantitative 31P NMR Analysis. 2. Hydrolyzable Tannins and Proanthocyanidins. J. Agric. Food Chem. **2013**, 61, 9307−9315.
186. Pu, Y.; Cao, S.; Ragauskas, A. J. Application of quantitative 31P NMR in biomass lignin and biofuel precursors characterization. Energy Environ. Sci. **2011**, 4, 3154−3166.
187. Siatka, T.; Kašparová, M. Seasonal Variation in Total Phenolic and Flavonoid Contents and DPPH Scavenging Activity of Bellis perennis L. Molecules **2010**, 15, 9450−9461.
188. Li, H.; Deng, Y.; Liu, B.; Ren, Y.; Liang, J.; Qian, Y.; Qiu, X.; Li, C.; Zheng, D. Preparation of Nanocapsules via the Self-Assembly of Kraft Lignin: A Totally Green Process with Renewable Resources. ACS Sustainable Chem. Eng. **2016**, 4, 1946−1953.
189. Xiong, F.; Han, Y.; Wang, S.; Li, G.; Qin, T.; Chen, Y.; Chu, F. Preparation and Formation Mechanism of Renewable Lignin Hollow Nanospheres with a Single Hole by Self-Assembly. ACS Sustainable Chem. Eng. **2017**, 5, 2273−2281.
190. Richert, L.; La valle, P.; Payan, E.; Shu, X. Z.; Prestwich, G. D.; Stoltz, J.-F.; Schaaf, P.; Voegel, J.-C.; Picart, C. Layer by Layer Buildup of Polysaccharide Films: Physical Chemistry and Cellular Adhesion Aspects. Langmuir **2004**, 20, 448−458.
191. Gaponik, N.;Radtchenko, I. L.; Gerstenberger, M. R.; Fedutik, Y. A.; Sukhorukov, G. B.; Rogach, A. L. Labeling of Biocompatible Polymer Microcapsules with Near-Infrared Emitting Nanocrystals. Nano Lett. **2003**, 3, 369−372.
192. Lazzarotto, M.; Nome, F. Interaction of Calix[4]arene and Aliphatic Amines: A Combined NMR, Spectrophotometric and Conductimetric Investigation Braz. J. Braz. Chem. Soc. **2002**, 13, 295−299.
193. Ito, K.; Miki, H.; Ohba, Y. Interaction between acyclic phenol–formaldehyde oligomers and quaternary ammonium ions J. Yakugaku Zasshi **2002**, 122, 413−417.
194. Sionkowska, A.; Kaczmarek, B.; Lewandowska, K. Modification of collagen and chitosan mixtures by the addition of tannic acid. J. Mol. Liq. **2014**, 199, 318−323.
195. Pan, X.; Kadla, J. F.; Ehara, K. Organosolv ethanol lignin from hybrid poplar as a radical scavenger: relationship between lignin structure, extraction conditions, and antioxidant activity. J. Agric. Food Chem. **2006**, 54, 5806−5813.
196. Dizhbite, T.; Telysheva, G.; Jurkjane, V.; Viesturs, U. Characterization of the Radical Scavenging Activity of. Lignins-Natural Antioxidants. Bioresour. Technol. **2004**, 95, 309−317.
197. Rao, S.; Padmasree, Y.; Padmasree, K. Preparation and characterization of lignin nanoparticles: evaluation of their potential as antioxidants and UV protectants. J. Exp. Nanosci. **2016**, 11, 289−302.
198. Li, Z.; Ge, Y. Extraction of lignin from sugar cane bagasse and its modification into a high-performance dispersant for pesticide formulations. J. Braz. Chem. Soc. **2011**, 22, 1866−1871.
199. Sarkanen, S.; Teller, D. C.; Abramowski, E.; McCarthy, J. L. Lignin. 19. Kraft Lignin Component Conformation and Associated Complex Configuration in Aqueous Alkaline Solution. Macromolecules **1982**, 15, 1098−1104.
200. Vainio, U.; Maximova, N.; Hortling, B.; Laine, J.; Stenius, P.; Simola, L. K.; Gravitis, J.; Serimaa, R.Morphology of Dry Lignins and Size and Shape of Dissolved Kraft Lignin Particles by X-Ray Scattering. Langmuir **2004**, 20, 9736−9744.
201. Pereira, A. A.; Martins, G. F.; Antunes, P. A.; Conrrado, R.; Pasquini, D.; Job, A. E.; Curvelo, A. A. S.; Ferreira, M.; Riul, A.; Constantino, C. J. L. Lignin from Sugar Cane Bagasse: Extraction, Fabrication of Nanostructured Films, and Application. Langmuir **2007**, 23, 6652−6659.
202. Sarkanen, S.; Teller, D. C.; Stevens, C. R.; McCarthy, J. L. Lignin. 20. Associative Interactions Between Kraft Lignin Components. Macromolecules **1984**, 17, 2588−2597.
203. Qian, Y.; Qiu, X.; Zhu, S. Sunscreen Performance of Lignin from Different Technical Resources and Their General Synergistic Effect with Synthetic Sunscreens. ACS Sustainable Chem. Eng. **2016**, 4, 4029−4035.
204. Bourbonnais, R.; Paice, M. Voltammetric Measurement of Lignin in Pulp and Paper Samples An Electron Transfer Catalytic Approach with Mediators. J. Electrochem. Soc. **2004**, 151, 246−249.
205. Gülçin, İ.; Huyut, Z.; Elmastaş, M.; Aboul-Enein, H. Y. Radical scavenging and antioxidant activity of tannic acid. Arabian J. Chem. **2010**, 3, 43−53.

206. Walczak, M. M.; Dryer, D. A.; Jacobson, D. D.; Foss, M. G.; Flynn, N. T. pH Dependent Redox Couple: An Illustration of the Nernst Equation. J. Chem. Educ. **1997**, 74, 1195.
207. Ghisellini, P.; Cialani, C.; Ulgiati, S. A review on circular economy: The expected transition to a balanced interplay of environmental and economic systems. J. Clean. Prod. **2016**, 114, 11–32.
208. Kaur, R.; Uppal, S.K. Structural characterization and antioxidant activity of lignin from sugarcane bagasse. Colloid Polym. Sci. **2015**, 293, 2585–2592.
209. Li, M.F.; Sun, S.N.; Xu, F.; Sun, R.C. Microwave-assisted organic acid extraction of lignin from bamboo: Structure and antioxidant activity investigation. Food Chem. **2012**, 134, 1392–1398.
210. Hatakeyama, H.; Hatakeyama, T. Biopolymers: Lignin, Proteins, Bioactive Nanocomposites; Abe, A., Dusek, K.,Kobayashi, S., Eds.; Springer: Berlin, Germany, **2010**; Volume 232, pp. 1–63.
211. Zimniewska, M.; Batog, J.; Bogacz, E.; Romanowska, B. Functionalization of natural fibres textiles by improvement of nanoparticles fixation on their surface. J. Fiber Bioeng. Inf. **2012**, 5, 321–339.
212. Ding, J.; Gu, L.; Dong,W.; Yu, H. Epoxidation Modification of Renewable Lignin to Improve the Corrosion Performance of Epoxy Coating. Int. J. Electrochem. Sci. **2016**, 11, 6256–6265.
213. Milczarek, G.; Nowicki, M. Carbon nanotubes/kraft lignin composite: Characterization and charge storage properties. Mater. Res. Bull. **2013**, 48, 4032–4038.
214. Thakur, V.K.; Thakur, M.K.; Raghavan, P.; Kessler, P. Progress in Green Polymer Composites from Lignin for Multifunctional Applications: A Review. ACS Sustain. Chem. Eng. **2014**, 2, 1072–1092.
215. Myint, A.A.; Lee, H.W.; Seo, B.; Son, W.-S.; Yoon, J.; Yoon, T.J.; Park, H.J.; Yu, J.; Yoon, J.; Lee, Y.-W. One pot synthesis of environmentally friendly lignin nanoparticles with compressed liquid carbon dioxide as an antisolvent. Green Chem. **2016**, 18, 2129–2146.
216. Zhang, S.; Jiang, Z.;Wang, X.; Yan, C.; Shi, J. A facile method to prepare microcapsules inspired by polyphenol chemistry for efficient enzyme immobilization. ACS Appl. Mater. Interface. **2015**, 7, 19570–19578.
217. Bezerra, C.S.; Gentil de Farias Lemos, M.G.; de Sousa, M.; Barros Goncalves, L.R. Ezyme immobilization onto renewable polymeric matrixes: Past, present, and future trends. J. Appl. Polym. Sci. **2015**, 42125, 1–15.
218. Frommhagen, M.; Koetsier, M.J.; Westphal, A.H.; Visser, J.; Hinz, S.W.A.; Vincken, J.-P. Lytic Polysaccharide monooxygenase from Myceliophthora thermophila C1 differ in substrate preference and reducing agent specificity. Biotechnol. Biofuels **2016**, 9, 186.
219. Fiorentino, D.; Gallone, A.; Fiocco, D.; Palazzo, G.; Mallardi, A. Mushroom tyrosinase in polyelectrolyte multilayers as an optical biosensor for o-diphenols. Biosens. Bioelectron. **2010**, 25, 2033–2037.
220. Yin, H.; Zhou, Y.; Xu, J.; Ai, S.; Cui, L.; Zhu, L. Amperometric biosensor based on tyrosinase immobilized onto multiwalled carbon nanotubes-cobalt phthalocyanine-silk fibroin film and its application to determine bisphenol A. Anal. Chim. Acta **2010**, 659, 144–150.
221. Dinçer, A.; Becerik, S.; Aydemir, T. Immobilization of tyrosinase on chitosan–clay composite beads. Int. J. Biol. Macromol. **2012**, 50, 815–820.
222. Guazzaroni, M.; Crestini, C.; Saladino, R. Layer-by-Layer coated tyrosinase: An efficient and selective synthesis of catechols. Bioorg. Med. Chem. **2012**, 20, 157–166.
223. Guazzaroni, M.; Pasqualini, M.; Botta, G.; Saladino, R. A Novel Synthesis of Bioactive Catechols by Layer-by-Layer Immobilized Tyrosinase in an Organic Solvent Medium. Chem. Cat. Chem. **2012**, 4, 89–99.
224. Subrizi, F.; Crucianelli, M.; Grossi, V.; Passacantando, M.; Pesci, L.; Saladino, R. Carbon Nanotubes as Activating Tyrosinase Supports for the Selective Synthesis of Catechols. ACS Catal. **2014**, 4, 810–822.
225. Bozzini, T.; Botta, G.; Delfino, M.; Onofri, S.; Saladino, R.; Amatore, D.; Sgarbanti, R.; Nencioni, L.; Palamara, A.T. Tyrosinase and Layer-by-Layer supported tyrosinases in the synthesis of lipophilic catechols with antiinfluenza activity. Bioorg. Med. Chem. **2013**, 21, 7699–7708.
226. Botta, L.; Bizzarri, B.M.; Crucianelli, M.; Saladino, R. Advances in biotechnological synthetic applications of carbon nanostructured systems. J. Mater. Chem. B **2017**, 5, 6490–6510.
227. Ismaya, W.T.; Rozeboom, H.J.; Schurink, M.; Boeriu, C.G.; Wichers, H.; Dijkstra, B.W. Crystallization and preliminary X-ray crystallographic analysis of tyrosinase from the mushroom Agaricus bisporus. Acta Crystallogr. **2011**, 67, 575–578.
228. El Hage, R.; Brosse, N.; Chrusciel, L.; Sanchez, C.; Sannigrahi, P.; Rag, A. Characterization of milled wood lignin and ethanol organosolv lignin from Miscanthus. Polym. Degrad. Stab. **2009**, 94, 1632–1638.
229. Hu, J.; Shen, D.;Wu, S.; Zhang, H.; Xiao, R. Composition Analysis of Organosolv Lignin and Its Catalytic Solvolysis in Supercritical Alcohol. Energy Fuels **2014**, 28, 4260–4266.
230. Granata, A.; Argyropoulos, D.S. 2-Chloro-4,4,5,5-tetramethyl-1,3,2-dioxaphospholane, a Reagent for the Accurate Determination of the Uncondensed and Condensed Phenolic Moieties in Lignins. J. Agric. Food Chem. **1995**, 43, 1538–1544.
231. Lu, F.; Ralph, J. The DFRC method for lignin analysis. 2. Monomers from isolated lignins. J. Agric. Food Chem. **1998**, 46, 547–552.
232. Jiang, C.; He, H.; Jiang, H.; Ma, L.; Jia, D.M. Nano-lignin filled natural rubber composites: Preparation and characterization. Express Polym. Lett. **2013**, 7, 480–493.
233. Cho, S.J.; Kwon, H.S. Tyrosinase Inhibitory Activities of Safrole from Myristica fragrans Houtt. J. Appl. Biol. Chem. **2015**, 58, 295–301.
234. Malik, A.; Khan, M.T.H.; Khan, S.B.; Ahmad, A.; Choudhary, M.I. Tyrosinase inhibitory lignans from the methanol extract of the roots of Vitex negundo Linn and their structure-activity relationship. Phytomedicine **2006**, 13, 255–260-

235. Grönqvist, S.; Viikari, L.; Niku-Paavola, M.-L.; Orlandi, M.; Canevali, C.; Buchert, J. Oxidation of milled wood lignin with laccase, tyrosinase and horseradish peroxidase. Appl. Microbiol. Biotechnol. **2005**, 67, 489–494.
236. Min, K.; Yum, T.; Kim, J.; Woo, H.M.; Kim, Y.; Sang, B.-I.; Yoo, Y.J.; Kim, Y.H.; Um, Y. Perspectives for biocatalytic lignin utilization: Cleaving 4-O-5 and Ca-Cb bonds in dimeric lignin model compounds catalysed by a promiscuous activity of tyrosinase. Biotech. Biofuels **2017**, 10, 212.
237. Cienska, M.; Labus, K.; Lewa´ nczuk, M.; Ko´zlecki, T.; Liesiene, J.; Bryjak, J.; Legault, C. Effective L-Tyrosine hydroxylation of native and immobilized tyrosinase. PLoS ONE **2016**, 11, e0164213.
238. Dai, L.; Liu, R.; Hu, L.-Q.; Zou, Z.-F.; Si, C.-L. Lignin Nanoparticle as a Novel Green Carrier for the Efficient Delivery of Resveratrol. ACS Sustain. Chem. Eng. **2017**, 5, 8241–8249.
239. Figueiredo, P.; Lintinen, K.; Kiriazis, A.; Hynninen, V.; Liu, Z.; Bauleth-Ramos, T.; Yli-Kauhaluoma, J. In vitro evaluation of biodegradable lignin-based nanoparticles for drug delivery and enhanced antiproliferation effect in cancer cells. Biomaterials **2017**, 121, 97–108.
240. Li, Y.; Qiu, X.; Qian, Y.; Xiong, W.; Yang, D. pH-responsive lignin-based complex micelles: Preparation, characterization and application in oral drug delivery. Chem. Eng. J. **2017**, 327, 1176–1183.
241. Caluey, A.N.;Wilson, J.N. Functionalized lignin biomaterials for enhancing optical properties and cellular interactions of dyes. Biomater. Sci. **2017**, 5, 2114–2121.
242. Hattori, Y.; Sakaguchi, M.; Maitani, Y. Folate-linked lipid-based nanoparticles deliver a NFB decoy into activated murine macrophage-like RAW264 7 cells. Biol. Pharm. Bull. **2006**, 29, 1516–1520.
243. Donaldson, L.A.; Radotic, K. Fluorescence lifetime imaging of lignin autofluorescence in normal and compression wood. J. Microsc. **2013**, 251, 178–187.
244. Piccinino, D.; Delfino, M.; Botta, G.; Crucianelli, M.; Grossi, V.; Passacantando, M.; Saladino, R. Highly efficient synthesis of aldehydes by layer-by-layer multi-walled carbon nanotubes (MWCNTs) laccase mediator systems. Appl. Catal. A Gen. **2015**, 499, 77–88.
245. Pillai, K.V.; Renneckar, S. Cation p-interactions as a mechanism in technical lignin adsorption to cationic surfaces. Biomacromolecules **2009**, 10, 798–804.
246. Shah, S.; Solanki, K.; Gupta, M.N. Enhancement of lipase activity in non-aqueous media upon immobilization on multi-walled carbon nanotubes. Chem. Cent. J. **2007**, 1, 1–30.
247. Masamoto, Y.; Kubo, M. Inhibitory effect of Chinese crude drugs on tyrosinase. Planta Med. **1980**, 40, 361–365.
248. Arslan, A.; Kiralp, S.; Toppare, L.; Yagci, Y. Immobilization of tyrosinase in polysiloxane/polypyrrole copolymer matrices. Int. J. Biol. Macromol. **2005**, 35, 163–167.
249. Tischer, W. Immobilized enzymes: Crystals or carriers? Trends Biotechnol. **1999**, 117, 326–335.
250. Fernández-Mar, M.I.; Mateos, R.; García-Parrilla, M.C.; Puertas, B.; Cantos-Villar, E. Bioactive compounds in wine: Resveratrol, hydroxytyrosol and melatonin: A review. Food Chem. **2012**, 130, 797–813.
251. Lekse, J.; Xia, L.; Stark, J.; Morrow, J.D.; May, J.M. Plant catechols prevent lipid peroxidation in human plasma and erythrocytes. Mol. Cell. Biochem. **2001**, 226, 89–95.
252. Farhoosh, R.; Johnny, S.; Asnaashari, M.; Molaahmadibahraseman, N.; Sharif, A. Structure–antioxidant activity relationships of o-hydroxyl, o-methoxy, and alkyl ester derivatives of p-hydroxybenzoic acid. Food Chem. **2016**, 194, 128–134.
253. Nolan, L.C.; O'Connor, K.E. Dioxygenase-and monooxygenase-catalysed synthesis of cis-dihydrodiols, catechols, epoxides and other oxygenated products. Biotechnol. Lett. **2008**, 30, 1879–1891.
254. Bradshaw, M.P.; Barril, C.; Clark, A.C.; Prenzler, P.D.; Scollary, G.R. Ascorbic acid: A review of its chemistry and reactivity in relation to a wine environment. Crit. Rev. Food Sci. Nutr. **2011**, 51, 479–498.
255. Xie, J.G.; Li, S.B.; Xue, Y.; Zhang, H.T.; Quan, J.; Nie, H.L.; Branford-White, C. 4-Hydroxyphenylacetic Acid as a Monophenolase Inhibitor and a Diphenolase Activator on Mushroom Tyrosinase. In Proceedings of the 3rd International Conference on Bioinformatics and Biomedical Engineering, Beijing, China, 11–13 June **2009**.
256. F. Xiong, Y. Han, S. Wang, G. Li, T. Qin, Y. Chen and F.Chu, Ind. Crops Prod., **2017**, 100, 146.
257. Y. Qian, X. Zhong, Y. Li and X. Qiu, Ind. Crops Prod.,**2017**, 101, 54.
258. F. R. Wurm and C. K. Weiss, Front. Chem., **2014**, 2, 49.
259. J. J. Richardson, M. Björnmalm and F. Caruso, Science, **2015**, 348, 2491.
260. D. Piccinino, E. Capecchi, L. Botta, B. M. Bizzarri, P. Bollella, R. Antiochia and R. Saladino, Biomacromolecules, **2018**, 19, 3883.
261. K. Piontek, M. Antorini and T. Choinowski, J. Biol. Chem.,**2002**, 277, 37663.
262. S. Shleev, A. Jarosz-Wilkolazka, A. Khalunina, O. Morozova, A. Yaropolov, T. Ruzgas and L. Gorton, Bioelectrochemistry, **2005**, 67, 115.
263. A. M. Mayer and R. C. Staples, Phytochemistry, **2002**, 60, 551
264. E. I. Solomon, U. M. Sundaram and T. E. Machonkin, Chem.Rev., **1996**, 96, 2563.
265. B. Viswanath, B. Rajesh, A. Janardhan, A. P. Kumar and G. Narasimha, Enzyme Res., **2014**, 2014, 163242.
266. J. R. Jeon, P. Baldrian, K. Murugesan and Y. S. Chang, Microb. Biotechnol., **2012**, 5, 318.
267. C. Crestini, F. Melone and R. Saladino, Bioorg. Med. Chem., **2011**, 19, 5071.
268. T. Kudanga and M. Le Roes-Hill, Appl. Microbiol. Biotechnol., **2014**, 98, 6525.
269. R. Bourbonnais, D. Leech and M. G. Paice, Biochim. Biophys. Acta, Gen. Subj., **1998**, 3, 381.
270. H. P. Call and I. Mücke, J. Biotechnol., **1997**, 53, 163.
271. C. Crestini, R. Perazzini and R. Saladino, Appl. Catal., A, **2010**, 1, 138.
272. S. Ba, A. Arsenault, T. Hassani, J. P. Jones and H. Cabana, Crit. Rev. Biotechnol., **2013**, 33, 404.

273. L. Botta, B. M. Bizzarri, M. Crucianelli and R. Saladino, J. Mater. Chem. B, **2017**, 5, 6490.
274. Z. Gao, Y. Yi, J. Zhao, Y. Xia, M. Jiang, F. Cao, H. Zhou, P. Wei, H. Jia and X. Yong, Bioresour. Bioprocess., **2018**, 5, 1.
275. J. Muzart, Tetrahedron, **2003**, 59, 5789.
276. S. S. Stahl, Angew. Chem., Int. Ed., **2004**, 43, 3400.
277. G. Milczarek and M. Nowicki, Mater. Res. Bull., **2013**, 48,4032.
278. . V. Gnedenkov, S. L. Sinebryukhov, D. P. Opra, L. A. Zemnukhova, A. K. Tsvetnikov, A. N. Minaev, A. A. Sokolov and V. I. Sergienko, Procedia Chem., **2014**, 11, 96.
279. C. Lin, C. Cheng, H. Dai, Y. Chung, Y. Ai, C. Chen and L. Wu, BioMed Res. Int., **2018**, 2018, 1.
280. E. Capecchi, D. Piccinino, I. Delfino, P. Bollella, R. Antiochia and R. Saladino, Nanomaterials, **2018**, 8, 438.
281. M. L. Mattinen, J. J. Valle-Delgado, T. Leskinen, T. Anttila, G. Riviere, M. Sipponen, A. Paananen, K. Lintinen, M.Kostiainen and M. Österberg, Enzyme Microb. Technol., **2018**, 111, 48.
282. D. R. Walt and V. I. Agayn, TrAC, Trends Anal. Chem., **1994**, 10.
283. C. Leitner, J. Hess, C. Galhaup, R. Ludwig, B. Nidetzky, K. D. Kulbe and D. Haltrich, Appl. Biochem. Biotechnol., **2002**, 98, 497.
284. S. Rouhani, A. Rostami and A. Salimi, RSC Adv., **2016**, 32,26709.
285. X. Yuan, G. Tian, Y. Zhao, L. Zhao, H. Wang and T. B. Ng, Molecules, **2016**, 21, 203.
286. L. Dai, R. Liu, L. Q. Hu, Z. F. Zou and C. L. Si, ACS Sustainable Chem. Eng., **2017**, 5, 8241.
287. P. Venkatesan, R. Manavalan and K. Valliappan, J. Pharm. Sci. Res., **2009**, 14, 26.
288. M. N. Singh, K. S. Y. Hemant, M. Ram and H. G. Shivakumar, Res. Pharm. Sci., **2010**, 5, 65.
289. K. Tsuiji, J. Microencapsulation, **2001**, 18, 137.
290. T. Kurosaki, T. Kitahara, S. Fumoto, K. Nishida, K. Yamamoto,H. Nakagawa, Y. Kodama, N. Higuchi, T. Nakamura and H. Sasaki, J. Pharm. Pharm. Sci., **2010**, 13, 351.
291. K. G. H. Desai and H. J. Park, Drying Technol., **2005**, 23,1361.
292. D. Yiamsawas, G. Baier, E. Thines, K. Landfester and F. R. Wurm, RSC Adv., **2014**, 23, 11661.
293. J. K. Saini, A. K. Patel, M. Adsul and R. R. Singhania, Renewable Energy, **2016**, 98, 29.
294. C. Salas, O. J. Rojas, L. A. Lucia, M. A. Hubbe and J. Genzer, ACS Appl. Mater. Interfaces, **2013**, 5, 199.
295. F. Xiong, Y. Han, S. Wang, G. Li, T. Qin, Y. Chen and F. Chu, ACS Sustainable Chem. Eng., **2017**, 5, 2273.
296. J. Azimvand, K. Didehban and S. A. Mirshokrai, BioResources, **2018**, 13, 2887.
297. A. Franco, S. Cebrián-García, D. Rodríguez-Padrón, A. R. Puente-Santiago, M. J. Munoz-Batista, A. Caballero, A. M. Balu, A. A. Romero and R. Luque, ACS Sustainable Chem. Eng., **2018**, 6, 11058.
298. A. I. El-Batal, N. M. Elkenawy, A. S. Yassin and M. A. Amin, Biotechnol. Rep., **2015**, 5, 31.
299. M. Hatada, N. Loew, Y. Inose-Takahashi, J. Okuda-Shimazaki, W. Tsugawa, A. Mulchandani and K. Sode, Bioelectrochemistry, **2018**, 121, 185.
300. S. Park, J. E. Jeong, V. S. Le, J. Seo, B. Yu, D. Y. Kim, S. H. Kwon, S. Jon, H. Y. Woo and H. Yang, J. Am. Chem. Soc.,**2018**, 140, 2409.
301. T. Rajh and J. Rabani, Langmuir, **1991**, 7, 2054.
302. S. Shankar, J. P. Reddy and J. W. Rhim, Int. J. Biol. Macromol., **2015**, 81, 267.
303. M. Ago, B. L. Tardy, L. Wang, J. Guo, A. Khakalo and O. J. Rojas, MRS Bull., **2017**, 42, 371.
304. R. B. Bird, W. E. Stewart and E. N. Lightfoot, Transport Phenomena, Revised, 2nd edn, **1961**.
305. I. W. C. E. Arends, Y. X. Li, R. Ausan and R. A. Sheldon,Tetrahedron, 2006, 62, 6659.
306. S. A. Tromp, I. Matijošyte, R. A. Sheldon, I. W. C. E. Arends, G. Mul, M. T. Kreutzer, J. A. Moulijn and S. De Vries, ChemCatChem, **2010**, 2, 827
307. C. Eggert, U. Temp, J. F. D. Dean and K. E. L. Eriksson, FEBS Lett., **1996**, 391, 144.
308. R. Anderson, K. Griffin, P. Johnston and P. L. Alsters, Adv. Synth. Catal., **2003**, 345, 517.
309. R. Sarma, M. S. Islam, A. F. Miller and D. Bhattacharyya, ACS Appl. Mater. Interfaces, **2017**, 9, 17.
310. F. Zheng, B. K. Cui, X. J. Wu, G. Meng, H. X. Liu and J. Si, Int. Biodeterior. Biodegrad., **2016**, 110, 69.
311. P. Baiocco, A. M. Barreca, M. Fabbrini, C. Galli and P. Gentili, Org. Biomol. Chem., **2003**, 1, 191.
312. M. Fabbrini, C. Galli and P. Gentili, J. Mol. Catal. B: Enzym.,**2002**, 16, 231.
313. A. Cecchetto, F. Fontana, F. Minisci and F. Recupero, Tetrahedron Lett., **2001**, 42, 6651
314. S. Kawai, T. Umezawa and T. Higuchi, Wood Res., **1989**, 76,10.
315. De Souza, W.F.; Guimaraes, I.; Guerreiro, M.C.; Oliveira, L.C.A. Catalytic oxidation of sulfur and nitrogen compounds from diesel fuel. Appl. Catal. A General **2009**, 360, 205–209.
316. Zannikos, F.; Lois E.; Stournas, S. Desulfurization of petroleum fractions by oxidation and solvent extraction. Fuel Process. Technol. **1995**, 42, 35–45.
317. Ismagilov, Z.; Yashnik, S.; Kerzhentsev, M.; Parman, V.; Bourane, A.; Al-Shahrani, F.M.; Haji, A.A.; Koseoglu, O.R. Oxidative desulfurization of hydrocarbon fuels. Catal. Rev. Sci. Eng. **2011**, 53, 199–255.
318. Gatan, R.; Barger, P.; Gembicki, V.; Cavanna, A.; Molinari, D. Oxidative desulfurization: a new technology for ULSD. Am. Chem. Soc. Div. Fuel Chem. **2004**, 49, 577–579.
319. Li, J.; Yang, Z.; Li, S.; Jin, Q.; Zhao, J. Review on oxidative desulfurization of fuel by supported heteropolyacid catalysts J. ind.eng. chem. **2020**, 82, 1–16.
320. Hossain, M.N.; Park, H.C.; Choi, H.S. A comprehensive review on catalytic oxidative desulfurization of liquid fuel oil. Catalysts **2019**, 9, 229.

321. Crucianelli, M.; Bizzarri, B.M.; Saladino R. SBA-15 Anchored Metal Containing Catalysts in the Oxidative Desulfurization Process. Catalysts **2019**, 9, 984–1015.
322. Houda, S.; Lancelot, C.; Blanchard, P.; Poinel, L.; Lamonier, C. Oxidative desulfurization of heavy oils with high sulfur content: A review. Catalysts **2018**, 8, 344.
323. Sikarwar, P.; Gosu, V.; Subbaramaiah, V. An overview of conventional and alternative technologies for the production of ultra-low-sulfur fuels. Rev. Chem. Eng. **2019**, 35, 669–705.
324. Mjalli, F.S.; Ahmed, O.U.; Al-Wahaibi, T.; Al-Wahaibi, Y.; Al-Nashef, I.M. Deep oxidative desulfurization of liquid fuels. Rev. Chem. Eng. **2014**, 30, 337–378.
325. Saladino, R.; Botta, G.; Crucianelli, M. Advances in Nanostrostructured Transition Metal Catalysis Applied to Oxidative Desulfurization. Applying Nanotechnology to the Desulfurization Process in Petroleum Engineering, Tawfik A. Saleh (Ed.), IGI Global: Hershey, PA, USA, **2016**; pp.180-215.
326. Piccinino D.; Abdalghani I.; Botta G.; Crucianelli M.; Passacantando M.; Di Vacri, M.L.; Saladino R. Preparation of wrapped carbon nanotubes poly(4-vinylpyridine)/MTO based heterogeneous catalysts for the oxidative desulfurization (ODS) of model and synthetic diesel fuel. Appl. Catal. B-Environ. **2017**, 200, 392–401.
327. Di Giuseppe, A.; Crucianelli, M.; De Angelis, F.; Crestini, C.; Saladino, R. Efficient Oxidation of Thiophene Derivatives with Homogeneous and Heterogeneous MTO/H2O2 systems: a novel approach for Oxidative Desulfurization (ODS) of Diesel Fuel. Appl.Catal. B-Environ. **2009**, 89, 239–245.
328. Davoodi-Dehaghania, F.; Vosoughi, M.; Ziaee, A.A. Biodesulfurization of dibenzothiophene by a newly isolated Rhodococcus erythropolis strain. *Bioresour. Technol*. **2010**, *101*, 1102–1105.
329. Wang, P.; Humphrey, A.E.; Krawiec, S. Kinetic Analyses of Desulfurization of Dibenzothiophene by Rhodococcus erythropolis in Continuous Cultures. *Appl. Environ. Microbiol.* **1996**, *62*, 3066–3068.
330. Chang, J.H.; Chang, Y.K.; Cho, K.; Chang, H.N.; Desulfurization of model and diesel oils by resting cells of Gordona sp. *Biotechnol. Lett*. **2000**, *22*, 193–196.
331. Villaseňor, F.; Loera, O.; Campero, A.; Viniegra-Gonzàlez, G. Oxidation of dibenzothiophene by laccase or hydrogen peroxide and deep desulfurization of diesel fuel by the later. Fuel Process. Technol. **2004**, 86, 49–59.
332. Bressler, D.C.; Fedorak, P.M.; Pickard, M.A. Oxidation of carbazole, N-ethylcarbazole, fluorene, and dibenzothiophene by the laccase of Coriolopsis gallica. Biotechnol. Letters **2000**, 14, 1119–1125.
333. Klyachko, N.L.; Klibanov, A.M.; Oxidation of dibenzothiophene catalyzed by hemoglobin and other hemoproteins in various aqueous– organic media. Appl. Biochem. Biotechnol. **1992**, 37, 53–68.
334. Vazquez-Duhalt, R.; Westlake, D.W.S.; Fedorak, P.M. Lignin Peroxidase Oxidation of Aromatic Compounds in Systems Containing Organic Solvents. Appl. Env. Micr. **1994**, 60, 459–466.
335. Eibes, G.; Cajthaml, T.; Moreira, M.T. Feijoo, J.; Lema, J.M. Enzymatic degradation of anthracene, dibenzothiophene and pyrene by manganese peroxidase in media containing acetone. Chemosphere **2006**, 64, 408–414.
336. Ichinose, H.; Wariishi, H.; Tanaka, H. Effective oxygen transfer reaction catalyzed by microperoxidase-11 during sulfur oxidation of dibenzothiophene. Enzyme Microb. Technol. **2002**, 30, 334–339.
337. Ayala, M.; Tinoco, R.; Hernandez, V.; Bremauntz, P.; Vazquez-Duhalt, R. Biocatalytic oxidation of fuel as an alternative to biodesulfurization. Fuel Process. Technol. **1998**, 57, 101–111.
338. Doerge, D.R.; Cooray, N.M.; Brewster, M.E. Peroxidase-catalyzed S-oxygenation: mechanism of oxygen transfer for lactoperoxidase. Biochemistry **1991**, 30, 8960.
339. Stachyra, T.; Guillochon, D.; Pulvin, S.; Thomas, D. Hemoglobin, horseradish peroxidase, and heme-bovine serum albumin as biocatalyst for the oxidation of dibenzothiophene. Appl. Biochem. Biotech. **1996**, 59, 231–244.
340. Da Silva Madeira, L.; Ferreira-Leitaŏ, V.S.; da Silva Bon, E.P. Dibenzothiophene oxidation by horseradish peroxidase in organic media: Effect of the DBT:H2O2 molar ratio and H2O2 addition mode. Chemosphere **2008**, 71, 189–194.
341. Bhasarkar, J.; Borah, A.J.; Goswami, P.; Moholkar, V.S. Mechanistic analysis of ultrasound assisted enzymatic desulfurization of liquid fuels using horseradish peroxidase. Bioresour. Technol. **2015**, 196, 88–98.
342. Ayala, M.; Verdin, J.; Vazquez-Duhalt, R. The prospects for peroxidase-based biorefining of petroleum fuels. Biocatal. Biotransform. **2007**, 25, 114–129.
343. Terrès, E.; Montiel, M.; Le Borgne, S.; Torres, E. Immobilization of chloroperoxidase on mesoporous materials for the oxidation of 4,6-dimethyldibenzothiophene, a recalcitrant organic sulfur compound present in petroleum fractions. Biotechnol. Lett. **2008**, 30, 173–179.
344. Wu, S.; Lin, J.; Chan, S. Oxidation of dibenzothiophene catalyzed by heme-containing enzymes encapsulated in sol-gel glass. Appl. Biochem. Biotechnol. **1994**, 47, 11–20.
345. Li, Y.; Huang, X.; Qu, Y. A strategy for efficient immobilization of laccase and horseradish peroxidase on single-walled carbon nanotubes. J. Chem. Technol. Biotechnol. **2013**, 88, 2227–2232.
346. Juarez-Moreno, K.; Díaz de León, J.N.; Zepeda, T.A.; Vazquez-Duhalt, R.; Fuentes, S. Oxidative transformation of dibenzothiophene by chloroperoxidase enzyme immobilized on (1D)-γ-Al2O3 nanorods J. Mol. Catal. B-enzym. **2015**, 115, 9095.
347. Mateo, C.; Palomo, J.M.; Fernandez-Lorente, G.; Guisan, J.M.; Fernandez-Lafuente, R. Improvement of enzyme activity, stability and selectivity via immobilization techniques. Enzyme Microb. Technol. **2007**, 40, 1451–1463.
348. Piccinino, D.; Capecchi, E.; Botta, L.; Bollella, P.; Antiochia, R.; Crucianelli, M.; Saladino, R. Layer by layer supported laccase on lignin nanoparticles catalyzes the selective oxidation of alcohols to aldehydes. Catal. Sci. Technol. **2019**, 9, 4125–4134.

349. Ortiza, E.; Gallay, P.; Galicia, L.; Eguílaz, M.; Rivas, G. Nanoarchitectures based on multi-walled carbon nanotubes non-covalently functionalized with Concanavalin A: A new building-block with supramolecular recognition properties for the development of electrochemical biosensors. Sens. And Actuators B: Chem. **2019**, 292, 254–262.
350. Liu, Y.; Yu. J. Oriented immobilization of proteins on solid supports for use in biosensors and biochips: a review. Microchim. Acta. **2016**, 183, 1–19.
351. Makky, A.; Michel, J.P.; Maillard, P.; Rosilio V. Biomimetic liposomes and planar supported bilayers for the assessment of glycodendrimeric porphyrins interaction with an immobilized lectin. Biochim. Biophys. Acta. Rev. Biomembr. **2011**, 1808, 656–666.
352. Zhang, Y.; Yong, Y.; Ge, J.; Liu, Z. Lectin agglutinated multienzyme catalyst with enhanced substrate affinity and activity. ACS Catal. **2016**, 6, 3789–3795.
353. Huang, J.; Zhuang, W.; Wei, C.; Mu, L.; Zhu, J.; Zhu, Y.; Jinglan, W.; Yong, C.; Ying, H. Concanavalin A induced orientation immobilization of Nuclease P1: The effect of lectin agglutination. Process Biochem. **2018**, 64, 160–169.
354. Yong, Y.; Su, R.; Liu, X.; Xu, W.; Zhang, Y.; Wang, R.; Ouyang, P.; Wu, J.; Ge, J.; Liu, Z. Lectin corona enhances enzymatic catalysis on the surface of magnetic nanoparticles. Biochem. Eng. J. **2018**, 129, 26–32.
355. Xu, X.; Yuan, Y.; Guixian, H.; Wang X.; Qi, P.; Wang, Z.; Wang, Q.; Wang, X.; Fu, Y.; Li, Y.; Yang, H.Exploiting pH-Regulated Dimer- Tetramer Transformation of Concanavalin A to Develop Colorimetric Biosensing of Bacteria. Sci. Rep. **2017,** 7, 2045–2322.
356. Xu, W.; Yong, Y.; Wang, Z.; Jiang, G.; Wu, J.; Liu, Z. Concanavalin A Coated Activated Carbon for High Performance Enzymatic Catalysis. ACS Sustainable Chem. Eng. **2017**, 5, 90–96.
357. Rong, J.; Zhou, Z.; Wang, Y.; Han, J.; Li, C.; Zhang, W.; Ni, L. Immobilization of Horseradish Peroxidase on Multi-Armed Magnetic Graphene Oxide Composite: Improvement of Loading Amount and Catalytic Activity. Food Technol. Biotech. **2019**, 57, 1330–1334.
358. Zhang, F.; Wang, M.; Liang, C.; Jiang, H.; Shen, J.; Li, H. Thin-Layer Polymer Wrapped Enzymes Encapsulated in Hierarchically Mesoporous Silica with High Activity and Enhanced Stability. Sci. Rep. **2014**, 4, 4421.
359. Tischer, W. Immobilized enzymes: Crystals or carriers? Trends Biotechnol. **1999**, 117, 326–335.
360. Won, K.; Kim, Y.H.; An, E.S.; Lee, Y.S.; Song, B.K. Horseradish Peroxidase-Catalyzed Polymerization of Cardanol in the Presence of Redox Mediators. Biomacromolecules **2004**, 5, 1–4.
361. Razola, S.S.; Aktas, E.; Viré, J.-C.;Kauffmann, J.-M. Reagentless enzyme electrode based on phenothiazine mediation of horseradish peroxidase for subnanomolar hydrogen peroxide determination. Analyst **2000**, 125, 79–85.
362. Saladino, R.; Guazzaroni, M.; Crestini, C.; Crucianelli, M. Dye Degradation by Layer-by-Layer Immobilised Peroxidase/Redox Mediator Systems. ChemCatChem **2013**, 5, 1407–1415.
363. Robert, T. Green ink in all colors'□printing ink from renewable resources. Prog. Org. Coat. **2015**, 78, 287−292.
364. Leach, R. H. The printing ink manual, 5th ed.; Springer: Dordrecht, **2007**.
365. Kipphan, H. Handbuch der Printmedien; Springer Verlag: Heidelberg, **2000**.
366. Park, J. M.; Kim, Y. H.; Kim, S. B. Development of Solvent-Free Offset Ink Using Vegetable Oil Esters and High Molecular Weight Resin. J. Oleo Sci. **2013**, 62, 345−352.
367. Roy, A. S.; Bhattacharjee, M.; Mondal, R.; Ghosh, S. Development of Mineral Oil Free Offset Printing Ink Using Vegetable Oil Esters. J. Oleo Sci. **2007**, 56, 623−628.
368. Karlberg, A. T. In Colophony: Rosin in Unmodified and Modified Form. In Occupational Dermatology; Springer: Berlin, Heidelberg, **2012**.
369. Erhan, S. Z.; Bagby, M. O. Vegetable Oil-based Printing Ink. US Patent US05122188, **1992**.
370. Mello, V. M.; Oliveira, G. V.; Suarez, P.A.Z. J. Turning used frying oil into a new raw material to printing inks. J. Braz. Chem. Soc. **2013**, 24, 314−319.
371. Bhattacharjee, M.; Roy, A. S.; Ghosh, S.; Dey, M. Development of Karanja Oil Based Offset Printing Ink in Comparison with Linseed Oil. J. Oleo Sci. **2011**, 60, 19−24.
372. Ha, Y. B.; Jin, M. Y.; Oh, S. S.; Ryu, D. H. Synthesis of an Environmentally Friendly Phenol-Free Resin for Printing Ink. Bull.Korean Chem. Soc. **2012**, 33, 3413−3416.
373. Shelton, A. M. C.; Posey-Dowty, J. D.; Rios Perdomo, L. G.; Dixon, D. W., Jr.; Lucas, P. L.; Wilson, A. K.; Walker, K. R.; Lawniczak, J. E.; Foulk, R. G.; Phan, H. D.; Freeman, C. C., Jr. Low Molecular Weight Cellulose Mixed Esters and their Use as Low Viscosity Binders and Modifiers in Coating Compositions. US Patent US2011/0282049A1; Eastman Chemical Co., **2011**,.
374. De Meester, A. S.; Callewaert, C.; De Mol, E.; Van Langenhove, H.; Dewulf, J. The resource footprint of biobased products: a key issue in the sustainable development of biorefineries Bio-fuels Bioprod. Biofuels, Bioprod. Biorefin. **2011**, 5, 570−580.
375. Ragauskas, A. J.; Beckham, G. T.; Biddy, M. J.; Chandra, R.; Chen, F.; Davis, M. F.; Davison, B. H.; et al. Lignin Valorization: Improving Lignin Processing in the Biorefinery. Science **2014**, 344, 1246843−1246843.
376. Finch, C. A. In Advanced wood adhesives technology; Pizzi, A.,Ed.; Dekker: New York, **1994**; Chapter V.
377. Michael, D. Matzinger Water-based ink jet ink compositions containing carboxylated lignin. US Patent US6045606A; Westvaco Co., **1999**.
378. Miller, J. E.; Dilling, P., Jr. Water-based printing ink compositions containing a lignin acetate binder US Patent US4612051A; Westvaco Co., **1985**.
379. Vukoje, M.; Miljanić, S.; Hrenović, J.; Rožić, M. Thermochromic ink−paper interactions and their role in biodegradation of UV curable prints. Cellulose **2018**, 25, 6121−6138.

380. Schilling, P. Submicron lignin-based binders for water-based black ink formulations. US Patent US005192361A; Westvaco Co.,**1992**.
381. Polak, J.; Jarosz-Wilkolazka, A. Structure/Redox potential relationship of simple organic compounds as potential precursors of dyes for laccase-mediated transformation. Biotechnol. Prog. **2012**, 28, 93−102
382. Decher, G. Fuzzy Nanoassemblies: Toward Layered Polymeric Multicomposites. Science **1997**, 277, 1232−1237.
383. Glazer, A. N.; Nikaido, H. In Microbial Biotechnology: fundamentals of applied microbiology; W. H. Freeman: San Francisco, **1995**; p 340.
384. Neifar, A.; Ben Abdelmalek, I.; Bouajila, G.; Kolsi, R.; Bradai, M. N.; Abdelmouleh, A.; Gargouri, A.; Ayed, N. Purification and incorporation of the black ink of cuttlefish Sepia officinalis in eye cosmetic products. Color. Technol. 2013, 129, 150−154.
385. Ito, S. A chemist's view of melanogenesis. Pigm. Cell Res. **2003**,16, 230−236.
386. Reale, S.; Crucianelli, M.; Pezzella, A.; d'Ischia, M.; de Angelis, F. Exploring the frontiers of synthetic eumelanin polymers by highresolution matrix-assisted laser/desorption ionization mass spectrometry. J. Mass Spectrom. **2012**, 47, 49−53.
387. Nofsinger, J. B.; Forest, S. E.; Eibest, L. M.; Gold, K. A.; Simon, J. D. Probing the Building Blocks of Eumelanins Using Scanning Electron Microscopy. Pigm. Cell Res. **2000**, 13, 179−184.
388. Kim, D. J.; Ju, K. Y.; Lee, J. K. The Synthetic Melanin Nanoparticles Having An Excellent Binding Capacity of Heavy Metal Ions. Bull. Korean Chem. Soc. **2012**, 33, 3788−3792.
389. Xiao, M.; Chen, W.; Li, W.; Zhao, J.; Hong, Y.; Nishiyama, Y.; Miyoshi, T.; Shawkey, M. D.; Dhinojwala, A. 2018 Elucidation of the hierarchical structure of natural eumelanins. J. R. Soc., Interface **2018**, 15, 20180045.
390. Xiong, F.; Han, Y.; Wang, S.; Li, G.; Qin, T.; Chen, Y.; Chu, F. Preparation and Formation Mechanism of Renewable Lignin Hollow Nanospheres with a Single Hole by Self-Assembly. ACS Sustainable Chem. Eng. **2017**, 5, 2273−2281.
391. Xing, Q.; Buono, P.; Ruch, D.; Dubois, P.; Wu, L.; Wang, W. J. Biodegradable UV-Blocking Films through Core−Shell Lignin−Melanin Nanoparticles in Poly(butylene adipate-co-terephthalate). ACS Sustainable Chem. Eng. **2019**, 7, 4147−4157.
392. Bizzarri, B. M.; Martini, A.; Serafini, F.; Aversa, D.; Piccinino, D.; Botta, L.; Berretta, N.; Guatteo, E.; Saladino, R. Tyrosinase mediated oxidative functionalization in the synthesis of DOPAderived peptidomimetics with anti-Parkinson activity. RSC Adv. **2017**, 7, 20502−20509.
393. Ilani, A.; Krakover, T. Diffusion- and reaction rate-limited redox processes mediated by quinones through bilayer lipid membranes. Biophys. J. **1987**, 51, 161−167.
394. Strube, O. I.; Büngeler, A.; Bremser, W. Site-Specific In Situ Synthesis of Eumelanin Nanoparticles by an Enzymatic Autodeposition- Like Process. Biomacromolecules **2015**, 16, 1608.
395. Xiong, F.; Han, Y.; Wang, S.; Li, G.; Qin, T.; Chen, Y.; Chu, F. Preparation and Formation Mechanism of Renewable Lignin Hollow Nanospheres with a Single Hole by Self-Assembly. ACS Sustainable Chem. Eng. **2017**, 5, 2273−2281.
396. Surwase, S. N.; Patil, S. A.; Jadhav, S. B.; Jadhav, J. P. Optimization of l-DOPA production by Brevundimonas sp. SGJ using response surface methodology. Microb. Biotechnol. **2012**, 5, 731−737.
397. Al Khatib, M.; Harir, M.; Costa, J.; Baratto, M.; Schiavo, I.; Trabalzini, L.; Pollini, S.; Rossolini, G.; Basosi, R.; Pogni, R. Spectroscopic Characterization of Natural Melanin from a Streptomyces cyaneofuscatus Strain and Comparison with Melanin Enzymatically Synthesized by Tyrosinase and Laccase. Molecules **2018**, 23, 1916.
398. Robbins, R. In Chemical and physical behavior of human hair, in Genetic Control/Involvement in Hair Fiber Traits, 5th ed.; Springer: Berlin, Germany, **2012**; Chapter 3, pp 177−203.
399. Yaropolov, A. I.; Skorobogat'ko, O. V.; Vartanov, S. S.; Varfolomeyev, S. D. Laccase. Appl. Biochem. Biotechnol. **1994**, 49, 257−280.
400. Riva, S. Laccases: blue enzymes for green chemistry. Trends Biotechnol. **2006**, 24, 219−226.
401. Crestini, C.; Perazzini, R.; Saladino, R. Oxidative functionalisation of lignin by layer-by-layer immobilised laccases and laccase microcapsules. Appl. Catal., A **2010**, 372, 115−123.
402. Jeon, J. R.; Kim, E. J.; Murugesan, K.; Park, H. K.; Kim, Y. M.; Kwon, J. H.; Chang, Y. S.; et al. Laccase-catalysed polymeric dye synthesis from plant-derived phenols for potential application in hair dyeing: Enzymatic colourations driven by homo- or hetero-polymer synthesis. Microb. Biotechnol. **2010**, 3, 324−335.
403. Polak, J.; Jarosz-Wilkolazka, A. Structure/Redox potential relationship of simple organic compounds as potential precursors of dyes for laccase-mediated transformation. Biotechnol. Prog. **2012**, 28, 93−102.
404. Song, J. E.; Su, J.; Noro, J.; Cavaco-Paulo, A.; Silva, C.; Kim, H. R. Bio-coloration of bacterial cellulose assisted by immobilized laccase. AMB Express **2018**, 8, 19.
405. Kim, S.; Moldes, D.; Cavaco-Paulo, A. Laccases for enzymatic colouration of unbleached cotton. Enzyme Microb. Technol. **2007**, 40, 1788−1793.
406. Slagman, S.; Zuilhof, H.; Franssen, M. C. R. Laccase-Mediated Grafting on Biopolymers and Synthetic Polymers: A Critical Review. ChemBioChem **2018**, 19, 288−311.
407. Maoela, M. S.; Arotiba, O. A.; Baker, P. G.; Mabusela, W. T.; Jahed, N.; Songa, E. A.; Iwuoha, E. I. Electroanalytical determination of catechin flavonoid in ethyl acetate extracts of medicinal plants. Int. J. Electrochem. Sci. **2009**, 4, 1497−1510.
408. Yang, J.; Cohen Stuart, M. A.; Kamperman, M. Jack of All Trades: Versatile Catechol Crosslinking Mechanisms. Chem. Soc. Rev. **2014**, 43, 8271−8298.

409. Nyanhongo, G. S.; Kudanga, T.; Nugroho Prasetyo, E.; Gubitz, G. M. Enzymatic Polymer Functionalisation: Advances in Laccase and Peroxidase Derived Lignocellulose Functional Polymers. Adv. Biochem. Eng./Biotechnol. **2010**, 125, 47−68.
410. Ajao, O.; Jeaidi, J.; Benali, M.; Restrepo, A. M.; El Mehdi, N.; Boumghar, Y. Quantification and Variability Analysis of Lignin Optical Properties for Colour-Dependent Industrial Applications. Molecules **2018**, 23, 377.
411. Aydemir, C.; Yenidogan, S. Light fastness of printing inks: A review. Journal of Graphic Engineering and Design. **2018**, 9, 37−43.
412. Mokrzycki, W. S.; Tatol, M. Colour difference Δ E-A survey. Machine Graphics and Vision. **2011**, 20, 383−411.
413. Solano, F. Melanins: Skin Pigments and Much More Types, Structural Models, Biological Functions, and Formation Routes. New Journal of Science. **2014**, 2014, 1−28.
414. Ragimov, A. V.; Mamedov, B. V.; Liogonkii, B. The alkali initiated polymerization of p-benzoquinone. Polym. Sci. U.S.S.R. **1977**, 19, 2922−2928.
415. Erdocia, X.; Prado, R.; Corcuera, M.Á.; Labidi, J. Base catalyzed depolymerization of lignin: Influence of organosolv lignin nature. Biomass Bioenergy **2014**, 66, 379−386.
416. S. Schoffelen and J. C. Van Hest, Curr. Opin. Struct. Biol., **2013**, 23, 613–621.
417. Y. Liu, T. L. Ogorzalek, P. Yang, M. M. Schroeder, E. N. G. Marsh and Z. Chen, J. Am. Chem. Soc., **2013**, 135, 12660–12669.
418. J. Turkov´a, J. Chromatogr. B: Biomed. Sci. Appl., **1999**, 722, 11–31.
419. J. Huang, W. Zhuang, C. Wei, L. Mu, J. Zhu, Y. Zhu and H. Ying, Process Biochem., **2018**, 64, 160–169.
420. F. Jia, S. K. Mallapragada and B. Narasimhan, Ind. Eng. Chem. Res., **2015**, 54, 10212–10220.
421. O. Idan and H. Hess, Curr. Opin. Biotechnol., **2013**, 24, 606–611.
422. H. H. Nguyen, S. H. Lee, U. J. Lee, C. D. Fermin and M. Kim, Materials, **2019**, 12, 121.
423. X. Zhu, J. Huang, J. Liu, H. Zhang, J. Jiang and R. Yu, Nanoscale, **2017**, 9, 5658–5663.
424. M. Stanisz, Ł. Klapiszewski and T. Jesionowski, Chem. Eng. J., **2020**, 397, 125409.
425. A. Je˛drzak, T. Re˛bi´s, M. Kuznowicz and T. Jesionowski, Int. J. Biol. Macromol., **2019**, 127, 677–682.
426. H. Yao, Q. Gan, J. Peng, S. Huang, M. Zhu and K. Shi, Sensors, **2016**, 16, 563.
427. Y. Yong, R. Su, X. Liu, W. Xu, Y. Zhang, R. Wang and Z. Liu, Biochem. Eng. J., **2018**, 129, 26–32.
428. W. Xu, Y. Yong, Z. Wang, G. Jiang, J. Wu and Z. Liu, ACS Sustainable Chem. Eng., **2016**, 5, 90–96.
429. L. Chen, Y. Fu, N. Wang, A. Yang, Y. Li, J. Wu and F. Yan, ACS Appl. Mater. Interfaces, **2018**, 10, 18470–18477.
430. A. F. Che, Z. M. Liu, X. J. Huang, Z.-G. Wang and Z. K. Xu, Biomacromolecules, **2008**, 9, 3397–3403.
431. F. Wu and S. D. Minteer, Biomacromolecules, **2013**, 14, 2739–2749.
432. B. C. Fish and L. U. Thompson, J. Agric. Food Chem., **1991**, 39, 727–731.
433. Y. Zhang, Y. Yong, J. Ge and Z. Liu, ACS Catal., **2016**, 6, 3789–3795.
434. A. Makky, J. P. Michel, P. Maillard and V. Rosilio, Biochim. Biophys. Acta Rev. Biomembr., **2011**, 1808, 656–666.
435. W. Xu, Y. Yong, Z. Wang, G. Jiang, J. Wu and Z. Liu, ACS Sustainable Chem. Eng., **2016**, 5, 90–96.
436. G. Palazzo, G. Colafemmina, C. Guzzoni Iudice and and A. Mallardi, Sens. Actuators, B, **2014**, 202, 217–223.
437. O. Idan and H. Hess, Curr. Opin. Biotechnol., **2013**, 24, 606–611.
438. V. Hitaishi, R. Clement, N. Bourassin, M. Baaden, A. de Poulpiquet, S. Sacquin-Mora and E. Lojou, Catalysts, **2018**,8, 192.
439. J. Fu, Y. R. Yang, A. Johnson-Buck, M. Liu, Y. Liu, N. G. Walter and H. Yan, Nat. Nanotechnol., **2014**, 9, 531–536.
440. A. Kuzmak, S. Carmali, E. von Lieres, A. J. Russell and S. Kondrat, Sci. Rep., **2019**, 9, 1.
441. G. N. Rivi`ere, A. Korpi, M. H. Sipponen, T. Zou, M. A. Kostiainen and M. ¨Osterberg, ACS Sustainable Chem.Eng., 2020, 8, 4167–4177.
442. F. P. Ramanery, A. A. Mansur and H. S. Mansur, Nanoscale Res. Lett., 2013, 8, 512.
443. M. Mayer, D. Dedovets, Y. Guari, J. Larionova, J. Long and J. Causse, J. Colloid Interface Sci., **2017**, 505, 364–372.
444. J. M. Khan, M. S. Khan, A. Qadeer, M. A. Alsenaidy, A. Ahmed, N. A. Al-Shabib and R. H. Khan, Colloids Surf., **2017**, 522, 494–502.
445. S. K. Chaturvedi, J. M. Khan, M. K. Siddiqi, P. Alam and R. H. Khan, Int. J. Biol. Macromol., 2016, 83, 315–325.
446. J. M. Khan, M. R. Khan, P. Sen, A. Malik, M. Irfan and R. H. Khan, J. Mol. Liq., **2018**, 269, 796–804.
447. B. A. M. Rocha, C. S. Teixeira, J. C. Silva-Filho, R. B. N´obrega, D. B. Alencar, K. S. Nascimento and P. Delatorre, Int. J. Biol. Macromol., **2015**, 72, 1136–1142.
448. D. H. Nagaraju, T. Rebis, R. Gabrielsson, A. Elfwing, G. Milczarek and O. Ingan¨as, Adv. Energy Mater., **2013**, 4, 1300443.
449. K. Gawluk, A. Modrzejwska-Sikorska, T. Re˛bi´s and G. Milczarek, Catalysts, **2017**, 7, 392.
450. T. Kamgaing, K. I. Tonle and Y. F. Emanbou, J. Anal. Chem., **2013**, 8, 64–77.
451. V. K. Thakur, M. K. Thakur, P. Raghvan and P. Kessler, ACS Sustainable Chem. Eng., **2014**, 2, 1072–1092.
452. P. C. Ray, Z. Fan, R. A. Crouch, S. S. Sinha and A. Pramanik, Chem. Soc. Rev., **2014**, 43, 6370–6404.
453. Y. He, Y. Li, S. Mukherjee, Y. Wu, H. Yan and H. P. Lu, J. Am. Chem. Soc., **2011**, 133, 14389–14395.
454. W. M. Shih, Z. Gryczynski, J. R. Lakowicz and J. A. Spudich, Cell, **2000**, 102, 683–694.
455. Y. Zhang, F. Lyu, J. Ge and Z. Liu, Chem. Commun., **2014**, 50, 12919–12922.
456. A. Kuzmak, S. Carmali, E. von Lieres, A. J. Russell and S. Kondrat, Sci. Rep., **2019**, 9, 1.
457. A. Palumbo, A. Napolitano, P. Barone and M. d' Ischia, Chem. Res. Toxicol., **1999**, 12, 1213–1222.
458. J. Li, M. A. Baird, M. A. Davis, W. Tai, L. S. Zweifel, K. M. A. Waldorf and X. Gao, Nat. Biomed. Eng., **2017**, 1, 6.